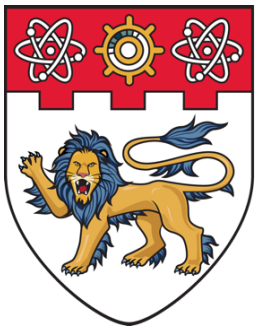

NANYANG TECHNOLOGICAL UNIVERSITY
SINGAPORE

Computational Modelling of the Biological and Social Factors of Type 2 Diabetes

Pritha Dutta

Interdisciplinary Graduate Programme

HealthTech NTU

2021

Computational Modelling of the Biological and Social Factors of Type 2 Diabetes

Pritha Dutta

Interdisciplinary Graduate Programme

A thesis submitted to the Nanyang Technological University
in partial fulfillment of the requirements for the degree of
Doctor of Philosophy

2021

Statement of Originality

I hereby certify that the work embodied in this thesis is the result of original research, is free of plagiarised materials, and has not been submitted for a higher degree to any other University or Institution.

8.1.2022
. . . . . .
Date

Pritha Dutta
. . . . . .
[Pritha Dutta]

Supervisor Declaration Statement

I have reviewed the content and presentation style of this thesis and declare it is free of plagiarism and of sufficient grammatical clarity to be examined. To the best of my knowledge, the research and writing are those of the candidate except as acknowledged in the Author Attribution Statement. I confirm that the investigations were conducted in accord with the ethics policies and integrity standards of Nanyang Technological University and that the research data are presented honestly and without prejudice.

8 JAN 2022

Date

[Dr. Cheong Siew Ann]

Authorship Attribution Statement

This thesis contains material from 3 papers published in the following peer-reviewed journals and one paper under preparation in which I am listed as an author.

Chapter 2 is published as L. Crielaard, P. Dutta, R. Quax, M. Nicolaou, N. Merabet, K. Stronks, and P.M.A Sloot. Social norms and obesity prevalence: From cohort to system dynamics models. *Obesity Reviews*, 21(9): e13044 (2020). DOI: 10.1111/obr.13044

The contributions of the co-authors are as follows:

- Loes Crielaard, Dr. Nicolaou and Prof. Stronks conceptualized the study.
- I along with Loes Crielaard, Dr. Quax, Dr. Merabet, and Prof. Sloot were responsible for the computational modelling component of the study.
- I and Loes Crielaard drafted the manuscript which was revised by Prof. Sloot, Dr. Nicolaou and Prof. Stronks, Dr. Quax and Dr. Merabet.

Chapter 3 is published as P. Dutta, R. Quax, L. Crielaard, and P.M.A Sloot. Inferring temporal dynamics from cross-sectional data using Langevin dynamics. Royal Society Open Science, 8(11): 211374 (2021). DOI: 10.1098/rsos.211374}

The contributions of the co-authors are as follows:

- Dr. Quax conceptualized the study.
- I along with Dr. Quax and Luca Badiali performed the mathematical derivations and carried out the simulations and analysis.
- I along with Dr. Quax drafted the manuscript which was revised by Loes Crielaard and Prof. Sloot.

Chapter 4 is published as P. Dutta, L. Ma, Y. Ali, P.M.A. Sloot, and J. Zheng. Boolean network modeling of β-cell apoptosis and insulin resistance in type 2 diabetes mellitus. *BMC systems biology*, 13(2):36, 2019. DOI: 10.1186/s12918-019-0692-0.

The contributions of the co-authors are as follows:

- Dr. Zheng initiated the project and idea.
- I along with Dr. Ma constructed the model.
- I carried out the simulations and analysis.
- Dr. Ali provided biological input.
- Prof. Sloot gave suggestions on modeling.
- I drafted the manuscript with critical input from Dr. Zheng. The manuscript was revised by all authors.

Chapter 5 is a paper under preparation: P. Dutta, N. Merabet, R. Quax, F. Carlotti, and P.M.A Sloot. An integrative approach to modelling compromised beta-cell identity in Type 2 Diabetes.

The contributions of the co-authors are as follows:

- I conceptualized the study with the help of Dr. Merabet and Dr. Carlotti.
- I along with Dr. Merabet and Dr. Quax constructed the model and the rate equations.
- I performed the simulations and analyses with input from Dr. Quax, Dr. Merabet and Prof. Sloot.
- I prepared the manuscript with critical input from Dr. Merabet, Dr. Quax and Prof. Sloot.

8.1.2022

. . . . . .

Date

. . . . . .

[Pritha Dutta]

Acknowledgements

First and foremost, my sincere thanks to Prof. Peter Sloot for his valuable guidance and support throughout my doctoral studies.

I am very grateful to Dr. Rick Quax for helping me at each step of my PhD. Particularly, his advice on computational modelling has greatly helped my research.

I would also like to thank Loes Crielaard, Nadege Merabet, Dr. Mary Nicolaou and Prof. Stronks. It has been a great learning experience working with them.

I would like to thank my TAC members, Dr. Cheong Siew Ann, Dr. Yusuf Ali, and Dr. Jie Zheng for their valuable advice on my research. I am grateful to my friends from CI: Joey, Alex, Vivek, Jaeyoung, and Bee Wee for their support during this journey.

On the personal front, I am grateful to my parents and brother for their continuous moral support and trust on my capabilities. Without their support this thesis would not have been possible. I would also like to thank my friends: Surjyasish, Debjyoti, Sandipan, Debanjana, Snehasish and Mainak for their support during this journey.

Contents

List of Figures

List of Tables

Symbols and Acronyms

Acronyms

AKT (PKB)	Protein kinase B
APAF1	Apoptotic protease-activating factor 1
ASK1	Apoptosis signal-regulating kinase 1
ATF4	Activating transcription factor 4
ATF6	Activating Transcription Factor 6
BCL2	B-cell lymphoma 2
BMI	Body mass index
BMR	Basal metabolic rate
CHOP	C/EBP homologous protein
CLD	Causal loop diagram
DIABLO	Direct IAP-binding protein with low pI
EIF2S1	Eukaryotic translation initiation factor 2 subunit 1
ER	Endoplasmic reticulum
ETC	Electron transport chain
FADD	Fas-associated death domain-containing protein
FasL	Fas ligand
FasR	Fas receptor
FFA	Free fatty acids
FOXO1	Forkhead box protein O1
GADD34	Growth arrest and DNA damage-inducible protein
G6PC	Glucose-6-phosphatase
GLUT1	Glucose transporter type 1
GLUT4	Glucose transporter type 4
GRP78	78 kDa glucose regulated protein
GS	Glycogen synthase

GSK3	Glycogen synthase kinase
HtrA2	High temperature requirement protein A2
i.i.d.	Independent and identically distributed
IL-6	Interleukin-6
INSR	Insulin receptor
IP3R	Inositol trisphosphate receptor
IRE1	Inositol Requiring 1
IRS	Insulin receptor substrate
JAK	Janus kinase
JNK	c-Jun N-terminal kinase
MCU	Mitochondrial Ca^{2+} uniporter
mTORC1	Mammalian target of rapamycin complex 1
mTORC2	Mammalian target of rapamycin complex 2
NCX	Na^{+}/Ca^{2+} exchanger
p38MAPK	p38 mitogen-activated protein kinase
PAL	Physical activity level
PDX1	Pancreatic and duodenal homeobox 1
PEPCK	Phosphoenolpyruvate carboxykinase
PERK	PKR-like ER kinase
PI3K	Phosphatidylinositide 3-kinase
PMCA	Plasma membrane Ca^{2+}-ATPase
Rheb	Ras homolog enriched in brain
RIPK1	Receptor-interacting serine/threonine-protein kinase 1
ROS	Reactive oxygen species
S6K	S6 kinase
SCC	Strongly connected component
SDM	system dynamics model
SERCA	Sarco/endoplasmic reticulum Ca^{2+}-ATPases
SOCS3	Suppressor of cytokine signaling 3
STAT3	Signal transducer and activator of transcription 3
T2D	Type 2 Diabetes
TCA	Tricarboxylic acid
TDEE	total daily energy expenditure
TDEI	total daily energy intake
TNFα	Tumor necrosis factor α

TNFR1	Tumor necrosis factor receptor superfamily member 1A
TNFR2	Tumor necrosis factor receptor superfamily member 1B
TRADD	TNFR1-associated death domain
TRAF2	TNF-receptor-associated factor 2
TRB3	Tribbles homolog 3
TSC	Tuberous sclerosis complex
UPR	Unfolded protein respons
VGCC	Voltage-gated calcium channel
XBP1	X-box protein binding 1
XIAP	X-linked inhibitor of apoptosis protein

Summary

Type 2 diabetes (T2D) is a metabolic disorder characterized by high levels of blood glucose resulting from defects in insulin secretion and insulin action. Of all the diagnosed cases of diabetes, T2D accounts for approximately 90% of the cases. The pathogenesis of T2D involves both biological factors as well as social factors. These factors have intricate interactions with each other, and to study the behaviour of such complex systems computational models are required. Computational models provide a framework to summarize existing knowledge, enable competing hypotheses to be compared qualitatively and quantitatively, and facilitate the interpretation of complex data. Moreover, computational models allow questions to be investigated that are difficult to approach experimentally. Theories can be tested in context, identifying the gaps in our understanding and potentially leading to new hypotheses.

In this thesis, three computational models are proposed: a system dynamics model of the system of social norms regarding body weight perception and obesity prevalence, a Boolean network model of the insulin resistance pathway and pancreatic beta-cell apoptosis pathway, and an ordinary differential equation model of the system of signalling components involved in insulin gene expression and beta-cell identity. In addition, this thesis also includes two methods for inferring computational models from cross-sectional data.

Group-level obesity can be seen as an emergent property of a complex system, consisting of feedback loops between individual body weight perception, individual weight-related behaviour and group-level social norms (a product of group-level 'normal' body mass index (BMI) and socio-cultural 'ideal' BMI). As overweight becomes normal, the norm might be counteracting health awareness in shaping individual weight-related behaviour. System dynamics modelling facilitates understanding and simulating this system's emergent behaviour. Six system dynamics models (SDMs) were constructed based on an expert-informed causal loop diagram and data from six socio-cultural groups (Dutch, Moroccan and South-Asian

Surinamese men and women). The SDMs served to explore the effect of three scenarios on group-level BMI: 'what if' weight-related behaviour were driven by (1) health awareness, (2) norms or (3) a combination of the two. Median BMI decreased approximately 50% and 30% less in scenarios 2 and 3, respectively, than in 1. In men, the drop in BMI was approximately two times larger in scenario 1 versus 3, whereas in women, the drop was approximately equal in these scenarios. This study indicates that the overweight norm in men holds group-level BMI close to overweight despite health awareness. Since norms are counteracting health awareness less strongly in women, other drivers of obesity must be more relevant.

The SDMs were calibrated using a multi-ethnic cohort data, which is a cross-sectional data; however, to study how the system evolves over time, longitudinal data is required. A method was developed to generate pseudo-time series data from the available cross-sectional data by generating a set of qualitative 'data-generating assumptions'. These assumptions are based on the system's temporal behaviour that is expected to exist across all groups. An example of such an assumption is that, on average, an individual can lose 2 kg/month. Here, linear dynamics was assumed for the system's short-term behaviour. The time steps in the SDMs were assumed as months to identify an approximate timescale of the system's behaviour. However, this timescale is not exact, and therefore, the relative trends are more important to interpret than the exact timescale they occur on.

Another method was developed for inferring computational models from cross-sectional data using Langevin dynamics. This method can be applied to any system that can be described as effectively following a free energy landscape which is stable and independent of any external force. A crucial assumption in this method is that the data-points are gathered from a system in (local) equilibrium. The result is a set of stochastic differential equations which capture the temporal dynamics, by assuming that groups of data-points are subject to the same free energy landscape and amount of noise. This is a 'baseline' method which initiates the development of computational models which can be iteratively enhanced through the inclusion of expert knowledge. The proposed method can only estimate directions of progression, not velocities. Hence, the timescale of the predicted dynamics remains unknown. This timescale can be estimated from the data or from known statistical properties of the rates of change in reality; for instance, the fact that the maximum sustainable rate of weight loss observed in a population is about 2 kg per

month. This method showed significant predictive power when compared against two population-based longitudinal datasets. The proposed method can facilitate the use of cross-sectional datasets to obtain an estimate of the underlying dynamics of the respective processes.

The metabolic disorder of T2D is characterized by insulin resistance, beta-cell dysfunction, and apoptosis. Chronic hyperglycemia causes deterioration of beta-cell function through oxidative stress, endoplasmic reticulum (ER) stress, and cytokines. In this thesis, two computational models are proposed to study beta-cell dysfunction in T2D. The first computational model is a Boolean network model integrating the insulin resistance pathway with the beta-cell apoptosis pathway. This model has five input signals, namely, ER stress, oxidative stress, tumor necrosis factor α (TNFα), Fas ligand (FasL), and interleukin-6 (IL-6). Simulations were performed using random order asynchronous update and with different combinations of the input signals. The model simulations were able to reproduce the expression levels of genes in T2D as reported in the literature. This model can be useful in studying the qualitative behaviour of important genes in the presence of oxidative stress, ER stress, and pro-inflammatory cytokines.

Compromised beta-cell identity is emerging as an important contributor of beta-cell dysfunction in T2D. Most evidence suggests that this identity loss results from hyperglycemia-induced inactivation of transcription factors involved in mature beta-cell identity. Beta-cells with compromised identity gradually become dysfunctional with defective insulin secretion in response to glucose. An integrated mathematical model was developed to study the underlying mechanisms that regulate two important beta-cell identity transcription factors and regulators of insulin promoter activity, PDX1 and MAFA, and lead to their downregulation in the presence of chronic hyperglycemia. The aim of this work was to investigate the loss of beta-cell function through loss of beta-cell identity in the presence of chronic hyperglycemia. This model was used to study the changes in PDX1, MAFA and insulin mRNA levels under the effect of different glucose concentrations. In addition, this model was used to analyse the effect of different inhibitors of PDX1 and MAFA on these transcription factors and insulin mRNA levels. This integrated model can be a useful tool to further extend our understanding of the mechanisms leading to compromised beta-cell identity and beta-cell dysfunction in the presence of chronic hyperglycemia and identify potential intervention targets.

Overall, the three studies of the social and biological factors of T2D demonstrate the importance of computational models in understanding the complex systems involved in the pathogenesis of T2D and designing effective intervention strategies. These computational models facilitate the evaluation of hypothetical scenarios in silico and simulation of the effect of interventions. This is especially advantageous for systems for which comparing counterfactual scenarios would not be possible or would be difficult in vivo.

Chapter 1

Introduction

1.1 Motivation and Objectives

Diabetes is a chronic condition that can have serious implications on the quality of life of the affected individuals, their families, and societies. According to the International Diabetes Federation (IDF), in 2019, the global prevalence of diabetes among adults aged 20-79 years was estimated to be 9.3% (463 million people), which is projected to rise to 10.2% (578 million) by 2030 and 10.9% (700 million) by 2045 [1]. The prevalence is higher in urban (10.8%) than rural (7.2%) areas, and in high-income (10.4%) than low-income countries (4.0%) [1]. One in two adults with diabetes (232 million people) are not aware of this fact. 10% of global health expenditure is spent on diabetes [1].

There are two main types of diabetes: type 1 diabetes (T1D), and type 2 diabetes (T2D). Other types of diabetes include gestational diabetes mellitus (GDM) and monogenic diabetes [1]. T2D is the most common type of diabetes, accounting for approximately 90% of total global cases of diabetes [1]. T2D occurs mostly in older adults, but due to an increase in the prevalence of obesity as a result of physical inactivity and unhealthy diet, it is increasingly diagnosed in children, adolescents and younger adults. T2D is a chronic metabolic disorder that results from defects in both insulin secretion and insulin action, which causes glucose levels to increase above physiological levels. In T2D, chronic hyperglycemia results in a state of insulin resistance, where insulin fails to facilitate glucose uptake by the body's peripheral cells, such as skeletal muscle, adipose tissue and liver. This leads to an

increased workload on the pancreatic beta-cells to produce more insulin. When this workload persists for longer periods, it leads to beta-cell dysfunction and failure.

T2D results from interaction between biological and social factors. To gain a comprehensive understanding of the pathogenesis of T2D, it is essential to study both the complex system of the biological factors as well as the complex system of the social factors, such as diet, physical activity, and ethnicity. Computational modelling can serve as a powerful tool to study complex systems, as it provides quantitative descriptions of the interactions between individual components as well as the control they exert over the whole system. Computational models allow the replication of the behaviour of the system based on known properties of the system components. These models can serve a wide variety of roles, including hypothesis testing, generating new insights, deepening understanding, tracing chains of causation, doing sensitivity analyses, integrating knowledge, and inspiring new approaches. In this thesis, three computational models have been developed to study the complex systems of the biological factors and the social factors of T2D.

1.2 Computational models of the social factors of T2D

A growing argument is that individuals are more likely to underestimate their own body weight as obesity prevalence increases [2]. This is because body weight perception, a determinant of overweight and obesity [3], is partly determined via social comparison [4]. Body weight perception is thus affected by what is normal. It however also affects what is normal via its impact on obesity prevalence, inducing feedback loops that may over time result in complex behaviour, possibly inducing group-level obesity [5] as an emergent property. Previous research have indicated that norms affect individual physical activity and dietary habits. The group-level weight strongly influences an individual's intention to change his/her weight-related behaviour [6]. It has been shown that weight loss achieved through interventions on weight-related behaviour is not long-lasting in most cases [7]. One possible explanation is that norms may counteract health awareness in shaping individual health-related behaviour. In that regard, the relevance of addressing norms

to change individual health-related behaviour as a policy strategy has received attention with respect to smoking [8]. Understanding the effect of the feedback loops between individual characteristics and group-level processes over time can guide similar policy strategies aiming to lower obesity prevalence, in which justice can be done to influences at both levels.

In the first study, a computational model of the system of social norms regarding body weight perception and obesity prevalence was developed using system dynamics models (SDMs). SDMs can reveal how variables interact by expressing the causal links between them using difference equations and hence can aid in understanding and simulating a complex system's non-linear behaviour in different scenarios [9]. This is valuable when evaluating the effect of 'what if' scenarios which is infeasible using conventional empirical methods, as holds for comparing the effect of health awareness versus norms on group-level body mass index (BMI). The SDMs for this study were designed to test the hypothesis that as overweight becomes normal, the norm might be counteracting health awareness in shaping individual weight-related behaviour. An expert-informed causal loop diagram (CLD) was first designed to conceptualize this system, which was subsequently used as a template for functioning SDMs. This system consists of feedback loops between individual body weight perception, individual weight-related behaviour and group-level norms towards body weight. These norms can be conceptualized as a product of social comparison and cultural preferences [4]: what is considered normal, i.e. group-level BMI, and ideal, i.e. socio-cultural ideal BMI. The SDMs simulated this system's behaviour for a multi-ethnic cohort in Amsterdam (registered in the HELIUS study) [10]—for whom body weight perception was measured. This data was used to calibrate the SDMs. These SDMs served to explore the effect of three scenarios on group-level BMI: 'what if' weight-related behaviour were driven (1) only by health awareness, (2) only by norms and (3) by their interaction, i.e. health awareness and norms.

The HELIUS [10] data is cross-sectional; however, to study how the system evolves over time, longitudinal data is required. Two different methods have been proposed in this work to generate pseudo-time series data from available cross-sectional data. The first method which was developed as part of the first study involved generating a set of qualitative 'data-generating assumptions'. These assumptions were based on the system's temporal behaviour that was expected to exist across all groups.

An example of such an assumption is that, on average, an individual can lose 2 kg/month [11, 12]. Here, linear dynamics was assumed for the system's short-term behaviour. In this study, the time steps in the SDMs were assumed as months to identify an approximate timescale of the system's behaviour. However, this timescale is not exact, and therefore, the relative trends are more important to interpret than the exact timescale they occur on.

The second method for inferring computational models from cross-sectional data was inspired from Langevin dynamics. This method would be applicable to systems where the data-points follow a free energy landscape which does not change with time and is not influenced by external force. The free energy landscape, which is a mapping of all possible states of the data-points in the system, was reconstructed from the cross-sectional data by assuming that groups of data-points having similar features follow similar trajectories. A free energy landscape can be considered analogous to an uneven hillside and the data-points in the landscape as balls rolling down the hillside. The balls will eventually come to rest in a stable state in the valleys. These valleys are the attractors in the free energy landscape. Trajectories across a landscape correspond to the progression of the data-points. This method estimates the free energy landscape based on the probability distribution of the data-points. Roughly speaking, the free energy landscape is approximately the inverse of the probability distribution of the data-points. Thus, the attractors in this estimated energy landscape will approximately correspond to the peaks in the probability distribution. For instance, following this assumption, a free energy landscape estimated from a probability distribution of the BMI values of a group of individuals will have attractors that will correspond approximately to the most probable BMI values in that group of individuals.

The proposed method is based on three assumptions. The first assumption is that the distribution depends only on the variable of interest. The second assumption is that the distribution of the data-points has converged to a stable distribution at the time of observation. The third assumption is that each data-point tends to follow the same free energy landscape in a 'downslope' manner. The temporal dynamics of the data-points were modelled using stochastic differential equations based on Langevin dynamics and the above-stated assumptions. The proposed method initiates the process of development of computational models from cross-sectional data and these 'baseline' models can be iteratively enhanced through the

inclusion of expert knowledge.

1.3 Computational models of the biological factors of T2D

To understand the pathogenesis of T2D, it is also necessary to study the underlying molecular mechanisms leading to this disorder. T2D results from defects in both insulin secretion and insulin action, which causes glucose levels to increase above physiological levels. The pancreas plays an important role in maintaining glucose homeostasis (Figure 1.1). When blood glucose levels are high, the pancreas secretes insulin which promotes glucose uptake into insulin-dependent muscle and adipose tissues and glycogenesis in the liver. When blood glucose levels are low, the pancreas secretes glucagon, which increases blood glucose levels through glycogenolysis. The pancreas consists of both exocrine and endocrine cells [13]. The endocrine cells account for only 1-2% of the pancreas and are clustered together forming the islets of Langerhans. These islets consist of five different cell types releasing various hormones [13]. Of these cell types two play an important role in maintaining glucose homeostasis; these are the glucagon producing alpha-cells which constitute 15-20% of the islets and the insulin-producing beta-cells which account for 65-80% of the islets [13]. The other cell types are the pancreatic-polypeptide producing gamma-cells, somatostatin-producing delta-cells, and ghrelin-producing epsilon cells [13]. When blood glucose level rises, the beta-cells secrete insulin. The insulin then binds to the insulin receptors on the peripheral cells, such as skeletal muscle, adipose tissue and liver, and facilitate glucose uptake by these cells. In the presence of chronic hyperglycemia, these peripheral cells stop responding to insulin and as a result lose their ability to absorb glucose. This state is termed as insulin resistance. Insulin resistance, in turn, increases the workload on beta-cells to produce more insulin. If this persists for a long time then it leads to beta-cell dysfunction and apoptosis.

The endoplasmic reticulum (ER) in the beta-cells is responsible for protein synthesis. Hyperglycemia places a high demand for insulin synthesis on the ER. A high inward flux of polypeptide molecules into the ER can overwhelm the protein-folding machinery, leading to an imbalance and the accumulation of unfolded and

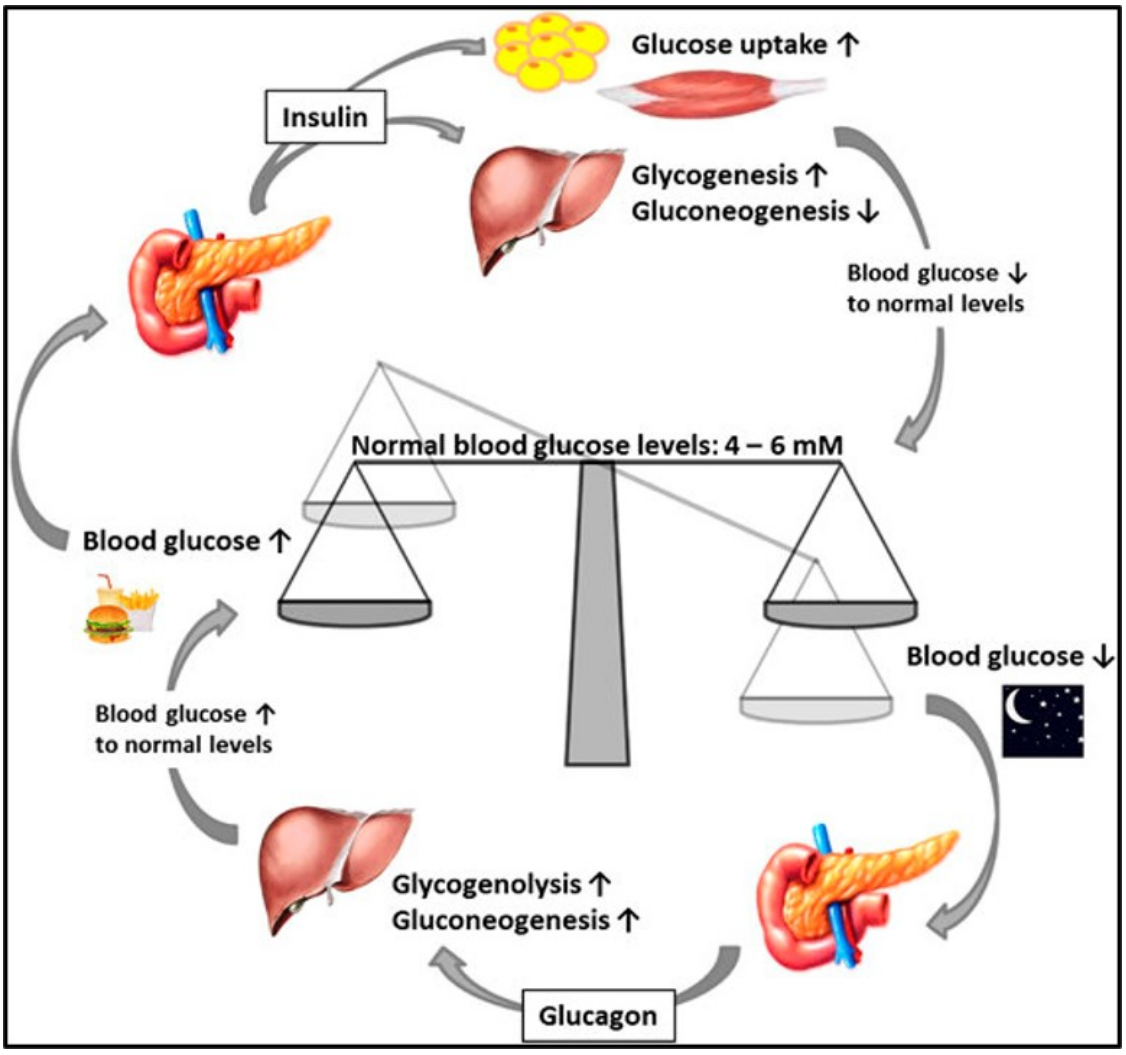

FIGURE 1.1: Regulation of glucose homeostasis by the pancreas. Figure is taken from [13].

misfolded proteins, which is toxic for the cell. This imbalance is known as "ER stress". To counteract this stress, the ER activates the unfolded protein response (UPR) [14]. The UPR initially attempts to mitigate ER stress by degrading misfolded proteins and preventing their further accumulation. However, when ER stress is not mitigated, the UPR activates the apoptosis signals [15, 16]. Hyperglycemia also causes oxidative stress by increasing the generation of reactive oxygen species (ROS) [17, 18]. Beta-cells are vulnerable to oxidative stress due to the low expression of anti-oxidant enzymes such as catalase and glutathione peroxidase [19, 20]. The increased level of ROS in the presence of hyperglycemia triggers the activation of oxidative stress-sensitive signaling pathways [21, 22]. Hyperglycemia also induces pro-inflammatory cytokines [23], such as, FasL, TNFα,

and IL-6, which activate signalling pathways for beta-cell apoptosis [24–28] as well as insulin resistance [29, 30].

There are several well-established computational modelling approaches for biological networks, such as, ordinary differential equations (ODEs) [31], Boolean networks [32], Petri nets [33], and agent-based modelling [34].
(1) ODE-based modelling approaches [31]: ODE based approaches are continuous dynamical modelling strategies. ODE-based methods reflect the time-varying effects of biological processes by representing interactions between different biological molecules, such as proteins and metabolites, using differential equations.These ODE-based methods are of 3 types: law of mass action, Hill function, and Michaelis-Menten kinetics. The choice of a specific method depends on the biological questions or the experimental data. ODE-based models are suitable for modelling the continuous dynamical changes in biological networks.
(2) Boolean network modelling approaches [32]: A Boolean network is a directed graph, where each node is represented by binary states, 1 and 0, denoting activation and inhibition of a protein respectively. Thus, Boolean network models can be used to simulate only the qualitative behaviour of a system. In these models, time is considered as discrete and at each time step, a new state of the network is determined by applying the defined Boolean functions. Boolean networks are useful for modelling large complex biological networks, where continuous ODE-based modelling is difficult due to unknown kinetic parameters.
(3) Petri net (PN)-based modelling approaches [33]: PN based approaches are graphical modelling approaches. A PN is a directed, weighted bipartite graph connecting places (proteins) and transitions (activation or inhibition events) through arcs. Places may store tokens but transitions cannot store tokens. The state of a net is its assignment of tokens to places. A transition is enabled when the number of tokens in each of its input places is at least equal to the arc weight going from the place to the transition. An enabled transition may fire at any time. When fired, the tokens in the input places are moved to output places, according to arc weights and place capacities. This results in a new state of the net. PN is a discrete dynamical modelling strategy. A disadvantage of PNs is that the graphical representation may become too complex for analysis.
(4) Agent-based modelling (ABM) approaches [34]: In ABM, a system is modeled as a collection of autonomous decision-making entities called agents. Each agent individually assesses its situation and makes decisions on the basis of a set of rules.

Thus, an ABM consists of a system of agents and the relationships between them. The cornerstone of ABM is its ability to understand macro phenomena by studying the behaviour at micro-scale level.
In this thesis, two computational models have been developed using ODE-based modelling approach and Boolean network modelling approach.

To study how chronic hyperglycemia causes insulin resistance and beta-cell apoptosis, a Boolean network model was developed in this work, which consists of the pathways involved in insulin resistance and beta-cell apoptosis. The aim of this model was to simulate how the different components evolve towards the state of beta-cell apoptosis in the presence of ER stress, oxidative stress, and the cytokines: TNFα, FasL, and IL-6.

The paradigm of beta-cell apoptosis being the primary inducer of beta-cell failure in T2D has been recently challenged. Beta-cells obtained from T2D cadaveric organ donors were found to have only a small number of apoptotic cells despite showing marked decrease in insulin immunostaining [35], suggesting that apoptosis may not be the predominant cause behind the decrease in beta-cell mass. Talchai et al. [36], in a landmark study, demonstrated that apoptosis is not the main contributor to loss of beta-cell function in T2D, rather loss of beta-cell function occurs due to a perturbation to the beta-cell identity. The loss of beta-cell identity involves impaired expression of specific beta-cell transcription factors [37] which leads to de-differentiation of beta-cells into progenitor cells or trans-differentiation into other pancreatic islet cells, such as alpha-cells [38–44] (Figure 1.2).

Compromised beta-cell identity is emerging as an important contributor of beta-cell dysfunction in T2D. Most evidence suggests that this identity loss results from hyperglycemia-induced inactivation of transcription factors involved in mature beta-cell identity. Beta-cells with compromised identity gradually become dysfunctional with defective insulin secretion in response to glucose. An integrated mathematical model was developed in this work to study the underlying mechanisms that regulate two important beta-cell identity transcription factors and regulators of insulin promoter activity, PDX1 and MAFA, and lead to their down-regulation in the presence of chronic hyperglycemia. The aim of this work was to investigate the loss of beta-cell function through loss of beta-cell identity in the presence of chronic hyperglycemia.

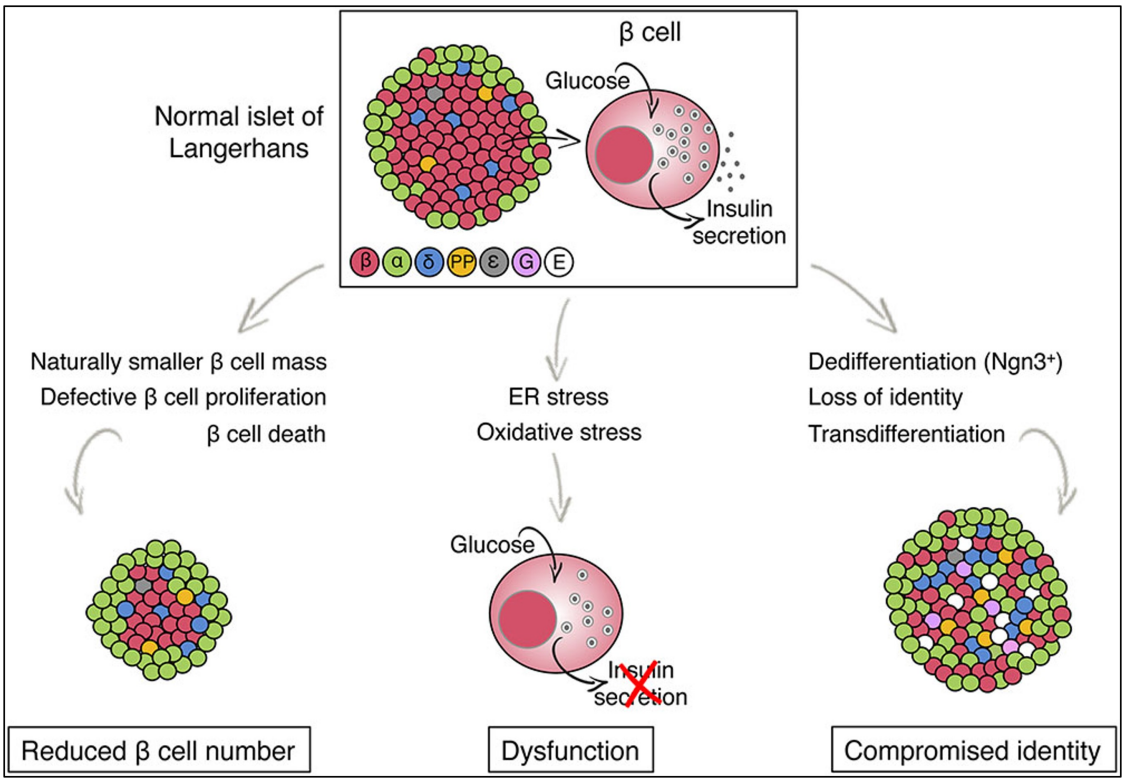

FIGURE 1.2: Possible mechanisms leading to beta-cell failure. Figure is taken from [42].

1.4 Guide through the thesis

This section provides a brief outline of the different chapters enclosed in this thesis.

Chapter 2 presents a detailed description of the development and validation of the system dynamics models (SDMs) of the system of social norms regarding body weight perception and obesity prevalence. The outcomes of the simulations and their interpretations are also discussed.

In chapter 3, the details of the method for inferring computational model from cross-sectional data and the comparison of the method with longitudinal datasets are provided. The outcomes of the method against different theoretical tests are also discussed.

Chapter 4 presents a detailed description of the development and validation of the Boolean network model of the pathways involved in insulin resistance and beta-cell apoptosis, and a discussion of the simulation results obtained with this model.

In chapter 5, a detailed description of the model development process and rate equations for the compromised beta-cell identity model are provided. The outcomes of parameter estimation, validation against experimental data and insights gained from different scenario tests are also discussed.

Finally, the thesis is concluded with relevant discussions and future outlook in Chapter 6.

Chapter 2

Social norms and obesity prevalence: From cohort to system dynamics models

2.1 Introduction

It has been argued that individuals are more likely to underestimate their own body weight as obesity prevalence increases [2]. That is because body weight perception, a determinant of overweight and obesity [3], is partly determined via social comparison [4]. That is, the typical weight at the group level influences how individuals evaluate their own weight [2]. Body weight perception is thus affected by what is normal. It however also affects what is normal via its impact on obesity prevalence, inducing feedback loops that may over time contribute to group-level obesity. These feedback loops result in complex behaviour, possibly inducing group-level obesity as an emergent property. An emergent property of a complex system cannot plainly be derived from its parts and is more than a direct outcome of their aggregation [45]. In addition, a complex system shows non-linear behaviour, with a large disproportionality between its inputs and outputs [46], which often results from the presence of feedback loops.

Previous research has indicated that norms affect individual dietary intake and physical activity and it is difficult for individuals to change their weight-related behaviour if others in their environment do not [6]. In fact, it has consistently been

shown that weight loss resulting from interventions targeting individual weight-related behaviour is likely to not be maintained [7]. One possible explanation is that norms may counteract health awareness in shaping individual health-related behaviour. In that regard, the relevance of addressing norms to change individual health-related behaviour as a policy strategy has received attention with respect to smoking [8]. That is, 'the shifts in social norms (...) that occur as a result of major tobacco control interventions and campaigns can strengthen smokers' motivation to quit and commitment to staying quit' [47]. Understanding the effect of the feedback loops between individual characteristics and group-level processes over time can guide similar policy strategies aiming to lower obesity prevalence, in which justice can be done to influences at both levels.

System dynamics models (SDMs) can aid in understanding and simulating this system's emergent behaviour [9]. SDMs can reveal how variables interact by expressing the causal links between them using difference equations. Specifically, system dynamics modelling is used to understand and simulate a complex system's non-linear behaviour in different scenarios [9]. This is valuable when evaluating the effect of health awareness versus norms on group-level body mass index (BMI) which is unfeasible using conventional empirical methods.

In this study, the system of social norms regarding body weight perception and obesity prevalence was modelled using SDMs. These SDMs were designed to test the hypothesis that as overweight becomes normal, the norm might be counteracting health awareness in shaping individual weight-related behaviour. Hereto, an expert-informed causal loop diagram (CLD) was designed to conceptualize this system, which was subsequently used as a template for functioning SDMs. This system consists of feedback loops between individual body weight perception, individual weight-related behaviour and group-level norms towards body weight. These norms can be conceptualized as a product of social comparison and cultural preferences [4]: what is considered normal, i.e. group-level BMI, and ideal, i.e. socio-cultural ideal BMI. The SDMs simulated this system's behaviour for a multi-ethnic cohort in Amsterdam (registered in the HELIUS study) [10], whose body weight perception was measured. This data was used to calibrate the SDMs.

This study was a proof-of-concept of studying feedback loops between individual characteristics and group-level processes using computational modelling, with the aim to simulate the effect of three scenarios on group-level BMI. These reflect

the question 'what if' weight-related behaviour were driven (1) only by health awareness, (2) only by norms and (3) by their interaction, i.e. health awareness and norms.

2.2 Methods

This section contains details of (1) the formulation of the expert-informed CLD, (2) the study population that was selected from the Amsterdam-based cohort whose data was used to quantify this CLD, (3) body weight perception as it was measured for this study population, (4) the conversion of the CLD to six SDMs using stocks, flows, auxiliaries and constants, (5) the variables and equations that were used in these SDMs, (6) the use of cross-sectional data for the quantification of the SDMs, (7) the use of validation statements to validate this quantification and (8) the scenarios that were tested using the validated SDMs.

2.2.1 Causal loop diagram

The expert-informed CLD of the system was formulated through iterative interviews, facilitating the integration of expert knowledge concerning public health, healthy inequalities, dietary behaviour, sociology and anthropology. The resulting diagram (Figure 2.1) shows these experts' understanding of the system, depicting its variables and causal links. Subsequently, the literature was used to confirm and support each individual causal link proposed by the experts.

The CLD shows that an increase in individual BMI increases group-level BMI (CL1) [4], which in turn drives up the norm (CL2) [4]. Socio-cultural ideal BMI also affects the norm (CL3) [4] and represents the relatively stable socio-cultural perception an individual has of the ideal BMI in their group, which induces an individual variation in how the norm is regarded. Individual ideal BMI, representing the BMI an individual strives for, is then driven both by the norm (CL4) [48] and by knowledge of what a healthy BMI is (CL5) [48], creating a possible conflict between these two influences. This sequence leading to individual ideal BMI drives two feedback loops in parallel (R1 and R2). In R1, an increase in individual ideal BMI increases food intake (total daily energy intake (TDEI)) (CL6) [49–52], which

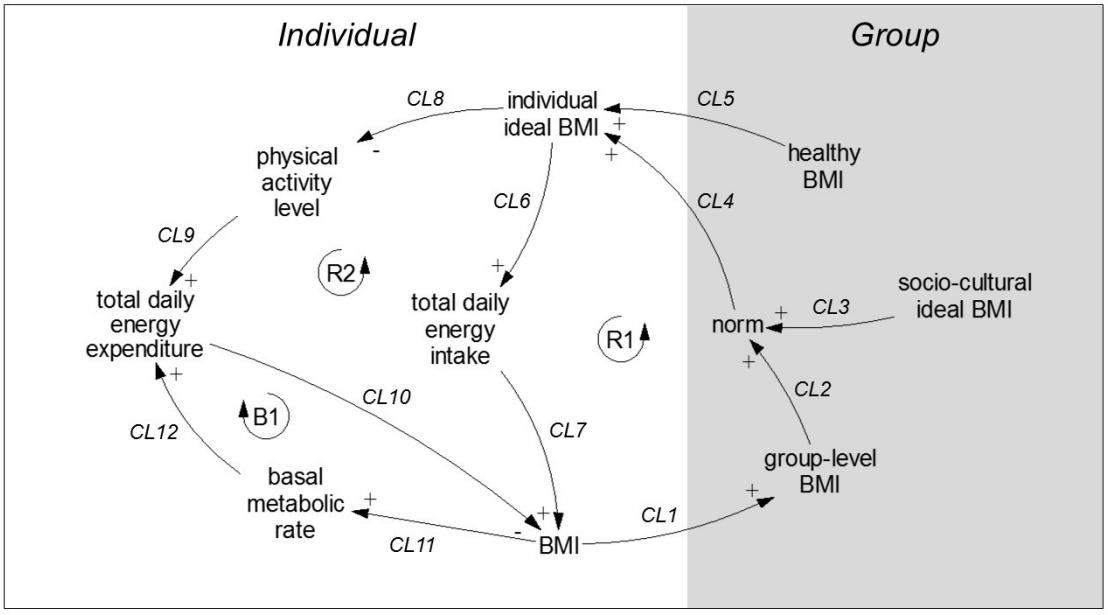

FIGURE 2.1: Causal loop diagram (CLD) of the system of social norms regarding body weight perception and obesity prevalence. Variables are connected by arrows indicating causal links, where a plus indicates that an increase in the variable at the tail of the arrow constitutes an increase in the variable at the head of the arrow whereas a minus indicates that an increase in the variable at the tail constitutes a decrease in the variable at the head. Reinforcing feedback loops R1 and R2 and balancing feedback loop B1 are indicated with loop symbols.

then increases BMI (CL7) [53]. In R2, this increase in individual ideal BMI causes a decrease in physical activity level (PAL) (CL8) [50, 54, 55] and consequently in total daily energy expenditure (TDEE) (CL9) [56], which similarly increases BMI (CL10) [53]. TDEE is also influenced by basal metabolic rate (BMR) (CL12) [57], which increases as BMI increases (CL11) [57], causing a balancing feedback loop (B1).

2.2.2 Study population

The CLD was then converted to SDMs, which required data that can quantitatively represent the CLD's variables. Therefore, the multi-ethnic HELIUS study [10] was used, in which data on characteristics reflecting these variables were collected.

The data include characteristics concerning sex, age, ethnicity, education, BMI and body weight perception for each individual. These data were collected through

questionnaires/interviews, except for BMI which was obtained using a standardised methodology during a physical examination [10, 58]. Individuals with missing values for any of these characteristics were excluded. Ethnicity was based on an individual's country of birth and those of his/her parents [10, 58], where an individual was regarded of non-Dutch ethnic origin when they were born abroad with one or two parent(s) born abroad or born in the Netherlands with two parents born abroad [10, 58]. BMI was calculated as $\frac{weight}{height^2}$ [57], averaged over two measurements taken while individuals were barefoot and lightly clothed [10, 58]. Body weight perception was self-reported [58]. In each of the groups, only those individuals were selected who have 'lower vocational schooling or lower secondary schooling' or 'intermediate vocational schooling or intermediate/higher secondary schooling' [10] as the highest educational level obtained. By selecting only certain education segments, educational differences could be disregarded when analysing the results. This resulted in 5,299 participants (Dutch men: n = 753; Moroccan men: n = 774; South-Asian Surinamese men: n = 839; Dutch women: n = 848; Moroccan women: n = 1,086; South-Asian Surinamese women: n = 999). Education, classified into four groups: "no schooling or elementary schooling only", "lower vocational schooling or lower secondary schooling", "intermediate vocational schooling or intermediate/higher secondary schooling", and "higher vocational schooling or university", was self-reported and determined according to the highest qualification that was gained either in the Netherlands or the country of origin [10, 58].

Six SDMs were constructed for three ethnic groups from this cohort, based on the hypothesis that norms influence individuals to a different extent in cultures that contrast concerning the degree of individualism/collectivism. The positions of these cultures were defined on the dimension of individualism/collectivism as previously identified based on the Hofstede model, a well-established paradigm for comparing cultures [59]. Here, collectivism, versus its opposite individualism, is 'the degree to which people in a society are integrated into groups' [59]. Accordingly, SDMs were constructed for three groups that differ in the degree of individualism/collectivism. These were then stratified by gender, as the influence of norms on women is expected to be greater [60], resulting in six groups. These are Dutch ('individualistic') [61], Moroccan ('collectivistic') [61] and South-Asian Surinamese (Suriname—'slightly collectivistic' [61]; South-Asian ancestry from India [62]—'both collectivistic and individualistic traits') [61] men and women. Constructing an SDM for each of these groups implies the assumption that, specifically

for social comparisons of body weight, a member of one group is unaffected by the individuals in other groups. This assumption was based on the similarity hypothesis that 'comparison with targets that are close on a variety of dimensions, such as age, gender, or family ties, have a greater affective impact' [4]. Thus, it is expected that individuals are most likely to compare themselves to others from their own socio-cultural group.

Differences in body weight perception between these socio-cultural groups were verified with statistical analyses using Kruskal Wallis H tests (an analysis of variance (ANOVA) test could not be used as parametric assumptions were violated), followed by Dunn's post-hoc tests, as well as two-sample Kolmogorov-Smirnov tests. Distributions between ethnic groups of the same gender and between male and female groups of the same ethnicity were compared, as it does not make sense to compare groups of both different ethnicity and different gender with respect to body weight perception. The idea was to test for any differences among the groups' distributions, not only those based on their mean ranks (as can be detected with the Kruskal Wallis H tests). This was because the distributions were considered as energy landscapes, and hence it was tested to see whether the landscapes differ among the groups. For this purpose, the two-sample Kolmogorov-Smirnov test was used. However, this test can only be used for comparing two groups, whereas distributions between ethnic groups of the same gender (three groups) also needed to be compared. Therefore, the Kruskal Wallis H tests were used to compare ethnic groups of the same gender (Table 2.1 and Table 2.2) and the two-sample Kolmogorov-Smirnov tests were used to compare male and female groups of the same ethnicity (Table 2.3) (both $p<0.05$). After the Kruskal Wallis H tests, Dunn's post-hoc tests ($p<0.05$) were performed to investigate the pairwise differences between ethnic groups of the same gender. This was done to pinpoint which specific mean ranks differ significantly from the others. These tests showed that the mean ranks and distributions of the characteristics regarding body weight perception: perceived BMI, individual ideal BMI (IIB), and socio-cultural ideal BMI (SCIB) at $t = 0$, were significantly different among the six groups. At least one pairwise difference was found in each Kruskal Wallis H test. Dunn's post hoc tests showed that for perceived BMI, IIB, and SCIB, all pairwise comparisons were significant among both male and female groups. Based on these statistical analyses it was concluded that there is significant diversity in body weight perception among Dutch, Moroccan, and South-Asian Surinamese men and women.

TABLE 2.1: Results of Kruskal Wallis H tests to compare mean ranks between ethnic groups of the same gender (male groups).

	Dutch men (n=753)	**Moroccan men (n=774)**	**South-Asian Surinamese men (n=839)**			
	median kg/m^2	median kg/m^2	median kg/m^2	df	χ^2	p
Perceived BMI	25.37	25.95	25.32	2	84.028	<0.01
Individual ideal BMI (IIB)	25.37	25.95	25.32	2	468.476	<0.01
Socio-cultural ideal BMI (SCIB)	25.37	25.95	25.32	2	414.918	<0.01

TABLE 2.2: Results of Kruskal Wallis H tests to compare mean ranks between ethnic groups of the same gender (female groups).

	Dutch women (n=848)	**Moroccan women (n=1086)**	**South-Asian Surinamese women (n=999)**			
	median kg/m^2	median kg/m^2	median kg/m^2	df	χ^2	p
Perceived BMI	25.02	25.73	25.06	2	111.707	<0.01
Individual ideal BMI (IIB)	22.18	22.75	22.47	2	312.060	<0.01
Socio-cultural ideal BMI (SCIB)	22.18	22.75	22.47	2	322.390	<0.01

2.2.3 Body weight perception

For the HELIUS study cohort, perceived BMI was determined via questionnaires, asking each individual to indicate which image they most looked like on a randomly ordered version of the body image scale developed by Pulvers et al. [63] (Figure 2.2).

For all groups, each image was mapped to a corresponding measured BMI, where each image was represented by the average BMI for all individuals that selected

TABLE 2.3: Results of two-sample Kolmogorov-Smirnov tests to compare distributions between male and female groups of the same ethnicity.

	Men and women (pooled)		**Dutch men and women**		**Moroccan men and women**		**South-Asian Surinamese men and women**	
	D-statistic	*p*	*D-statistic*	*p*	*D-statistic*	*p*	*D-statistic*	*p*
Perceived BMI	0.194	<0.01	0.348	<0.01	0.273	<0.01	0.207	<0.01
Individual ideal BMI (IIB)	0.589	<0.01	0.612	<0.01	0.615	<0.01	0.542	<0.01
Socio-cultural ideal BMI (SCIB)	0.621	<0.01	0.664	<0.01	0.616	<0.01	0.590	<0.01

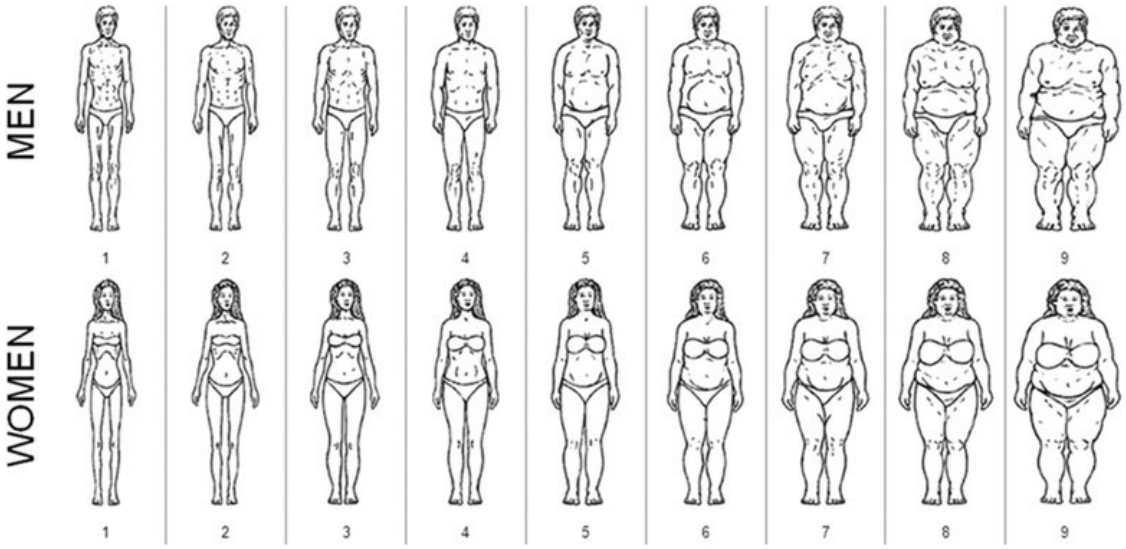

FIGURE 2.2: Body image scale.

that image as their perceived BMI (Table 2.4). In addition, each individual was asked which image they would prefer to look like and which image they thought others in their environment would find most attractive. The answers to these two questions were used to quantitatively represent individual ideal BMI and socio-cultural ideal BMI, respectively, based on the above-mentioned calibration. A visual representation of the calibration between perceived BMI as indicated by the body image scale and average measured BMI for each group is given in Figure 2.3.

TABLE 2.4: Perceived body mass index (BMI) (body image scale) in kg/m^2 corresponding to average measured BMI per group.

Image	**Dutch men (n=753)**	**Moroccan men (n=774)**	**South-Asian Surinamese men (n=839)**	**Dutch women (n=848)**	**Moroccan women (n=1086)**	**South-Asian Surinamese women (n=999)**
1	20.1 (n=10)	19.3 (n=14)	20.8 (n=22)	18.5 (n=9)	18.6 (n=25)	20.4 (n=18)
2	22.0 (n=70)	21.8 (n=61)	20.9 (n=74)	20.2 (n=76)	20.3 (n=89)	21.1 (n=75)
3	23.0 (n=146)	23.6 (n=157)	23.2 (n=151)	22.2 (n=202)	22.8 (n=215)	22.5 (n=172)
4	25.4 (n=234)	26.0 (n=254)	25.3 (n=230)	25.0 (n=263)	25.7 (n=293)	25.1 (n=236)
5	28.4 (n=243)	29.1 (n=227)	27.8 (n=299)	28.1 (n=168)	28.4 (n=242)	27.8 (n=240)
6	32.2 (n=36)	31.8 (n=38)	31.2 (n=38)	31.5 (n=71)	31.6 (n=114)	30.9 (n=132)
7	33.0 (n=10)	34.1 (n=15)	31.7 (n=16)	34.2 (n=40)	34.0 (n=67)	32.0 (n=69)
8	38.0 (n=2)	33.3 (n=6)	34.8 (n=7)	38.0 (n=14)	37.7 (n=33)	34.2 (n=44)
9	40.2 (n=2)	36.3 (n=2)	41.9 (n=2)	41.7 (n=5)	39.8 (n=8)	40.0 (n=13)

2.2.4 Stocks, flows, auxiliaries and constants

Using these data, the CLD was then converted into six SDMs. The structure of the SDMs was considered representative for each of the groups, but quantification of the strengths of the causal links for each SDM was dependent on each group's data. From here onward, the conceptual variables in the CLD are defined as quantifiable variables based on the cohort data (see Section 2.2.5).

The SDMs' structure (Figure 2.4) was designed to mirror the CLD but contains a number of additional variables (e.g. 'Age' and 'Height') that were necessary to meet the mathematical and structural SDM requirements. These requirements have been described in detail elsewhere [64–68]. To facilitate the conversion of the CLD into six SDMs, the CLD's variables were classified into stocks, flows, auxiliaries and constants. A stock represents a 'concrete aspect [...] of the system that can be

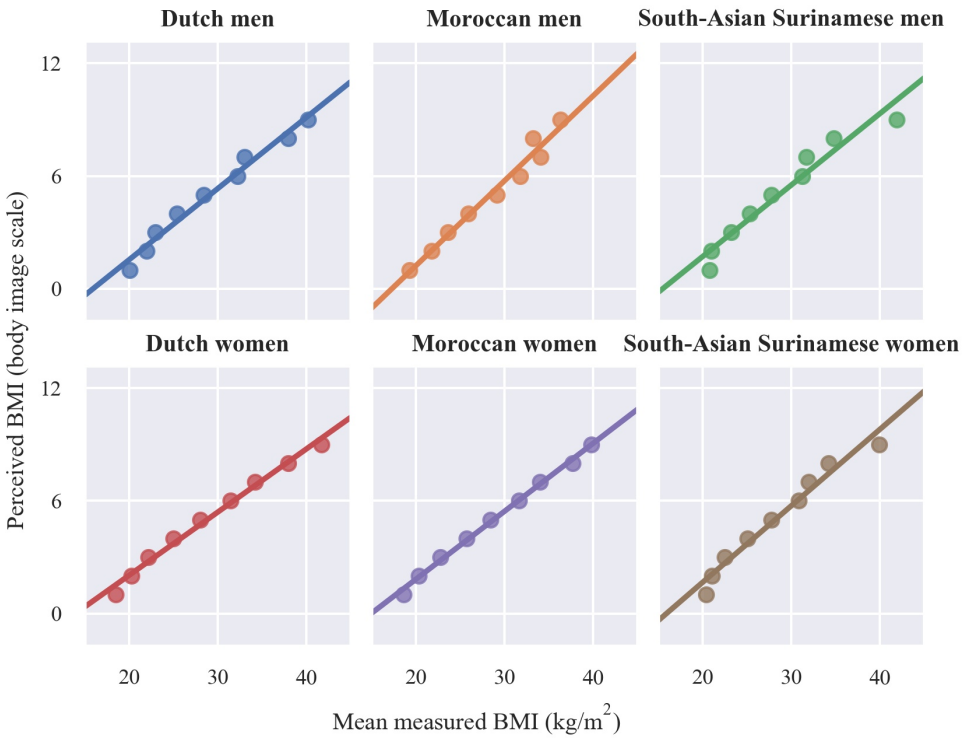

FIGURE 2.3: Visual representation of the calibration between perceived BMI as indicated by the body image scale and mean measured BMI for each group. The solid line represents the linear regression line between the dependent variable y = perceived BMI as indicated by the body image scale, and the independent variable x = mean measured BMI. Accordingly, the dots represent the mean measured BMI corresponding to each of the nine images from the body image scale.

seen and measured' ('Weight' in Figure 2.4), whereas a flow is connected to a stock and determines how it changes over time; it can be perceived as a rate (e.g. 'Weight loss rate') [68]. An auxiliary is 'any dynamic variable that is computed from other variables at a given time' (e.g. 'BMI'), whereas a constant is a variable that does not change during the simulation (e.g., 'Height') [69].

2.2.5 Variables and equations

The variables are formulated based on the cohort data (Table 2.5) and are displayed in italics. The SDMs' structure is represented by a list of equations (Table 2.6), that take the values corresponding to all variables in Table 2.5 for a given individual as inputs and generates their values for the next time point as outputs. These

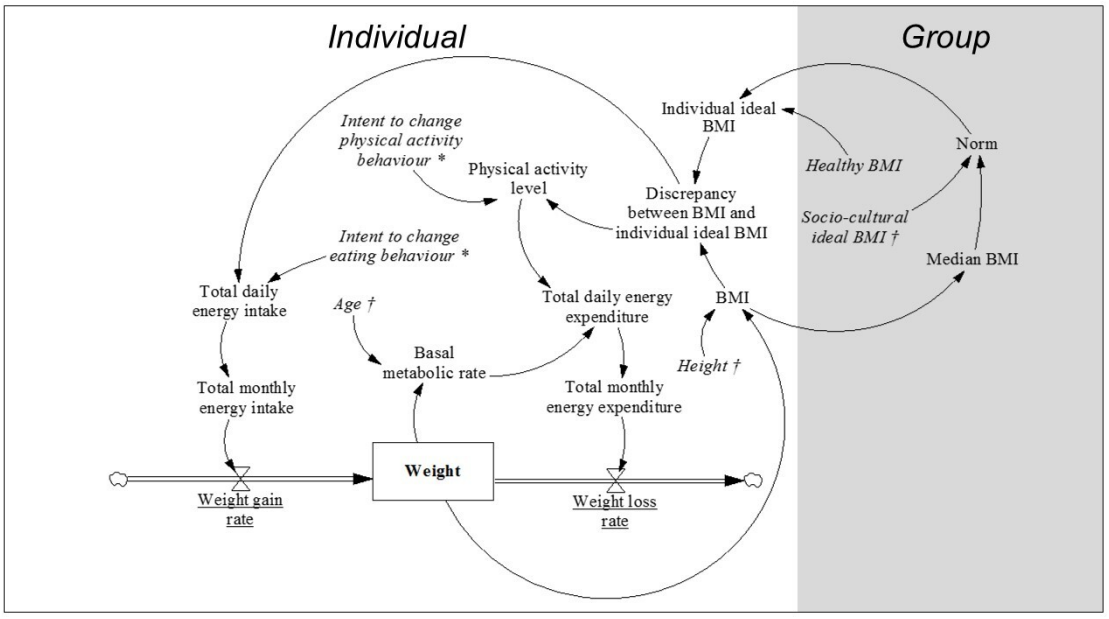

FIGURE 2.4: System dynamics model (SDM) mirroring the expert-informed causal loop diagram (CLD) of the system of social norms regarding body weight perception and obesity prevalence. Variables are connected by arrows indicating causal links. The stock is shown as a box (variable name displayed in bold, i.e. 'Weight'), whereas flows are displayed as thick arrows (regulated by valves, variable names are underlined). Auxiliaries and constants are indicated in regular font and italics, respectively. Optimized parameters and constants based on initial values from the cohort data are marked with * and †, respectively.

equations should be solved in the order as defined in Figure 2.4 (starting from *IIB* (individual ideal BMI) and following the causal links). These equations ensure that dimensional consistency is preserved within the SDMs, that is, the units between the left- and the right-hand side of all equations are consistent [64–68]. The descriptions of the different variables, and their updating procedures are described below.

Anthropometric and demographic variables

These variables are directly derived from the cohort data, where H (height) and *Age* are constants. *BMI* is calculated at each time step as

$$BMI_{t+1} = \frac{W_{t+1}}{{H_{t=0}}^2}, \tag{2.1}$$

Table 2.5: Description of variables used in the system dynamics models (SDMs).

	Variable	**Abbreviation**	**Units**	**Type**
Anthropometric and demographic variables	Gender	-	-	-
	Ethnicity	-	-	-
	Weight	W	kg	Stock
	Height	H	m	Constant (initial value)
	BMI	BMI	kg/m^2	Auxiliary
	Median BMI	$MedBMI$	kg/m^2	Auxiliary
	Age	Age	years	Constant (initial value)
Body weight perception variables	Individual ideal BMI	IIB	kg/m^2	Auxiliary
	Socio-cultural ideal BMI	$SCIB$	kg/m^2	Constant (initial value)
	Norm	$Norm$	kg/m^2	Auxiliary
	Discrepancy between BMI and individual ideal BMI	$Discrepancy_{\mathrm{BMIandIIB}}$	kg/m^2	Auxiliary
	Healthy BMI	HB	kg/m^2	Constant
Energy balance variables	Physical activity level	PAL	-	Auxiliary
	Total daily energy intake	$TDEI$	kcal/day	Auxiliary
	Total monthly energy intake	$TMEI$	kcal/month	Auxiliary
	Basal metabolic rate	BMR	kcal/day	Auxiliary
	Total daily energy expenditure	$TDEE$	kcal/day	Auxiliary
	Total monthly energy expenditure	$TMEE$	kcal/month	Auxiliary
	Weight gain rate	$Rate_{\mathrm{Weightgain}}$	kg/month	Flow
	Weight loss rate	$Rate_{\mathrm{Weightloss}}$	kg/month	Flow
Optimised parameters	Intent to change physical activity behaviour	$Intent_{\mathrm{PAB}}$	$1/kg/m^2$	Constant
	Intent to change eating behaviour	$Intent_{\mathrm{EB}}$	$(kcal/day)/kg/m^2$	Constant
Fitted parameter	Impact of healthy BMI on individual ideal BMI	$Impact_{\mathrm{HBonIIB}}$	-	Constant

(Equation (7) in Table 2.6) [57], where W (weight) is updated according to Equation (6) in Table 2.6. *MedBMI* is the median BMI of the group (Equation (9) in Table 2.6) and is also updated at every time step.

Body weight perception variables

The updating procedure for *IIB* takes *HB* (healthy BMI), *Norm* and $Impact_{\text{HBonIIB}}$ (impact healthy BMI on individual ideal BMI) into account (Equation (1) in Table 2.6). *HB* is defined as a constant that equals 22.5 kg/m^2 for all groups, representing a conservative estimate of a healthy BMI and corresponding to the cut-off point for an elevated type 2 diabetes risk [70, 71]. The updating procedure for $Discrepancy_{\text{BMIandIIB}}$ (discrepancy between BMI and individual ideal BMI) is then defined by the difference between *BMI* and *IIB* at a particular time step, which describes the gap between the BMI an individual has and the BMI they would like to attain (Equation (2) in Table 2.6).

Norm is defined as the average between a group's *MedBMI* (median BMI), representing group-level BMI, and the respective individual's initial value for *SCIB* (socio-cultural ideal BMI) (Equation (10) in Table 2.6). The median is selected here, as opposed to the average, because it is hypothesized that an individual might be inclined to alter their BMI based on the frequency of individuals in their group with a different BMI. The average is considered unsuitable as it would also be affected by a relatively small fraction of the group with a different BMI, which is not expected to change the behaviour of most individuals. The initial value for *SCIB* is used as a constant, which via the calibration explained in Section 2.2.3 could be derived from the cohort data. This initial value for *SCIB* is used as a constant to introduce individual variation to the norm, as it represents the socio-cultural perception an individual has of the ideal BMI in their group, which is considered to be relatively stable. Note that both *MedBMI* and *SCIB* are allowed to exert an equal influence on *Norm*, that is, the most conservative ratio of 50/50, as research that has specifically addressed this issue is not known.

Equation (1) in Table 2.6 is formed by rewriting the output of regression through the origin between distance *Norm* and *HB*, represented by

$$x = Norm - HB$$

TABLE 2.6: The list of equations that represents the system dynamics models (SDMs).

	Equation				**Causal link**
(1)	$IIB_t = Impact_{\text{HBonIIB}} \times HB + (1 - Impact_{\text{HBonIIB}}) \times Norm_{\text{t}}$				CL4, CL5
(2)	$Discrepancy_{\text{BMIandIIB}t} = BMI_t - IIB_t$				
(3)	$PAL_{\text{t+1}} = PAL_{\text{t=0}} + Intent_{\text{PAB}} \times Discrepancy_{\text{BMIandIIB}t}$				CL8
(4)	$TDEI_{\text{t+1}} = TDEI_{\text{t=0}} + Intent_{\text{EB}} \times Discrepancy_{\text{BMIandIIB}t}$				CL6
(5)	$TDEE_{\text{t+1}} = BMR_t \times PAL_{\text{t+1}}$				CL9, CL12
(6)	$W_{\text{t+1}} = W_t + (Rate_{\text{Weightgain}} - Rate_{\text{Weightloss}})$ $= W_t + \left(\frac{TMEI_{\text{t+1}}}{7700} - \frac{TMEE_{\text{t+1}}}{7700}\right)$ $= W_t + \left(\frac{TDEI_{\text{t+1}}}{7700} \times \frac{365}{12} - \frac{TDEE_{\text{t+1}}}{7700} \times \frac{365}{12}\right)$ $= W_t + \left(\frac{73 \times TDEI_{\text{t+1}}}{18480} - \frac{73 \times TDEE_{\text{t+1}}}{18480}\right)$				CL7, CL10
(7)	$BMI_{\text{t+1}} = \frac{W_{\text{t+1}}}{H_{\text{t=0}}{}^2}$				
(8)	$BMR_{\text{t+1}}$	Men	$Age_{\text{t=0}}$ 18-30	$BMR_{t+1} = 15.057 \times W_{t+1} + 692.2$	CL11
			$Age_{\text{t=0}}$ 30-60	$BMR_{t+1} = 11.472 \times W_{t+1} + 873.1$	
			$Age_{\text{t=0}} \geq 60$	$BMR_{t+1} = 11.711 \times W_{t+1} + 587.7$	
		Women	$Age_{\text{t=0}}$ 18-30	$BMR_{t+1} = 14.818 \times W_{t+1} + 486.6$	
			$Age_{\text{t=0}}$ 30-60	$BMR_{t+1} = 8.126 \times W_{t+1} + 845.6$	
			$Age_{\text{t=0}} \geq 60$	$BMR_{t+1} = 9.082 \times W_{t+1} + 658.5$	
(9)	$MedBMI_{\text{t+1}} = Median(BMI_{t+1})$				CL1
(10)	$Norm_{t+1} = \frac{MedianBMI_{\text{t+1}} + SCIB_{t=0}}{2}$				CL2, CL3

and distance *Norm* and *IIB*, i.e.

$$y = Norm - IIB,$$

which is conducted for each group. This provides the value for $Impact_{\text{HBonIIB}}$ for each group, given by

$$Norm - IIB = Impact_{\text{HBonIIB}} \times (Norm - HB),$$

which can be rewritten to get Equation (1) given in Table 2.6. The value for $Impact_{\text{HBonIIB}}$ is thus determined directly from the cohort data, where the interpretation of Equation (1) in Table 2.6 is that *IIB* is a weighted average of *HB*

TABLE 2.7: Values for $Impact_{\text{HBonIIB}}$ for each group.

Socio-cultural group	**Impact$_{\text{HBonIIB}}$**
Dutch men	0.21
Moroccan men	0.18
South-Asian Surinamese men	0.27
Dutch women	0.37
Moroccan women	0.47
South-Asian Surinamese women	0.51

and *Norm*, where $Impact_{\text{HBonIIB}}$ determines the relative weight of each. A larger $Impact_{\text{HBonIIB}}$ implies a larger effect of *HB* on *IIB* and, as a consequence, a lower effect of *Norm* on *IIB*. This is based on the assumptions that 1) if *Norm* equals *HB*, then *IIB* equals *HB*; implying that individuals prefer to be healthy and 2) *HB* and *Norm* work against each other. The values for $Impact_{\text{HBonIIB}}$ for each group are given in Table 2.7.

$Impact_{\text{HBonIIB}}$ can also be regarded as uniquely determining an individual's behaviour with respect to *HB* and *Norm* , as is shown using Figure 2.5. Here each blue dot represents 1-370 individuals that have that particular combination of distance *Norm* and *HB* and distance *Norm* and *IIB*. If $Impact_{\text{HBonIIB}}$ is close to 0, an individual does not let their *IIB* deviate from their perception of the norm, even if that perception of the norm is far from healthy. Conversely, if $Impact_{\text{HBonIIB}}$ is close to 1, the more equal *IIB* and *HB* are for an individual, i.e. the more that individual adapts what they strive for based on what is healthy, regardless of their perception of the norm. Accordingly, when the regression is plotted through the origin line in Equation (1) in Table 2.6, the line for $Impact_{HBonIIB} = 1$, and the line for $Impact_{HBonIIB} = 0$, the separate regions of the plane can be divided defined by distance *Norm* and *HB* and distance *Norm* and *IIB* created by these lines according to different behaviours with respect to *HB* and *Norm*. As shown in Figure 2.5, the values for $Impact_{\text{HBonIIB}}$ fall between 0 and 1 for each group. This implies that the assumptions are representative of the average behaviour of all individuals in a particular group, as depicted in the region shaded in green in Figure 2.5. The behaviour for Moroccan men and Dutch women are shown as they represent the groups that on an individual level behave the most and the least, respectively, according to the assumptions. For Moroccan men, it is shown that for most individuals their *IIB* is indeed lower than the norm, but higher than healthy. For Dutch women, even though the regression through the origin line falls in the

region shaded in green, many individuals in fact strive to be thinner than both the norm and healthy, i.e. in the region shaded in red. Conversely, individuals that strive to be heavier than both the norm and healthy fall in the region shaded in blue.

Descriptive characteristics of the study population at t = 0 corresponding to the SDMs' variables are presented in Table 2.8.

Energy balance variables

PAL (physical activity level) at $t = 0$ is estimated based on the SQUASH (Short QUestionnaire to ASsess Health-enhancing physical activity) validation study, where *PAL* was determined for a sub-sample of the HELIUS study cohort (n=500) using a combined accelerometer and heart rate measurement device (Actiheart) [72]. This study shows that the mean *PAL* of individuals adhering to the Dutch physical activity norm is 1.65 (no units: expressed as *TDEE/BMR*, where *TDEE* and *BMR* refer to total daily energy intake and basal metabolic rate, respectively) [57], whereas the mean *PAL* of individuals not adhering is 1.6 [72]. This cut-off point is extrapolated to all individuals in the study population, based on an available binary variable indicating whether an individual adheres to the norm. The *PAL* of adhering individuals is rounded up to 1.7 to correspond to accepted cut-off points [57] of 1.40-1.69 for a sedentary/light activity lifestyle and 1.70-1.99 for an active/moderately active lifestyle. Accordingly, a value of 1.7 is assigned to adhering individuals and 1.6 to those that do not. *PAL* is updated at each time step according to Equation (3) in Table 2.6. This equation also takes *PAL* at $t = 0$ into account as a constant so that an individual's value for *PAL* does not deviate significantly from their initial value to ensure that *PAL* evolves smoothly over time.

BMR is estimated at each time step based on the Schofield equation (Equation (8) in Table 2.6), which takes sex, *Age*, and *W* into account [57].

For *TDEI* (total daily energy intake) and *TDEE* it is assumed that individuals are weight stable at $t = 0$, thus the initial value of *TDEI* is set equal to the value of *TDEE*. After this, *TDEI* varies at each time step according to Equation (4) in Table 2.6, taking *TDEI* at $t = 0$ into account as a constant to ensure that *TDEI* evolves smoothly over time.

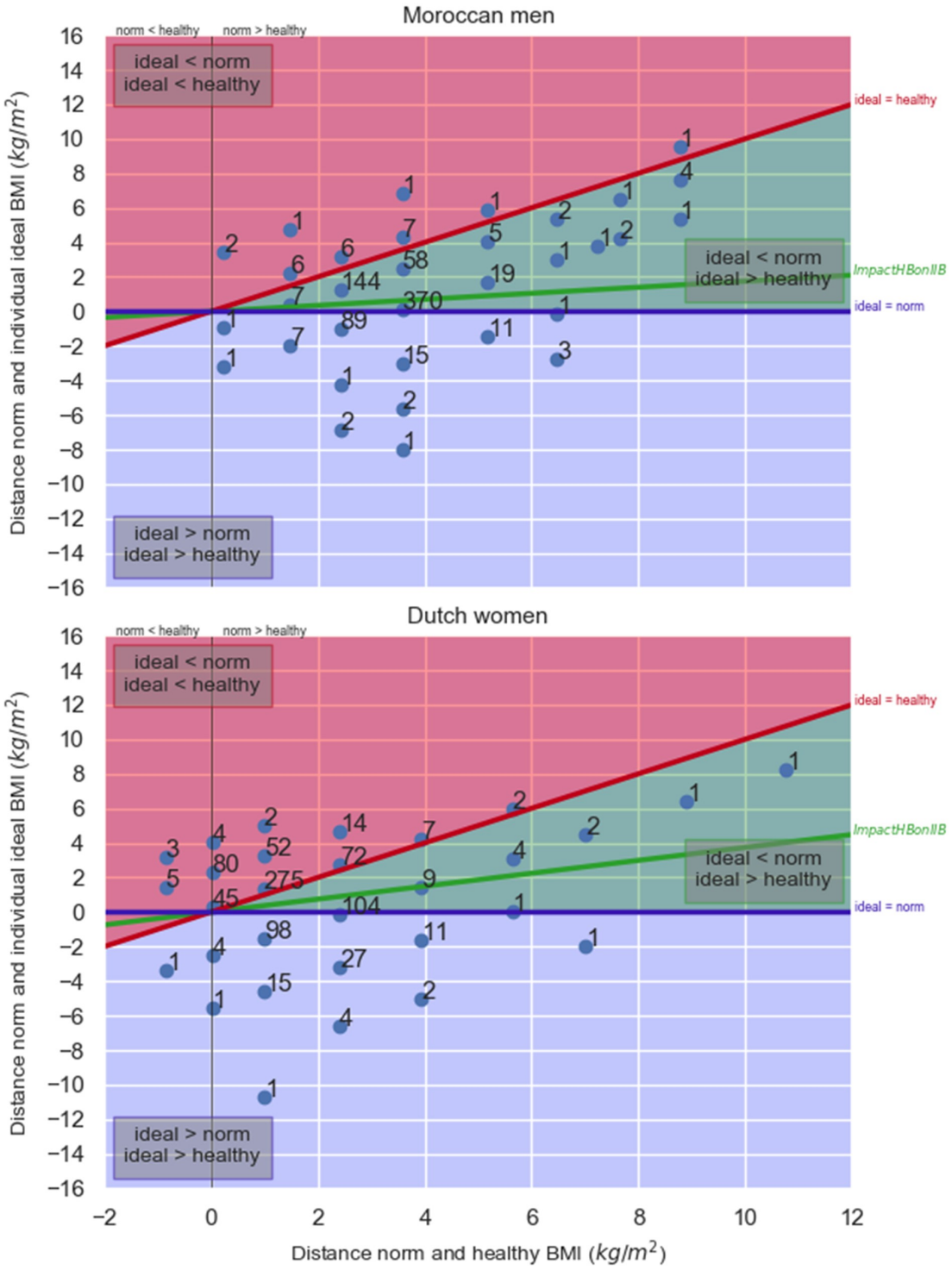

FIGURE 2.5: Regions corresponding to different behaviours with respect to *HB* and *Norm*. Each blue dot represents 1-370 individuals that have that particular combination of distance *Norm* and *HB* and distance *Norm* and *IIB*. The distance between *Norm* and *HB* (x-axis) can only have a limited amount of values. This is because *Norm* depends on *MedBMI* and *SCIB*, where *SCIB* only has nine possible values (as it is estimated based on the body image scale), and because *HB* is the same for all individuals (22.5 kg/m2). The distance between *Norm* and *IIB* (y-axis) can only have a fairly limited amount of values because there are also only nine possible values for *IIB* (as it is estimated based on the body image scale).

TABLE 2.8: Descriptive characteristics of the study population at t = 0, where median values for all descriptives are provided in accordance with the use of BMI.

		Dutch men (n=753)	**Moroccan men (n=774)**	**South-Asian Surinamese men (n=839)**	**Dutch women (n=848)**	**Moroccan women (n=1086)**	**South-Asian Surinamese women (n=999)**
Age (years), median (IQR)		52 (24)	39 (18)	46 (23)	51 (20)	33 (18)	48 (18)
BMI (kg/m^2), median (IQR)		25.6 (5.0)	26.2 (5.2)	25.4 (4.5)	24.8 (6.3)	26.1 (6.9)	26.0 (6.6)
BMI $\geq$ 25.0 kg/m^2 (%)		57.2	62.7	55.5	48.2	59.4	57.6
IIB (kg/m^2), median (IQR); mean $\pm$ SD *		25.4 (2.4); 24.6 $\pm$ 1.8	26.0 (2.3) 25.3 $\pm$ 1.6	25.3 (2.1) 24.5 $\pm$ 1.6	22.2 (2.8) 23.0 $\pm$ 2.3	22.8 (3.0) 23.7 $\pm$ 2.4	22.5 (2.6) 23.6 $\pm$ 2.3
SCIB (kg/m^2), median (IQR); mean $\pm$ SD *		25.4 (2.4); 24.7 $\pm$ 1.8	26.0 (2.3) 25.4 $\pm$ 2.0	25.3 (2.1) 24.7 $\pm$ 2.2	22.2 (2.8) 22.9 $\pm$ 2.3	22.8 (3.0) 23.8 $\pm$ 2.9	22.5 (2.6) 23.6 $\pm$ 2.7
Norm (kg/m^2), median (IQR)		25.5 (1.2)	26.1 (1.2)	25.4 (1.0)	23.5 (1.4)	24.4 (1.5)	24.2 (1.3)
Discrepancy between perceived BMI and IIB (kg/m^2) †	<0 (%)	12.2	18.7	14.1	3.1	9.5	4.0
	= 0 (%)	38.8	34.6	34.2	31.6	25.0	24.9
	>0 (%)	49.0	46.6	51.7	65.3	65.6	71.1
PAL	1.6 (%)	27.5	45.0	41.1	24.4	58.5	49.3
	1.7 (%)	72.5	55.0	58.9	75.6	41.6	50.8
TDEI (kcal), median (IQR)		3002 (448)	2981 (379)	2854 (398)	2354 (297)	2332 (308)	2251 (273)
BMR (kcal), median (IQR)		1797 (267)	1800 (216)	1727 (229)	1402 (176)	1422 (174)	1370 (162)

TDEE is calculated at each time step as

$$TDEE_{t+1} = BMR_t \times PAL_{t+1}. \tag{2.2}$$

TDEE is defined based on *PAL* and *BMR*, so that it can be estimated independent of self-reported energy intake, which is often unreliable [73]. TMEI (total monthly energy intake) and TMEE (total monthly energy expenditure) can be derived from their daily counterparts by multiplying them by 365/12 (average number of days/ month) (Equation (6) in Table 2.6).

$Rate_{\text{Weightgain}}$ (weight gain rate) and $Rate_{\text{Weightloss}}$ (weight loss rate) are calculated by converting TMEI and TMEE from kcal/month to kg/month (Equation (6) in Table 2.6). Here, it is assumed that a surplus of 7,700 kilocalories accounts for a one kilogram increase in weight [74, 75].

2.2.6 Cross-sectional data

The HELIUS data are cross-sectional; however, to construct operational SDMs, data from multiple time points are required. There are several techniques in the literature for estimating pseudo-longitudinal data from cross-sectional data, which include employing distance metrics and graph theoretical operations [76–83]. They aim to construct realistic trajectories through the feature space by using techniques such as ordering of the data-points and selecting start-points and end-points based on known class labels. For instance, one way to order data-points is by assuming that the label 'healthy' precedes the label 'diseased'. Another way to order biological samples or RNA-seq data is by using their gene expression levels. Of course, these methods rely on the presence of suitable variables in the dataset, as well as the assumptions about how these labels induce an ordering.

In contrast, the method proposed in this work generated pseudo-time series data from the available cross-sectional data by generating a set of qualitative 'data-generating assumptions'. These assumptions are based on the system's temporal behaviour that is expected to exist across all groups. An example of such assumptions is that, on average, an individual can lose 2 kg/month [11, 12]. Here, linear dynamics was assumed for the system's short-term behaviour. The time steps in the

SDMs were assumed as months in this study to identify an approximate timescale of the system's behaviour. However, this timescale is not exact, and therefore, the relative trends are more important to interpret than the exact timescale they occur on.

The values for the parameters $Intent_{\mathrm{PAB}}$ and $Intent_{\mathrm{EB}}$ were optimized such that the SDMs reproduced the data-generating assumptions and fit the cohort data. $Intent_{\mathrm{PAB}}$ and $Intent_{\mathrm{EB}}$ represent the change that individuals make in physical activity behaviour (changing their PAL) and eating behaviour (changing their $TDEI$), respectively, based on how much their BMI differs from their IIB (captured in $Discrepancy_{\mathrm{BMIandIIB}}$). The basin-hopping optimization method was used to find the optimal values for these parameters [84]. The basin-hopping algorithm [84] was selected because this algorithm is generally efficient in finding the global optimum in the presence of large number of local optima. This algorithm is essentially a stochastic gradient-descent algorithm, where the height of the landscape represents the model fit error (cost). This strategy allows the algorithm to avoid getting stuck in a local optimum (minimum cost). If a randomly proposed move improves the solution (reduces cost) then it is always accepted. Otherwise, the algorithm accepts the move with some probability less than 1, which decreases exponentially with the increased cost of the move. Over time the probability of accepting such a 'bad' move decreases to zero to ensure convergence. The SciPy basin-hopping function (scipy.optimize.basinhopping) was used to perform the optimisation. The default values for all parameters were used in this function except the take_step and niter_success parameters. Since $Intent_{\mathrm{EB}}$ (intent to change eating behaviour) and $Intent_{\mathrm{PAB}}$ (intent to change physical activity behaviour) are of different scales, their step sizes should be different: $Intent_{\mathrm{EB}}$ should have a larger step size compared to $Intent_{\mathrm{PAB}}$. To take this difference into account a custom step taking function was defined and called through the take_step parameter. The parameter niter_success was set to 50.

Six sets of two optimized parameter values were generated: one set for each group. The parameter values were optimized using a cost function that was designed to include a mathematical representation of each of the data-generating assumptions. This cost function enables the introduction of a temporal aspect to the available cross-sectional data by constraining the parameter space for $Intent_{\mathrm{PAB}}$ and $Intent_{\mathrm{EB}}$ to include only SDMs which satisfy the data-generating assumptions.

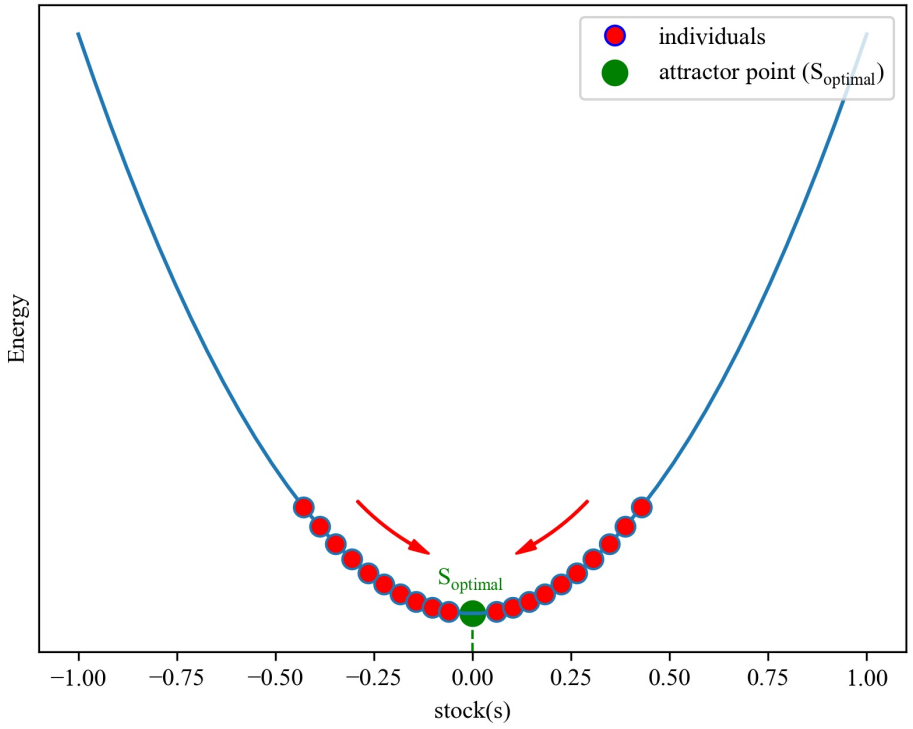

FIGURE 2.6: Energy landscape and behaviour of attractor for stock s. The green dot represents the attractor point (s_{optimal}) which is at stock value s=0 and the red dots represent the individuals, whose motion is towards the attractor point as indicated by the red arrows.

That is, the cost function can be thought of as implicitly placing a next time point in the data for each individual (resulting in a so-called pseudo-time series) and then evaluating how far off a given SDM is from reproducing this second data point. These optimized parameter values thus correspond to the SDM that best fits the cohort data for that group in conjunction with the data-generating assumptions.

2.2.7 Data-generating assumptions

In the field of computational modelling, the underlying dynamics of certain complex systems can be operationalised in terms of an energy (or attractor) landscape, inspired by statistical mechanics and Hamiltonian dynamics [85]. In short, an energy landscape assigns an energy value to a particular sequence of values for the variables (configuration). The energy value of a configuration is inversely related

to its likelihood: a configuration with a lower energy value has a higher likelihood. The intuition is that the system configuration will explore slightly different configurations around its current state, and statistically is more likely to 'choose' a new configuration with lower energy (downhill as shown by the red arrows in Figure 2.6). The stocks within an SDM represent the dimensions of the energy landscape, so in the present case the energy landscape has only one dimension (of the stock W). The configurations with the lowest energy value in the energy landscape are called the attractor points and they "correspond to stable equilibrium states" for the stocks [86].

In the present study, the following assumptions were made about the energy landscape shown in Figure 2.6 and the updating procedure of the stock value s for each individual:

Assumption 1: Over iterations t the stock value $s_t \rightarrow s_{\text{optimal}}$ as $t \rightarrow \infty$. In Figure 2.6, this is represented by $s_{\text{optimal}} = 0$ (the green dot) as the attractor point. This means that the expected value of individuals are modelled, i.e. no noise effects (random fluctuations) are modelled. As a consequence, the population variance should decrease monotonically over time.

Assumption 2: The energy landscape is convex and shallow. The latter is intended to make the instantaneous change per time unit small enough to warrant a linear approximation of causal effects (linear response theory), and to exclude pathological cases such as a delta function. Note that this linear approximation describes individual causal links; the response of the system over time may still be non-linear. This implies that each individual, i, is slowly moving towards the attractor point s_{optimal}, and their displacement $s^i_{t+1} - s^i_t$ per time step is very small.

Assumption 3: All individuals (red dots in Figure 2.6) are symmetrically distributed in the neighbourhood of s_{optimal}. This allows identifying the position of s_{optimal} as the center point of the point cloud of the individuals. Also, as a consequence, the displacements $s^i_{t+1} - s^i_t$ of all individuals are expected to add up to zero.

Assumption 4: Following from assumptions 1 and 2, for all individuals near s_{optimal},

$$\lim_{t \rightarrow \infty} \frac{dE}{ds_i} \rightarrow 0, \tag{2.3}$$

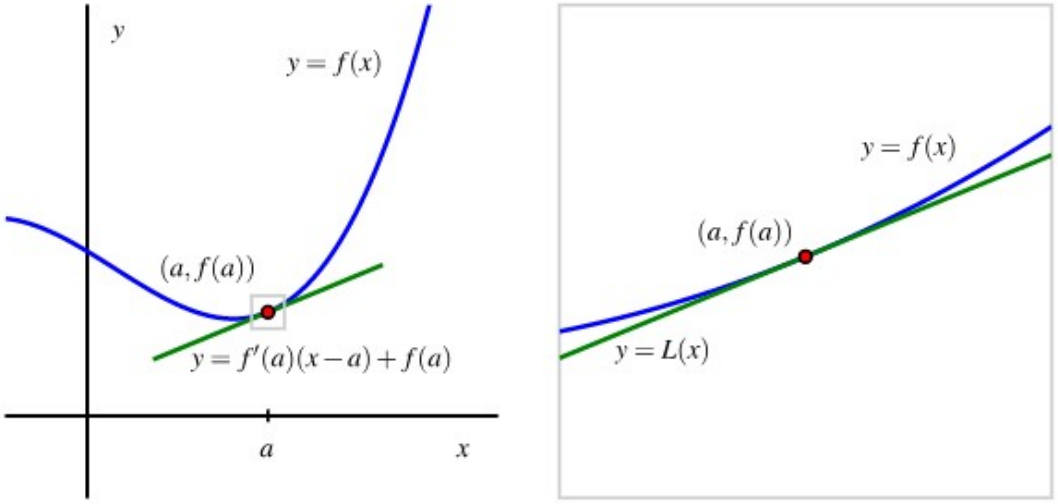

FIGURE 2.7: Illustration of local linearity [87]

which leads to the approximation of local linearity as explained in the following paragraph.

The updating procedure of each variable value for each individual at each time step is assumed to be a linear function of other variables in the system. The rationale is that non-linear behaviour cannot be inferred from data at a single time point. This approximation of local linearity is convenient for modelling short time spans and/or small changes of variables, as locally the slope of every smooth curve is approximately linear (Figure 2.7). This implies a limited range of validity (variables may not vary strongly) and therefore this work is only concerned with short-term dynamics in these proof-of-concept SDMs.

In the present study, only the deterministic (conforming) tendency of individuals as driven by norms was modelled, i.e. the next downhill state in the energy landscape was always selected. Non-conforming events can be modelled as noise (occasional uphill movements) and can be used to explain the current variation around the attractor point (not everyone in the cohort is driven purely by norms), but here the focus was only on the deterministic tendency to the attractor point. The consequence of this is that the variation of values for W was under-estimated in the predictions (i.e. it was assumed that the weight of all individuals tends to the attractor point as driven by norms). This is acceptable in this case because the variation is not part of the research question, but it can easily be added in the future.

For each group, the 'small' average displacement in assumption 2 was represented in the form of a parameter α. This parameter was defined as the average absolute displacement (for standardised data) expected in each time step.

The dataset was first standardized to have zero mean and unit standard deviation (SD) because under the restriction of linear causal relations the only possible location for a single attractor is the zero vector $s = \vec{0}$. Standardisation occurs through applying the formula:

$$x_{\text{standardised}} = \frac{x_{\text{original}} - \mu}{\sigma}. \tag{2.4}$$

The state vector at $t = 0$ was standardised as:

$$s_{t=0}^{\text{standardised}} = \frac{s_{t=0} - \mu_{s_{t=0}}}{\sigma_{s_{t=0}}}. \tag{2.5}$$

So, the state vector at $t = 0$ has zero mean and unit SD. When standardising the state vector at $t = 1$, its SD was assumed to be less than 1 since the state vectors are moving towards the zero vector, thereby decreasing their variance. So, the state vector at $t = 1$ was standardized by dividing by the SD of the state vector at $t = 0$ and not by the SD of the state vector at $t = 1$.

$$s_{t=1}^{\text{standardised}} = \frac{s_{t=1} - \mu_{s_{t=1}}}{\sigma_{s_{t=0}}}. \tag{2.6}$$

The value of α can be calibrated to match the amount of change that individuals on average experience in a certain time span, defining the time scale of the SDMs, which was selected to correspond to one month. The timescale of the model was determined by the choice of α but cannot be determined exactly without temporal data. Accordingly, α represents the average displacement, meaning that $\frac{1}{\alpha}$ represents the number of time steps it takes for an individual to reach a close approximate of the attractor point. That is, if $\alpha = 0.2$, then an individual reaches a close approximate of the stable value for W as driven by norms in five time steps. As it cannot be determined exactly what the attractor point s_∞ of W is, for the purpose of approximating the value of α for each group, the attractor point was assumed to be the average weight for that group. The value of α was estimated

TABLE 2.9: The fitted α value for each group.

	Dutch men	**Moroccan men**	**South-Asian Surinamese men**	**Dutch women**	**Moroccan women**	**South-Asian Surinamese women**
α	0.159	0.169	0.172	0.150	0.157	0.162

such that an individual can on average lose 2 kg of weight per month (i.e. the amount of change that individuals on average experience in a certain time span), which is in line with the literature addressing healthy weight loss [11, 12]. The role of α is to scale the curves along the x-axis, implying that the relative ordering of the curves remains the same for any value of α and accordingly making the exact value of α of secondary importance. The fitted α values are given in Table 2.9.

The optimised parameters are constrained as $Intent_{\text{PAB}} > 0$ and $Intent_{\text{EB}} < 0$, which are based on Equation (3) and (4) for the SDMs in Table 2.6.

$$PAL_{t+1} = PAL_{t=0} + Intent_{\text{PAB}} \times Discrepancy_{\text{BMIandIIB}_t} \tag{2.7}$$

$$TDEI_{t+1} = TDEI_{t=0} + Intent_{\text{EB}} \times Discrepancy_{\text{BMIandIIB}_t} \tag{2.8}$$

This constraint is a sanity check: $Intent_{\text{PAB}}$ and $Intent_{\text{EB}}$ represent the change that individuals make in physical activity behaviour (by changing their PAL) and in eating behaviour (by changing their $TDEI$) based on how much their BMI differs from their IIB (which is captured in $Discrepancy_{\text{BMIandIIB}}$ (discrepancy between BMI and individual ideal BMI). Accordingly:

- If $Discrepancy_{\text{BMIandIIB}} < 0$, individuals think they should gain weight;
- if $Discrepancy_{\text{BMIandIIB}} = 0$, individuals are satisfied with their weight;
- if $Discrepancy_{\text{BMIandIIB}} > 0$, individuals think they should lose weight.

Based on $Discrepancy_{\text{BMIandIIB}}$, the new values for PAL and $TDEI$ were calculated based on the hypothesis that individuals want to change their eating behaviour and their physical activity behaviour depending on their (dis)satisfaction with their weight. This was done by multiplying $Discrepancy_{\text{BMIandIIB}}$ with $Intent_{\text{PAB}}$ to

calculate the change in *PAL* to determine *PAL* at the next time step and by multiplying $Discrepancy_{\text{BMIandIIB}}$ with $Intent_{\text{EB}}$ to calculate the change in *TDEI* to determine *TDEI* at the next time step.

Therefore, $Intent_{\text{PAB}}$ should always be positive:

- If $Discrepancy_{\text{BMIandIIB}} < 0$, this results in a negative change in *PAL* at the next time step (reduce physical activity and gain weight);
- if $Discrepancy_{\text{BMIandIIB}} = 0$, the multiplication becomes zero (same physical activity and same weight);
- if $Discrepancy_{\text{BMIandIIB}} > 0$, this results in a positive change in *PAL* at the next time step (increase physical activity and lose weight).

Similarly, it can be said that $Intent_{\text{EB}}$ should always be negative:

- If $Discrepancy_{\text{BMIandIIB}} < 0$, this results in a positive change in *TDEI* at the next time step (eat more and gain weight);
- if $Discrepancy_{\text{BMIandIIB}} = 0$, the multiplication becomes zero (eat the same and keep the same weight);
- if $Discrepancy_{\text{BMIandIIB}} > 0$, this results in a negative change in *TDEI* at the next time step (eat less and lose weight).

Using these assumptions, a cost function was designed that enables the introduction of a temporal aspect to the available cross-sectional data. That is, a cost function was used to constrain the parameter space to include only SDMs which satisfy these assumptions. The function implicitly placed a next time point in the data for each individual (pseudo time-series) and evaluated how far off a given set of SDMs was from reproducing this second data point. Thus, even though a second data point was not explicitly added to the cohort data – as the aim was to elucidate the direction an individual takes and not the exact value for each variable – it was still evaluated whether a set of SDMs satisfies the assumptions. Namely, whether the dynamics that the SDMs exhibit were according to the assumptions. The definition of the cost function based on the aforementioned assumptions is described below.

2.2.8 Cost function

Recall that the data were standardised to have zero mean and unit SD to conform with the assumption that the attractor point is the zero vector ($s_\infty = 0$).

According to assumption 2, the displacement of each individual towards the attractor point $s_\infty = 0$ is small. Accordingly, it was assumed that the short-term behaviour of each individual, i, can be approximated by a linear equation for displacement defined as:

$$s^i_{t+1} = s^i_t + M \times s^i_t + c. \tag{2.9}$$

Here s^i_{t+1} and s^i_t are column vectors, M is a square matrix of dimension (size of vector s) and c is a constant column vector of dimension (size of vector s).

Now, a parameter α was defined as the average absolute displacement expected in each time step. Since the data were standardised, it must be true that $0 < \alpha < 1$. So,

$$< ||s^i_{t+1} - s^i_t|| >_i = < ||M \times s^i_t + c|| >_i = \alpha. \tag{2.10}$$

If an SDM is allowed to run for unit time step, the displacement of each individual, i, can be defined as:

$$\frac{\Delta s}{\Delta t} = \frac{s^i_{t+1} - s^i_t}{1} = s^i_{t+1} - s^i_t. \tag{2.11}$$

Now, according to assumption 2, the sum of the displacements of individuals at each time step equals zero since they are symmetrically distributed around the attractor point. So,

$$\begin{aligned} \sum_i \left(s^i_{t+1} - s^i_t\right) &= 0, \\ \sum_i \left(M \times s^i_t + c\right) &= 0, \\ M \times \sum_i s^i_t + N \times c &= 0. \end{aligned} \tag{2.12}$$

Here, N is the number of individuals. Also, the sum of the vectors representing the individuals, $\sum_i s_t^i$, equals the zero vector. Thus,

$$\begin{aligned} M \times 0 + N \times c &= 0, \\ c &= 0. \end{aligned} \tag{2.13}$$

Therefore, having derived that $c = 0$ as a consequence of the assumptions, equation 2.9 and equation 2.21 can be written as

$$s_{t+1}^i = s_t^i + M \times s_t^i, \tag{2.14}$$

$$\left\langle \left| \left| s_{t+1}^i - s_t^i \right| \right| \right\rangle_i = \left\langle \left| \left| M \times s_t^i \right| \right| \right\rangle_i = \alpha. \tag{2.15}$$

The displacements of individuals should not only match an absolute value (α) but also 'point' towards the origin (zero vector). So, it was assumed that each individual, i, will simply reduce their norm, i.e. is multiplied by a constant $0 < f_i < 1$ for all i:

$$\sqrt{\sum_x \left(s_t^i(x) \times f_i\right)^2} = \sqrt{\sum_x \left(s_t^i(x)\right)^2 \times f_i^2} = f_i \times \sqrt{\sum_x \left(s_t^i(x)\right)^2}. \tag{2.16}$$

Here, x denotes the elements of the vector s_t^i. Each individual i will have their own constant f_i which controls the individual's speed with which he/she moves towards the zero vector and which is also the constant with which the individual's norm is multiplied. The average over that should match with α. That is, in case of perfect movement to the origin,

$$\begin{aligned} < ||s_t^i|| - f_i \times ||s_t^i|| >_i &= \alpha, \\ < ||s_t^i|| >_i - < f_i \times ||s_t^i|| >_i &= \alpha. \end{aligned} \tag{2.17}$$

Now, we assume that the covariance between f_i and $||s_t^i||$ is zero, following which we can rewrite equation 2.17 as

$$\begin{aligned} < ||s_t^i|| >_i - < f_i >_i \times < ||s_t^i|| >_i = \alpha, \\ (1 - < f_i >_i) \times < ||s_t^i|| >_i = \alpha, \\ 1 - < f_i >_i = \frac{\alpha}{< ||s_t^i|| >_i}. \end{aligned} \tag{2.18}$$

To illustrate, if the model would rotate the individuals around the zero vector, i.e. along the circumference of a circle with the zero vector as the centre, then α may be matched but $< f_i >_i = 1$, since the norm of the individuals does not change. From now on $< f_i >_i$ will be denoted as f.

The first sub-cost function C_1, controls the contraction of the individuals, i.e. the ratio of the observed norm at the time step t+1 and the observed norm at the time step t should be close to f.

$$C_1 = \sqrt{< \left[\frac{\frac{||s_{t+1}^i||}{||s_t^i||} - f}{\sigma\left(\frac{||s_{t+1}^i||}{||s_t^i||}\right)} \right]^2 >_i}, \tag{2.19}$$

where $\sigma(.)$ denotes the standard deviation and is used to standardise C_1.

The second sub-cost function C_2 is based on the ratio of the contribution of *TDEI* and *PAL* on W, which is 75/25 according to expert knowledge (where 75% and 25% of the weight change are due to *TDEI* and *PAL* respectively). *TDEI* and *PAL* contribute to W through the weight gain rate (wgr in the equations below) and weight loss rate (wlr in the equations below), respectively. So, C_2 ensures that the ratio of the change in wgr and wlr given in equation 2.20 is close to the ideal ratio of 75/25. Also, Δwgr and Δwlr should have opposite signs. If an individual loses weight then Δwgr should be negative and Δwlr should be positive; the opposite will happen if an individual gains weight. When calculating wlr_{t+1}, BMR_t (i.e. the same BMR is considered for calculating wlr_t and wlr_{t+1}) and PAL_{t+1} are considered to take into account only the effect of PAL in wlr.

$$ratio = \frac{\Delta wgr}{\Delta wlr} = \frac{|wgr_{t+1}| - |wgr_t|}{|wlr_{t+1}| - |wlr_t|}, \tag{2.20}$$

$$C_2 = \sqrt{< \left[\frac{ratio - \left(-\frac{75}{25}\right)}{\sigma\left(ratio\right)} \right]^2 >_i}, \tag{2.21}$$

where $\sigma(.)$ denotes the standard deviation and is used to standardise C_2.

The final cost function, C, is a combination of the two sub-cost functions given in equations Equations 2.19 and 2.21.

$$C = C_1 + C_2. \tag{2.22}$$

2.2.9 Validation statements

The SDMs were validated using a number of validation statements. Formal model validation for SDMs can be divided into two stages: structural validation and behaviour validation [88]. Structural validity refers to whether the internal structure of the SDMs accurately describes the components of the system that are relevant to the phenomenon, whereas behaviour validity refers to whether the behaviour of the SDMs adequately reproduces real behaviour [88]. Behaviour validation requires longitudinal data, that is, data that enables the validation of the behaviour patterns over time. Here, only structural validation was addressed, which consists of two components: tests addressing direct structure and structure-oriented behaviour. Direct structure tests 'assess the validity of the model structure, by direct comparison with knowledge about real system structure', without simulation, which 'involves taking each relationship (mathematical equation or any form of logical relationship) individually and comparing it with available knowledge about the real system' [88]. The direct structure was addressed by basing the CLD on literature, using equations that were previously defined and validated elsewhere where possible and maintaining dimensional consistency in the SDMs.

As structure-oriented behaviour tests, which 'assess the validity of the structure indirectly, by applying certain behaviour tests on model-generated behavior patterns' using simulation [88], 32 qualitative validation statements derived from expert knowledge and literature were generated. The majority of the literature behind the statements is based on previous empirical research that addresses the Dutch population in particular, which adds to the internal validity of the statements. These statements contain comparisons concerning how the SDMs' behaviours are

expected to differ among the groups. It is hypothesized, for instance, that norms tend to have a larger effect in the Moroccan than the Dutch, as Moroccan culture is regarded as being more collectivistic than Dutch culture [61]. It is expected that a representative set of SDMs will reproduce a considerable number of these validation statements. A set can obtain a validation score out of 32 points (one for each statement), representing its quality.

The validation statements (Table 2.10) should be distinct from the expert knowledge used to construct the CLD and SDMs. In general this is difficult to ensure. Since the expert knowledge used for the CLD is of a 'local' nature (pertaining to a direct cause-and-effect), therefore for the validation statements, 'long-range' statements which span multiple causal links in the SDMs as well as statements which compare different ethnic and gender groups were used.

Validation statements 1-9 tested whether the effect of *PAL* on *BMI* is of the same order of magnitude for different pairs of SDMs. To calculate the effect of *PAL* on BMI, *PAL* was increased by 10% and the stable *MedBMI* (denoted as $MedBMI_{10\%\text{increasedPAL}}(stable)$ in the following equation) was determined. Then, the effect of *PAL* on BMI was calculated as the percentage difference between $MedBMI_{10\%\text{increasedPAL}}$ (stable) and the stable *MedBMI* corresponding to the original *PAL* ($MedBMI_{\text{original}}$ (stable)) divided by $MedBMI_{\text{original}}(stable)$. This is represented by the following equation:

$$^{\text{Effect}}PALonBMI = \frac{MedBMI_{10\%\text{increasedPAL}}(stable) - MedBMI_{\text{original}}(stable)}{MedBMI_{\text{original}}(stable)} \times 100. \tag{2.23}$$

Then, to determine the order of magnitude of the $Effect_{\text{PALonBMI}}$, the logarithm (base 10) of this value was taken for each group. Validation statements 1-9 state that the $Effect_{\text{PALonBMI}}$ is of the same order of magnitude in the respective groups mentioned in each of the statements. To verify this, the rounded ratio of the logarithmic values of the $Effect_{\text{PALonBMI}}$ was taken for the respective groups and a rounded ratio equalling 1 validated that the values of $Effect_{\text{PALonBMI}}$ for the respective groups are of the same order.

For validation statements 10-18, the effect of *Norm* on *IIB* was compared among different pairs of SDMs. *IIB* is a weighted average of *HB* and *Norm*, where

the parameter $Impact_{\text{HBonIIB}}$ determines the relative weight of each. A larger $Impact_{\text{HBonIIB}}$ implies a larger effect of *HB* on *IIB* and as a consequence a lower effect of *Norm* on *IIB*. Hence, to estimate the effect of *Norm* on *IIB*, the impact of *Norm* on *IIB*, as represented by (1 – $Impact_{\text{HBonIIB}}$), was directly compared between the respective pair of SDMs.

For validation statements 19-25, the absolute values of $Intent_{\text{PAB}}$ were compared for the different pairs of SDMs specified in the statements.

Similarly, for validation statements 26-29, the absolute values of $Intent_{\text{EB}}$ were compared for the different pairs of SDMs specified in the statements. For validation statements 30-32, before comparing their absolute values, the $Intent_{\text{EB}}$ values for the male and female groups were scaled based on the fact that when adhering to a healthy, balanced diet, a man needs around 2,500 kcal per day whereas a woman needs around 2,000 kcal per day to maintain his/her weight [89–91]. To account for this discrepancy in required calorie intake to maintain weight, the $Intent_{\text{EB}}$ values for the male and female groups were made comparable, as the aim was to determine the relative change in eating behaviour in a particular group. Accordingly, the $Intent_{\text{EB}}$ values of the male groups were multiplied with the factor 2,000/2,500, to obtain an estimate of the $Intent_{\text{EB}}$ values of the male groups if they were to need 2,000 kcal per day to maintain weight, to make them comparable with the values of the female groups.

2.2.9.1 Weighting cohort data of the HELIUS study

To verify that the study population is representative of the population of the Netherlands (with its different ethnic groups), as most of the supporting literature refers to the population of the Netherlands, it was also checked how many validation statements were correct after the cohort data was weighted according to the age distribution of the population of the Netherlands corresponding to each group.

Hence, to make the comparisons between groups as described in the statements more reliable, the age distribution of the cohort data was adjusted to reflect the age distribution of the population of the Netherlands, based on a dataset that reflects the population of the Netherlands as stratified by age, migration background, sex, and region [92].

For this purpose, the cohort data was divided into five age groups: 18-29, 30-39, 40-49, 50-59, and 60+. In the weight adjustment technique, if a particular age group was under-represented then individuals were added to that age group in the cohort data based on the fraction of individuals in that age group in the population of the Netherlands. For instance, the fraction of South-Asian Surinamese men in the age group of 18-29 in the population of the Netherlands is 0.28. Now, the number of South-Asian Surinamese men in the cohort data is 839. So, to make this age group in the cohort data representative of the population of the Netherlands, 0.28 fraction of the of South-Asian Surinamese men should belong to the age group of 18-29, i.e. 0.28 x 839 = 235 South-Asian Surinamese men. Now, the cohort data contains 179 South-Asian Surinamese men in the age group of 18-29, i.e. it is under-represented based on the fraction of individuals in that age group in the population of the Netherlands. In this case, in the weighting technique, 235-179 = 56 individuals were randomly selected from the age group of 18-29 and then added to the cohort sample. Similarly, if a particular age group was over-represented then individuals were removed from that age group in the cohort data based on the fraction of individuals in that age group in the population of the Netherlands. The same weighting technique was repeated with respect to the population of Amsterdam.

TABLE 2.10: Validation statements

	Validation Statement	**Literature**	**Operationalisation**
1.	There are no significant physiological differences between Dutch and South-Asian Surinamese men regarding the effect of physical activity on weight loss.	[93]	For the male groups, the effect of *PAL* on *BMI* should be of the same order of magnitude in the Dutch as the South-Asian Surinamese group.
2.	There are no significant physiological differences between Dutch and Moroccan men regarding the effect of physical activity on weight loss.	[93, 94]	For the male groups, the effect of *PAL* on *BMI* should be of the same order of magnitude in the Dutch as the Moroccan group.
3.	There are no significant physiological differences between South-Asian Surinamese and Moroccan men regarding the effect of physical activity on weight loss.	[93, 94]	For the male groups, the effect of *PAL* on *BMI* should be of the same order of magnitude in the South-Asian Surinamese as the Moroccan group.
4.	There are no significant physiological differences between Dutch and South-Asian Surinamese women regarding the effect of physical activity on weight loss.	[93, 94]	For the female groups, the effect of *PAL* on *BMI* should be of the same order of magnitude in the Dutch as the South-Asian Surinamese group.
5.	There are no significant physiological differences between Dutch and Moroccan women regarding the effect of physical activity on weight loss.	[93, 94]	For the female groups, the effect of *PAL* on *BMI* should be of the same order of magnitude in the Dutch as the Moroccan group.

Table 2.10 (continued): Validation statements

6.	There are no significant physiological differences between South-Asian Surinamese and Moroccan women regarding the effect of physical activity on weight loss.	[93, 94]	For the female groups, the effect of *PAL* on *BMI* should be of the same order of magnitude in the South-Asian Surinamese as the Moroccan group.
7.	There are no significant physiological differences between Dutch men and women regarding the effect of physical activity on weight loss.	[93, 94]	For the Dutch group, the effect of *PAL* on *BMI* should be of the same order of magnitude in the male as in the female group.
8.	There are no significant physiological differences between South-Asian Surinamese men and women regarding the effect of physical activity on weight loss.	[93, 94]	For the South-Asian Surinamese group, the effect of *PAL* on *BMI* should be of the same order of magnitude in the male as in the female group.
9.	There are no significant physiological differences between Moroccan men and women regarding the effect of physical activity on weight loss.	[93, 94]	For the Moroccan group, the effect of *PAL* on *BMI* should be of the same order of magnitude in the male as in the female group.
10.	Norms tend to have a larger effect on Moroccan than on Dutch men, as Moroccan culture is regarded as being more collectivistic than Dutch culture.	[60, 95–98]	For the male groups, $(1 - Impact_{\text{HBonIIB}})$, which is the impact of *Norm* on *IIB*, should be higher in the Moroccan than in the Dutch group.
11.	Norms tend to have a larger effect on South-Asian Surinamese than on Dutch men, as South-Asian Surinamese culture is regarded as being more collectivistic than Dutch culture.	[60, 96–98]	For the male groups, $(1 - Impact_{\text{HBonIIB}})$, representing the impact of *Norm* on *IIB*, should be higher in the South-Asian Surinamese than in the Dutch group.

Table 2.10 (continued): Validation statements

12.	Norms tend to have a larger effect on Moroccan than on South-Asian Surinamese men, as Moroccan culture is regarded as being more collectivistic than South-Asian Surinamese culture.	[60, 95–100]	For the male groups, (1 – $Impact_{\text{HBonIIB}}$), representing the impact of *Norm* on *IIB*, should be higher in the Moroccan than in the South-Asian Surinamese group.
13.	Norms tend to have a larger effect on Moroccan than on Dutch women, as Moroccan culture is regarded as being more collectivistic than Dutch culture.	[60, 95–98]	For the female groups, (1 – $Impact_{\text{HBonIIB}}$), representing the impact of *Norm* on *IIB*, should be higher in the Moroccan than in the Dutch group.
14.	Norms tend to have a larger effect on South-Asian Surinamese than on Dutch women, as South-Asian Surinamese culture is regarded as being more collectivistic than Dutch culture.	[60, 96–98]	For the female groups, (1 – $Impact_{\text{HBonIIB}}$), representing the impact of *Norm* on *IIB*, should be higher in the South-Asian Surinamese than in the Dutch group.
15.	Norms tend to have a larger effect on Moroccan than on South-Asian Surinamese women, as Moroccan culture is regarded as being more collectivistic than South-Asian Surinamese culture.	[60, 95–100]	For the female groups, (1 – $Impact_{\text{HBonIIB}}$), representing the impact of *Norm* on *IIB*, should be higher in the Moroccan than in the South-Asian Surinamese group.
16.	Dutch women tend to be more prone to be influenced by norms than Dutch men.	[60]	For the Dutch group, (1 – $Impact_{\text{HBonIIB}}$), representing the impact of *Norm* on *IIB*, should be higher in the female than in the male group.

Table 2.10 (continued): Validation statements

17.	South-Asian Surinamese women tend to be more prone to be influenced by norms than South-Asian Surinamese men.	[60]	For the South-Asian Surinamese group, $(1 - Impact_{\text{HBonIIB}})$, which is the impact of *Norm* on *IIB*, should be higher in the female than in male group.
18.	Moroccan women tend to be more prone to be influenced by norms than Moroccan men.	[60]	For the Moroccan group, $(1 - Impact_{\text{HBonIIB}})$, representing the impact of *Norm* on *IIB*, should be higher in the female than in the male group.
19.	The intent to change physical activity behaviour tends to be greater in Dutch than in Moroccan men, as physical activity is more embedded in Dutch than in Moroccan culture.	[101–104]	For the male groups, $Intent_{\text{PAB}}$ should be higher in the Dutch than in the Moroccan group.
20.	The intent to change physical activity behaviour tends to be greater in Dutch than in South-Asian Surinamese men, as physical activity is more embedded in Dutch than in South-Asian Surinamese culture.	[101–107]	For the male groups, $Intent_{\text{PAB}}$ should be higher in the Dutch than in the South-Asian Surinamese group.
21.	The intent to change physical activity behaviour tends to be greater in Dutch than in Moroccan women, as physical activity is more embedded in Dutch than in Moroccan culture.	[101–104, 108]	For the female groups, $Intent_{\text{PAB}}$ should be higher in the Dutch than in the Moroccan group.

Table 2.10 (continued): Validation statements

22.	The intent to change physical activity behaviour tends to be greater in Dutch than in South-Asian Surinamese women, as physical activity is more embedded in Dutch than in South-Asian Surinamese culture.	[101, 102] [105–107]	For the female groups, $Intent_{\text{PAB}}$ should be higher in the Dutch than in the South-Asian Surinamese group
23.	The intent to change physical activity behaviour tends to be greater in Dutch women than in Dutch men.	[109, 110]	For the Dutch group, $Intent_{\text{PAB}}$ should be higher in the female than in the male group.
24.	The intent to change physical activity behaviour tends to be greater in South-Asian Surinamese men than in South-Asian Surinamese women.	[111–117]	For the South-Asian Surinamese group, $Intent_{\text{PAB}}$ should be higher in the male than in the female group.
25.	The intent to change physical activity behaviour tends to be greater in Moroccan men than in Moroccan women.	[111, 118, 119]	For the Moroccan group, $Intent_{\text{PAB}}$ should be higher in the male than in the female group.
26.	The intent to change eating behaviour tends to be greater in Dutch than in Moroccan men, as eating behaviour is more important in Moroccan than in Dutch culture.	[120–123]	For the male groups, $Intent_{\text{EB}}$ should be higher in the Dutch than in the Moroccan group.

Table 2.10 (continued): Validation statements

27.	The intent to change eating behaviour tends to be greater in Dutch than in South-Asian Surinamese men, as eating behaviour is more important in South-Asian Surinamese than in Dutch culture.	[107]	For the male groups, $Intent_{\mathrm{EB}}$ should be higher in the Dutch than in the South-Asian Surinamese group.
28.	The intent to change eating behaviour tends to be greater in Dutch than in Moroccan women, as eating behaviour is more important in Moroccan than in Dutch culture.	[108, 120–123]	For the female groups, $Intent_{\mathrm{EB}}$ should be higher in the Dutch than in the Moroccan group.
29.	The intent to change eating behaviour tends to be greater in Dutch than in South-Asian Surinamese women, as eating behaviour is more important in South-Asian Surinamese than in Dutch culture.	[107]	For the female groups, $Intent_{\mathrm{EB}}$ should be higher in the Dutch than in the South-Asian Surinamese group.
30.	The intent to change eating behaviour tends to be greater in Dutch women than in Dutch men.	[124]	For the Dutch group, $Intent_{\mathrm{EB}}$ should be higher in the female than in the male group.
31.	The intent to change eating behaviour tends to be greater in Moroccan women than in Moroccan men.	[125]	For the Moroccan group, $Intent_{\mathrm{EB}}$ should be higher in the female than in the male group.
32.	The intent to change eating behaviour tends to be greater in South-Asian Surinamese women than in South-Asian Surinamese men.	[107]	For the South-Asian Surinamese group, $Intent_{\mathrm{EB}}$ should be higher in the female than in the male group.

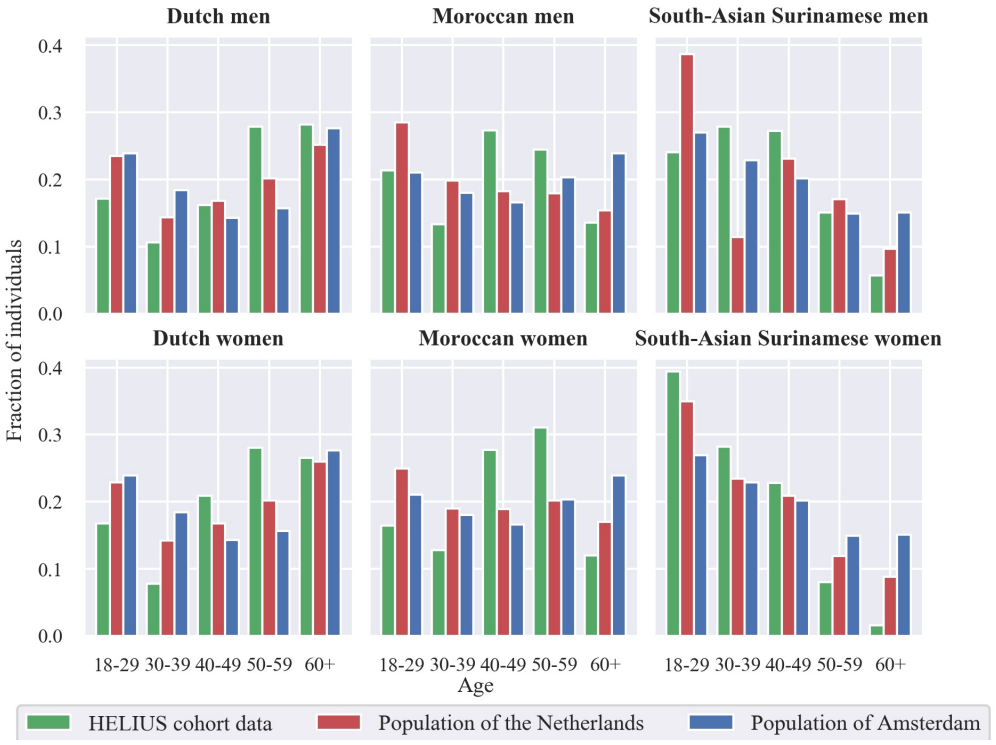

FIGURE 2.8: The age distributions of the cohort data of the HELIUS study, the population of the Netherlands, and the population of Amsterdam.

To gain more insight into how weighting might adjust the validation score, this weight adjustment technique was also performed to make the age distribution of the cohort data reflect the age distribution of the population of Amsterdam, based on a dataset that reflects the population of Amsterdam as stratified by age and migration background [126]. The age distributions of the cohort data, the population of the Netherlands, and the population of Amsterdam are given in Figure 2.8.

The results of the number of validation statements satisfied by the SDMs (out of 32 validation statements in total) according to the different age distributions are given in Table 2.11. The number of validation statements satisfied by the SDMs with the weight adjusted cohort data are given in the form of mean $\pm$ SD because the weight adjustment technique involves the addition or removal of random individuals in a particular age group based on the fraction of individuals in that age group in the population (of the Netherlands and Amsterdam). To take into account the variance in the sampling distribution, the weight adjustment process was repeated 1,000 times for each population (of the Netherlands and Amsterdam), from which a distribution of the number of validation statements satisfied was obtained.

Secondly, the results of which particular validation statements are satisfied by the SDMs under which age weighting adjustments are shown in Table 2.12. Here, the majority vote (in terms of Yes/No) of the 1,000 repetitions of the adjustment process for each population (of the Netherlands and Amsterdam) for each statement are provided.

For the age distribution reflecting the population of the Netherlands, the same set of validation statements was correct as for the original age distribution of the cohort data. For the age distribution reflecting the population of Amsterdam, validation statement 13 was correct (shown in bold in Table 2.12) whereas it was not for the original age distribution of the cohort data. Taking these results together, it can be concluded that weighting does not considerably alter the behaviour of the SDMs, implying that the cohort data are representative for the functioning of this system.

TABLE 2.11: Number of validation statements (out of 32) satisfied by the SDMs according to the original age distribution of the cohort data of the HELIUS study, reflecting the age distribution of the population of the Netherlands, and reflecting the age distribution of the population of Amsterdam.

Number of validation statements (out of 32) satisfied by the SDMs	The original age distribution of the cohort data of the HELIUS study	20
	Reflecting the age distribution of the population of the Netherlands, mean ± SD	20 ± 0.65
	Reflecting the age distribution of the population of Amsterdam, mean ± SD	21 ± 0.35

2.2.10 Scenarios

The validated SDMs were subsequently used to simulate the effect of health awareness versus norms on group-level median BMI. The effect of three scenarios on group-level BMI were simulated in all six groups: 'what if' weight-related behaviour were driven (1) only by health awareness, (2) only by norms and (3) by health awareness and norms combined.

For driven only by health awareness scenario, $Impact_{\text{HBonIIB}}$ was set to 1 in Equation 1 (given in Table 2.6), making IIB only dependent on (equal to) HB:

$$\begin{aligned} IIB_t &= Impact_{\text{HBonIIB}} \times HB + (1 - Impact_{\text{HBonIIB}}) \times Norm_t, \\ IIB_t &= 1 \times HB + (1 - 1) \times Norm_t, \\ IIB_t &= HB. \end{aligned} \tag{2.24}$$

For driven only by norms scenario, $Impact_{\text{HBonIIB}}$ was set to 0 in Equation 1 (given in Table 2.6), making IIB only dependent on (equal to) $Norm$:

$$\begin{aligned} IIB_t &= Impact_{\text{HBonIIB}} \times HB + (1 - Impact_{\text{HBonIIB}}) \times Norm_t, \\ IIB_t &= 0 \times HB + (1 - 0) \times Norm_t, \\ IIB_t &= Norm_t. \end{aligned} \tag{2.25}$$

For driven by health awareness and norms combined scenario, Equation 1 (given in Table 2.6) was kept unchanged, with $Impact_{\text{HBonIIB}}$ as estimated from the cohort data using regression through the origin (Table 2.7), where IIB is dependent on both HB and $Norm$:

$$IIB_t = Impact_{\text{HBonIIB}} \times HB + (1 - Impact_{\text{HBonIIB}}) \times Norm_t \tag{2.26}$$

2.3 Results

The results of this work are divided into three sections corresponding to the results of the (1) optimization, (2) validation and (3) scenarios.

2.3.1 Optimization

Table 2.13 shows the optimal values for $Intent_{\text{PAB}}$ and $Intent_{\text{EB}}$ and the corresponding minimum cost value for 20 optimisation runs (using the basin-hopping algorithm) for each group, referring to the change that individuals make in eating behaviour and physical activity behaviour. These are expressed as a change in

PAL and in *TDEI* per unit of BMI that their *BMI* differs from their *IIB* (their target weight loss/gain expressed by $Discrepancy_{\text{BMIandIIB}}$). South-Asian Surinamese women, for instance, decrease their energy intake by 234 kcal/day for each unit of BMI that they consider to be excessive, according to the cohort data in conjunction with the data-generating assumptions. Since each of the two sub-cost functions were standardised, the minimum cost value can be 2. Also, the results for all 20 optimisation runs were found to be similar.

2.3.1.1 Sensitivity analysis of $Intent_{\text{EB}}$ and $Intent_{\text{PAB}}$

Test 1: varying $Intent_{\text{EB}}$ and keeping $Intent_{\text{PAB}}$ fixed at its optimal value

In this sensitivity analysis test, $Intent_{\text{EB}}$ was varied from -50 to -1,200, whilst keeping $Intent_{\text{PAB}}$ fixed at its optimal value. The sensitivity analysis results were found to be similar for all groups and therefore only the results for South-Asian Surinamese men and women are shown, as they are representative for all groups. The results of this sensitivity analysis test (test 1) for South-Asian Surinamese men and women are shown in Figure 2.9 and Figure 2.10, respectively. From these figures it is observed that as the value for $Intent_{\text{EB}}$ increases, the decrease in *MedBMI* gradually becomes sharp and that *MedBMI* reaches its stable value faster. For $Intent_{\text{EB}}$ values smaller than -500, the system gradually becomes unstable and tends towards oscillatory behaviour. From these results it can be concluded that the SDMs are robust against small changes in $Intent_{\text{EB}}$.

Test 2: varying $Intent_{\text{PAB}}$ and keeping $Intent_{\text{EB}}$ fixed at the optimal value

In this sensitivity analysis test, $Intent_{\text{PAB}}$ was varied from 0.01 to 0.5, whilst keeping $Intent_{\text{EB}}$ fixed at its optimal value. The sensitivity analysis results were again found to be similar for all groups and therefore only the results for South-Asian Surinamese men and women are shown, as they are representative for all groups. The results of this sensitivity analysis test (test 2) for South-Asian Surinamese men and women are shown in Figure 2.11 and Figure 2.12, respectively. From these figures it is observed that as the value for $Intent_{\text{PAB}}$ increases, the decrease in *MedBMI* gradually becomes sharp and that *MedBMI* reaches its stable value faster. For $Intent_{\text{PAB}}$ values greater than 0.2, the system gradually becomes unstable and tends towards oscillatory behaviour. From these results it can be concluded that the SDMs are robust against small changes in $Intent_{\text{PAB}}$.

TABLE 2.12: Behaviours exhibited by the SDMs according to the actual cohort data of the HELIUS study, reflecting the age distribution of the population of the Netherlands, and reflecting the age distribution of the population of Amsterdam.

	Operationalisation	**Behaviour exhibited by the SDMs (Yes/No)**		
		The original age distribution of the cohort data of the HELIUS study	**Reflecting the age distribution of the population of the Netherlands, majority vote out of 1,000**	**Reflecting the age distribution in the population of Amsterdam, majority vote out of 1,000**
1.	For the male groups, the effect of *PAL* on *BMI* should be of the same order of magnitude in the Dutch as the South-Asian Surinamese group.	Yes	Yes	Yes
2.	For the male groups, the effect of *PAL* on *BMI* should be of the same order of magnitude in the Dutch as the Moroccan group.	Yes	Yes	Yes
3.	For the male groups, the effect of *PAL* on *BMI* should be of the same order of magnitude in the South-Asian Surinamese as the Moroccan group.	Yes	Yes	Yes
4.	For the female groups, the effect of *PAL* on *BMI* should be of the same order of magnitude in the Dutch as the South-Asian Surinamese group.	Yes	Yes	Yes

Table 2.12 (continued): Behaviours exhibited by the SDMs according to the actual cohort data of the HELIUS study, reflecting the age distribution of the population of the Netherlands, and reflecting the age distribution of the population of Amsterdam.

5.	For the female groups, the effect of *PAL* on *BMI* should be of the same order of magnitude in the Dutch as the Moroccan group.	Yes	Yes	Yes
6.	For the female groups, the effect of *PAL* on *BMI* should be of the same order of magnitude in the South-Asian Surinamese as the Moroccan group.	Yes	Yes	Yes
7.	For the Dutch group, the effect of *PAL* on *BMI* should be of the same order of magnitude in the male as in the female group.	Yes	Yes	Yes
8.	For the South-Asian Surinamese group, the effect of *PAL* on *BMI* should be of the same order of magnitude in the male as in the female group.	Yes	Yes	Yes
9.	For the Moroccan group, the effect of *PAL* on *BMI* should be of the same order of magnitude in the male as in the female group.	Yes	Yes	Yes
10.	For the male groups, (1 – $Impact_{\mathrm{HBonIIB}}$), representing the impact of *Norm* on *IIB*, should be higher in the Moroccan than in the Dutch group.	Yes	Yes	Yes
11.	For the male groups, (1 – $Impact_{\mathrm{HBonIIB}}$), representing the impact of *Norm* on *IIB*, should be higher in the South-Asian Surinamese than in the Dutch group.	No	No	No

Table 2.12 (continued): Behaviours exhibited by the SDMs according to the actual cohort data of the HELIUS study, reflecting the age distribution of the population of the Netherlands, and reflecting the age distribution of the population of Amsterdam.

12.	For the male groups, (1 – $Impact_{\text{HBonIIB}}$), representing the impact of *Norm* on *IIB*, should be higher in the Moroccan than in the South-Asian Surinamese group.	Yes	Yes	Yes
13.	For the female groups, (1 – $Impact_{\text{HBonIIB}}$), representing the impact of *Norm* on *IIB*, should be higher in the Moroccan than in the Dutch group.	No	No	**Yes**
14.	For the female groups, (1 – $Impact_{\text{HBonIIB}}$), representing the impact of *Norm* on *IIB*, should be higher in the South-Asian Surinamese than in the Dutch group.	No	No	No
15.	For the female groups, (1 – $Impact_{\text{HBonIIB}}$), representing the impact of *Norm* on *IIB*, should be higher in the Moroccan than in the South-Asian Surinamese group.	Yes	Yes	Yes
16.	For the Dutch group, (1 – $Impact_{\text{HBonIIB}}$), representing the impact of *Norm* on *IIB*, should be higher in the female than in the male group.	No	No	No
17.	For the South-Asian Surinamese group, (1 – $Impact_{\text{HBonIIB}}$), representing the impact of *Norm* on *IIB*, should be higher in the female than in male group.	No	No	No

Table 2.12 (continued): Behaviours exhibited by the SDMs according to the actual cohort data of the HELIUS study, reflecting the age distribution of the population of the Netherlands, and reflecting the age distribution of the population of Amsterdam.

18.	For the Moroccan group, (1 – $Impact_{\text{HBonIIB}}$), representing the impact of *Norm* on *IIB*, should be higher in the female than in the male group.	No	No	No
19.	For the male groups, $Intent_{\text{PAB}}$ should be higher in the Dutch than in the Moroccan group.	No	No	No
20.	For the male groups, $Intent_{\text{PAB}}$ should be higher in the Dutch than in the South-Asian Surinamese group.	Yes	Yes	Yes
21.	For the female groups, $Intent_{\text{PAB}}$ should be higher in the Dutch than in the Moroccan group.	No	No	No
22.	For the female groups, $Intent_{\text{PAB}}$ should be higher in the Dutch than in the South-Asian Surinamese group.	Yes	Yes	Yes
23.	For the Dutch group, $Intent_{\text{PAB}}$ should be higher in the female than in the male group.	Yes	Yes	Yes
24.	For the South-Asian Surinamese group, $Intent_{\text{PAB}}$ should be higher in the male than in the female group.	No	No	No
25.	For the Moroccan group, $Intent_{\text{PAB}}$ should be higher in the male than in the female group.	No	No	No
26.	For the male groups, $Intent_{\text{EB}}$ should be higher in the Dutch than in the Moroccan group.	No	No	No

Table 2.12 (continued): Behaviours exhibited by the SDMs according to the actual cohort data of the HELIUS study, reflecting the age distribution of the population of the Netherlands, and reflecting the age distribution of the population of Amsterdam.

27.	For the male groups, $Intent_{\text{EB}}$ should be higher in the Dutch than in the South-Asian Surinamese group.	Yes	Yes	Yes
28.	For the female groups, $Intent_{\text{EB}}$ should be higher in the Dutch than in the Moroccan group.	No	No	No
29.	For the female groups, $Intent_{\text{EB}}$ should be higher in the Dutch than in the South-Asian Surinamese group.	Yes	Yes	Yes
30.	For the Dutch group, $Intent_{\text{EB}}$ should be higher in the female than in the male group.	Yes	Yes	Yes
31.	For the Moroccan group, $Intent_{\text{EB}}$ should be higher in the female than in the male group.	Yes	Yes	Yes
32.	For the South-Asian Surinamese group, $Intent_{\text{EB}}$ should be higher in the female than in the male group.	Yes	Yes	Yes

TABLE 2.13: Optimisation results including value for the cost function corresponding to the set of optimised parameters.

Socio-cultural group	**Intent$_{EB}$ (kcal/day)/(kg/m^2)**	**Intent$_{PAB}$ 1/(kg/m^2)**	**Cost**
Dutch men	-295.46	0.056	2.00
Moroccan men	-301.31	0.056	2.00
South-Asian Surinamese men	-283.19	0.055	2.00
Dutch women	-251.46	0.060	2.00
Moroccan women	-258.81	0.061	2.00
South-Asian Surinamese women	-233.65	0.057	2.00

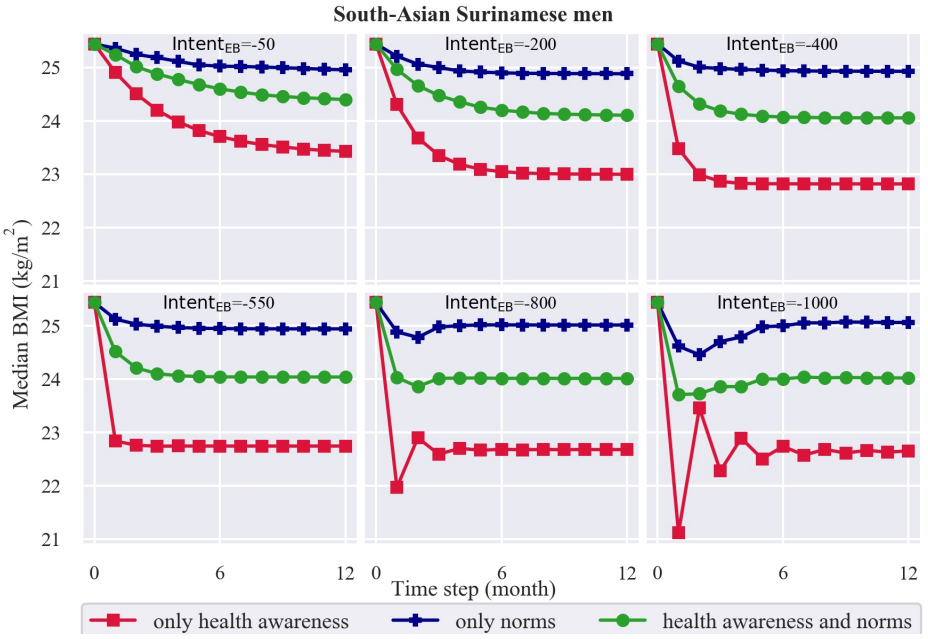

FIGURE 2.9: Test 1 of sensitivity analysis of $Intent_{EB}$ and $Intent_{PAB}$ on *MedBMI* for South-Asian Surinamese men. $Intent_{EB}$ is varied whilst keeping $Intent_{PAB}$ fixed at its optimal value.

From Figures 2.9-2.12, it is also observed that the red line, representing 'what if' group-level BMI were driven only by health awareness, becomes oscillatory quickly and that the oscillatory peaks are high. The reason behind this behaviour is that the value for *IIB* is constant in this scenario (as *Norm* does not play a role anymore). However, if $Intent_{EB}$ or $Intent_{PAB}$ has a very high value, then the *MedBMI* change is large, and this makes $Discrepancy_{BMIandIIB}$ become alternatively highly positive and negative. So, this oscillating behaviour appears instantly with high oscillatory peaks in the scenario representing driven only by health awareness (red line). In the scenario representing driven only by norms (blue line), and in the scenario representing driven by health awareness and norms combined (green line),

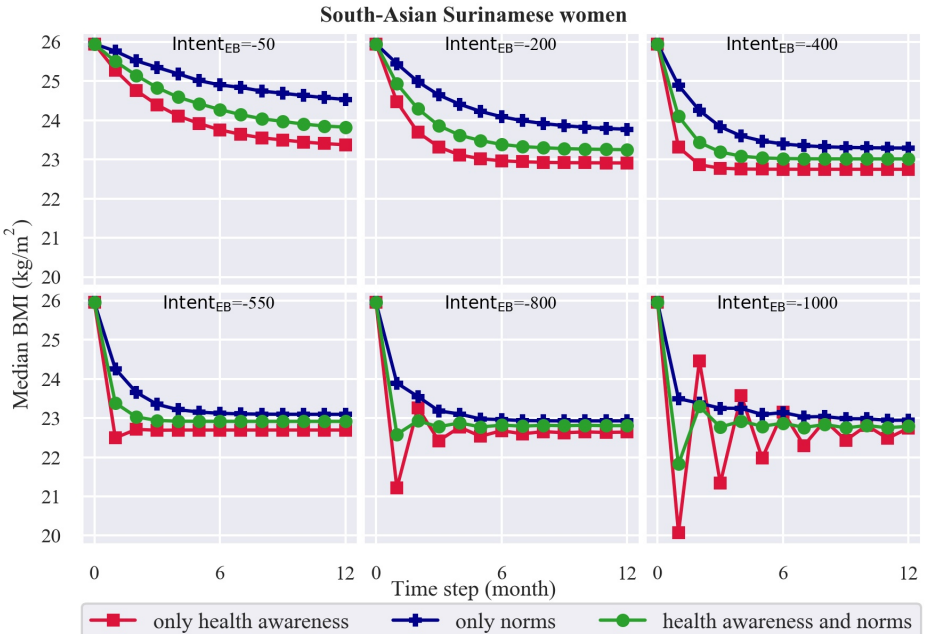

FIGURE 2.10: Test 1 of sensitivity analysis of $Intent_{\text{EB}}$ and $Intent_{\text{PAB}}$ on *MedBMI* for South-Asian Surinamese women. $Intent_{\text{EB}}$ is varied whilst keeping $Intent_{\text{PAB}}$ fixed at its optimal value.

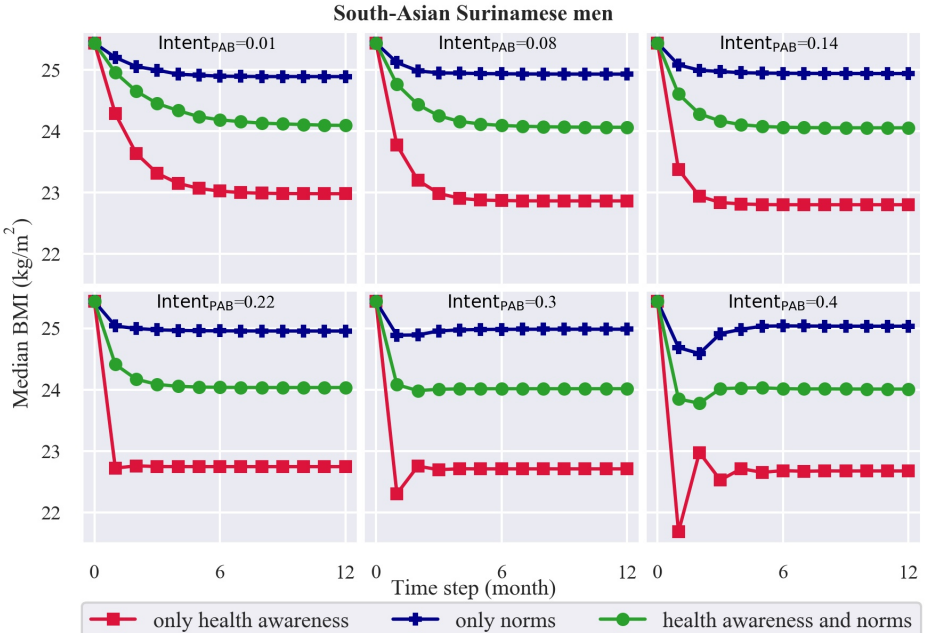

FIGURE 2.11: Test 2 of sensitivity analysis of $Intent_{\text{EB}}$ and $Intent_{\text{PAB}}$ on *MedBMI* for South-Asian Surinamese men. $Intent_{\text{PAB}}$ is varied whilst keeping $Intent_{\text{EB}}$ fixed at its optimal value.

the oscillations start later, and the oscillatory peaks are small because the value for *IIB* also changes based on the change in *MedBMI* (which adjusts *Norm*).

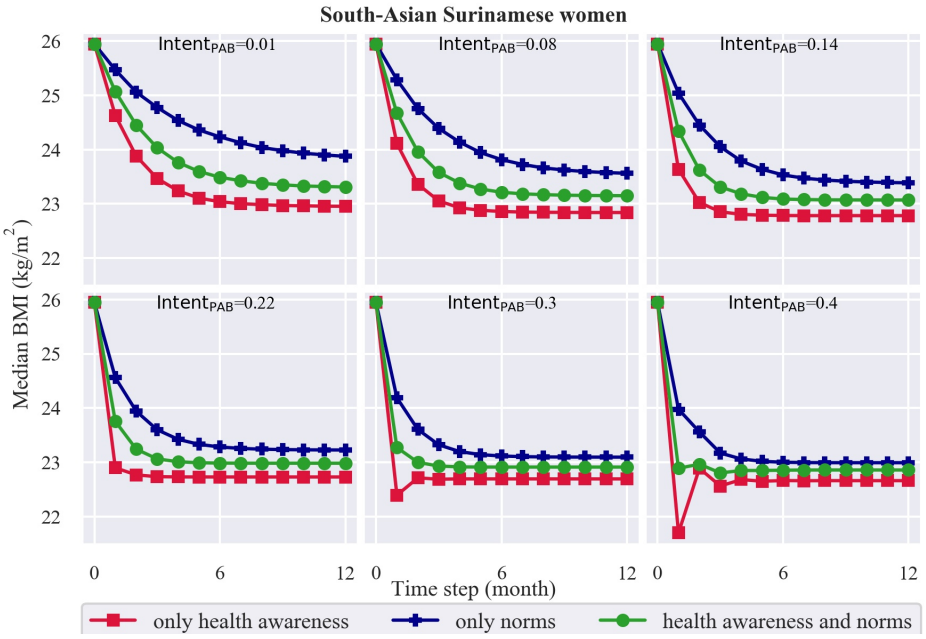

FIGURE 2.12: Test 2 of sensitivity analysis of $Intent_{\mathrm{EB}}$ and $Intent_{\mathrm{PAB}}$ on *MedBMI* for South-Asian Surinamese women. $Intent_{\mathrm{PAB}}$ is varied whilst keeping $Intent_{\mathrm{EB}}$ fixed at its optimal value.

2.3.1.2 Sensitivity analysis of $Impact_{\mathrm{HBonIIB}}$

To test the sensitivity of the change in *MedBMI* to $Impact_{\mathrm{HBonIIB}}$, the value of $Impact_{\mathrm{HBonIIB}}$ was increased and decreased by 50% and the change in stable *MedBMI* at convergence was analyzed as follows:

$$\Delta MedBMI = \frac{MedBMI_{\mathrm{altered}}(stable) - MedBMI_{\mathrm{original}}(stable)}{MedBMI_{\mathrm{original}}(stable)} \times 100, \quad (2.27)$$

where $MedBMI_{\mathrm{altered}}(stable)$ is the stable *MedBMI* with the 50% altered $Impact_{\mathrm{HBonIIB}}$ and $MedBMI_{\mathrm{original}}(stable)$ is the stable *MedBMI* with the original $Impact_{\mathrm{HBonIIB}}$. From the results given in Table 2.14, it is observed that the percentage change in stable *MedBMI* for a 50% change in $Impact_{\mathrm{HBonIIB}}$ is very small (<2%). Thus, it can be concluded that *MedBMI* is not sensitive to changes in $Impact_{\mathrm{HBonIIB}}$.

2.3.2 Validation

A validation score of 20/32 points (62.5% correct) was obtained for the set of SDMs. This implies that the set of equations that were used in the model was

TABLE 2.14: Sensitivity analysis of $Impact_{\text{HBonIIB}}$, showing the percentage change in stable *MedBMI* for a 50% increase and decrease in the value for $Impact_{\text{HBonIIB}}$.

Socio-cultural group	**ΔMedBMI (50% increase in $\text{Impact}_{\text{HBonIIB}}$), %**	**ΔMedBMI (50% decrease in $\text{Impact}_{\text{HBonIIB}}$), %**
Dutch men	-1.13	0.16
Moroccan men	-1.19	1.37
South-Asian Surinamese men	-1.30	1.62
Dutch women	-0.18	0.16
Moroccan women	-0.85	1.09
South-Asian Surinamese women	-0.75	0.79

capable of capturing the expected behaviour to a large extent. Table 2.15 shows for each behaviour whether it is exhibited by the respective SDMs.

2.3.3 Scenarios

For all groups (Figure 2.13), it is observed that if weight-related behaviour were driven by a combination of health awareness and norms (green), then group-level median BMI would be lower than if driven only by norms (blue) and higher than if driven only by health awareness (red). If driven only by health awareness (red), there would only be minor differences between the male and female groups: median BMI would drop 11% (3 BMI points) among groups of both genders, which is trivial given the definition of this scenario.

If driven by only health awareness, median BMI decreases by 10% (3 BMI points) among Dutch, 12% (3 points) among Moroccan, and 10% (3 points) among South-Asian Surinamese men. It drops 8% (2 points) among Dutch, 12% (3 points) among Moroccan, and 12% (3 points) among South-Asian Surinamese women.

If driven by only norms, there is a reduction in median BMI of 2% (1 point) among Dutch, 3% (1 point) among Moroccan, and 2% (1 point) among South-Asian Surinamese men. The drop is 7% (2 points) among Dutch, 8% (2 points) among Moroccan, and 9% (2 points) among South-Asian Surinamese women.

If driven by health awareness and norms, median BMI drops 5% (1 points) among Dutch, 5% (1 point) among Moroccan, and 5% (1 point) among South-Asian Surinamese men. It decreases by 8% (2 points) among Dutch, 11% (3 points) among Moroccan, and 11% (3 points) among South-Asian Surinamese women.

For the other scenarios, that is, if driven only by norms (blue) and by health awareness and norms combined (green), different emergent behaviours are observed between the male versus female groups, while they demonstrate only slight differences between groups of the same gender. These small quantitative differences are not as reliable as the large qualitative differences that the simulations show, given the cross-sectional data that is used. Therefore, mostly the qualitative differences are considered, that is, those between genders.

If driven only by norms (blue), there would be an average reduction in median BMI of 5% (1 point). However, it is observed that among the male groups, median BMI would only decrease by 2% (1 point), whereas among the female groups, it would reduce by 8% (2 points). This pattern is observed in all three ethnic groups.

If driven by health awareness and norms combined (green), median BMI would drop 7% (2 points) on average. Again, it would decrease less in the male groups, with only 5% (1 point). In the female groups, the decrease would be larger: 10% (2 points).

The male groups thus demonstrated an over two times larger drop if driven by health awareness than if driven by health awareness and norms combined. In contrast, their female counterparts showed a more equal drop in both these scenarios. When driven only by norms, median BMI in all groups would decrease to a lesser extent. In the female groups, however, being driven only by norms leads to a similar decrease in median BMI as being driven only by health awareness and being driven by health awareness and norms combined. In the male groups, the decrease in median BMI is different for all scenarios.

The confidence interval (CI) of the group-level BMI at each time step were determined for the three scenarios, shown in Figure 2.13 as the shaded area around the group-level BMI at each time step. Since the group-level BMI at each time step is the median of the individual values for BMI at that time step, the formula of CI for medians was used to determine the CIs at each time step. The lower

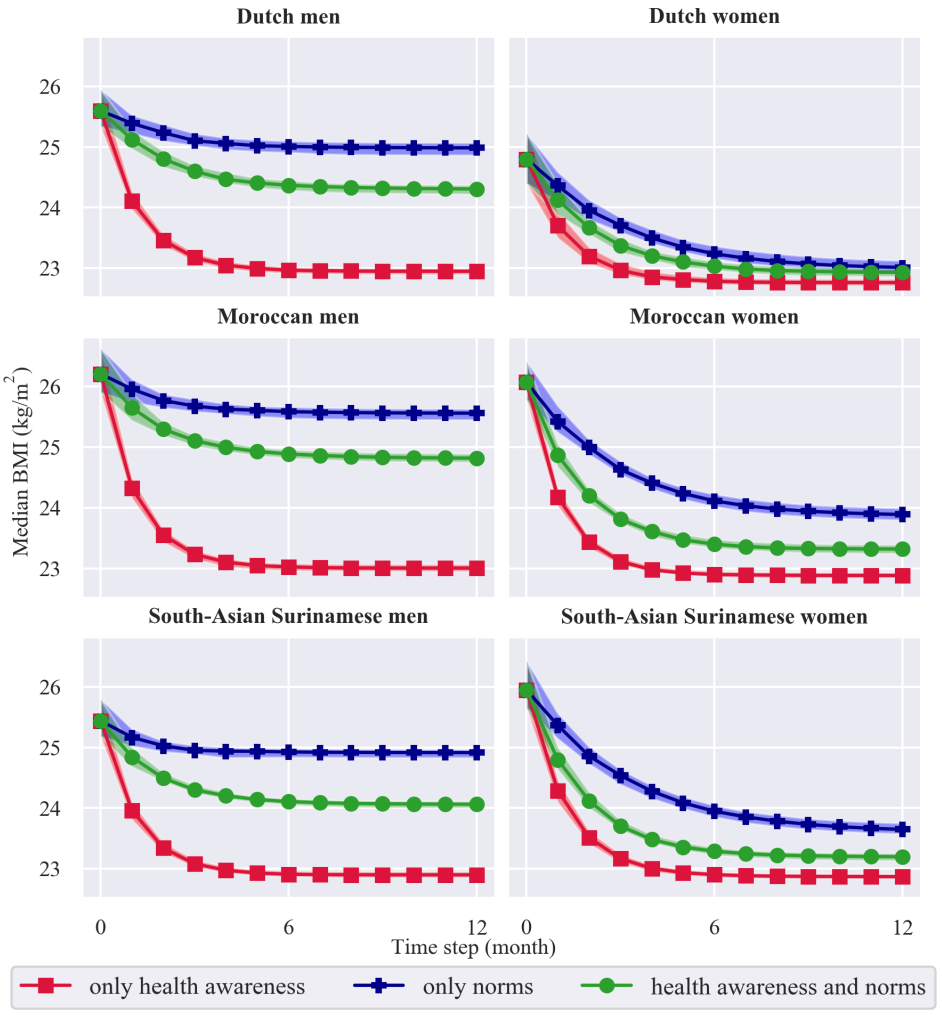

FIGURE 2.13: Change in group-level body mass index (BMI) over time for three scenarios: 'what if' weight-related behaviour were driven (1) only by health awareness (red), (2) only by norms (blue) and (3) by health awareness and norms combined (green). The 95% confidence interval corresponding to each of these scenarios is shaded in red, blue and green, respectively.

95% confidence limit is given by the value at rank: $\frac{n}{2} - \frac{1.96\sqrt{n}}{2}$. The upper 95% confidence limit is given by the value at rank: $1 + \frac{n}{2} + \frac{1.96\sqrt{n}}{2}$.

Table 2.15: Behaviours exhibited by the SDMs.

	Validation statement	**Operationalisation: Behaviour exhibited by the SDMs?**
1.	There are no significant physiological differences between Dutch and South-Asian Surinamese men regarding the effect of physical activity on weight loss.	Yes: In the male groups, the effect of *PAL* on *BMI* is of the same order of magnitude in the Dutch as the South-Asian Surinamese group.
2.	There are no significant physiological differences between Dutch and Moroccan men regarding the effect of physical activity on weight loss.	Yes: In the male groups, the effect of *PAL* on *BMI* is of the same order of magnitude in the Dutch as the Moroccan group.
3.	There are no significant physiological differences between South-Asian Surinamese and Moroccan men regarding the effect of physical activity on weight loss.	Yes: In the male groups, the effect of *PAL* on *BMI* is of the same order of magnitude in the South-Asian Surinamese as the Moroccan group.
4.	There are no significant physiological differences between Dutch and South-Asian Surinamese women regarding the effect of physical activity on weight loss.	Yes: In the female groups, the effect of *PAL* on *BMI* is of the same order of magnitude in the Dutch as the South-Asian Surinamese group.
5.	There are no significant physiological differences between Dutch and Moroccan women regarding the effect of physical activity on weight loss.	Yes: In the female groups, the effect of *PAL* on *BMI* is of the same order of magnitude in the Dutch as the Moroccan group.
6.	There are no significant physiological differences between South-Asian Surinamese and Moroccan women regarding the effect of physical activity on weight loss.	Yes: In the female groups, the effect of *PAL* on *BMI* is of the same order of magnitude in the South-Asian Surinamese as the Moroccan group.
7.	There are no significant physiological differences between Dutch men and women regarding the effect of physical activity on weight loss.	Yes: In the Dutch group, the effect of *PAL* on *BMI* is of the same order of magnitude in the male as in the female group.

Table 2.15 (continued): Behaviours exhibited by the SDMs.

8.	There are no significant physiological differences between South-Asian Surinamese men and women regarding the effect of physical activity on weight loss.	Yes: In the South-Asian Surinamese group, the effect of *PAL* on *BMI* is of the same order of magnitude in the male as in the female group.
9.	There are no significant physiological differences between Moroccan men and women regarding the effect of physical activity on weight loss.	Yes: In the Moroccan group, the effect of *PAL* on *BMI* is of the same order of magnitude in the male as in the female group.
10.	Norms tend to have a larger effect on Moroccan than on Dutch men, as Moroccan culture is regarded as being more collectivistic than Dutch culture.	Yes: In the male groups, (1—$Impact_{\mathrm{HBonIIB}}$), representing the impact of *Norm* on *IIB*, is higher in the Moroccan than in the Dutch group.
11.	Norms tend to have a larger effect on South-Asian Surinamese than on Dutch men, as South-Asian Surinamese culture is regarded as being more collectivistic than Dutch culture.	No: In the male groups, (1—$Impact_{\mathrm{HBonIIB}}$), representing the impact of *Norm* on *IIB*, is not higher in the South-Asian Surinamese than in the Dutch group.
12.	Norms tend to have a larger effect on Moroccan than on South-Asian Surinamese men, as Moroccan culture is regarded as being more collectivistic than South-Asian Surinamese culture.	Yes: In the male groups, (1—$Impact_{\mathrm{HBonIIB}}$), representing the impact of *Norm* on *IIB*, is higher in the Moroccan than in the South-Asian Surinamese group.
13.	Norms tend to have a larger effect on Moroccan than on Dutch women, as Moroccan culture is regarded as being more collectivistic than Dutch culture.	No: In the female groups, (1—$Impact_{\mathrm{HBonIIB}}$), representing the impact of *Norm* on *IIB*, is not higher in the Moroccan than in the Dutch group.
14.	Norms tend to have a larger effect on South-Asian Surinamese than on Dutch women, as South-Asian Surinamese culture is regarded as being more collectivistic than Dutch culture.	No: In the female groups, (1—$Impact_{\mathrm{HBonIIB}}$), representing the impact of *Norm* on *IIB*, is not higher in the South-Asian Surinamese than in the Dutch group.

Table 2.15 (continued): Behaviours exhibited by the SDMs.

15.	Norms tend to have a larger effect on Moroccan than on South-Asian Surinamese women, as Moroccan culture is regarded as being more collectivistic than South-Asian Surinamese culture.	Yes: In the female groups, (1—$Impact_{\text{HBonIIB}}$), representing the impact of *Norm* on *IIB*, is higher in the Moroccan than in the South-Asian Surinamese group.
16.	Dutch women tend to be more prone to be influenced by norms than Dutch men.	No: In the Dutch group, (1—$Impact_{\text{HBonIIB}}$), representing the impact of *Norm* on *IIB*, is not higher in the female than in the male group.
17.	South-Asian Surinamese women tend to be more prone to be influenced by norms than South-Asian Surinamese men.	No: In the south-Asian Surinamese group, (1—$Impact_{\text{HBonIIB}}$), representing the impact of *Norm* on *IIB*, is not higher in the female than in male group.
18.	Moroccan women tend to be more prone to be influenced by norms than Moroccan men.	No: In the Moroccan group, (1—$Impact_{\text{HBonIIB}}$), representing the impact of *Norm* on *IIB*, is not higher in the female than in the male group.
19.	The intent to change physical activity behaviour tends to be greater in Dutch than in Moroccan men, as physical activity is more embedded in Dutch than in Moroccan culture.	No: In the male groups, $Intent_{\text{PAB}}$ is not higher in the Dutch than in the Moroccan group.
20.	The intent to change physical activity behaviour tends to be greater in Dutch than in South-Asian Surinamese men, as physical activity is more embedded in Dutch than in South-Asian Surinamese culture.	Yes: In the male groups, $Intent_{\text{PAB}}$ is higher in the Dutch than in the South-Asian Surinamese group.

Table 2.15 (continued): Behaviours exhibited by the SDMs.

21.	The intent to change physical activity behaviour tends to be greater in Dutch than in Moroccan women, as physical activity is more embedded in Dutch than in Moroccan culture.	No: In the female groups, $Intent_{\text{PAB}}$ is not higher in the Dutch than in the Moroccan group.
22.	The intent to change physical activity behaviour tends to be greater in Dutch than in South-Asian Surinamese women, as physical activity is more embedded in Dutch than in South-Asian Surinamese culture.	Yes: In the female groups, $Intent_{\text{PAB}}$ is higher in the Dutch than in the South-Asian Surinamese group.
23.	The intent to change physical activity behaviour tends to be greater in Dutch women than in Dutch men.	Yes: In the Dutch group, $Intent_{\text{PAB}}$ is higher in the female than in the male group.
24.	The intent to change physical activity behaviour tends to be greater in South-Asian Surinamese men than in South-Asian Surinamese women.	No: In the South-Asian Surinamese group, $Intent_{\text{PAB}}$ is not higher in the male than in the female group.
25.	The intent to change physical activity behaviour tends to be greater in Moroccan men than in Moroccan women.	No: In the Moroccan group, $Intent_{\text{PAB}}$ is not higher in the male than in the female group.
26.	The intent to change eating behaviour tends to be greater in Dutch than in Moroccan men, as eating behaviour is more important in Moroccan than in Dutch culture.	No: In the male groups, $Intent_{\text{EB}}$ is not higher in the Dutch than in the Moroccan group.
27.	The intent to change eating behaviour tends to be greater in Dutch than in South-Asian Surinamese men, as eating behaviour is more important in South-Asian Surinamese than in Dutch culture.	Yes: In the male groups, $Intent_{\text{EB}}$ is higher in the Dutch than in the South-Asian Surinamese group.

Table 2.15 (continued): Behaviours exhibited by the SDMs.

28.	The intent to change eating behaviour tends to be greater in Dutch than in Moroccan men, as eating behaviour is more important in Moroccan than in Dutch culture.	No: In the female groups, $Intent_{\mathrm{EB}}$ is not higher in the Dutch than in the Moroccan group.
29.	The intent to change eating behaviour tends to be greater in Dutch than in South-Asian Surinamese women, as eating behaviour is more important in South-Asian Surinamese than in Dutch culture.	Yes: In the female groups, $Intent_{\mathrm{EB}}$ is higher in the Dutch than in the South-Asian Surinamese group.
30.	The intent to change eating behaviour tends to be greater in Dutch women than in Dutch men.	Yes: In the Dutch group, $Intent_{\mathrm{EB}}$ is higher in the female than in the male group.
31.	The intent to change eating behaviour tends to be greater in Moroccan women than in Moroccan men.	Yes: In the Moroccan group, $Intent_{\mathrm{EB}}$ is higher in the female than in the male group.
32.	The intent to change eating behaviour tends to be greater in South-Asian Surinamese women than in South-Asian Surinamese men.	Yes: In the South-Asian Surinamese group, $Intent_{\mathrm{EB}}$ is higher in the female than in the male group.

2.4 Discussion

In this work, SDMs of the system of social norms regarding body weight perception and obesity prevalence were constructed, which were used to compare the effect of health awareness versus norms on group-level BMI. These SDMs were developed to explicitly describe the causal mechanism underlying this system and to get insights into the long-term consequences of this mechanism at the group level. The results show that group-level BMI shifts to a lesser extent in all groups if norms have an influence on weight-related behaviour, confirming that norms are counteracting health awareness in shaping this behaviour. Particularly, in groups where overweight is the norm, that is, all male groups, the norm holds group-level BMI close to overweight despite of health awareness.

These results should be seen in light of a number of methodological considerations. SDMs were selected as they allow the assumption that within a group all individuals compare themselves to that group equivalently, that is, their interactions are homogeneous. The data necessary to model possible heterogeneity in behaviour or in social connectivity were not available, as would be required to make, for example, an agent-based modelling approach [127], with diverse interactions of unique agents with others and with their environment, valuable. It was also assumed that there is no interaction between the socio-cultural groups with respect to this system, implying that individuals are most likely to compare themselves to others from their own socio-cultural group. Although it cannot be ruled out that there is interaction affecting this system, the similarity hypothesis on which the assumption was based is well-established [4]. In the SDMs, individuals compare themselves to their entire socio-cultural group, whereas this comparison group might actually be more confined. Stratifying by other characteristics that also affect body weight perception and the influence of norms in addition to gender and ethnicity, for example, age [128], would result in smaller comparison groups. Zooming in on these subgroups could reveal additional emergent behaviours, which were not detected in this study as it was focused on the current groups' average dynamics.

In addition, it was assumed that median BMI and socio-cultural ideal BMI exert an equal influence on the norm, as the most conservative ratio, which might not be accurate. It was also assumed that individuals adjust their weight-related behaviour to narrow the gap between their actual and ideal BMI and that their

behaviour is driven by health awareness and norms. This assumption implies that these are the only determinants of weight change, which is a simplification of reality. The scope of the SDMs were deliberately kept limited, omitting other drivers of weight-related behaviour. This is related to the proof-of-concept function of this study, where the objective was to demonstrate the methods required to design functioning SDMs with the aim to study feedback loops relevant to the field of public health. The SDMs therefore include only those factors that were deemed necessary and sufficient to describe this system, as the aim is to understand the implications of its feedback loops on the long term, rather than to propose interventions or make predictions. In reality, broader environmental variables as well as individual characteristics such as education and income could affect whether individuals are willing and able to adjust their behaviour. Given that the aim of these SDMs was to unravel a specific causal mechanism and its long-term effects at the group level, it was not considered essential to take individual physiological factors or genetic predispositions into account. Nevertheless, it is acknowledged that these factors have a role to play in weight loss and weight gain at the individual level. However, norms and their impact on weight-related behaviour are crucial factors to study in light of the obesity epidemic as changes in physiology or genetics at the group level are unable to exclusively explain the trend in obesity rates. All other variables and characteristics being equal, the SDMs show the impact of norms in groups that differ regarding body weight perception, group-level norms and the strengths of the causal links between them. The SDMs thus do not constitute a description of reality but serve to explore 'what if' scenarios in a restricted, specific context. These SDMs may serve as seed models for iterative extensions to include additional variables, which would make weight-related behaviour dependent on more determinants, possibly introducing more divergence in emergent behaviour. However, it was considered important to understand the impact of norms in isolation before compounding additional causal mechanisms into the same SDMs.

As the data were cross-sectional, expert-informed data-generating assumptions were used to optimize the values for the parameters for intent to change physical activity and eating behaviour, respectively. This means that in each group, the simulations were based on the same hypothesized fundamental behaviours, as supported by literature, with respect to weight gain/loss, for example, concerning physiological constraints (rate of weight change). These fundamental behaviours however do not markedly influence the differences that were observed between the

groups over time. These differences are primarily based on the initial characteristics and the fitted parameters, which differ per group, in conjunction with the equations.

Lastly, structural validation is ideally followed by behaviour validation. Behaviour validation, however, requires the use of longitudinal data, that is, data that enable the validation of the behaviour patterns over time. Still, the sequence of stages of the formal model validation for SDMs implies that the SDMs in this study were validated according to the gold standard in the case that longitudinal data are unavailable. In practice, behaviour validation is often used without going through structural validation. Given the inherent importance of the latter in system dynamics modelling in particular, that is, 'it is often said that a system dynamics model must generate "the right output for the right reasons"' [88], the efforts concerning this type of validity shown in this study can be seen as an asset. The manner in which the structural validation of the SDMs were addressed, for example, by supporting the expert-informed CLD with literature, using established equations, maintaining dimensional consistency and employing validation statements, serves to establish that the assumptions made currently hold. Nevertheless, this does not rule out the possibility that new empirical evidence might call for readjustments of these assumptions.

The results of this study can be placed in the context of the current debate on addressing group-level determinants in policy aiming to reduce obesity prevalence. In public health, it seems widely accepted that solutions for the increasing rates of overweight and obesity cannot solely be found in individual-level actions such as health education. An additional focus on group-level determinants such as the food environment or norms regarding body weight seems imperative. Although policies often start with a commitment to deal with group-level determinants, they frequently end up with the implementation of individualized interventions aimed at changing individual weight-related behaviour [129, 130]. A failure to tackle group-level determinants may be because, although there is a large body of knowledge on the way these determinants shape public health problems, the knowledge base regarding the impact of interventions addressing these determinants is limited.

Currently, the evaluation of interventions aimed at higher level determinants is largely dependent on 'natural experiments', an approach that has proven to be extremely complex and heavily dependent on the very few actual policies that

lend themselves for impact evaluation [131]. The use of complexity science, more specifically systems dynamic modelling, applied to relevant processes at the group level, is likely to speed up knowledge production in this field. This study is an attempt to explore the value of this approach, specifically for the issue of tackling overweight and obesity. The results of this study should not be interpreted as predictions that can directly be applied to policy but rather as 'what if' scenarios that attempt to clarify a causal mechanism. The SDMs enable this mechanism to be unravelled by exhibiting patterns that could not have been predicted by only considering group-level characteristics. For instance, this way of considering the individual values for socio-cultural ideal BMI, which during the simulations remain initialized by every individual's own value for this variable as derived from the cohort data, presents a group-level pattern that could not have been predicted otherwise. This observed pattern at the group level can be interpreted as an emergent behaviour of the system.

The following lessons can be drawn from this study regarding the underlying causal mechanism that was modelled. Firstly, this study adds understanding to how group-level processes, in this case in relation to norms, work. Specifically, previous research has shown that obesity spreads through social ties [132]. This work explores a potential causal mechanism for this process by specifying that individual body weight perception is affected by what is normal while also affecting what is normal via its impact on obesity prevalence, inducing feedback loops that may over time contribute to group-level obesity. This study investigated this hypothesized causal mechanism by operationalising it using system dynamics modelling, where all causal links are supported by literature and implemented mathematically in an intuitive, explainable manner. This is contrary to the majority of other quantitative epidemiological methods, which are based on statistical models attempting to discover correlations, without explicitly studying causal mechanisms. The approach used in this study enables the simulation of each group's emergent behaviour as a function of the hypothesized causal mechanisms. The results of this study confirm that the hypothesized feedback loops can be an explanation for group-level obesity, where group-level BMI is reinforced by individual body weight perception via the norm.

In this study, it was also shown that if norms were the only determinant of weight change, men would not lose weight, whereas women would. This implies that norms

are counteracting health awareness less strongly in women, suggesting that they must be subject to additional drivers of obesity. The major driver of this divergence in behaviour is the norm, which is closer to the healthy weight range in women. This is in line with previous research showing that women are generally more engaged in health and weight-related behaviour [133, 134]. Previous research has also shown 'that appearance norms encountered by women in daily life are more rigid, homogeneous and pervasive than those for men, and that more messages implying the attainability of the ideal appearance are directed at women' [135]. For women, having this pressure to conform to the socio-cultural ideal BMI might add to the discrepancy between the results of the scenarios and reality. That is, despite of being aware of the socio-cultural ideal BMI and the socio-cultural ideal BMI being healthy, which under the assumptions used in this study should lead to weight loss in women, in reality it is seen that, at the group level, women are not losing weight. In this regard, it has for instance been shown that weight stigma increased the inclination to avoid exercise, independent of BMI and body satisfaction, among college-aged females [136].

In addition, under the assumptions used in this study, the cohort data underlying the SDMs suggest that the relative impact of norms on individual ideal BMI is larger among men. This is of interest, as usually the effect of norms on weight change is considered to be indicative of their strength. That is, norms towards body weight are generally regarded as being stronger in women, as women more likely to want to adjust their weight based on norms [137]. The results of this study however show that norms are stronger in men. This suggests that even though for men norms do not contribute to weight loss, they do establish the reinforcing feedback loops of group-level obesity. As the cohort data also show that the norm is approximately equal to group-level BMI in men, this might indicate that what is normal may be more important than what is ideal in determining what body weight men strive for. This is supported by findings from previous research showing that men are less likely to recognize their own overweight status and are more satisfied with their body weight than women [124, 138].

Secondly, this study adds evidence that efforts to address the obesity epidemic need to consider norms, as an example of group-level processes. The results indicate that in populations where overweight is the norm, the potential impact of policies is

greater if they address these norms, as compared with policies that use individual-level approaches only. Here, addressing the norm does not equal enforcing stricter weight ideals, as the norm is dependent on both median BMI and socio-cultural ideal BMI, where the latter refers to weight ideals. The norm is thus influenced by median BMI, that is, what you see around you. From a policy perspective, this might mean that making individuals aware of their obesity status is not the road forward, but taking measures at the group level to reduce the obesity prevalence is. A commitment to deal with the norm can thus be independent of socio-cultural ideal BMI, by attending to median BMI at the group level.

Studying 'what if' scenarios using computational modelling approaches allow policy strategies to be tested under the exact same conditions. Although the SDMs do not include potential solutions for influencing norms, they show that influences on both the individual as well as the group level should be considered. The results of this study suggest that norms limit the effectiveness of interventions targeting individual weight-related behaviour, especially in men. A restricted focus on individual weight-related behaviour, which places the responsibility for body weight on the individual in a context where overweight is the norm, might even have adverse effects [5]. The results indicate that shifting the focus to group-level interventions aiming to change the norm can contribute to the prevention of group-level obesity. A starting point for this can be considering how the effects of policy strategies may diverge among groups based on the prevailing norm towards body weight. Given that in this study population overweight prevalence is high in both men and women, the results of the scenarios imply that failing to consider the norm and its effect over time might result in a similar policy strategy for both genders, which would be misguided. The SDMs constructed in this study can be instrumental in considering the norms of groups that, besides gender and ethnicity, differ with respect to characteristics such as socio-economic status. This can be explored in future research using these SDMs and would allow the differentiation of policy based on the group-level norm towards body weight, in addition to obesity prevalence.

Chapter 3

Temporal dynamics from cross-sectional data using Langevin dynamics

3.1 Introduction

Longitudinal studies require a huge investment in terms of time, money, and effort, depending on the system studied. For instance, biological experiment techniques such as sequencing-based assays destroy cells in order to measure certain concentrations; population-based cohort studies in public health, such as HELIUS [10], involve asking each of the participants to visit the hospital, measuring various physiological variables, and assessing psychological well-being through interviews and questionnaires. This leads to a relative abundance of cross-sectional datasets in these fields. However, the price to pay is that cross-sectional data lack the temporal information needed to study the evolution of the underlying processes. This hampers the development of models which can make predictions (predictive models) or even simulate the effects of interventions (causal models) in these fields. Therefore, in order to utilize the abundant cross-sectional data to study the dynamics of system behaviour it is important to design methods that aim to infer the temporal dynamics from these data.

There are several techniques in the literature for estimating pseudo-longitudinal data from cross-sectional data, which include employing distance metrics and graph

theoretical operations [76–83]. They aim to construct realistic trajectories through the feature space by using techniques such as ordering of the data-points and selecting start-points and end-points based on known class labels. For instance, one way to order data-points is by assuming that the label 'healthy' precedes the label 'diseased'. Another way to order biological samples or RNA-seq data is by using their gene expression levels. Of course, these methods rely on the presence of suitable variables in the dataset, as well as the assumptions about how these labels induce an ordering. The proposed method, on the other hand, infers the temporal dynamics from the distribution of the data-points, and hence, is not dependent on the ordering of the data-points or the presence of order-inducing variables.

In this work, a method for inferring predictive computational models from cross-sectional data using Langevin dynamics [139] was proposed. The free energy landscape, which is a mapping of all possible states of the data-points in the system, was reconstructed from the cross-sectional data by assuming that groups of data-points having similar features follow similar trajectories. A free energy landscape can be considered analogous to an uneven hillside and the data-points in the landscape as balls rolling down the hillside. The balls will eventually come to rest in a stable state in the valleys. These valleys are the attractors in the free energy landscape. Trajectories across a landscape correspond to the progression of the data-points. This method estimates the free energy landscape based on the probability distribution of the data-points. Roughly speaking, the free energy landscape is approximately the inverse of the probability distribution of the data-points. Thus, the attractors in this estimated energy landscape will approximately correspond to the peaks in the probability distribution. For instance, following this assumption, a free energy landscape estimated from a probability distribution of the BMI values of a group of individuals will have attractors that will correspond approximately to the most probable BMI values in that group of individuals.

The proposed method was based on the following assumptions. The first assumption was that the distribution depends only on the variable of interest. For instance, for a cross-sectional data of the BMI of a sub-population, it was assumed that the distribution of these BMIs does not depend on other variables such as physiological factors, physical activity, diet, stress, etc. The second assumption was that the distribution of the data-points has converged to a stable distribution at the

time of observation. For instance, for a cross-sectional data of the BMIs of a sub-population, it was assumed that the sub-population is not currently subjected to any intervention that will change the distribution of BMIs within a short time-span. That is, even though, at the individual level, the BMIs might change, but at the population level, the distribution of the BMIs remains stationary. The third assumption was that each data-point tends to follow the same free energy landscape in a 'downslope' manner. This was based on the fact that systems have a tendency to minimize their energy and hence, even though the changes over time for two data-points may be different, they move in time in the same direction, i.e., downslope of a convex free energy landscape. It is important to note that, in a population of data-points that exhibits a stationary distribution, no state is a permanent condition for any data-point, that is, the data-points undergo continual change. However, a force constrains the state space that can be explored by the data-points and this force is proportional to the gradient of the free energy landscape.

The temporal dynamics of the data-points were modelled using stochastic differential equations based on Langevin dynamics and the above-stated assumptions. The heterogeneity of the data-points was modelled using a noise term which causes random movement of the data-points within the landscape. With the help of expert knowledge, this noise term can be defined by considering the dependencies on other variables and factors. It should be noted that since at the individual level the data-points exhibit random movement, the assumption that the data-points have a statistical tendency to move towards the stable attractor states is only valid at the population level and cannot be applied to the individual level.

This method would be applicable to systems where the data-points follow a free energy landscape which does not change with time and is not influenced by external force. This stable landscape, however, does not enforce that the data-points do not change their position with time. At the individual level, there may be continual change in the position of the data-points, but at the population level the distribution of these data-points remains stable. That is, the movement of the data-points is constrained by the force field of the landscape.

This method would not be applicable to systems which change frequently or are

undergoing intervention. This is because, the landscapes representing these systems will tend to change within short time spans. For example, a particular sub-population whose current norm is over-weight will follow a landscape where the attractor represents overweight BMI. However, if that sub-population is undergoing an intervention where regular exercise and diet control are made compulsory, then the free energy landscape of that population will change within short time spans with the attractor moving towards healthy BMI. In such a situation, this method will not be applicable. However, the proposed method can be applied to this system when the intervention has resulted in a stable distribution of BMI for the sub-population after a considerable time has passed from the start of the intervention, so that changes in BMI in the individual level does not result in changes in the distribution of BMI in the population level.

The estimates of the temporal dynamics obtained by the proposed method were compared against two population-based datasets from the public health domain. As these datasets contain data reflective of the health-related behaviour of a group of individuals, these data are at least in part representative of the outcomes of human interaction and social norms that determine behaviour. It was assumed that the use of Langevin dynamics can provide an indication of the underlying mechanisms in scenarios where individuals in groups tend to follow norms and adhere to social conventions [140, 141]. This is because these 'forces' are hypothesised to lead individuals to move towards the same norm behaviour, making it possible to identify the 'force field' that the individuals are following. There are many cross-sectional studies of human behaviours influenced by social norms, such as physical activity, dietary habits, smoking, and alcohol consumption [142–145]. However, cross-sectional data cannot readily be used to develop predictive computational models to study how these behaviours evolve over time. Predictive computational models may however be valuable in this context since they enable the assessment of competing hypotheses by allowing the evaluation of hypothetical scenarios in silico and simulation of the effect of interventions. This is especially advantageous for systems for which comparing counterfactual scenarios would not be possible in vivo, as is the case for systems involving human interaction and social norms. It would, for instance, never be possible to conduct an empirical study to assess the effect of group-level social norms versus individual-level health-related behaviour on body weight [146].

The goal of this study was to formulate a method to infer a computational model that predicts the temporal evolution of the data-points. The proposed method should be viewed as the starting point for inferring temporal dynamics from cross-sectional data. This method only presents a means to obtain an approximate idea of the underlying dynamics from the cross-sectional data without considering any other factors and dependencies. This method is not a causal inference technique in itself, which is a term reserved for automated techniques that identify causes of an effect by establishing that a cause-and-effect relationship exists purely based on data [147]. The proposed method selects a stochastic differential equation model which best fits the landscape dynamics derived from the data. Even though a differential equation can always be interpreted as a causal model, since it specifies how one variable changes as function of other variable values, the inferred predictive model does not by itself encode valid causal relationships, i.e., the model is not causally interpretable. In other words, it can be used to predict the system behaviour, but not how this behaviour will change in response to interventions. To illustrate this point, consider a dataset of BMIs of a group of individuals. It may be reasonable to predict that on average this group of individuals will have a statistical tendency to move towards the norm BMI. However, it is an entirely different question what would happen to this group-level BMI after an intervention, for instance, a sudden and large change in diet or physical activity level. The inferred model does not address the question of 'how' mechanistically the group-level BMI increases or decreases, only 'that' it will statistically tend to increase or decrease.

The model can be made causally interpretable by adding expert knowledge to the presented 'baseline' method in the form of (constraints on the) causal relationships between the different variables in the system. This should in turn increase the out-of-sample predictive power (generalizability). For example, in a previous work [146] discussed in Chapter 2, an expert-informed causal model was constructed between individual body weight perception, individual weight-related behaviour, and group-level norms towards body weight. Expert knowledge was incorporated to gather statements of causal and non-causal relationships to infer a computational model which can be causally interpreted. These statements of causal relations (e.g., 'physical exercise directly affects weight loss') essentially constitute constraints on the functional forms of the differential equations that are permitted (the differential equation for 'weight loss' must at least include a variable 'physical exercise'). The remaining uncertainties (parameter values, functional forms) were then estimated

from a cross-sectional dataset by using assumptions. The proposed method can be considered as a starting point of this model-building process for systems that can be described as effectively following a stable free energy landscape: in its naive form it produces a predictive model, and the more expert-informed constraints on functional forms are added based on causal or non-causal statements, the better the causal interpretation of the resulting model.

3.2 Methods

3.2.1 Langevin dynamics

Each data-point, denoted as x, was considered as vector-valued and capable of changing over time. A data-point represents a set of attributes (such as BMI) of an individual. It was assumed that all data-points in a cross-sectional dataset of size N have had sufficient time to mix and explore the state space by the time at which they were observed. Thus, it was assumed that even if there was a major perturbation, a system of data-points has converged to a stable distribution at the time of observation. This implies that all the data-points follow a probability distribution, $p(x)$, which is stationary. Further, this implies that N is large enough to effectively estimate $p(x)$ from the dataset.

It was also assumed that the probability distribution depends only on the variable of interest (such as BMI) and not on any other variables and factors. As it was explained previously in the Introduction, this method only presents a means to obtain an approximate idea of the underlying dynamics from the cross-sectional data without considering any other factors and dependencies and is not a causal inference technique. The 'baseline' model obtained with this method can be improved by incorporating expert knowledge in the form of the correlation between the variable of interest and other variables and factors.

In general, it is not possible to derive the temporal evolution, dx/dt, from the stationary probability distribution $p(x)$. This is because there are multiple dx/dt which can lead to the same stationary distribution. For example, a data-point rotating clock-wise and another data-point rotating anti-clockwise both have the same circular stationary distribution, but their dx/dt are different. This problem

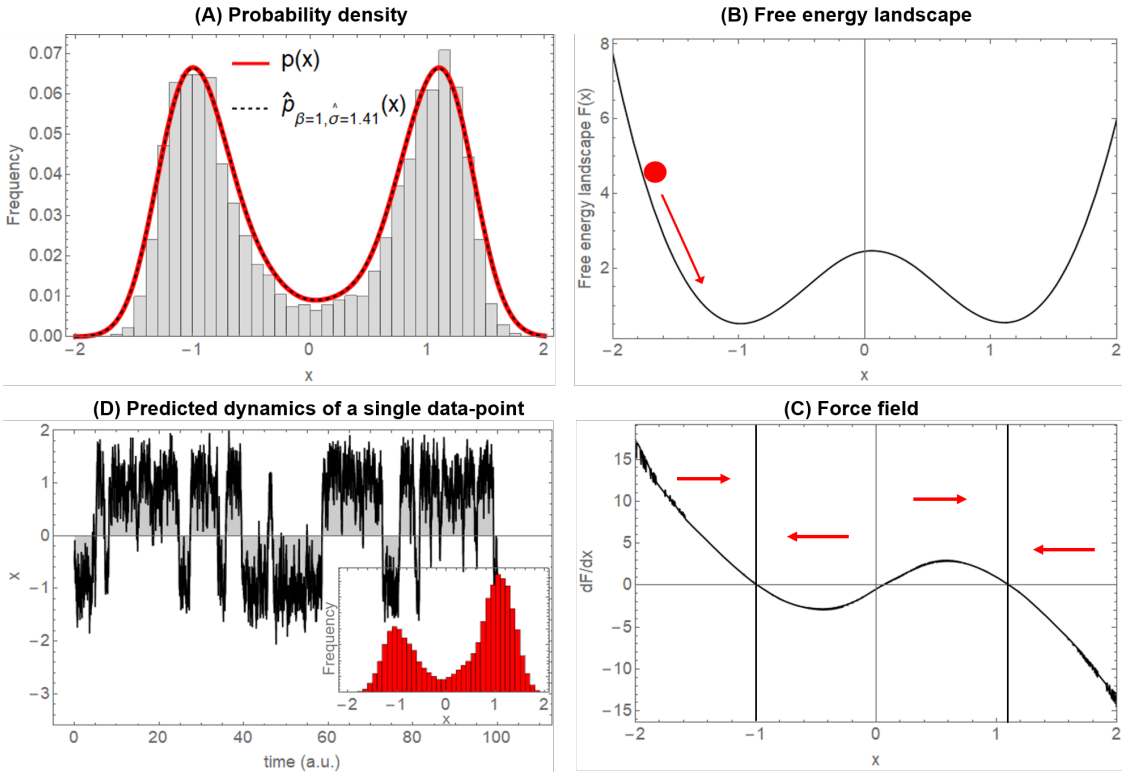

FIGURE 3.1: The proposed procedure to infer a computational model from a cross-sectional dataset. (A) The energy landscape $F(x) = -ax^2 + bx^4$ is used to generate a surrogate dataset, using the true probability density (solid red line). The dashed black line is the estimated probability density. (B) From the estimated probability density and the Boltzmann distribution, the free energy landscape $F(x)$ is estimated. The red ball represents a data-point moving downslope towards the attractor as shown by the red arrow. (C) The force field which is the derivative of the free energy landscape leads to the deterministic dynamics of the Langevin equation. The red arrows show the direction in which a data-point in any of the four partitions will be forced to move by the force field. The regions around 1 and -1 correspond to the two attractors. (D) The resulting predicted dynamics of a single data-point and the occasional transition from one attractor to the other, across the tipping point at $x = 0$. The inset figure is the histogram of the values of this data-point across time. The histogram almost captures the shape of the histogram of the cross-sectional data shown in (A) and is slightly different because a short time range is considered to improve visibility of the predicted dynamics.

was solved by assuming that each data-point tends to follow the same free energy landscape, $F(x)$, in a 'downslope' manner, i.e., moves in time in the direction of $-dF/dx$. $F(x)$ effectively assigns an energy value to each possible vector x. This assumption is based on the fact that systems have a tendency to minimize their energy, although random fluctuations may sometimes have the opposite effect. The minimum energy states correspond to the attractors in $F(x)$. This assumption

could be valid for social systems where individuals tend to follow norms, adhere to social conventions, and identify themselves with groups [140, 141]. These influences could lead individuals to move towards the same attractors. Thus, in these applications, the probability distribution of data-points could be used to make predictions, whereas in other applications this may not be the case.

The energy landscape, $F(x)$, can be derived from $p(x)$ through the Boltzmann distribution [148],

$$\beta F(x) = -\log p(x). \tag{3.1}$$

Here, the constant β is interpreted as the inverse of temperature, or noise level: the lower the value of β, the larger is the effect of random fluctuations on x, and thus the lower the influence of F on the data-points. The assumption behind this relation is that the data-points are in equilibrium, which is already met by the assumption of $p(x)$ having reached stationarity.

In addition to this deterministic tendency given by F, there is a random movement (noise) which is irrespective of F and is uncorrelated over time, defined by a Wiener process $W(t)$ [149]. Thus, the displacement of each data-point consists of the sum of a deterministic component and a stochastic component which leads to the following overdamped Langevin dynamics equation [139]:

$$dx = -\beta \frac{dF}{dx} dt + \sigma dW(t). \tag{3.2}$$

Here, β controls the relative strength of the deterministic force and σ controls the relative strength of the noisy movement. When $\beta \to 0$, the deterministic component becomes negligible, and thus the data-points diffuse randomly over the state space in all directions. When $\sigma \to 0$, the stochastic component becomes negligible , and all data-points converge to one or more local minima of $F(x)$, after which no further change occurs. Clearly, a balance is needed between these two opposing processes, which will control the degree of clustering and the amount of variance observed in the predicted distribution, $\hat{p}_{\beta,\sigma}(x)$, and match with the $p(x)$ from the data.

For determining the values of β and σ, it is important to realize that only their ratio changes the stationary data distribution. Thus, if the timescale of the deterministic component is fixed by setting $\beta = 1$ without loss of generality, then the remaining

free parameter σ controls the ratio of the random and deterministic forces. This timescale can be fixed because if both parameters in Eq. 3.2 are multiplied with a constant τ, the velocity dx/dt is also multiplied by τ. This means that x changes τ times faster. In principle, it is impossible to derive how fast x changes per unit time from the data available at a single time-point. However, it is still possible to predict the directions of the data-points, which is the main interest of this method.

3.2.2 Numerical algorithm

To explain how the algorithm recovers the dynamics, a set of data-points moving over a known free energy landscape was generated. Consider a true underlying free energy landscape, $F(x) = -ax^2 + bx^4$, from Landau's second order phase transition formalism, which contains two attractor states as long as $a > 0, b > 0$. The parameters a and b were set to 3 and 1 respectively, where a controls the height of the energy barrier separating the two attractors. Assuming the Boltzmann distribution (Eq. 3.1), a dataset consisting of 5000 i.i.d. data-points was generated from the probability density function, $p(x) = e^{ax^2 - bx^4}/Z$, where Z is the normalizing constant. $p(x)$ is shown in Fig. 3.1A as a solid red line. The sampling was done through the inverse transform sampling method [150].

Now, this dataset was considered as given and the $F(x)$ used to generate it was 'forgotten'. The true $p(x)$ always has an exponential form due to the assumption of a Boltzmann distribution. Therefore, a Gaussian kernel density estimation algorithm was used to estimate the data distribution. A Gaussian kernel density estimate is defined as $\hat{p}(x) = (nh\sqrt{2\pi})^{-1} \sum_i^n e^{-\frac{(x-x_i)^2}{2h^2}}$, where x_i are the data-points and the parameter h was determined using Silverman's optimization procedure [151]. Even though the parameters h and σ represent similar concepts (both are standard deviation controlling parameters), they implement different components. The parameter h controls the standard deviation of the Gaussian kernel density estimate obtained from the data, whereas, σ controls the the ratio of the random and deterministic forces in Eq. 3.2. The estimated $\hat{p}(x)$ from the dataset is shown in Fig. 3.1A as a dashed black line. This estimated $\hat{p}(x)$ was then used to estimate the free energy landscape as $\hat{F}(x) = -\log \hat{p}(x)$. By fixing the timescale of the deterministic dynamics through $\beta = 1$, the deterministic term, $d\hat{F}/dx$, of the

Langevin dynamics (Eq. 3.2) is given as,

$$\begin{aligned}\frac{d\hat{F}}{dx} &= \frac{d}{dx}(-\log \hat{p}(x)) \\ &= \frac{d}{dx}(-\log((nh\sqrt{2\pi})^{-1}\sum_{i}^{n} e^{-\frac{(x-x_i)^2}{2h^2}})) \\ &= -\sum_{i=1}^{n} \frac{\left(\frac{x_i e^{-\frac{(x-x_i)^2}{2h^2}}}{h^2} - \frac{x e^{-\frac{(x-x_i)^2}{2h^2}}}{h^2}\right)}{e^{-\frac{(x-x_i)^2}{2h^2}}}.\end{aligned} \tag{3.3}$$

The stochastic part was then fully determined by an optimal choice for σ. The optimal σ was determined by using the Hellinger distance, $H\left(\hat{p}_{\beta=1,\sigma}(x), p(x)\right)$, as the cost function. The Hellinger distance is defined as,
$H(p,q) = \frac{1}{2}\int_x \left(\sqrt{dp(x)} - \sqrt{dq(x)}\right)^2 dx$. To evaluate the goodness of fit for each choice of σ during this optimization process, the stationary probability density $\hat{p}_{\beta=1,\sigma}(x)$ has to be estimated numerically. Since integration techniques for stochastic differential equations are computationally intensive, the domain of the data, x, was divided into discrete points with distance Δx, which was calculated as $\Delta x = \sqrt{\Delta t}/f$. The time-step Δt was selected such that $\sigma\sqrt{1000\Delta t} = (x_{\max} - x_{\min})/2$. This means that it would take a random Wiener diffusion process with diffusion parameter σ about 1000 time-steps to reach the entire range of x values. The expected displacement of a random diffusion process after Δt time is $\sqrt{\Delta t}$, which was divided up into f discrete points. Thus, f controls the 'fineness' of this grid. It was found that $f = 10$ produced accurate results at low memory cost. $x_{\min}$ and $x_{\max}$ were calculated from the data by taking the floor of the minimum value and ceiling of the maximum value from the standardized data respectively. In this case, the generated dataset produced $x_{\max} = -x_{\min} = 3$. This resulted in 601 discrete values for x and a sparse, approximately band-diagonal transition matrix of dimension 601×601, denoted by W. To calculate the transition probabilities in W, the possible positions that a data-point, starting at position x, can reach after Δt time-steps were first determined. The displacement due to the deterministic force is given by $x + (-\frac{dF}{dx}\Delta t)$. Taking this value as the mean, the 601 discrete values of x were used to determine the values (y) that fall within 4 standard deviations of this mean, i.e., within $\pm 4\sigma\sqrt{\Delta t}$ of the mean. Then the probabilities of displacement to these y values due to random diffusion were calculated, by assuming a normal distribution with mean as $x + (-\frac{dF}{dx}\Delta t)$ and standard deviation as $\sigma\sqrt{\Delta t}$. Thus,

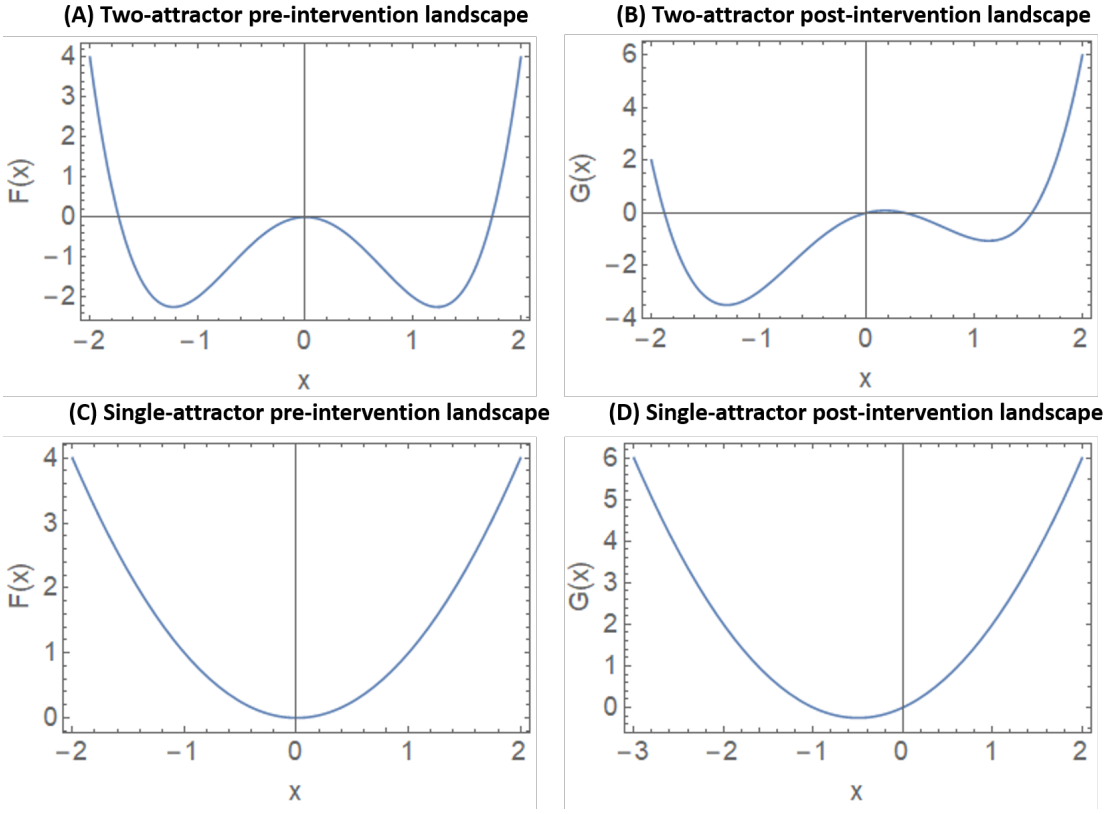

FIGURE 3.2: (A) Two-attractor pre-intervention landscape, (B) Two-attractor post-intervention landscape, (C) Single-attractor pre-intervention landscape, (D) Single-attractor post-intervention landscape.

$W_{x \xrightarrow{y}} = \mathcal{P}\left(y \mid \mathcal{N}\left(x - \frac{dF}{dx}\Delta t, \sigma\sqrt{\Delta t}\right)\right)$, where $\mathcal{P}(.)$ denotes probability density function.

For discrete Markov processes, the stationary distribution vector π can be found directly by solving the set of linear equations $\pi = W\pi$, which is computationally an efficient operation since it reduces to finding the (left) eigenvector of W, having an eigenvalue of 1. Before performing this operation, the rows of W were normalized. The initial distribution vector, π_0, was calculated from the data as, $\pi_0(x) = \int_{x-\Delta x/2}^{x+\Delta x/2} p(x)$. Finally, the Hellinger distance, $H\left(\hat{p}_{\beta=1,\sigma}(x), p(x)\right)$, was computed for which π was converted to a continuous function, $\hat{p}_{\beta=1,\sigma}(x)$, using third-order spline interpolation. If changing σ no longer reduces the Hellinger distance, the procedure terminates and the Langevin dynamics (Eq. 3.2) is completely specified. In Fig. 3.1D the resulting predicted dynamics of a data-point is shown, where the optimal $\hat{\sigma} \approx 1.41$.

This free energy landscape can be manipulated to favour a particular attractor or

shift the attractor. Here, it is demonstrated that the landscape can be changed by an intervention, and if it is changed then what possible comparisons can be performed using the pre-intervention and post-intervention landscapes. It is to be pointed out that *how* an intervention should be implemented is not known, which requires expert knowledge such as, which are the causal relationships which should be exploited in order to achieve such an intervention. This should be viewed as only a theoretical test where a term (analogous to an intervention) was added to the free energy function, and then potential comparison measures between the pre-intervention and post-intervention cases were presented.

Suppose, $F(x)$ denotes the pre-intervention free energy landscape and $G(x) = F(x) + cx$ represents the post-intervention free energy landscape. Here, cx represents the intervention and c controls the strength of the effect of the intervention. Let, $x_1(t)$ be a stochastic process with respect to the landscape $F(x)$ defined as

$$dx_1 = -\beta \frac{dF}{dx_1} dt + \sigma dW(t). \tag{3.4}$$

Let, $x_2(t)$ be another stochastic process with respect to the landscape $G(x)$ defined as

$$dx_2 = -\beta \frac{dG}{dx_2} dt + \sigma dW(t). \tag{3.5}$$

For a two-attractor landscape, suppose the pre-intervention free energy landscape is defined as $F(x) = -ax^2 + bx^4$. Adding a term cx makes the left attractor preferred. The pre-intervention and post-intervention landscapes are shown in Fig. 3.2A and B. The average rate of transition from the attractor at x_+ to the attractor at x_-, with x_0 as the local maximum (tipping point) can be approximated using Kramer's formula for energy barrier crossing as

$$r(+ \to -) = \frac{1}{2\pi} \sqrt{F''(x_+)\,|F''(x_0)|}\, e^{-2\frac{F(x_0)-F(x_+)}{\sigma^2}}. \tag{3.6}$$

Similarly, the average rate of transition in the opposite direction, $r(- \to +)$ can be obtained by

$$r(- \to +) = \frac{1}{2\pi} \sqrt{F''(x_-)\,|F''(x_0)|}\, e^{-2\frac{F(x_0)-F(x_-)}{\sigma^2}}. \tag{3.7}$$

Now, for the pre-intervention landscape, $F(x) = -ax^2 + bx^4$, the average transition rates in both direction will be equal since the landscape is symmetric. Using a=3, b=1, the average transition rates are obtained as $r(+ \rightarrow -) = r(- \rightarrow +) = 12.9867$. For the post-intervention landscape, $G(x)$, the average rate of transition from the right attractor at x_+ to the left attractor at x_- will be higher than that in the opposite direction. Using a=3, b=1, and c=1, the average transition rates are obtained as $r(+ \rightarrow -) = 0.448$ and $r(- \rightarrow +) = 0.031$.

For a single-attractor landscape, suppose the pre-intervention free energy landscape is defined as $F(x) = ax^2$. Adding a term cx shifts the attractor to the left. The pre-intervention and post-intervention landscapes are shown in Fig. 3.2C and D. In this case, the pre-intervention and post-intervention landscapes can be compared by using the first moments (means) of stochastic processes $x_1(t)$ and $x_2(t)$ respectively. Let μ_1 and μ_2 be the means of the stochastic processes $x_1(t)$ and $x_2(t)$ respectively and they are defined as

$$\mu_1 = e^{-2at} x_{10}, \tag{3.8}$$

$$\mu_2 = \frac{e^{-2at}(c + 2ax_{20}) - c}{2a}, \tag{3.9}$$

where x_{10} and x_{20} are the initial states of $x_1(t)$ and $x_2(t)$ respectively.

3.2.3 Comparison with longitudinal dataset

The estimates of the temporal dynamics obtained by the proposed method were compared against longitudinal datasets where the first time-point was used as the cross-sectional data and the subsequent time-points were used for comparison with the model predictions. For this purpose, the displacement of each individual which is influenced by a force towards the attractor and a random movement was estimated. This estimated displacement is not deterministic, but is random and hence represented as a normal distribution, whose mean is the gradient of the free energy landscape and standard deviation is the noise parameter. Mathematically, the displacement of an individual i for a Δt time-increment is represented by a normal distribution with the displacement due to the deterministic force, $\frac{-dF}{dx}\Delta t$ as the mean and $\sigma\sqrt{\Delta t}$ as the standard deviation. Using this normal distribution,

for each individual i the probability of positive displacement and the probability of negative displacement, denoted as P^i_{PD} and P^i_{ND}, respectively were determined as

$$P^i_{\mathrm{PD}} = P(x > 0, x \sim N(-\frac{dF}{dx}\Delta t, \sigma\sqrt{\Delta t})), \tag{3.10}$$

$$P^i_{\mathrm{ND}} = P(x < 0, x \sim N(-\frac{dF}{dx}\Delta t, \sigma\sqrt{\Delta t})). \tag{3.11}$$

The prediction accuracy of the model for individual i, denoted as A^i, was quantified as follows. If the observed displacement (D_{data}) for individual i from the data was positive, then P^i_{PD} was assigned as the prediction accuracy of the model, and if the observed displacement was negative, the P^i_{ND} was assigned as the prediction accuracy of the model for individual i. The average prediction accuracy of the model, denoted as A^{average}, was then determined as the average of the prediction accuracy over all individuals. Mathematically, A^i and A^{average} are defined as

$$A^i = \begin{cases} P^i_{\mathrm{PD}}, & \text{if } D_{data} \in \mathbb{R}_{>0}. \\ P^i_{\mathrm{ND}}, & \text{if } D_{data} \in \mathbb{R}_{<0}. \end{cases} \tag{3.12}$$

$$A^{\mathrm{average}} = \langle A^i \rangle_i. \tag{3.13}$$

In addition, the maximum prediction accuracy of the model for individual i, A^i_{max}, and the average maximum prediction accuracy of the model over all individuals, $A^{\mathrm{average}}_{\mathrm{max}}$, were determined as

$$A^i_{\mathrm{max}} = max(P^i_{\mathrm{PD}}, P^i_{\mathrm{ND}}), \tag{3.14}$$

$$A^{\mathrm{average}}_{\mathrm{max}} = \langle A^i_{\mathrm{max}} \rangle_i. \tag{3.15}$$

To determine the optimal value of Δt, the metric of Euclidean distance was used, by varying its value from 1 to 100 with increments of 1, and selecting the value that gives the minimum Euclidean distance between the displacement due to the deterministic force ($-\frac{dF}{dx}\Delta t$) predicted by the model and the observed displacement from data.

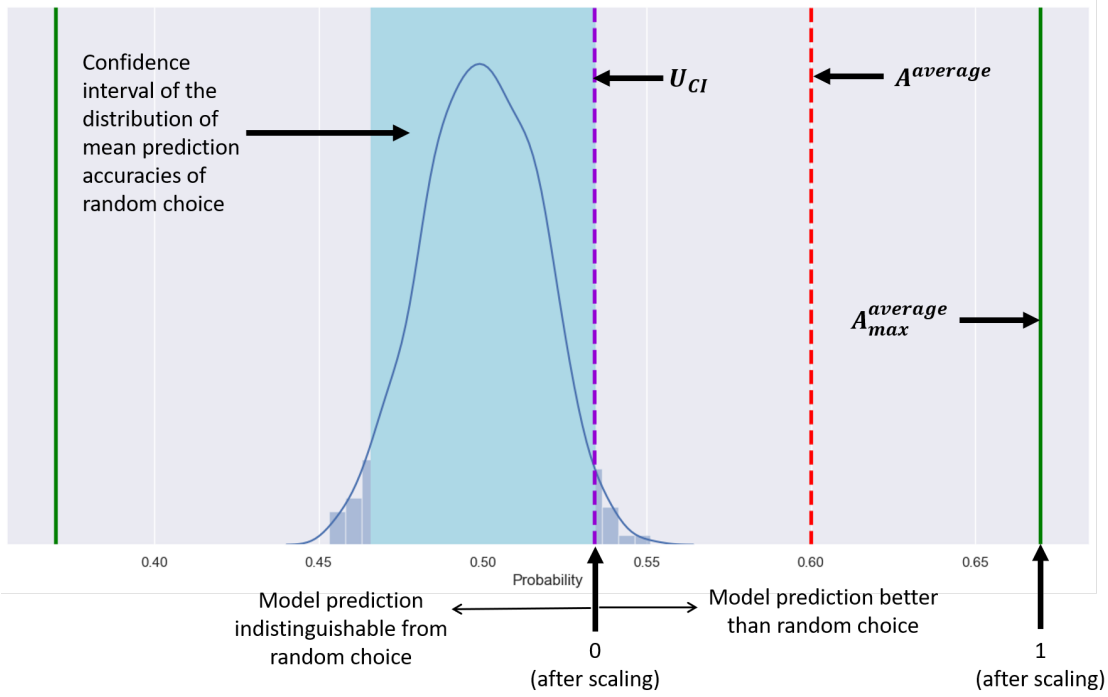

FIGURE 3.3: Comparison of the prediction accuracy of the model to random choice under the null hypothesis of random displacement. The blue shaded area is the confidence interval of the distribution of 1000 mean prediction accuracies of random choice. The violet dashed line denotes the upper limit (U_{CI}) of this confidence interval (Eq. 3.16). The red dashed line denotes average prediction accuracy (A^{average}) (Eq. 3.13) and the green solid line denotes the average maximum prediction accuracy ($A^{\mathrm{average}}_{\mathrm{max}}$) (Eq. 3.15) (refer to section 3.2.3).

In addition to the above tests, the prediction accuracy of the model was also compared to random choice under the null hypothesis of random displacement. A random selection between P^i_{PD} and P^i_{ND} for each individual i was performed and then the average over all individuals was calculated to obtain the prediction accuracy by random choice. This random choice step was repeated for 1000 times to obtain a distribution of mean prediction accuracies of random choice whose 95% confidence interval was then calculated. The upper limit of this confidence interval is defined as

$$U_{\mathrm{CI}} = \overline{X} + 1.96\frac{s}{\sqrt{1000}}, \tag{3.16}$$

where, $\overline{X}$ is the mean of the distribution of 1000 mean prediction accuracies of random choice and s is the standard deviation of this distribution. If the average prediction accuracy of the model was greater than the upper limit (U_{CI}) of this confidence interval, then the model prediction was concluded as significantly

better than the prediction obtained by random choice. The average prediction accuracy (A^{average}) was scaled to better compare with U_{CI} and the average maximum prediction accuracy ($A^{\text{average}}_{\text{max}}$) as

$$A^{average}_{scaled} = \frac{A^{average} - U_{CI}}{A^{average}_{maximum} - U_{CI}}. \tag{3.17}$$

After the above scaling, U_{CI} will correspond to zero and $A^{\text{average}}_{\text{maximum}}$ will correspond to 1. If $A^{\text{average}}_{\text{scaled}}$ is above zero, it can be said that the model prediction is better than random choice; if it is below zero, then the model prediction is indistinguishable from random choice. This comparison process with random choice is explained in Fig. 3.3. Thus, the predictions of the proposed model were compared against data as well as a random choice method.

3.2.4 Data

The predictions of the proposed method were compared against two population-based longitudinal datasets: the College study dataset [152] and the Hoorn study dataset [153–155], where the first time-point was considered as the cross-sectional data and the subsequent time-points were compared to the model predictions.

The College study dataset [152] is a longitudinal dataset with weights and heights measured over 5 time-points: baseline, 6 weeks, 6 months, 12 months, and 24 months. This study was conducted with 294 female first-year students [age: 18.24± 0.44 years; all values are expressed as mean ± SD unless otherwise specified] recruited from two universities in Philadelphia. This dataset was preprocessed to include only those participants who had their weights and heights measured for all the 5 time-points and obtained 162 participants. The BMI (in kg/m^2) of these 162 participants were calculated from their weights and heights and their baseline BMI distribution was 23.59 ± 2.69 kg/m^2.

The Hoorn study dataset [153–155] is a longitudinal dataset with BMIs measured over 2 time-points: baseline, and 7 years. The baseline study [153, 155] was conducted in 2006-2007 in the Dutch city of Hoorn and included 2,807 participants. The follow-up study [154, 155] was conducted in 2013-2015 which included 1,734 participants out of the 2,807 participants in the baseline study. This dataset was

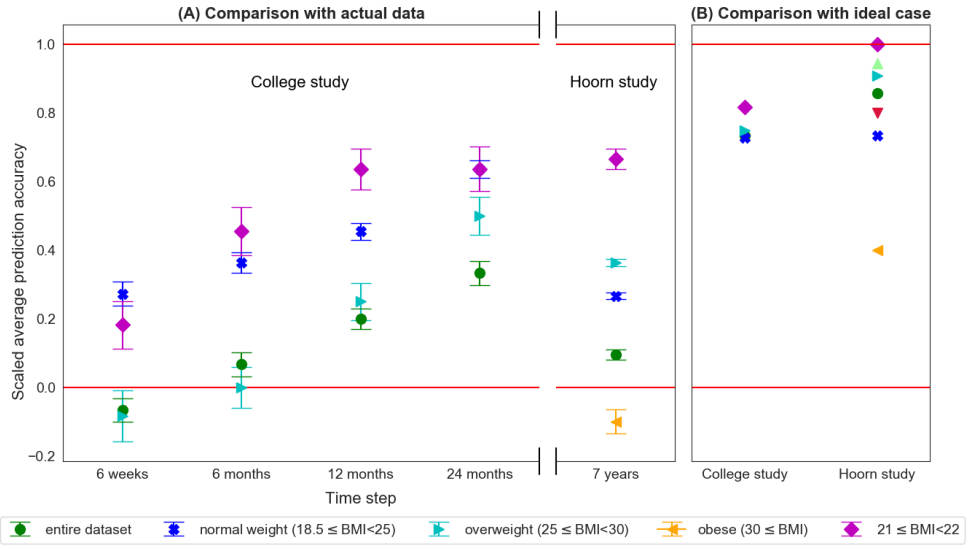

FIGURE 3.4: (A) The scaled average prediction accuracies, $A^{\text{average}}_{\text{scaled}}$ (Eq. 3.17) corresponding to the 4 time-points: 6 weeks, 6 months, 12 months, and 24 months of the College study dataset, and the single time-point of 7 years of the Hoorn study dataset. The vertical bars at each point represent the error bar for the respective model prediction accuracy calculated from 1000 bootstrap samples. The solid red line at 0 corresponds to the upper limit of the 95% confidence interval of the distribution of mean prediction accuracies of random choice, U_{CI} (Eq. 3.16), and the solid red line at 1 corresponds to the average maximum model prediction accuracy, $A^{\text{average}}_{\text{max}}$ (Eq. 3.15). Model prediction accuracies above the line at 0 are significantly better than the prediction accuracy of random choice. (B) The 'maximally achievable' scaled average prediction accuracy of the model obtained by comparing against the theoretical test that the statistical tendency to move towards the attractor which is displayed at the population level was also displayed at the individual level, that is, if all individuals have a tendency to move towards the attractor (refer to section 3.3).

preprocessed to include only those participants who had their BMI measured for both the time-points and obtained 1,727 participants with age 53.62 ± 6.53 years and baseline BMI 26.11 ± 3.88 kg/m^2.

3.3 Results

In this work, a baseline method for inferring predictive computational models from cross-sectional data based on Langevin dynamics was presented. The model predictions were compared against two longitudinal datasets: the College study dataset [152] and the Hoorn study dataset [153–155], where the first time-point was considered as the cross-sectional data and the subsequent time-points were

compared to the model predictions. The College study dataset contains BMI values over 5 time-points: baseline, 6 weeks, 6 months, 12 months, and 24 months. The Hoorn study dataset contains BMI values over 2 time-points: baseline, and 7 years. Fig. 3.4 shows the model prediction accuracies ($A_{\text{scaled}}^{\text{average}}$ (Eq. 3.17)) using these two datasets. The model showed significant predictive power (green circles in Fig. 3.4(A)) compared to the prediction of a random choice algorithm (solid red line 0 in Fig. 3.4). Additionally, the model prediction accuracy improved further when expert knowledge was incorporated to the model, as shown by the blue crosses, cyan left triangles, and magenta diamonds in Fig. 3.4(A).

To test if the predictive power of the model is enhanced with the incorporation of domain expert knowledge, the empirical observation from epidemiology that individuals from different BMI categories follow different landscapes [156, 157] was applied. In accordance, the datasets were clustered based on the standard BMI categories: underweight (BMI $<$ 18.5), normal weight (18.5 $\leq$ BMI $<$ 25), overweight (25 $\leq$ BMI $<$ 30), and obese (30 $\leq$ BMI) [158]. Clusters of sizes 0, 119, 39, and 4 respectively were obtained from the College study dataset, and 12, 739, 729, and 247 respectively were obtained from the Hoorn study dataset. Since the underweight and obese clusters from the College study dataset had only 0 and 4 individuals, respectively, and the underweight cluster from the Hoorn study dataset had only 12 individuals, those clusters were disregarded. It was observed that on considering separate attractor landscapes for these different clusters, the model prediction accuracy increased significantly (Fig. 3.4A). The attractor in each cluster approximately corresponded to the BMI that was most prevalent relative to the group of individuals in that cluster. From the above results (Fig. 3.4A), it can be concluded that the incorporation of domain expert knowledge to the baseline method further enhances the predictive power of the model. Next, a theoretical test was performed by further narrowing the BMI range to see if clustering individuals having almost exact BMIs further improves the prediction accuracy. Accordingly, all individuals having BMI in the narrow range of 21 $\leq$ BMI $<$ 22 were selected, and 29 individuals from the College study dataset, and 96 individuals from the Hoorn study dataset were obtained. It was observed that the model prediction accuracy increased further (Fig. 3.4A).

Next, a theoretical test was performed to see the how the proposed method performs if the statistical tendency to move towards the attractor that is displayed

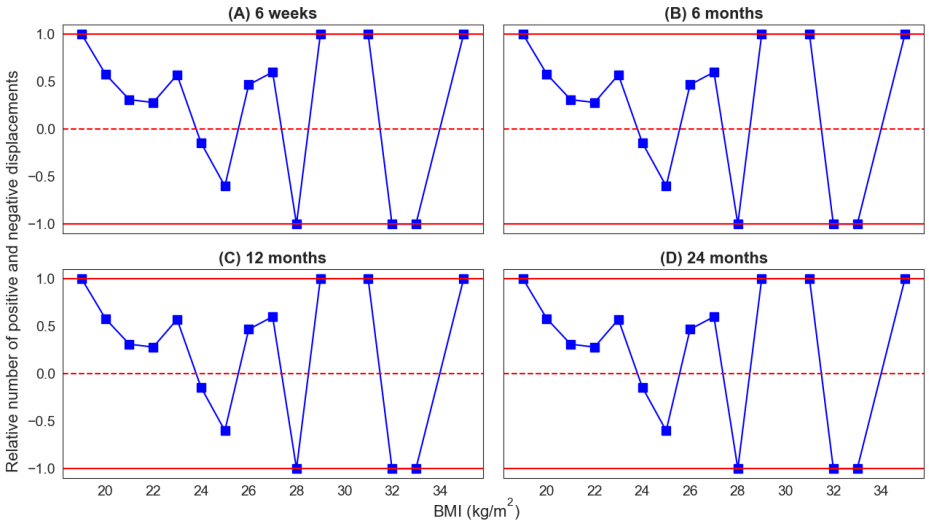

FIGURE 3.5: The relative number of positive and negative displacements in each BMI bin at (A) 6 weeks, (B) 6 months, (C) 12 months, and (D) 24 months obtained from the College study dataset. The relative number of positive and negative displacements in each BMI bin is calculated as $\frac{\text{number of positive displacements - number of negative displacements}}{\text{number of positive displacements + number of negative displacements}}$. This relative number will be 1 or -1 if all displacements at a particular BMI bin are in the same direction (either positive or negative). If a particular BMI bin has mixed displacement directions then the relative number will be between -1 and 1. A positive relative number indicates that there are more positive displacements than negative displacements and vice-versa (refer to section 3.3).

at the population level was also displayed at the individual level, that is, if all individuals have a tendency to move towards the attractor. In that case, individuals with a BMI that is greater than the attractor BMI should decrease their BMI and vice-versa. Assuming this ideal behaviour, the 'maximally achievable' prediction accuracy of the model was determined. As observed from Fig. 3.4B, these 'maximally achievable' model prediction accuracies are significantly higher than the actual prediction accuracies using the real data.

Another theoretical test was performed by analysing the data to see if individuals having the same BMI have displacements in the same direction. Accordingly, 15 BMI bins were selected based on the data (the bins are shown as x axis labels in Fig. 3.5). An individual was placed in BMI bin x if the individual's BMI was in the range of $\mathrm{x} \leq \text{BMI} < \mathrm{x} + 1$. For example, an individual was placed in BMI bin 25 if the individual's BMI was in the range of $25 \leq \text{BMI} < 26$. Then, the displacements from baseline to 6 weeks, 6 months, 12 months, and 24

months were calculated. Fig. 3.5 shows the relative number of individuals having positive and negative displacements in each BMI bin, which was calculated as $\frac{\text{number of positive displacements - number of negative displacements}}{\text{number of positive displacements + number of negative displacements}}$. If all individuals in a particular BMI bin have displacements in the same direction, then this relative number will be 1 or -1 as shown by the red solid lines in Fig. 3.5. If individuals in a particular BMI bin have mixed displacement directions then this relative number will be between 1 and -1. The purpose of Fig. 3.5 was to show that individual behaviour is inherently random and that individuals having almost same BMI may not have displacements in the same direction. That is, two individuals having BMI of 28 may not both decrease their BMI: one may increase, and one may decrease. If all individuals in a particular BMI bin had displacements in the same direction, then the relative number of individuals having positive and negative displacements in each BMI bin would be exactly 1 or -1. However, this is not the case that is observed from Fig. 3.5. It should be noted that this analysis was based on the assumption that the distribution does not depend on other variables, which in reality is probably not true. And it is because of these other variables that the relative number of individuals having positive and negative displacements in each BMI bin was not exactly 1 or -1. However, the purpose of this analysis was to show that, even without considering the other variables and factors, the proposed method was already able to provide a good starting estimate of the underlying dynamics from the cross-sectional data. This estimate can be further enhanced by adding domain expert knowledge in the form of (constraints on the) causal relationships between the different variables in the system.

Next, the performance of the proposed method was analyzed on a small cross-sectional dataset. The free energy landscape, $F(x) = -ax^2 + bx^4$, from Landau's second order phase transition formalism was used to generate data-points as shown in section 3.2.2. A large dataset consisting of 5000 data-points and 1000 small datasets consisting of 40 data-points were generated. Fig. 3.6 shows the estimated probability densities from the large dataset (in red) and the 1000 small datasets (in blue). In addition, the probability densities estimated from each of the 1000 small datasets were compared against the probability density estimated from the large dataset using the two-sample Kolmogorov–Smirnov test. With a significance level of 0.01, only 7 out of the 1000 small datasets (0.7%) rejected the null hypothesis that the large dataset and the small dataset were drawn from the same distribution.

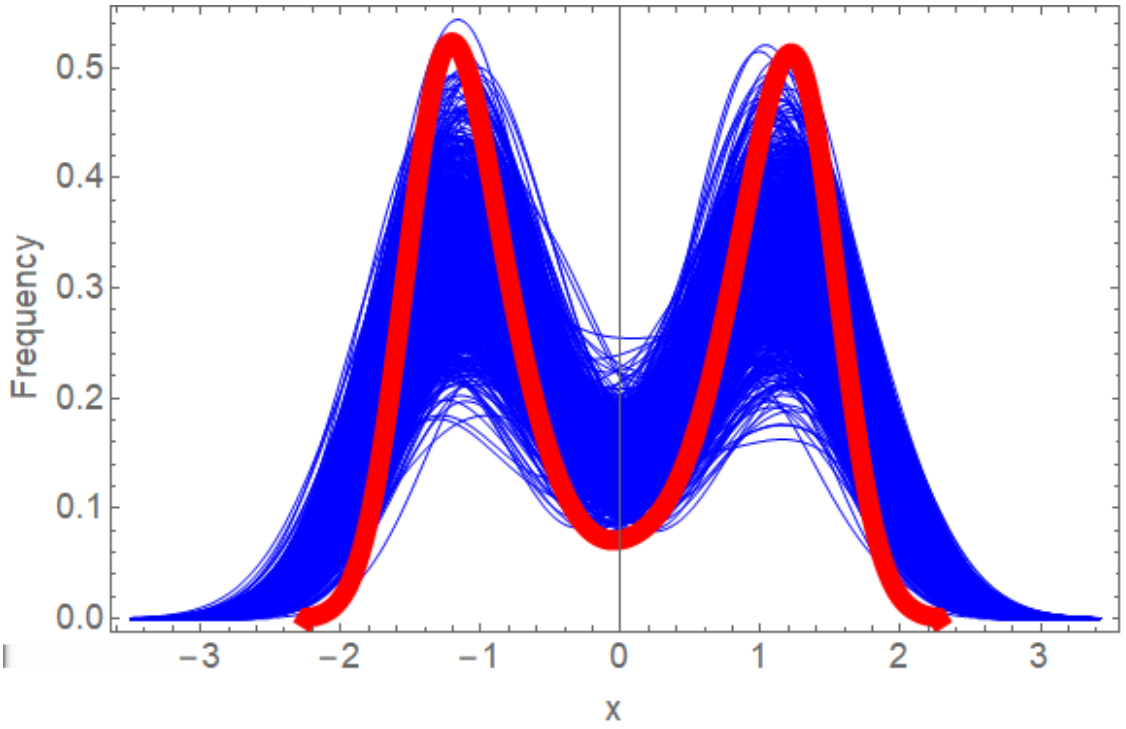

FIGURE 3.6: The estimated probability densities from the large dataset (in red) consisting of 5000 data-points and the 1000 small datasets (in blue) each consisting of 40 data-points. The datasets were generated from the probability density function, $p(x) = e^{ax^2 - bx^4}/Z$, where Z is the normalizing constant based on the free energy landscape, $F(x) = -ax^2 + bx^4$, from Landau's second order phase transition formalism (details given in section 3.2.2).

From these results, it can be concluded that even with a small dataset, the proposed method is able to generate a close estimate of the true probability density.

3.4 Discussion

Cross-sectional studies are widely prevalent since they require less investment in terms of time, money and effort compared to longitudinal studies. However, since these data lack temporal information, they cannot be used directly to study the evolution of the underlying processes. Nevertheless, this temporal information is essential to develop predictive computational models which is the first step towards causal modelling. In this work, a method to infer predictive computational models from cross-sectional data using Langevin dynamics was presented. This method can be applied to any system that can be described as effectively following a stable free energy landscape which is not influenced by any external force. The proposed

method should be viewed as the starting point for inferring temporal dynamics from cross-sectional data. This method only presents a means to obtain an approximate idea of the underlying dynamics from the cross-sectional data without considering any other factors and dependencies. This method is not a causal inference technique in itself. The inferred model can be made causally interpretable by adding expert knowledge to the presented 'baseline' method in the form of (constraints on the) causal relationships between the different variables in the system.

The proposed method is based on three assumptions. The first assumption is that of well-mixedness or ergodicity, i.e., the data-points are sufficiently mixed at the time of observation and are at (local) equilibrium. Thus, it is assumed that even if there was a major perturbation, a system of data-points has converged to a stable distribution at the time of observation. This means that the mean value of all data-points at a particular time-point and the mean value of any one data-point across time remain the same. This assumption would be valid for short-term where any major perturbation to the system is not expected. The second assumption is that the distribution depends only on the variable of interest and not on other variables and factors. The third assumption is that each data-point tends to follow the same free energy landscape in a 'downslope' manner, i.e., two data-points will not follow each other even if they have the same stationary distribution. For instance, one data-point rotating clock-wise and another data-point rotating anti-clockwise will have the same circular stationary distribution, but the changes over time, dx/dt, are different. The third assumption is based on the fact that systems have a tendency to minimize their energy and hence, even though the changes over time for the two data-points may be different, they move in time in the same direction, i.e., downslope of a convex free energy landscape.

As opposed to black-box machine learning techniques, the presented technique is based on interpretable assumptions such that domain expert knowledge can be readily incorporated. That is, the resulting model can be made causally interpretable by adding domain expert knowledge in the form of statements of causal and non-causal relationships. This should lead to increased and more robust predictive power, as is indeed demonstrated by the clustering of different categories of BMI.

It is important to realize that the proposed method can only estimate directions of progression, not velocities. This is because, in principle, it is impossible to derive

how fast a data-point changes per unit of time from a single time-point data. In other words, the timescale of the predicted dynamics remains unknown. It can only be estimated, for example, whether an individual will increase or decrease his/her BMI, and whether another individual progresses slower or faster. In some cases it is possible to estimate a timescale from the data, for instance by quantifying the relative frequency of tipping point transitions in the model and comparing it to knowledge or data about it. It can also be inferred from known statistical properties of the rates of change in reality; for instance, the fact that the maximum sustainable rate of weight loss observed in a population is about 2 kg per month used in the previous work [146].

The usefulness of the proposed method lies in the fact that it provides an approximate estimate of the underlying dynamics from the cross-sectional data. This will be useful when there is no knowledge of how other factors or variables are related to the variable of interest. This method can be a useful tool to get an approximate idea of the underlying dynamics of the system when data is available only for a single time-point. Later, this 'baseline' model can be developed into causal model and the timescale of the model predictions can be estimated with the help of expert knowledge. The proposed method is sufficiently simple to use as well as interpretable to initiate the iterative development of computational models for any system that can be described as effectively following a free energy landscape and thus help in studying the progression of important processes.

Chapter 4

Boolean Network Modelling of beta-cell Apoptosis and Insulin Resistance in Type 2 Diabetes

4.1 Introduction

Type 2 diabetes (T2D) is characterized by insulin resistance at its onset. Persistence of insulin resistance leads to pancreatic beta-cell dysfunction and in extreme cases to beta-cell apoptosis [159–161]. Insulin resistance increases the load on beta-cells to produce more insulin in order to maintain blood glucose at normal levels. This homeostasis is maintained as long as beta-cells can meet the increased insulin demand. However, persistence of excess nutrients could lead to hyperglycemia, elevated free fatty acids (FFA), and inflammation, which severely impairs beta-cell function, leading to insulin resistance and beta-cell apoptosis.

The endoplasmic reticulum (ER) in the beta-cell is responsible for the production and secretion of insulin. The increased demand for insulin synthesis in the presence of hyperglycemia triggers the accumulation of misfolded proteins in the ER, causing ER stress and the consequent activation of the unfolded protein response (UPR). UPR initially attempts to mitigate ER stress by degrading misfolded proteins and preventing their further accumulation. However, when ER stress is not mitigated, UPR activates the apoptosis signal [14–16]. 78 kDa glucose regulated protein

(GRP78) serves as a sensor of protein misfolding [162]. Under non-stressed conditions, GRP78 binds to three UPR initiator proteins, inositol requiring 1 (IRE1), PKR-like ER kinase (PERK), and activating transcription factor 6 (ATF6) and maintains them in the inactive state [163]. Under stressed conditions, GRP78 dissociates from these three proteins, causing their activation and initiation of UPR.

When ER stress can be resolved, the UPR assists beta-cell survival. However, when ER stress cannot be resolved the UPR activates the pro-apoptotic signals [164]. Hyperglycemia causes oxidative stress through the generation of reactive oxygen species (ROS) [165]. In the absence of an appropriate antioxidant response, the system experiences redox imbalance, leading to the activation of oxidative stress-sensitive signaling pathways. Hyperglycemia also activates cytokines, such as FasL, TNFα, and IL-6, which are important inducers of beta-cell apoptosis [24–28] as well as insulin resistance [29, 30]. Caspases serve as the final mediators of apoptosis. The upstream apoptosis initiator caspases 8, and 9 are activated on receiving death signal from death-inducing signaling complex (DISC) and apoptosome respectively, which in turn activate the downstream apoptosis effector caspases 3, 6, and 7, which ultimately execute apoptosis [166].

Computational modelling is necessary to consolidate information from various sources, such as listed above, in order to obtain a comprehensive understanding of the pathogenesis of T2D and investigate possible interventions by performing *in silico* simulations. A few dynamic models of insulin resistance in T2D have been proposed recently. For instance, Brannmark et al. [167] proposed an ordinary differential equation (ODE) model of insulin signaling in T2D. Rajan et al. proposed an ODE model to study the contribution of Forkhead box protein O1 (FOXO1) to insulin resistance in T2D [168]. Another paper [169] presented an ODE model to simulate the development of insulin resistance by hyperglycemia, FFA, ROS, and inhibition of glucose transporter type 1 (GLUT1) and glucose transporter type 4 (GLUT4). However, there exists no model of beta-cell apoptosis occurring in the T2D condition. Also, there is no existing work that attempts to integrate the insulin resistance and beta-cell apoptosis pathways in order to obtain a comprehensive understanding of the molecular mechanisms underlying T2D. To discover potential therapeutic interventions for T2D, it is essential to have a more comprehensive model for the mechanisms causing T2D pathogenesis.

In this work, a Boolean network model integrating the insulin resistance pathway and beta-cell apoptosis pathway was proposed for the purpose of obtaining deeper insights into the mechanisms of development and progression of T2D. The aforementioned existing models are ODE models, whereas in this work a Boolean network model was constructed. The reason behind this selection was that, ODE models require detailed kinetic knowledge and time-series data for accurate parameter estimation. However, the size of the proposed network is relatively big (consisting of 72 nodes) and hence obtaining time-series expression data for all the genes would be expensive as well as time-consuming. Further, in a Boolean network model, gene expression is represented by either TRUE (1) or FALSE (0). By simplifying the gene regulatory network into binary states, Boolean networks are feasible for simulating the behaviour of large regulatory networks in a qualitative way.

In a Boolean network model the state of each gene is represented by either 1 (TRUE), indicating the gene is highly expressed, or 0 (FALSE) when the gene is lowly expressed. An edge in a Boolean network can be either activating or inhibiting [170]. In this work, the random asynchronous Boolean simulation [171, 172] was used, which updates genes in a random order in each iteration. This random asynchronous update method is inspired from the stochastic nature of gene regulatory networks, where gene expression alteration occurs in a random order rather than simultaneously [172].

Due to the lack of experimental gene expression data, the simulation results were validated by comparing predicted patterns of gene expression levels with experimental observations reported in the literature. The dynamical behaviors of the model were also analysed by visualizing the state transition graphs under different combinations of input signals. The results show that the simple Boolean network model can capture some qualitative trends of the genetic circuits regulating the cell fate decision of beta-cells, and shed light on the causes and processes of dysfunctional insulin metabolism and loss of beta-cell homeostasis that occur in T2D.

TABLE 4.1: The gene interactions incorporated into the model with reference to the existing literature.

Gene interactions	**Reference**
IRE1 ↑ → XBP1 ↑ → beta-cell dysfunction	[173]
(IRE1 + TRAF2 + ASK1) ↑ → JNK ↑ → BCL2 (anti-apoptotic gene)↓	[174–176]
BCL2 ↓ → (BAX + BAK) (pro-apoptotic) ↑	[177, 178]
PERK ↑ → EIF2S1 ↓ → ATF4 ↑ → CHOP (pro-apoptotic) ↑	[179]
ATF6 ↑ → CHOP (pro-apoptotic) ↑ → BCL2 (anti-apoptotic gene)↓	[178, 180]
Oxidative stress ↑ → ASK1 ↑, JNK ↑, p38 ↑	[21, 181, 182]
p38 ↑ → CHOP (pro-apoptotic) ↑	[183]
FasL ↑ → (FasR + FADD + pro-caspase-8) ↑ → caspase-8 ↑ → caspase-3 ↑ → apoptosis	[184]
TNFα ↑ → (TNFR1 + TRADD) ↑ → RIPK1 ↑, FADD ↑, TRAF2 ↑	[185]
FADD ↑ → caspase-8 ↑	[185]
RIPK1 ↑ → RAIDD ↑ → caspase-8 ↑	[185]
TNFα ↑ → TNFR2 ↑ → TRAF2 ↑ →...→ JNK ↑, NF-kB ↑	[186–188]
(BAX + BAK) (pro-apoptotic) ↑ → Cytochrome c ↑ → (APAF1 + caspase-9) ↑ → caspase-3 ↑	[14, 189]
XIAP ↑ → caspase-3 ↓, caspase-7 ↓, caspase-9 ↓	[190, 191]
DIABLO ↑, HtrA2 ↑ → XIAP ↓	[192]
INSR ↑ → IRS ↑ → PI3K ↑ → ...→ AKT ↑ → FOXO1 ↓, GSK3beta ↓, GLUT4 ↑	[193–195]
GSK3beta ↑ → GS ↓ → glycogen synthesis ↓	[196, 197]
FOXO1 ↑ → PEPCK ↑, G6PC ↑ → glucose synthesis ↑	[198, 198–200]
(mTORC1 + S6K) ↑ → IRS ↓	[201–203]
IKKbeta ↑ → TSC1/2 ↓ → mTORC1 ↑	[204]
ER stress ↑ → ...→ IRE1 ↑ → ...→ JNK ↑ → IRS ↓	[205–207]
ER stress ↑ → ...→ IRE1 ↑ → XBP1 ↑ → FOXO1 ↓	[208]
PERK ↑ → FOXO1 ↑	[209]
ER stress ↑ → ...→ ATF4 ↑ → CHOP ↑ → TRB3↑ → AKT ↓	[210, 211]
IL-6 ↑ → JAK ↑ → STAT3 ↑ → SOCS3 ↑ → IRS ↓	[212–214]

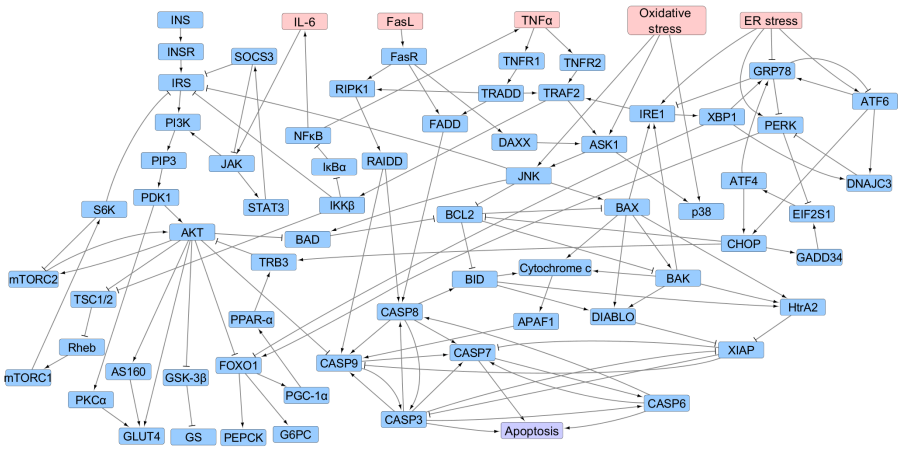

FIGURE 4.1: Gene Regulatory Network. Insulin resistance and beta-cell apoptosis pathways involved in the pathogenesis of T2D. The red nodes denote the five input signals and the purple node represents beta-cell apoptosis. A $\rightarrow$ B indicates activation of gene B by gene A, and A $-|$ B indicates inhibition of gene B by gene A.

4.2 Methods

In this work, a Boolean network model of beta-cell fate in T2D was proposed. The model was constructed by extracting information from KEGG pathways [215] and literature. The gene interactions incorporated into the model with reference to the existing literature are listed in Table 4.1. In this model, the beta-cell apoptosis pathway was integrated with the insulin resistance pathway, as shown in Figure 4.1. The apoptosis pathway consists of the signaling pathways triggered by ER stress (UPR pathway), oxidative stress, and cytokines, FasL, TNFα, and IL-6. The insulin resistance pathways consist of phosphatidylinositide 3-kinase (PI3K)-protein kinase B (PKB or AKT) (KEGG ID: hsa04151), mammalian target of rapamycin (mTOR) (KEGG ID: hsa04150), janus kinase (JAK)- signal transducer and activator of transcription (STAT) (KEGG ID: hsa04630), and insulin (KEGG ID: hsa04910) signaling pathways. T2D first causes insulin resistance, i.e. insulin fails to bind to insulin receptors in cells, thereby blocking the uptake of blood glucose by cells. Sustained insulin resistance finally leads to beta-cell failure and apoptosis.

The Boolean update functions, listed in Table 4.2, for the target genes in the model were defined by combining activating input genes using OR functions and inhibiting input genes using AND functions. The reason behind this combination strategy is that a target gene will be expressed when at least one of its activating genes is expressed and all of its inhibiting genes are absent.

The proposed Boolean network consists of seventy two nodes, of which five are input signals, one node represents Apoptosis, and the remaining sixty six nodes represent genes. The random asynchronous Boolean update [171, 172] method was used to perform the simulations. The random asynchronous Boolean method first generates a random permutation of the nodes at each time step and updates the nodes in the order specified by the permutation. This allows to capture the stochastic change in gene expressions that occur in real gene regulatory networks.

For example, suppose a gene regulatory network consists of 3 genes, $\{g_1, g_2, g_3\}$. The Boolean update function for each gene is as follows:

$$g_1 = g_3$$

$$g_2 = g_1 \vee g_3$$

$$g_3 = g_2$$

Suppose an iteration generates the permutation of nodes as $\{3, 1, 2\}$. Then the asynchronous Boolean updates will be carried out as follows:

$$g_3(t+1) = g_2(t)$$

$$g_1(t+1) = g_3(t+1)$$

$$g_2(t+1) = g_1(t+1) \vee g_3(t+1)$$

From the above equations, it can be seen that the nodes are updated in a randomly generated order, rather than simultaneously.

Table 4.2: Boolean functions for the Boolean model

Node	**Boolean Function**	**Node**	**Boolean Function**
ER	ER	OS	OS
FasL	FasL	TNFα	TNFα or NFκB
IL-6	IL-6 or NFκB		
GRP78	ATF6 or XBP1 or ATF4 and (not ER)	ATF6	ER and (not GRP78)
PERK	ER and (not GRP78) and (not DNAJC3)	IRE1	ER or BAX or BAK and (not GRP78)
EIF2S1	GADD34 and (not PERK)	DNAJC3	ATF6 or XBP1
ATF4	EIF2S1	CHOP	ATF6 or ATF4
XBP1	IRE1	GADD34	CHOP
TNFR1	TNFα	TNFR2	TNFα
TRAF2	IRE1 or TNFR2 or TRADD	ASK1	OS or TRAF2 or DAXX
JNK	OS or ASK1	p38	OS or ASK1
BCL2	(not JNK) and (not CHOP) and (not BAD)	BID	CASP8 and (not BCL2)
BAX	JNK and (not BCL2)	BAK	BAX and (not BCL2)
DIABLO	BAX or BAK or BID	HtrA2	BAX or BAK or BID
FasR	FasL	TRADD	TNFR1
DAXX	FasR	RIPK1	FasR or TRADD
RAIDD	RIPK1	FADD	FasR or TRADD
CASP8	RAIDD or FADD or CASP3 or CASP6	CASP9	RAIDD or CASP8 or CASP3 or APAF1 and (not XIAP) and (not AKT)

Table 4.2 (continued): Boolean functions for the Boolean model

CASP3	CASP9 or CASP8 and (not XIAP)	CASP7	CASP9 or CASP8 or CASP3 or CASP6 and (not XIAP)
CASP6	CASP7 or CASP3		
XIAP	(not DIABLO) and (not HtrA2) and (not CASP3)	CytochromeC	BAX or BAK or BID
APAF1	CytochromeC	Apoptosis	CASP3 or CASP6 or CASP7
INS	INS	INSR	INS
IRS	INSR and (not SOCS3) and (not JNK) and (not IKKβ) and (not S6K)	PI3K	IRS or JAK
PIP3	PI3K	PDK1	PIP3
AKT	PDK1 or mTORC2 and (not TRB3)	AS160	AKT
PKCα	PDK1	GLUT4	AKT or AS160 or PKCα
GSK3β	not AKT	GS	not GSK3β
FOXO1	PERK and (not AKT) and (not XBP1)	PGC1α	FOXO1
PEPCK	FOXO1	G6PC	FOXO1
PPARα	PGC1α	TRB3	PPARα or CHOP
TSC1/2	(not AKT) and (not IKKβ)	Rheb	not TSC1/2
mTORC1	Rheb	S6K	mTORC1
mTORC2	AKT and (not S6K)	BAD	JNK and (not AKT)
JAK	IL-6 and (not SOCS3)	STAT3	JAK
SOCS3	STAT3	IKKβ	TRAF2
NFκB	not IKBα	IKBα	not IKKβ

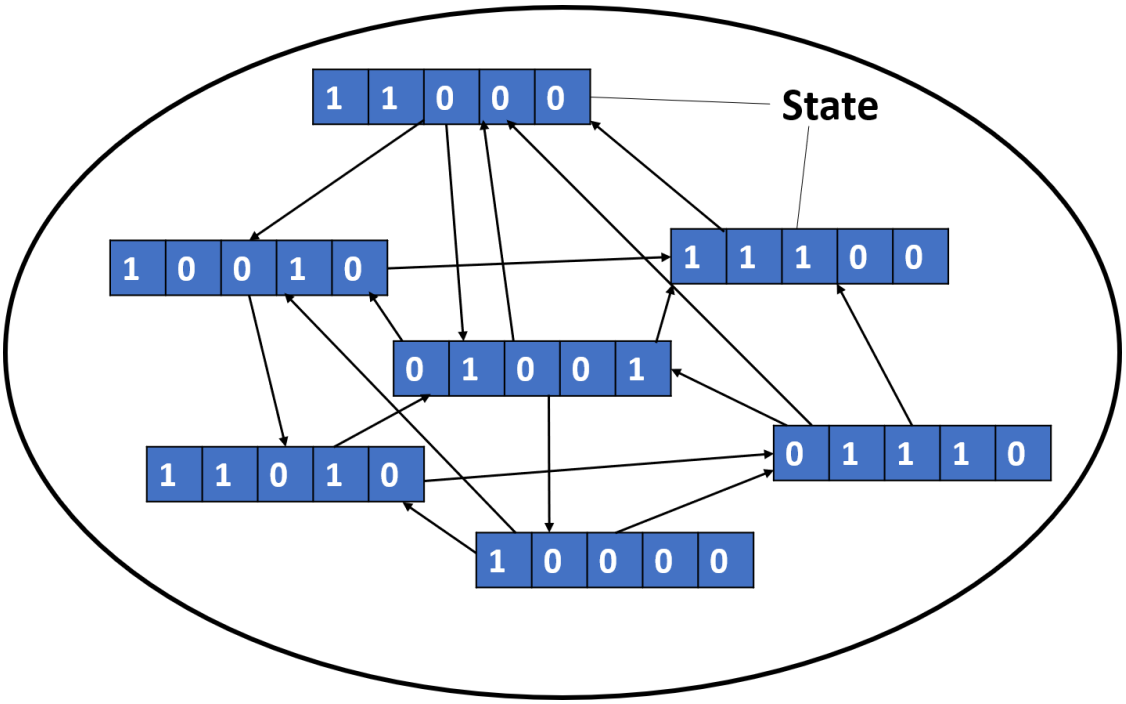

FIGURE 4.2: Strongly Connected Component. An example of a strongly connected component (SCC). Suppose the network consists of five genes. Then each node is a state which contains the expression levels of the five genes. An arrow from state S_1 to state S_2 indicates an update step. In a SCC all states can be reached from every other state.

After performing the simulations for a fixed number of iterations, a directed graph of states was obtained, where each state was a vector representing the expression levels of all genes at a particular time step. The strategy of strongly connected components (SCCs) was employed on this directed graph to capture the dynamic nature of the states [171]. An SCC of a directed graph is a sub-graph that is strongly connected, i.e., each node is reachable from every other node in the sub-graph. An illustration of SCC is given in Figure 4.2. Each node is a state with the expression levels of all the genes in the network (the example considers a network with five genes) and there is a path between each pair of nodes in both directions. Suppose, an SCC consists of a set of N states $\{S_1, S_2, ..., S_N\}$. The probability of state $S_i \in SCC$ is given by

$$P(S_i) = \frac{number\ of\ occurrences\ of\ S_i}{\sum_j^N number\ of\ occurrences\ of\ S_j}.$$

The gene expression level for any gene in a particular SCC was calculated by multiplying the sum of probabilities of states where the gene is in the ON state by

the sum of probabilities of all states in the SCC. Therefore, the expression level of a gene, g_i, with respect to an SCC is determined as follows:

$$Exp(g_i) = \sum_{S_j \in OnSt(g_i)} P(S_j) \times \sum_{j}^{N} P(S_j),$$

where

$$OnSt(g_i) = \{S_j \in SCC \mid g_i(S_j) = 1\},$$

and

$$\sum_{j}^{N} P(S_j) = 1.$$

ER stress, oxidative stress, TNFα, FasL, and IL-6 were used as input signals. Also, based on the literature, some of the nodes were assigned specific values (Table 4.3) and the rest were set to random values as initial conditions. Simulations were performed using different combinations of the input signals, as shown in Table 4.4. 1000 simulation runs and 1000 Boolean update steps per simulation were carried out for each input signal. The results of the simulations are presented and discussed in the following section.

TABLE 4.3: Initial conditions

Node	**Initial value**	**Reason**
Apoptosis	False	Apoptosis was set to False to see whether the input signals can cause apoptosis.
Caspases 3, 6, 7, 8, 9	False	Caspases serve as the final mediators of apoptosis. So, they were set to False to see whether the input signals can activate them.

Due to the lack of experimental data, the proposed Boolean network model was validated using relevant literature (see Table 4.1). The literature was quantified as follows. For each gene g_i,

$$g_i = \begin{cases} 1 & \text{if } g_i \text{ is reported as expressed in the literature,} \\ 0 & \text{if } g_i \text{ is reported as not expressed in the literature.} \end{cases}$$

In this model, the expression level of each gene was determined with respect to a particular SCC. Thus the gene expression levels are in the range [0, 1]. It was

assumed that if the expression value of a gene was greater than 0.50, then the gene was expressed, otherwise, it was not expressed.

TABLE 4.4: Different combinations for the input signal nodes

	ER stress	**Oxidative stress**	**TNFα**	**FasL**	**IL-6**
Case 1	True	False	False	False	False
Case 2	False	True	False	False	False
Case 3	True	True	False	False	False
Case 4	False	False	True	False	False
Case 5	False	False	False	True	False
Case 6	False	False	False	False	True
Case 7	False	False	True	True	True
Case 8	True	True	True	True	True

For the purpose of validating the proposed model, the performance metrics of precision, recall (sensitivity), specificity, and F1 score were used. The simulation result of the proposed model was verified against the literature as follows. For each gene g_i,

$$g_i \in \begin{cases} \text{True positive}, & \text{if } g_i = 1 \text{ (simulation result) and } g_i = 1 \text{ (literature)}, \\ \text{True negative}, & \text{if } g_i = 0 \text{ (simulation result) and } g_i = 0 \text{ (literature)}, \\ \text{False positive}, & \text{if } g_i = 1 \text{ (simulation result) and } g_i = 0 \text{ (literature)}, \\ \text{False negative}, & \text{if } g_i = 0 \text{ (simulation result) and } g_i = 1 \text{ (literature)}. \end{cases}$$

The four evaluation metrics were calculated using the following formulae:

$$Precision = \frac{True\ positive}{True\ positive + False\ positive},$$

$$Recall or sensitivity = \frac{True\ positive}{True\ positive + False\ negative},$$

$$Specificity = \frac{True\ negative}{True\ negative + False\ positive},$$

$$F1_{score} = \frac{2 \times precision \times recall}{precision + recall}.$$

4.3 Results

4.3.1 Comparison with the literature

The expression levels of genes in the SCCs obtained by performing simulations with the proposed Boolean model are listed in Tables 4.5 and 4.6. Simulations performed using input signal cases 1, 2, 3, 4, 5, 7, and 8 (Table 4.4) resulted in two attractors (SCCs). Apoptosis was ON in both the attractors. Simulations performed using input signal case 6 (Table 4.4) resulted in six attractors (SCCs). Apoptosis was ON in four attractors and OFF in the remaining two attractors. These observations are consistent with the literature where ER stress, oxidative stress, and cytokines have been shown to cause apoptosis of beta-cells individually as well as together [14–16].

From the model simulation results, it was observed that Caspases 3, 6, 7, 8, and 9, which serve as the final mediators of apoptosis [166] were TRUE in the attractors, even though in the initial condition they were set to FALSE. The ER stress sensor IRE1 and its downstream gene X-box protein binding 1 (XBP1) were TRUE in some attractors, and FALSE in others [173]. Another ER stress sensor, PERK was observed to be FALSE in all the attractors. Also, eukaryotic translation initiation factor 2 subunit 1 (EIF2S1), activating transcription factor 4 (ATF4), and C/EBP homologous protein (CHOP) were TRUE in some attractors and FALSE in the others. PERK phosphorylates and inactivates EIF2S1, which inhibits protein synthesis. Phosphorylated EIF2S1 increases the translation of ATF4 [163], which in turn activates pro-apoptotic CHOP, causing beta-cell dysfunction and death [179]. The attractors where IRE1, XBP1, EIF2S1, ATF4, and CHOP had expression levels of 0 may have denoted the transition states when these genes are not contributing to apoptosis.

IRE1 associates with TNF-receptor-associated factor 2 (TRAF2) and apoptosis signal-regulating kinase 1 (ASK1) and activates jun N-terminal kinase (JNK) [174, 175], which in turn inhibits the anti-apoptotic protein B-cell lymphoma 2 (BCL2) [176]. Oxidative stress activates ASK1 [181, 182], JNK and p38 [21]. Activated p38 phosphorylates and elevates the expression of pro-apoptotic CHOP [183]. From the simulation results, it was observed that the pro-apoptotic genes, TRAF2, ASK1, JNK, p38, BAX, and BAK were TRUE and the anti-apoptotic gene BCL2 was

FALSE in one attractor, while the reverse states were observed in the other. X-linked inhibitor of apoptosis protein (XIAP), which inhibits caspases 3, 7, and 9 [190, 191], had an expression level of 0, whereas, DIABLO and HtrA2, which inhibit XIAP [192], had expression levels of 1.

JNK phosphorylates and inhibits insulin receptor substrate (IRS) [206, 207]. IRS gene was FALSE in both the attractors. PI3K had an expression level of around 0.50 in all the attractors. Tribbles homolog 3 (TRB3) is induced by ER stress through the ATF4-CHOP pathway [210]. Over-expression of TRB3 inhibits AKT and decreases glucose uptake [211]. TRB3 was TRUE in one attractor and FALSE in the other. AKT had an expression level of 0.50 in both the attractors. Thus, from the results, it is observed that ER stress inhibits the PI3K-AKT signaling pathway and promotes insulin resistance.

Insulin promotes conversion of glucose to glycogen by inhibiting glycogen synthase kinase-3beta (GSK3beta) through the PI3K-AKT signaling pathway, which leads to the activation of glycogen synthase (GS) [197]. From the simulation results, it was observed that the expression level of GSK3beta, which inhibits glycogen synthesis through inhibition of GS [196, 197] was approximately 0.49 and that of GS was approximately 0.50. From these simulation results, it can be inferred that glycogen synthesis is reduced which contributes to insulin resistance.

In T2D, the mammalian target of rapamycin complex 1 (mTORC1)/ S6 kinase (S6K) signaling is activated [201] leading to the inhibition of IRS [202, 203]. It was observed from the simulation results that mTORC1 and S6K had expression levels of 1 thus inhibiting IRS which had an expression of 0. These events caused PI3K and AKT to have low expression levels of approximately 0.50, which in turn reduced glucose uptake through GLUT4 whose expression level was around 0.65.

FOXO1 increases the expression of phosphoenolpyruvate carboxykinase (PEPCK) and glucose-6-phosphatase (G6PC) and thus promotes glucose synthesis [198]. Insulin inhibits the expression of FOXO1 through the activation of the PI3K/AKT signalling pathway, which in turn suppresses PEPCK and G6PC and reduces glucose synthesis [198–200]. From the simulation results, it was observed that FOXO1, PEPCK, and G6PC were FALSE. This could be due to the fact that PI3K and AKT are not completely inactive, though they may have low expression levels, and hence is still able to inhibit the expressions of FOXO1, PEPCK, and G6PC.

TABLE 4.5: Gene expressions of the significant genes in the model for input signal cases 1-5 and 7-8. Here A1 and A2 denote SCC1 and SCC2 respectively.

Node	**Case 1**		**Case 2**		**Case 3**		**Case 4**		**Case 5**		**Case 7**		**Case 8**	
	A1	**A2**	**A1**	**A2**	**A1**	**A2**	**A1**	**A2**	**A1**	**A2**	**A1**	**A2**	**A1**	**A2**
Apoptosis	1	1	1	1	1	1	1	1	1	1	1	1	1	1
AKT	0.50	0.50	0.49	0.49	0.49	0.49	0.49	0.49	0.50	0.49	0.49	0.50	0.50	0.49
APAF-1	1	1	1	1	1	1	1	1	1	1	1	1	1	1
ASK1	1	1	1	1	1	1	1	1	1	1	1	1	1	1
ATF4	1	0	1	0	1	0	1	0	1	0	1	0	1	0
ATF6	0	0	0	0	0	0	0	0	0	0	0	0	0	0
BAK	1	1	1	1	1	1	1	1	1	1	1	1	1	1
BAX	1	1	1	1	1	1	1	1	1	1	1	1	1	1
BCL2	0	0	0	0	0	0	0	0	0	0	0	0	0	0
Caspase-3	1	1	1	1	1	1	1	1	1	1	1	1	1	1
Caspase-6	1	1	1	1	1	1	1	1	1	1	1	1	1	1
Caspase-7	1	1	1	1	1	1	1	1	1	1	1	1	1	1
Caspase-8	1	1	1	1	1	1	1	1	1	1	1	1	1	1
Caspase-9	1	1	1	1	1	1	1	1	1	1	1	1	1	1
CHOP	1	0	1	0	1	0	1	0	1	0	1	0	1	0
DIABLO	1	1	1	1	1	1	1	1	1	1	1	1	1	1
EIF2S1	1	0	1	0	1	0	1	0	1	0	1	0	1	0

Table 4.5 (continued): Gene expressions of the significant genes in the model for input signal cases 1-5 and 7-8. Here A1 and A2 denote SCC1 and SCC2 respectively.

FADD	1	1	1	1	1	1	1	1	1	1	1	1	1	1
FASR	0	0	0	0	0	0	0	0	0	0	0	0	0	0
FOXO1	0	0	0	0	0	0	0	0	0	0	0	0	0	0
G6PC	0	0	0	0	0	0	0	0	0	0	0	0	0	0
GADD34	1	0	1	0	1	0	1	0	1	0	1	0	1	0
GLUT4	0.65	0.65	0.65	0.65	0.65	0.65	0.65	0.65	0.65	0.65	0.65	0.65	0.65	0.65
GRP78	1	1	1	1	1	1	1	1	1	1	1	1	1	1
GS	0.50	0.50	0.50	0.49	0.49	0.49	0.49	0.49	0.50	0.50	0.50	0.50	0.50	0.49
GSK3β	0.49	0.49	0.50	0.50	0.50	0.50	0.50	0.50	0.49	0.49	0.49	0.49	0.49	0.50
HtrA2	1	1	1	1	1	1	1	1	1	1	1	1	1	1
IKBα	0	0	0	0	0	0	0	0	0	0	0	0	0	0
IKKβ	1	1	1	1	1	1	1	1	1	1	1	1	1	1
INS	1	1	1	1	1	1	1	1	1	1	1	1	1	1
INSR	1	1	1	1	1	1	1	1	1	1	1	1	1	1
IRE1	1	1	1	1	1	1	1	1	1	1	1	1	1	1
IRS	0	0	0	0	0	0	0	0	0	0	0	0	0	0
JAK	0.50	0.49	0.50	0.49	0.49	0.50	0.49	0.49	0.49	0.49	0.49	0.50	0.50	0.50
JNK	1	1	1	1	1	1	1	1	1	1	1	1	1	1
NFKB	1	1	1	1	1	1	1	1	1	1	1	1	1	1

Table 4.5 (continued): Gene expressions of the significant genes in the model for input signal cases 1-5 and 7-8. Here A1 and A2 denote SCC1 and SCC2 respectively.

PEPCK	0	0	0	0	0	0	0	0	0	0	0	0	0	0
PERK	0	0	0	0	0	0	0	0	0	0	0	0	0	0
PI3K	0.50	0.49	0.49	0.49	0.50	0.50	0.50	0.50	0.50	0.49	0.49	0.50	0.50	0.49
RAIDD	1	1	1	1	1	1	1	1	1	1	1	1	1	1
RIPK1	1	1	1	1	1	1	1	1	1	1	1	1	1	1
S6K	1	1	1	1	1	1	1	1	1	1	1	1	1	1
SOCS3	0.49	0.49	0.50	0.49	0.50	0.50	0.49	0.49	0.50	0.50	0.49	0.49	0.49	0.50
STAT3	0.50	0.49	0.49	0.49	0.49	0.50	0.49	0.49	0.50	0.50	0.49	0.49	0.50	0.50
TNFR1	1	1	1	1	1	1	1	1	1	1	1	1	1	1
TNFR2	1	1	1	1	1	1	1	1	1	1	1	1	1	1
TRADD	1	1	1	1	1	1	1	1	1	1	1	1	1	1
TRAF2	1	1	1	1	1	1	1	1	1	1	1	1	1	1
TRB3	1	0	1	0	1	0	1	0	1	0	1	0	1	0
TSC2	0	0	0	0	0	0	0	0	0	0	0	0	0	0
XBP1	1	1	1	1	1	1	1	1	1	1	1	1	1	1
XIAP	0	0	0	0	0	0	0	0	0	0	0	0	0	0
mTORC1	1	1	1	1	1	1	1	1	1	1	1	1	1	1
p38	1	1	1	1	1	1	1	1	1	1	1	1	1	1

TABLE 4.6: Gene expressions of the significant genes in the model for input signal case 6. Here A1-A6 denote SCC1-SCC6 respectively

Node	Case 6						Node	Case6					
	A1	**A2**	**A3**	**A4**	**A5**	**A6**		**A1**	**A2**	**A3**	**A4**	**A5**	**A6**
Apoptosis	1	1	1	1	0	0	AKT	0.49	0.49	0.63	0.55	0.65	0.56
APAF-1	1	1	0	1	0	0	ASK1	1	1	0	0	0	0
ATF4	1	0	0	1	0	1	ATF6	0	0	0	0	0	0
BAK	1	1	0	0	0	0	BAX	1	1	0	0	0	0
BCL2	0	0	1	0	1	0	Caspase-3	1	1	1	1	0	0
Caspase-6	1	1	1	1	0	0	Caspase-7	1	1	1	1	0	0
Caspase-8	1	1	1	1	0	0	Caspase-9	1	1	1	1	0	0
CHOP	1	0	0	1	0	1	DIABLO	1	1	0	1	0	0
EIF2S1	1	0	0	1	0	1	FADD	1	1	0	0	0	0
FASR	0	0	0	0	0	0	FOXO1	0	0	0	0	0	0
G6PC	0	0	0	0	0	0	GADD34	1	0	0	1	0	1
GLUT4	0.65	0.65	0.75	0.70	0.78	0.71	GRP78	1	1	0	1	0	1
GS	0.49	0.49	0.62	0.54	0.65	0.55	GSK3β	0.50	0.50	0.38	0.45	0.36	0.45
HtrA2	1	1	0	1	0	0	IKBα	0	0	1	1	1	1
IKKβ	1	1	0	0	0	0	INS	1	1	1	1	1	1
INSR	1	1	1	1	1	1	IRE1	1	1	0	0	0	0
IRS	0	0	0.19	0.22	0.18	0.22	JAK	0.49	0.49	0.49	0.49	0.49	0.50
JNK	1	1	0	0	0	0	NFKB	1	1	0	0	0	0

Table 4.6 (continued): Gene expressions of the significant genes in the model for input signal case 6. Here A1-A6 denote SCC1-SCC6 respectively.

PEPCK	0	0	0	0	0	0		PERK	0	0	0	0	0	0
PI3K	0.49	0.49	0.54	0.55	0.54	0.56		RAIDD	1	1	0	0	0	0
RIPK1	1	1	0	0	0	0		S6K	1	1	0.62	0.55	0.62	0.56
SOCS3	0.49	0.50	0.50	0.49	0.49	0.49		STAT3	0.49	0.49	0.49	0.49	0.49	0.50
TNFR1	1	1	0	0	0	0		TNFR2	1	1	0	0	0	0
TRADD	1	1	0	0	0	0		TRAF2	1	1	0	0	0	0
TRB3	1	0	0	1	0	1		TSC2	0	0	0.37	0.45	0.36	0.44
XBP1	1	1	0	0	0	0		XIAP	0	0	0	0	1	1
mTORC1	1	1	0.63	0.55	0.63	0.57		p38	1	1	0	0	0	0

In Case 6 where only signal IL6 was active, six attractors were obtained (Table 4.6), of which four indicated apoptosis and two did not. For the attractors where apoptosis was observed, the expression of genes were similar to those mentioned above for the other input signal cases. When apoptosis was not observed, i.e. in the two remaining attractors, the caspases, JNK, BAX, and BAK were FALSE. In one of these two attractors, BCL2 was FALSE and CHOP was TRUE. In the other attractor the reverse expressions were observed. Thus, in the presence of only IL-6, apoptosis may or may not be activated.

The performance of the proposed Boolean network model was further assessed by comparing model predictions of gene expressions against the literature. Considering the simulation results obtained using the 8 input signals listed in Table 4.4, the average precision, recall (sensitivity), specificity, and F1 score obtained for the model are 0.9524, 0.8, 0.875, and 0.8696, respectively. It is observed that the validation scores for the model are not very high. This may be due to the fact that the model is sensitive to some missing interactions.

4.3.2 State transition graphs

Figure 4.3 shows the state transition graph of the state space generated by simulations conducted using input signal combination given in case 8 (Table 4.4). The two dense red regions represent the two SCCs where apoptosis is ON. The blue nodes represent states where apoptosis is OFF. Thus, in the presence of all input signals, apoptosis is eventually activated, even though in the initial condition it is set to FALSE.

Figure 4.4 shows the state transition graph of the state space generated by simulations conducted using input signal combination given in case 6 (Table 4.4). The four dense red regions represent the four SCCs where apoptosis is ON. The two dense blue regions represent the two SCCs where apoptosis is OFF. Thus, in the presence of only IL-6, apoptosis may or may not be activated.

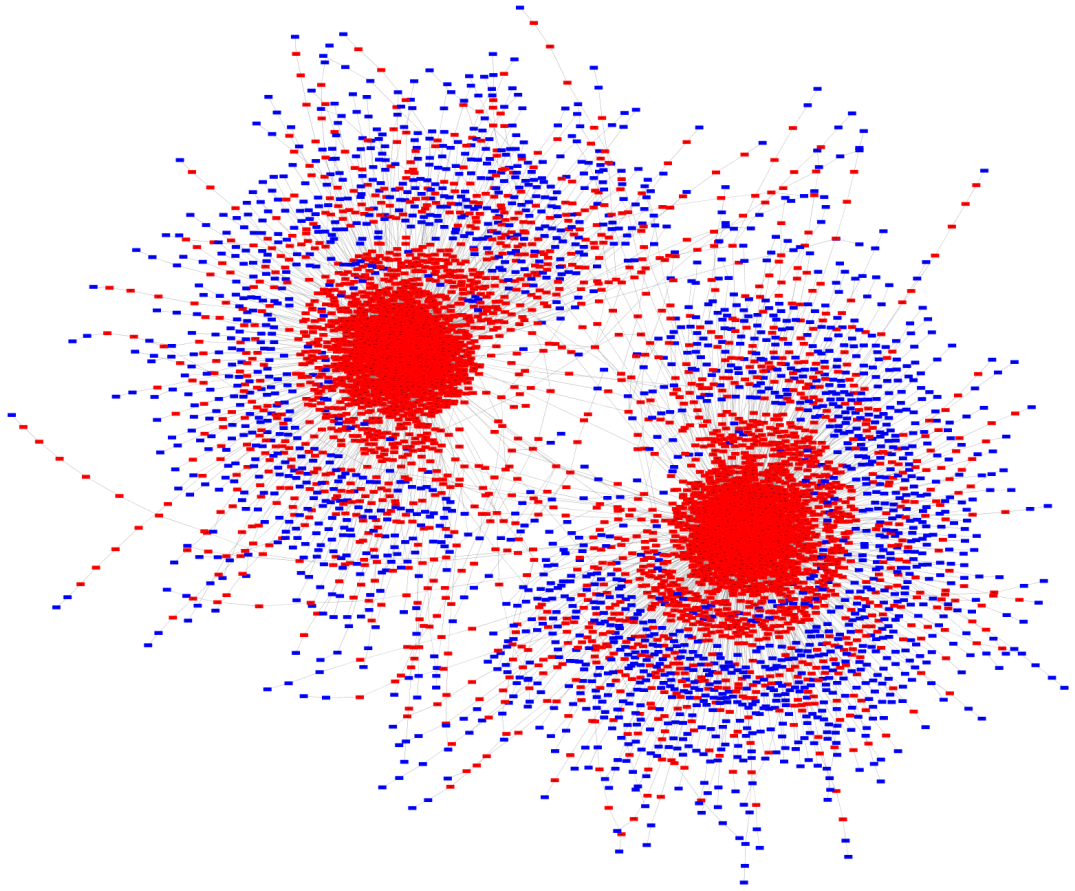

FIGURE 4.3: State Transition Graph 1. State transition graph obtained by simulating the proposed Boolean network model using input signal condition given in Case 8 of Table 4.4. Simulations generate 2 attractors, having the Apoptosis node activated. Apoptosis is ON in the red coloured states and OFF in the blue colored states.

4.3.3 Comparison with random Boolean networks

The proposed Boolean network model was also compared with random Boolean network models using the 8 input signal combinations given in Table 4.4. For cases 1, 2, 3, 4, 5, 7, and 8 it was found that the number of attractors obtained by simulating the random Boolean networks ranged from 28 to 177, whereas for the proposed Boolean network model the number of attractors was 2. Similarly, for case 6, the number of attractors obtained by simulating the random Boolean networks ranged from 25 to 180, whereas for the proposed Boolean network model the number of attractors was 6. Thus, from the results it was observed that the random Boolean networks typically have large number of attractors.

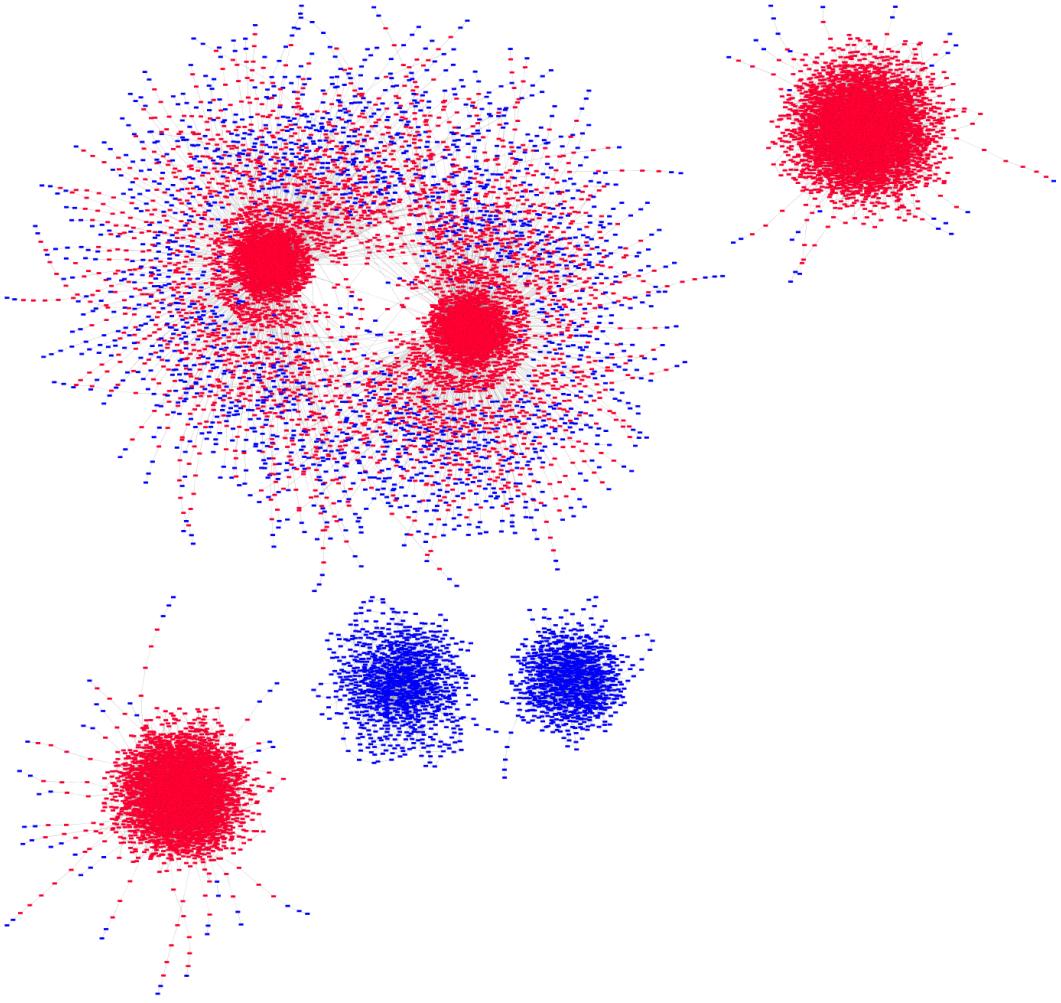

FIGURE 4.4: State Transition Graph 2. State transition graph obtained by simulating the proposed Boolean network model using input signal condition given in Case 6 of Table 4.4. Simulations generate 6 attractors. In four of the attractors Apoptosis is ON, denoted by red colour, and in the remaining two attractors Apoptosis is OFF, denoted by blue colour.

4.4 Discussion

In this paper, a Boolean network model of the integrated insulin resistance and beta-cell apoptosis pathways was proposed. The model was used to simulate different combinations of the five input signals, i.e. ER stress, oxidative stress, and cytokines (TNFα, FasL, IL-6), which serve as triggers for insulin resistance and beta-cell apoptosis.

The random order asynchronous update method was implemented to perform the simulations, i.e. all nodes were updated in a random order at each update step. The performance of the model was assessed using the metrics of precision, recall

(sensitivity), specificity, and F1 score, when testing the model predictions against the literature. The precision score obtained was high, but sensitivity, specificity, and F1 scores were low. One possible reason behind the low scores may be that some missing interactions affected the predictions of the model. The proposed Boolean network model was also compared with random Boolean network models and it was observed that random Boolean networks typically have a large number of attractors ranging from around 25 to 180, whereas this model resulted in small number of attractors ranging from 2 to 6.

Such Boolean network models can help in the identification of potential intervention targets. The strongly connected components (SCCs) represent the long-term behaviour of Boolean networks and their analysis can provide crucial biological insights. For instance, we want to analyse the effect of a set of inhibitors which are known to have the potential to prevent beta-cell apoptosis. These inhibitors could be used individually or in different combinations to perturb the model and the resulting SCCs could be compared to identify the most effective inhibitor or combination of inhibitors. The sequences of the successor states could also be compared to get a better understanding of how the inhibitors are affecting the dynamics of the system. Boolean networks have been successfully used before in the identification of potential intervention targets [216–219].

Chapter 5

An integrative approach to modelling compromised beta-cell identity in Type 2 Diabetes

5.1 Introduction

Type 2 diabetes (T2D) is a chronic metabolic disorder that is characterized by defects in both insulin secretion and insulin action, which causes glucose levels to increase above physiological levels. The beta-cells of the pancreatic islets play an important role in maintaining glucose homeostasis by secreting the hormone, insulin, which is capable of lowering plasma glucose by facilitating glucose uptake by skeletal muscle, liver and adipose tissue.

Progressive deterioration in beta-cell function, reduction of glucose-stimulated insulin secretion (GSIS) and decreased beta-cell mass has been observed in diabetic human islets. Post-mortem histological analysis of beta-cell mass of people with T2D has shown up to 50% reduction in beta-cell mass compared with healthy individuals of the same BMI [160, 220]. Previously, this loss in beta-cell mass was entirely attributed to beta-cell apoptosis. However, it has been demonstrated in multiple studies in both animal models [36, 38] and humans [37, 40, 41, 221], that apoptosis is not the primary inducer of loss of beta-cell mass; rather loss in functional beta-cell mass results from compromised beta-cell identity. Maintenance of

beta-cell identity requires active regulation of gene expression. Post-mortem studies of pancreatic islets from type 2 diabetic patients have demonstrated a marked and selective loss of transcription factors involved in mature beta-cell identity including MAFA and PDX1 [37, 40, 221]. Since PDX1 and MAFA are also critical regulators of insulin promoter activity [222–224], their reduced expressions in response to chronic hyperglycemia is accompanied by a reduction in insulin gene expression and insulin levels [37, 40].

Loss of transcription factors PDX1 and MAFA is caused by a multitude of factors of which a leading factor is glucotoxicity caused by chronic hyperglycemia [43]. Glucotoxicity is defined in terms of the detrimental effects of hyperglycemia on the phenotype and function of beta-cells. Glucotoxicity in the presence of chronic hyperglycemia has been shown to lead to decreased insulin gene expression together with depleted insulin stores as well as downregulation of beta-cell identity transcription factors such as PDX1 and MAFA. Along with other causes, it has been found that two main processes contribute to glucotoxicity: oxidative stress and endoplasmic reticulum (ER) stress.

Chronic hyperglycemia increases the formation of reactive oxygen species (ROS) that, in excess and over time, can lead to chronic oxidative stress. Oxidative stress reflects an imbalance between the production of ROS (free radicals) and the antioxidant defense. Beta-cells are particularly vulnerable to oxidative stress due to the low expression of anti-oxidant enzymes such as catalase and glutathione peroxidase [19, 20]. In addition, chronic hyperglycemia places a high demand for insulin synthesis on the ER, which is responsible for synthesizing polypeptides from mRNA and converting them into mature proteins. A high inward flux of polypeptide molecules into the ER can overwhelm the protein-folding machinery, leading to an imbalance and the accumulation of unfolded and misfolded proteins, which is toxic for the cell. This imbalance is known as ER stress.

The processes involved in the regulation of the transcription factors PDX1 and MAFA and insulin gene expression include glucose transport, glucose metabolism, calcium dynamics, insulin signalling, and protein folding among others. These processes are complex and non-linear since they involve multiple interactions and feedback processes. Computational models and simulations could be useful tools to gain a comprehensive understanding of these intricate interactions by replicating the behaviour of the system based on known properties of the system components.

In addition, these models could be used to test hypotheses and scenarios to gain new insights.

The goal of the proposed computational model was to gain a better understanding of the underlying mechanisms that regulate the beta-cell identity transcription factors, PDX1 and MAFA, and lead to their downregulation in the presence of chronic hyperglycemia. The aim was to investigate the loss of beta-cell function through loss of beta-cell identity in the presence of chronic hyperglycemia induced oxidative stress and ER stress. Beta-cell function involves multiple processes including glucose metabolism, calcium dynamics, electrical activity, protein folding among others. There are many computational models of these processes in the literature. These models focus on particular processes involved in beta-cell function. However, in order to understand the mechanisms leading to compromised beta-cell identity and beta-cell dysfunction in the presence of chronic hyperglycemia, it is important to integrate these models of the different processes to obtain a complete picture of beta-cell function. This is because all these different processes are interlinked and a perturbation to any one of these processes can affect another process. Hence, in this work, these different processes were integrated as well as new equations were developed for the insulin transcription process and its regulation by stress-activated kinases and insulin signalling pathway. In-silico experiments performed with this integrated mathematical model can help to further extend our understanding of the mechanisms leading to compromised beta-cell identity and beta-cell dysfunction in the presence of chronic hyperglycemia.

Various computational models have been established to address different functions of the beta-cell. Chay and Keizer [225] proposed the first model of the electrical activity in the beta-cells. Their model included a potassium channel activated by intracellular calcium ions, a voltage-gated K^+ channel, a voltage-gated calcium channel, and glucose-dependent cytoplasmic changes of intracellular calcium concentration. Keizer and Magnus [226–228] and Smolen and Keizer [229, 230] introduced K-ATP channels to the models of beta-cells in order to analyze the role of the cyclical changes in the ATP/ADP ratio in beta-cell electrical activity. Magnus and Keizer [227, 228, 231] proposed models which included glucose metabolism and Ca^{2+} handling in the cytoplasm and mitochondria and the electrical activity in the plasma and inner mitochondrial membranes of the beta-cell. Bertram et al. [232] and Chay et al. [233] included the ER as a second Ca^{2+} compartment in beta-cell

models. The literature contains many other models of glucose transport, glucose metabolism, Ca^{2+} handling, electrical activity, and glucose-stimulated insulin secretion [234–239, 239–247].

From these above-mentioned models in literature, the models of of Luni et al. [245], Fridlyand et al. [241], Wacquier et al. [242], Chay et al. [225], Smolen et al. [229], and Graham [248] were used to model the processes of glucose metabolism, calcium dynamics, electrical activity and protein folding in the beta-cell. These models were integrated with the proposed model of insulin gene transcription. The model was parameterized using values from the literature as well as estimating from experimental data. This model was used to simulate the changes in the levels of PDX1, MAFA and insulin mRNA in the presence of different glucose concentrations. In addition, the influence of different inhibitors of PDX1 and MAFA on these transcription factors and insulin mRNA levels were analyzed.

5.2 Method

5.2.1 Model development

Insulin biosynthesis and secretion are stimulated by elevated glucose levels. There are multiple processes involved from the uptake of glucose by beta-cells and secretion of insulin from beta-cells. These processes occur in different organelles. A schematic diagram of the model is given in Figure 5.1. Four compartments are considered in this model: cytosol, mitochondria, ER, and nucleus. From Figure 5.1 it is seen that glucose enters the beta-cell through GLUT1 and then undergoes metabolism through the processes of glycolysis, tricarboxylic acid (TCA) cycle and electron transport chain (ETC) to produce ATP and reactive oxygen species (ROS). The rise in ATP/ADP ratio causes closure of the K-ATP channel and influx of Ca^{2+} into the beta-cell through the voltage-gated calcium channel (VGCC). Ca^{2+} leaves the beta-cell through the plasma membrane Ca^{2+}-ATPase (PMCA). Ca^{2+} enters the mitochondria through the mitochondrial Ca^{2+} uniporter (MCU) complex and leaves through the mitochondrial Na^{+}/Ca^{2+} exchanger (NCX). Ca^{2+} enters the ER through the sarco/endoplasmic reticulum Ca^{2+}-ATPases (SERCA) and leaves through the inositol trisphosphate receptor (IP3R). Extra-cellular insulin activates AKT which in turn phosphorylates glycogen synthase kinase (GSK3) and FOXO1

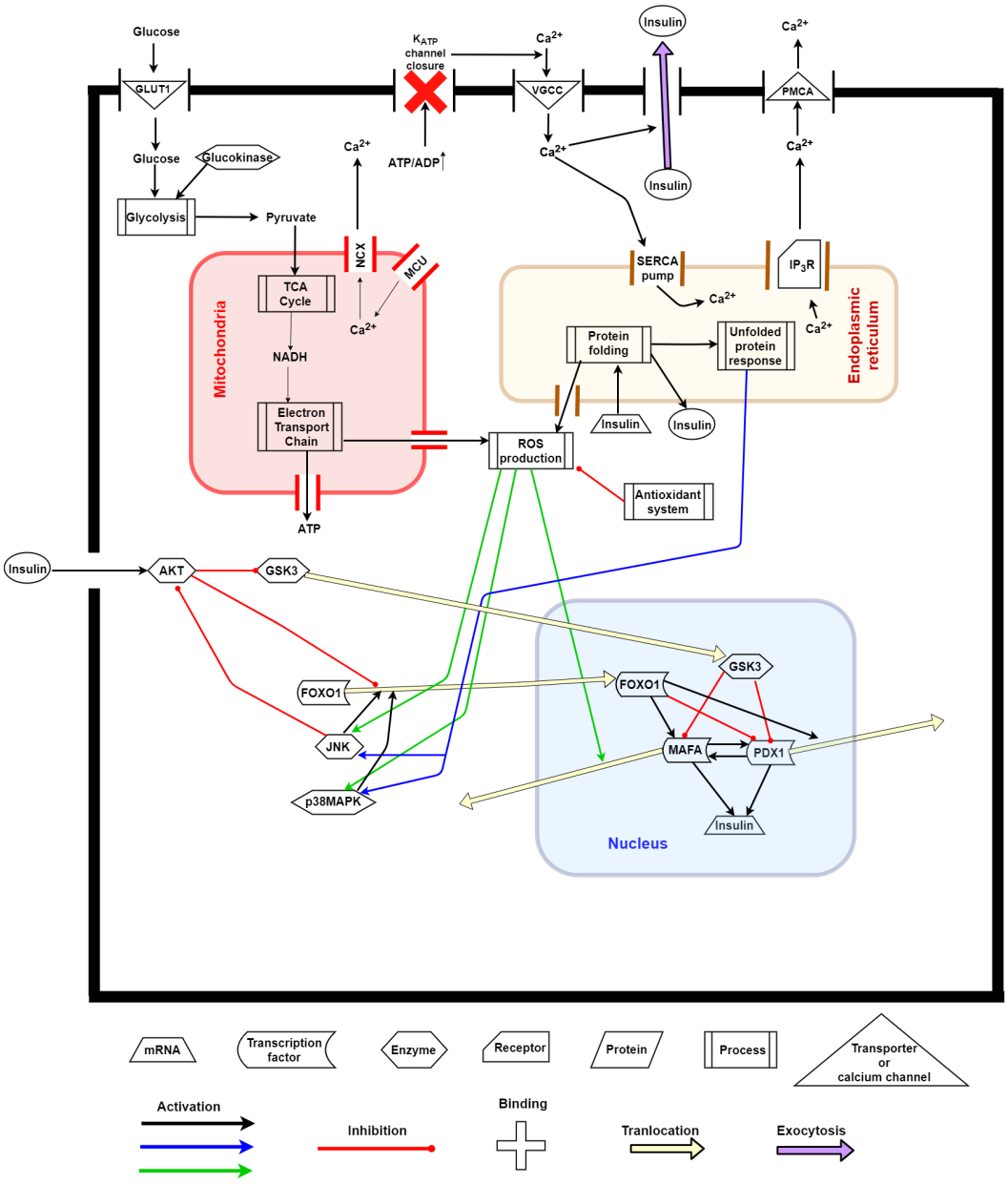

FIGURE 5.1: Schematic diagram of the model.

and prevents their translocation to the nucleus. On the other hand, ROS and the unfolded protein response (UPR) activate the kinases, JNK and p38MAPK, which in turn inhibit AKT and also promote nuclear translocation of FOXO1. PDX1 and MAFA are the activator transcription factors of insulin as well as of each other. FOXO1 is a repressor transcription factor of PDX1 and an activator transcription factor of MAFA. FOXO1 also causes nuclear expulsion of PDX1. GSK3 causes proteasomal degradation of both PDX1 and MAFA. Insulin mRNA then undergoes translation and enters the ER for folding. A high flux of insulin mRNA into

the protein folding machinery activates the UPR. After folding, insulin is secreted from the beta-cell depending on the Ca^{2+} concentration in the cytosol.

The following sections provide detailed descriptions of all these important processes involved in beta-cell function, namely, glucose transport, glucose metabolism, calcium dynamics, electrical activity, insulin signalling, ROS generation and signalling, insulin transcription, translation and folding, UPR and insulin secretion. The rate equations used to describe these processes are also explained. The rate equations describing the processes of glucose transport, glucose metabolism, calcium dynamics, and protein folding were derived from the previous models of Luni et al. [245], Fridlyand et al. [241], Wacquier et al. [242], Chay et al. [225], Smolen et al. [229], and Graham [248]. In this model, new rate equations were defined to describe the processes of insulin signalling, ROS signalling, UPR signalling, and insulin transcription. The details of these are given in the following sections. The equations taken from the literature are cited and the equations without any citations have been developed in this work. The resulting system consists of 31 differential equations given in Table 5.1, and 9 constraints summarized in Table 5.2.

TABLE 5.1: The system of differential equations used in the model.

Differential equations	**Reference**
$\frac{d[Gluc]_{\text{e.c.}}}{dt} = 0$	[245]
$\frac{d[Gluc]_{\text{i.c.}}}{dt} = J_{\text{G1I}} - J_{\text{G1E}} - J_{\text{GK}}$	[245]
$\frac{d[Pyr]}{dt} = J_{\text{GK}} - J_{\text{PDH}}$	[241]
$\frac{d[NADH]}{dt} = J_{\text{PDH}} - J_{\text{O}}$	[242]
$\frac{d[ATP]_{\text{M}}}{dt} = J_{\text{FIFO}} - J_{\text{ANT}}$	[242]
$\frac{d[ATP]_{\text{C}}}{dt} = J_{\text{GK}} + \frac{V_{\text{M}}}{V_{\text{C}}} \times J_{\text{ANT}} - J_{\text{HYD}}$	[242]
$\frac{dV_{\text{p}}}{dt} = \frac{-(I_{\text{Ca}}+I_{\text{K}}+I_{\text{K-ATP}})}{C_{\text{cm}}}$	[229, 230]
$\frac{dP_{\text{C}}}{dt} = -\alpha \times P_{\text{C}} + \beta \times P_{\text{O}}$	[229, 230]
$\frac{dP_{\text{O}}}{dt} = k_{\text{neg}} \times (1 - P_{\text{O}} - P_{\text{C}}) - k_{\text{star}} \times g_{\text{hk}} \times P_{\text{O}} + \alpha \times P_{\text{C}} - \beta \times P_{\text{O}}$	[229, 230]
$\frac{dJ}{dt} = \frac{J_{\text{inf}}-J}{\tau_{\text{j}}}$	[229, 230]
$\frac{dn}{dt} = \frac{n_{\text{inf}}-n}{\tau_{\text{n}}}$	[229, 230]
$\frac{d\Psi_{\text{M}}}{dt} = \frac{a_1 \times J_{\text{O}} - \text{J}_{\text{FIFO}} - \text{J}_{\text{ANT}} - \text{J}_{\text{NCX}} - 2 \times \text{J}_{\text{MCU}}}{C_{\text{p}}}$	[242]
$\frac{d\left[Ca^{2+}\right]_{\text{C}}}{dt} = f_{\text{C}} \times \left(J_{\text{PM}} + \frac{V_{\text{ER}}}{V_{\text{C}}} \times J_{\text{IP3R}} - \frac{V_{\text{ER}}}{V_{\text{C}}} \times J_{\text{SERCA}} - \frac{V_{\text{M}}}{V_{\text{C}}} \times J_{\text{MCU}} + \frac{V_{\text{M}}}{V_{\text{C}}} \times J_{\text{NCX}}\right)$	[242]
$\frac{d\left[Ca^{2+}\right]_{\text{M}}}{dt} = f_{\text{M}} \times (J_{\text{MCU}} - J_{\text{NCX}})$	[242]
$\frac{d\left[Ca^{2+}\right]_{\text{ER}}}{dt} = f_{\text{ER}} \times (J_{\text{SERCA}} - J_{\text{IP3R}})$	[242]

Table 5.1 (continued): The system of differential equations used in the model.

$\frac{dR_{\mathrm{i}}}{dt} = k_{\mathrm{pos}} \times [Ca^{2+}]_{\mathrm{C}}^{\mathrm{ni}} \times \frac{(1-R_{\mathrm{i}})}{1+\left(\frac{[Ca^{2+}]_{\mathrm{C}}}{K_{\mathrm{a}}}\right)^{\mathrm{na}}} - k_{\mathrm{neg}} \times R_{\mathrm{i}}$	[242]
$\frac{d\left[Ca^{2+}\right]_{\mathrm{e.c.}}}{dt} = -V_{\mathrm{C}} \times J_{\mathrm{PM}}$	this work
$\frac{d[AKT]}{dt} = -v_{\mathrm{AKT-insulin}} + v_{\mathrm{AKTp}} + v_{\mathrm{AKT-JNK}}$	this work
$\frac{d[GSK3]}{dt} = -v_{\mathrm{GSK3-AKT}} + v_{\mathrm{GSK3p}}$	this work
$\frac{d[JNK]}{dt} = v_{\mathrm{JNKp}} - v_{\mathrm{JNK-ROS}} - v_{\mathrm{JNK-UPR}}$	this work
$\frac{d[p38MAPK]_C}{dt} = v_{\mathrm{p38p}} - v_{\mathrm{p38-ROS}} - v_{\mathrm{p38-UPR}}$	this work
$\frac{d[FOXO1]}{dt} = -v_{\mathrm{FOXO1C-AKT}} + v_{\mathrm{FOXO1C-MAPK}}$	this work
$\frac{d[PDX1]}{dt} = v_{\mathrm{PDX1-prod}} - v_{\mathrm{PDX1-efflux-FOXO1}} - v_{\mathrm{PDX1-pdeg-GSK3}}$	this work
$\frac{d[MAFA]}{dt} = v_{\mathrm{MAFA-prod}} - v_{\mathrm{MAFA-efflux-ROS}} - v_{\mathrm{MAFA-pdeg-GSK3}}$	this work
$\frac{d[INS_{\mathrm{mRNA}}]}{dt} = v_{\mathrm{INS-prod}} - v_{\mathrm{INS-deg}} - v_{\mathrm{proinsulin-prod}}$	this work
$\frac{d[INS_{\mathrm{UF}}]}{dt} = v_{\mathrm{proinsulin-prod}} - v_{\mathrm{folding-deg-chap}}$	[248]
$\frac{d[CP]}{dt} = v_{\mathrm{chap-act}} - v_{\mathrm{chap-deg}}$	[248]
$\frac{d[Ins]_{\mathrm{i.c.}}}{dt} = v_{\mathrm{insulin-folding}} - v_{\mathrm{insulin-secretion}}$	[248]
$\frac{dR_{\mathrm{s}}}{dt} = v_{\mathrm{superoxide-prod}} - v_{\mathrm{superoxide-to-H2O2}}$	[248]
$\frac{dR_{\mathrm{h}}}{dt} = v_{\mathrm{superoxide-to-H2O2}} + v_{\mathrm{H2O2-prod-ER}} - v_{\mathrm{H2O2-clearance}}$	[248] and this work ($v_{\mathrm{H2O2-prod-ER}}$)
$\frac{d[Ins]_{\mathrm{e.c.}}}{dt} = v_{\mathrm{insulin-secretion}} - v_{\mathrm{insulin-clearance}}$	this work

TABLE 5.2: Constraints used in the model.

Constraints	**Reference**
$[NADH] + [NAD^+] = 250\mu M$	[242]
$[ATP]_M + [ADP]_M = 15000\mu M$	[242]
$[ATP]_C + [ADP]_C = 2500\mu M$	[242]
$\frac{1}{V_C} \times [Ca^{2+}]_{e.c.} + \frac{[Ca^{2+}]_C}{f_C} + \frac{V_M}{V_C} \times \frac{[Ca^{2+}]_M}{f_M}$ $+\frac{V_{ER}}{V_C} \times \frac{[Ca^{2+}]_{ER}}{f_{ER}} = Tot_{Ca}$	[242] and this work ($\frac{1}{V_C} \times [Ca^{2+}]_{EC}$)
$[AKT] + [AKT_p] = Tot_{AKT}$	this work
$[GSK3] + [GSK3_p] = Tot_{GSK3}$	this work
$[JNK] + [JNK_p] = Tot_{JNK}$	this work
$[p38MAPK] + [p38MAPK_p] = Tot_{p38MAPK}$	this work
$[FOXO1] + [FOXO1_p] = Tot_{FOXO1}$	this work

5.2.1.1 Rate equations for glucose transport

Glucose is transported into beta-cell by facilitated diffusion through plasma membrane-resident glucose transporter, GLUT1. This glucose uptake through GLUT1 is modelled using Michaelis-Menten equations from Luni et al. [245].

Influx of extra-cellular glucose ($[Gluc]_{e.c.}$) through GLUT1 [245]:

$$J_{G1I} = \frac{V_{mG1}\,[Gluc]_{e.c.}}{K_{mG1} + [Gluc]_{e.c.}}.$$

Efflux of intra-cellular glucose ($[Gluc]_{i.c.}$) through GLUT1 [245]:

$$J_{G1E} = \frac{V_{mG1}\,[Gluc]_{i.c.}}{K_{mG1} + [Gluc]_{i.c.}}.$$

where, V_{mG1} is the maximum reaction rate for GLUT1 that is observed at saturating glucose concentrations, and K_{mG1} is the glucose concentration at which the reaction rate is half of V_{mG1}.

5.2.1.2 Rate equations for glucose metabolism

Glucose is metabolized to produce energy in the form of adenosine triphosphate (ATP). Glucose metabolism consists of three main processes: glycolysis, TCA cycle and ETC [249].

Glycolysis is modelled by the activity of glucokinase which is described by the rate equation [241]:

$$J_{\mathrm{GK}} = V_{\mathrm{mGK}} \left(\frac{Gluc_{\mathrm{i.c.}}^{\mathrm{nGK}}}{K_{\mathrm{GK}}^{\mathrm{nGK}} + Gluc_{\mathrm{i.c.}}^{\mathrm{nGK}}} \right) \left(\frac{[ATP]_{\mathrm{C}}}{K_{\mathrm{mATP}} + [ATP]_{\mathrm{C}}} \right),$$

where, $[ATP]_{\mathrm{C}}$ denotes the concentration of cytosolic ATP, V_{mGK} is the maximum rate of glucose consumption, K_{mATP} is the Michaelis-Menten constant, K_{GK} is the glucose concentration at which the reaction rate is half of V_{mGK}, and n_{GK} is the Hill coefficient.

Pyruvate is the main end-product of glycolysis and it enters the mitochondria for supply to the TCA cycle [249]. The TCA cycle generates reducing equivalent, NADH, which is transferred to the ETC for ATP synthesis [249]. TCA cycle is modelled by the activity of pyruvate dehydrogenase (PDH) which is described by the rate equation [241, 242]:

$$J_{\mathrm{PDH}} = V_{\mathrm{mPDH}} \left(\frac{[Pyr]}{K_{\mathrm{mPyr}} + [Pyr]} \right) \left(\frac{1}{q_1 + [NADH]\,/\,[NAD]} \right) \left(\frac{[Ca^{2+}]_{\mathrm{M}}}{q_2 + [Ca^{2+}]_{\mathrm{M}}} \right),$$

where, $[Pyr]$ denotes the concentration of pyruvate, $[Ca^{2+}]_{\mathrm{M}}$ denotes the concentration of mitochondrial calcium, V_{mPDH} is the maximum rate of PDH reaction, K_{mPyr} is the Michaelis-Menten constant, q_1 is the Michaelis-Menten-like constant for NAD^+ consumption by the TCA cycle, and q_2 is the $S_{0.5}$ value for activation of the TCA cycle by $[Ca^{2+}]_{\mathrm{M}}$. The TCA cycle reduces NAD^+ into NADH, hence the dependency on the adenine nicotinamide ratio. The calcium-dependent factor reflects the activation of both the PDH and the TCA cycle by Ca^{2+}.

NADH is then oxidized in the ETC to extrude protons from mitochondria. The flux, J_{O} [242], thus represents both the rate at which NADH is oxidized and the rate at which H^+ are extruded. The exponential factor takes into account the change of this flux with variation in the proton concentration gradient. That is,

protons extrusion leads to an increase in the mitochondrial membrane potential (Ψ_{M}). This flux is defined as

$$J_{\mathrm{O}} = V_{\mathrm{O}} \left(\frac{[NADH]}{q_3 + [NADH]} \right) \left(1 + e^{\frac{\Psi_{\mathrm{M}} - q_4}{q_5}} \right)^{-1},$$

where, $[NADH]$ denotes the concentration of mitochondrial NADH, V_{O} is the maximum rate of NADH oxidation by ETC, q_3 is the Michaelis-Menten constant for NADH consumption by the ETC, q_4 is the voltage dependence coefficient 1 of ETC activity, and q_5 is the voltage dependence coefficient 2 of ETC activity.

The rate of ATP synthesis by the mitochondrial $\mathrm{F_1F_0}$ATPase is described by the rate equation [242, 250]

$$J_{\mathrm{FIFO}} = V_{\mathrm{FIFO}} \left(\frac{q_6}{q_6 + [ATP]_{\mathrm{M}}} \right) \left(1 + e^{\frac{q_7 - \Psi_{\mathrm{M}}}{q_8}} \right)^{-1},$$

where, $[ATP]_{\mathrm{M}}$ denotes the concentration of mitochondrial ATP, V_{FIFO} is the maximum rate of $\mathrm{F_1F_0}$ATPase, q_6 is the inhibition constant of ATPase activity by ATP, q_7 is the voltage dependence coefficient 1 of ATPase activity, and q_8 is the voltage dependence coefficient 2 of ATPase activity. ATP synthesis is driven by the proton flux from the cytosol into the mitochondria, which depolarizes the mitochondrial membrane. Thus, J_{FIFO} has a steep sigmoidal dependency on mitochondrial membrane potential (Ψ_{M}).

The exchange flux of $[ADP]_{\mathrm{C}}$ and $[ATP]_{\mathrm{M}}$ across mitochondrial membrane through adenine nucleotide translocator (ANT) is defined as [242]

$$J_{\mathrm{ANT}} = V_{\mathrm{ANT}} \left(\frac{1 - \frac{\alpha_{\mathrm{C}}}{\alpha_{\mathrm{M}}} \frac{[ATP]_{\mathrm{C}}}{[ADP]_{\mathrm{C}}} \frac{[ADP]_{\mathrm{M}}}{[ATP]_{\mathrm{M}}} e^{-F' \Psi_{\mathrm{M}}}}{\left(1 + \alpha_{\mathrm{C}} \frac{[ATP]_{\mathrm{C}}}{[ADP]_{\mathrm{C}}} e^{-0.5 \times F' \Psi_{\mathrm{M}}} \right) \left(1 + \frac{1}{\alpha_{\mathrm{M}}} \frac{[ADP]_{\mathrm{M}}}{[ATP]_{\mathrm{M}}} \right)} \right),$$

where, $[ADP]_{\mathrm{C}}$ and $[ADP]_{\mathrm{M}}$ denote the concentrations of cytosolic and mitochondrial ADP respectively, V_{ANT} is the maximum rate of the ANT, α_{C} and α_{M} are factors taking cytosolic ADP and ATP buffering, and mitochondrial ADP and ATP buffering respectively into account, and $F' = \frac{F}{R \times T}$, where F is the Faraday constant, R is the perfect gas constant and T is the temperature.

The rate equation for ATP hydrolysis is given by

$$J_{\mathrm{HYD}} = \frac{J_{\mathrm{SERCA}}}{2} + k_{\mathrm{HYD}} \times [ATP]_{\mathrm{C}}\,,$$

where, k_{HYD} is the maximum rate of ATP hydrolysis. The first term of the equation taken from [242] denotes the hydrolysis of ATP required to provide energy to the ER SERCA pumps to transport Ca^{2+} into the ER. J_{SERCA} is the flux of Ca^{2+} from cytosol into ER through SERCA and is described in the section 5.2.1.4. The second term represents all other ATP-consuming processes in the cytosol.

5.2.1.3 Rate equations for electrical activity

When stimulated with glucose, beta-cells exhibit repetitive, bursting electrical activity. These oscillations in the beta-cell are caused by voltage-gated K^+ channels, voltage-gated calcium channels, K-ATP channels modulated by cytoplasmic ATP/ADP ratio, and glucose-dependent cytoplasmic changes of intracellular calcium concentration.

The conductance, g_{K}, and current, I_{K}, through the voltage-gated K^+ channels is described as [229, 230]

$$\begin{aligned} g_{\mathrm{K}} &= \overline{g_{\mathrm{K}}} \times n^4, \\ I_{\mathrm{K}} &= g_{\mathrm{K}} \times (V_{\mathrm{K}} - V_{\mathrm{p}})\,, \end{aligned}$$

where, $\overline{g_{\mathrm{K}}}$ is the maximum conductance per cell and n is the fraction of activated K^+ channel. The conductance, g_{Ca}, and current, I_{Ca}, through the voltage-gated calcium channels is described as [229, 230]

$$\begin{aligned} g_{\mathrm{Ca}} &= \overline{g_{\mathrm{Ca}}} \times (P_{\mathrm{O}} \times X_{\mathrm{f}} + m_{\mathrm{infs}} \times J \times (1 - X_{\mathrm{f}}))\,, \\ I_{\mathrm{Ca}} &= g_{\mathrm{Ca}} \times g_{\mathrm{hk}}, \end{aligned}$$

where, $g_{\mathrm{hk}} = [Ca^{2+}]_{\mathrm{e.c.}} \times \frac{V_{\mathrm{p}}}{1 - e^{V_{\mathrm{p}}/RT\_2F}}$.

In the above equations, $\overline{g_{\mathrm{Ca}}}$ is the maximum conductance per cell and X_{f} is a fraction of the maximum conductance. P_{O} denotes the fraction of open fast channels

and is defined as [229, 230]

$$\frac{dP_{\mathrm{O}}}{dt} = k_{\mathrm{neg}} \times (1 - P_{\mathrm{O}} - P_{\mathrm{C}}) - k_{\mathrm{star}} \times g_{\mathrm{hk}} \times P_{\mathrm{O}} + \alpha \times P_{\mathrm{C}} - \beta \times P_{\mathrm{O}},$$

where, P_{C} is the fraction of closed fast channels defined as [229, 230]

$$\frac{dP_{\mathrm{C}}}{dt} = -\alpha \times P_{\mathrm{C}} + \beta \times P_{\mathrm{O}},$$

where, $\alpha = \frac{m_{\mathrm{inff}}}{\tau_{\mathrm{m}}}$ and $\beta = \frac{1-m_{\mathrm{inff}}}{\tau_{\mathrm{m}}}$. m_{inff} denotes the voltage-dependent activation of the fast channels and is defined as [229, 230]

$$m_{\mathrm{inff}} = \frac{1}{1 + e^{(V_{\mathrm{mf}} - V_{\mathrm{p}})/S_{\mathrm{mf}}}}.$$

J is the fraction of activated slow channels defined as [229, 230]

$$\frac{dJ}{dt} = \frac{J_{\mathrm{inf}} - J}{\tau_{\mathrm{j}}},$$

where, J_{inf} is the steady-state value of J and is determined by the following equation [229, 230]

$$J_{\mathrm{inf}} = \frac{1}{1 + \mathrm{e}^{(\mathrm{V_P} - \mathrm{V_J})/\mathrm{S_J}}}.$$

m_{infs} denotes the voltage-dependent activation of the slow channels and is defined as [229, 230]

$$m_{\mathrm{infs}} = \frac{1}{1 + e^{(V_{\mathrm{ms}} - V_{\mathrm{p}})/S_{\mathrm{ms}}}}.$$

ATP produced from glucose metabolism in the mitochondria is released into the cytosol which increases the ATP/ADP ratio and closes the $\mathrm{K_{ATP}}$-channel on the plasma membrane causing depolarization [249]. This facilitates the entry of Ca^{2+} into the cytosol [249]. The conductance, $g_{\mathrm{K-ATP}}$, and current, $I_{\mathrm{K-ATP}}$, through the K-ATP channels modulated by cytosolic ATP/ADP ratio is described as [229]

$$g_{\mathrm{K-ATP}} = \overline{g_{\mathrm{K-ATP}}} \times \frac{1 + \frac{[ADP]_{\mathrm{C}}}{K_{\mathrm{ADP-bind}}}}{1 + \frac{[ADP]_{\mathrm{C}}}{K_{\mathrm{ADP-bind}}} + \frac{[ATP]_{\mathrm{C}}}{K_{\mathrm{ATP-bind}}}},$$

$$I_{\mathrm{K-ATP}} = g_{\mathrm{K-ATP}} \times (V_{\mathrm{K}} - V_{\mathrm{p}}),$$

where, $\overline{g_{\mathrm{K-ATP}}}$ is the maximum conductance per cell, $K_{\mathrm{ADP-bind}}$ is the ADP binding constant, and $K_{\mathrm{ATP-bind}}$ is the ATP binding constant.

5.2.1.4 Calcium dynamics

The cytosolic Ca^{2+} concentration regulates a vast number of processes, including metabolism, transcription, and secretion. The cytosolic Ca^{2+} concentration is maintained by the bi-directional movement of Ca^{2+} between cytosol and extracellular, mitochondria and ER.

Calcium handling by mitochondria

Mitochondrial Ca^{2+} is important for stimulation of Ca^{2+}-dependent dehydrogenases of the TCA cycle such as pyruvate dehydrogenase and hence increases ATP production. The flux of Ca^{2+} from cytosol into mitochondria mediated by the mitochondrial Ca^{2+} uniporter (MCU) is defined as [242]

$$J_{\mathrm{MCU}} = V_{\mathrm{MCU}} \times \left(\frac{[Ca^{2+}]_{\mathrm{C}}^2}{K_{\mathrm{MCU}}^2 + [Ca^{2+}]_{\mathrm{C}}^2} \right) e^{p_1 \times \Psi_{\mathrm{M}}},$$

where, V_{MCU} is the maximum Ca^{2+} flux through MCU, K_{MCU} is the half-maximal activation constant for MCU, and p_1 is the voltage dependence coefficient of MCU activity. This flux is cooperatively stimulated by cytosolic Ca^{2+} through the MICU1 subunit and increases exponentially with the potential difference across the mitochondrial membrane.

The flux of Ca^{2+} from mitochondria to cytosol through the mitochondrial Na^+/Ca^{2+} exchanger (NCX) is defined as [242]

$$J_{\mathrm{NCX}} = V_{\mathrm{NCX}} \times \left(\frac{[Ca^{2+}]_{\mathrm{M}}}{[Ca^{2+}]_{\mathrm{C}}} \right) e^{p_2 \times \Psi_{\mathrm{M}}},$$

where, V_{NCX} is the maximum Ca^{2+} flux through NCX and p_2 is the voltage dependence coefficient of NCX activity. This channel exchanges 1 Ca^{2+} for 3 Na^+. It is assumed that the cytosolic Na^+ concentration remains constant and that channel activity is favoured by a large ratio of Ca^{2+} concentrations between the cytosol and mitochondria.

Calcium handling by ER

The flux of Ca^{2+} from cytosol into ER through the unidirectional sarco/endoplasmic reticulum Ca^{2+} ATPase (SERCA) is defined as [242]

$$J_{\text{SERCA}} = V_{\text{SERCA}} \times \left(\frac{[Ca^{2+}]_{\text{C}}^2}{K_{\text{p}}^2 + [Ca^{2+}]_{\text{C}}^2} \right) \left(\frac{[ATP]_{\text{C}}}{K_{\text{e}} + [ATP]_{\text{C}}} \right),$$

where, V_{SERCA} is the maximum Ca^{2+} flux through SERCA, K_{p} is the dissociation constant of Ca^{2+} from SERCA, and K_{e} is the dissociation constant of ATP from SERCA. The SERCA transports Ca^{2+} from the cytosol into the ER, against the concentration gradient, using the energy provided by the hydrolysis of ATP.

The flux of Ca^{2+} from ER to cytosol through inositol trisphosphate receptor (IP3R) is defined as [242]

$$J_{\text{IP3R}} = V_{\text{IP3R}} \times IR_{\text{a}} \times \left(\left[Ca^{2+}\right]_{\text{ER}} - \left[Ca^{2+}\right]_{\text{C}} \right),$$

where, $[Ca^{2+}]_{\text{ER}}$ denotes the concentration of calcium in the ER, V_{IP3R} is the maximum Ca^{2+} flux through IP3R, and IR_{a} is the fraction of active (open) IP3 receptors given by

$$IR_{\text{a}} = 0.5 \times (1 - R_i) \times \frac{IP3^3}{K_{\text{IP3}}^3 + IP3^3},$$

where, R_{i} is the fraction of inactive receptors which changes with Ca^{2+} as [242]

$$\frac{dR_{\text{i}}}{dt} = k_{\text{pos}} \times \left[Ca^{2+}\right]_{\text{C}}^{\text{ni}} \times \frac{(1 - R_{\text{i}})}{1 + \left(\frac{[Ca^{2+}]_{\text{C}}}{K_{\text{a}}} \right)^{\text{na}}} - k_{\text{neg}} \times R_{\text{i}}.$$

The Ca^{2+} flux across the plasma membrane, where Ca^{2+} enters the cytosol through the voltage-gated calcium channels (VGCC) and is removed from the cytosol through the plasma membrane Ca^{2+}-ATPase (PMCA) is defined as [225, 229]

$$J_{\text{PM}} = -\gamma \times I_{\text{Ca}} - k_{\text{PMCa}} \times \left[Ca^{2+}\right]_{\text{C}},$$

where, γ converts fA to $\mu\text{M.s}^{-1}$, and k_{PMCa} is the rate constant for the removal of $[\text{Ca}^{2+}]_{\text{C}}$ through PMCA.

5.2.1.5 Insulin signalling pathway, stress-activated kinases, and transcription factors

The transcription factors, PDX1 and MAFA, are important transcription factors for insulin gene transcription [251, 252]. In normal conditions, MAFA is localized in the nucleus and PDX1 is shuttled between the cytoplasm and nucleus [251, 252]. However, prolonged hyperglycemia impairs insulin gene expression by diminishing the expression and binding activity of PDX1 and MAFA to the insulin gene promoter [252]. The signalling pathways mediating inhibition of insulin gene expression by oxidative stress and ER stress appear to involve, at least in part, the stress-activated kinases, JNK and p38MAPK [252].

Glucose stimulates insulin secretion which results in the autocrine stimulation of the insulin receptors in the beta-cell and the insulin signalling pathway is activated. This activates AKT which phosphorylates FOXO1 and keeps it in the cytosol [253, 254]. If FOXO1 translocates to the nucleus it exerts its repressive action on PDX1 by two ways: downregulating PDX1 transcription, and causing nuclear expulsion of PDX1 [255–257]. AKT also inhibits GSK3 [258] which phosphorylates PDX1 and MAFA and causes their proteasomal degradation [259–261]. Nuclear translocation of FOXO1 increases transcription of MAFA [262]. Thus, FOXO1 has opposing effects on the two transcription factors responsible for insulin transcription.

Oxidative stress and ER stress activate the downstream proteins JNK and p38MAPK [263, 264] which are responsible for downregulating insulin gene expression. JNK causes serine phosphorylation of the insulin signalling protein, IRS1, which inhibits its ability to phosphorylate AKT [265]. As a result, AKT cannot have its inhibitory actions on FOXO1 and GSK3. JNK and p38MAPK also directly phosphorylate FOXO1 and increase its nuclear translocation [257]. Oxidative stress causes translocation of MAFA from the nucleus to the cytoplasm through covalent dimer formation by the C-terminal cysteines [266]. Thus, in the presence of prolonged hyperglycemia, oxidative stress and ER stress mediate the nuclear expulsion and degradation of the insulin gene transcription factors, PDX1 and MAFA, mainly through the stress-activated kinases, JNK and p38MAPK, and hence inhibit insulin gene expression.

Since AKT is responsible for controlling the activation of the important repressors of the insulin transcription factors, and the aim is to reduce the number of complex

terms in the model and only consider the important proteins, the direct effect of insulin on AKT is considered without considering the intermediate proteins.

All the regulating actions among the proteins described in the previous paragraphs are modelled using simple mass action kinetics. AKT is phosphorylated and activated by insulin and inhibited by JNK. The rate equations for the phosphorylation of AKT by insulin, $v_{\mathrm{AKT-insulin}}$, and dephosphorylation of AKT, v_{AKTp}, are given by

$$v_{\mathrm{AKT-insulin}} = k_{\mathrm{AKT}} \times [AKT] \times \frac{[Ins]_{\mathrm{e.c.}}}{[Ins]_{\mathrm{e.c.t=0}}},$$
$$v_{\mathrm{AKTp}} = k_{\mathrm{AKTp}} \times [AKT_{\mathrm{p}}],$$

where, $[AKT]$ and $[AKT_{\mathrm{p}}]$ denote the concentrations of unphosphorylated and phosphorylated AKT respectively, $[Ins]_{\mathrm{e.c.}}$ denotes the concentration of extracellular insulin, k_{AKT} is the phosphorylation rate of AKT by insulin and k_{AKTp} is the dephosphorylation rate of AKT. The rate equation for the inactivation of AKT by JNK is defined as

$$v_{\mathrm{AKT-JNK}} = k_{\mathrm{AKT-JNK}} \times [AKT_{\mathrm{p}}] \times [JNK_{\mathrm{p}}],$$

where, $[JNK_{\mathrm{p}}]$ denotes the concentration of phosphorylated JNK, $k_{\mathrm{AKT-JNK}}$ is the rate of inactivation of AKT by JNK.

AKT phosphorylates GSK3 and keeps it inactive. The rate equations for the phosphorylation of GSK3 by AKT, $v_{\mathrm{GSK3-AKT}}$, and dephosphorylation of GSK3, v_{GSK3p}, are given by

$$v_{\mathrm{GSK3-AKT}} = k_{\mathrm{GSK3}} \times [GSK3] \times [AKT_{\mathrm{p}}],$$
$$v_{\mathrm{GSK3p}} = k_{\mathrm{GSK3p}} \times [GSK3_{\mathrm{p}}],$$

where, $[GSK3]$ and $[GSK3_{\mathrm{p}}]$ denote the concentrations of unphosphorylated and phosphorylated GSK3 respectively, k_{GSK3} is the phosphorylation rate of GSK3 by AKT and k_{GSK3p} is the dephosphorylation rate of GSK3.

The stress-activated kinases, JNK and p38MAPK, are activated by ROS ($[R_{\mathrm{h}}]$) and UPR (U_{PR}). The rates of phosphorylation of JNK by ROS, $v_{\mathrm{JNK-ROS}}$, and UPR,

$v_{\mathrm{JNK-UPR}}$, and dephosphorylation of JNK, v_{JNKp}, are given by

$$v_{\mathrm{JNK-ROS}} = k_{\mathrm{JNK-ROS}} \times [JNK] \times \frac{[R_{\mathrm{h}}]}{[R_{\mathrm{h}}]_{t=0}},$$
$$v_{\mathrm{JNK-UPR}} = k_{\mathrm{JNK-UPR}} \times [JNK] \times v_{\mathrm{UPR}},$$
$$v_{\mathrm{JNKp}} = k_{\mathrm{MAPKp}} \times [JNK_{\mathrm{p}}],$$

where, $[JNK]$ denotes the concentration of unphosphorylated JNK, $k_{\mathrm{JNK-ROS}}$ is the phosphorylation rate of JNK by ROS (H_2O_2), $k_{\mathrm{JNK-UPR}}$ is the phosphorylation rate of JNK by UPR, and k_{MAPKp} is the dephosphorylation rate of JNK.

The rates of phosphorylation of p38MAPK by ROS, $v_{\mathrm{p38-ROS}}$, and UPR, $v_{\mathrm{p38-UPR}}$, and dephosphorylation of p38MAPK, v_{p38p}, are given by

$$v_{\mathrm{p38-ROS}} = k_{\mathrm{p38-ROS}} \times [p38MAPK] \times \frac{[R_{\mathrm{h}}]}{[R_{\mathrm{h}}]_{t=0}},$$
$$v_{\mathrm{p38-UPR}} = k_{\mathrm{p38-UPR}} \times [p38MAPK] \times v_{\mathrm{UPR}},$$
$$v_{\mathrm{p38p}} = k_{\mathrm{MAPKp}} \times [p38MAPK_{\mathrm{p}}],$$

where, where $[p38MAPK]$ and $[p38MAPK_{\mathrm{p}}]$ denote the concentrations of unphosphorylated and phosphorylated p38MAPK respectively, $k_{\mathrm{p38-ROS}}$ is the phosphorylation rate of p38MAPK by ROS (H_2O_2), $k_{\mathrm{p38-UPR}}$ is the phosphorylation rate of p38MAPK by UPR, and k_{MAPKp} is the dephosphorylation rate of p38MAPK.

AKT phosphorylates FOXO1 and keeps it in the cytosol. JNK and p38MAPK phosphorylate FOXO1 and facilitate its nuclear translocation. The rate of phosphorylation of FOXO1 by AKT, $v_{\mathrm{FOXO1-AKT}}$, is given by

$$v_{\mathrm{FOXO1-AKT}} = k_{\mathrm{FOXO1-AKTp}} \times [FOXO1] \times [AKT_{\mathrm{p}}],$$

where, $[FOXO1]$ denotes the concentration of unphosphorylated FOXO1, and k_{FOXO1} is the phosphorylation rate of FOXO1 by AKT. The rate of phosphorylation of FOXO1 by JNK and p38MAPK, $v_{\mathrm{FOXO1-MAPK}}$, is given by

$$v_{\mathrm{FOXO1-MAPK}} = k_{\mathrm{FOXO1p-MAPKp}} \times [FOXO1_{\mathrm{p}}] \times ([JNK_{\mathrm{p}}] + [p38MAPK_{\mathrm{p}}]),$$

where, $[FOXO1_{\mathrm{p}}]$ denotes the concentration of phosphorylated FOXO1, $k_{\mathrm{FOXO1p-MAPKp}}$ is the phosphorylation rate of FOXO1 by JNK and p38MAPK.

PDX1 production is increased by transcription factor MAFA and decreased by transcription factor FOXO1. FOXO1 also causes nuclear exclusion of PDX1. GSK3 causes proteasomal degradation of PDX1. The rate of production of PDX1 due to the binding of the activator transcription factor, MAFA, and repressor transcription factor, FOXO1, is given by

$$v_{\mathrm{PDX1-prod}} = V_{\mathrm{mPDX1}} \times \frac{[MAFA]}{K_{\mathrm{MAFA-PDX1}} + [MAFA]} \times \frac{K_{\mathrm{FOXO1-PDX1}}}{K_{\mathrm{FOXO1-PDX1}} + [FOXO1]},$$

where, $[MAFA]$ is the concentration of MAFA, V_{mPDX1} is the maximum rate of PDX1 mRNA production, $K_{\mathrm{MAFA-PDX1}}$ is the dissociation constant of MAFA from the binding site of PDX1 promoter, and $K_{\mathrm{FOXO1-PDX1}}$ is the dissociation constant of FOXO1 from the binding site of PDX1 promoter. The rate of efflux of PDX1 from the nucleus by FOXO1 is given by

$$v_{\mathrm{PDX1-efflux-FOXO1}} = k_{\mathrm{PDX1-FOXO1-efflux}} \times [PDX1] \times [FOXO1]\,,$$

and the rate of proteasomal degradation of PDX1 by GSK3 is defined as

$$v_{\mathrm{PDX1-pdeg-GSK3}} = k_{\mathrm{GSK3-PDX1-pdeg}} \times [PDX1] \times [GSK3]\,,$$

where, $[PDX1]$ is the concentration of PDX1, $k_{\mathrm{PDX1-FOXO1-efflux}}$ is the efflux rate of PDX1 from nucleus by FOXO1 and $k_{\mathrm{GSK3-PDX1-pdeg}}$ is the rate of PDX1 protein degradation by GSK3.

MAFA production is increased by transcription factors PDX1 and FOXO1. ROS causes nuclear exclusion of MAFA and GSK3 causes proteasomal degradation of MAFA. The rate of production of MAFA due to the binding of the activator transcription factors, PDX1 and FOXO1, is defined as

$$v_{\mathrm{MAFA-prod}} = V_{\mathrm{mMAFA}} \times \frac{[PDX1]}{K_{\mathrm{PDX1-MAFA}} + [PDX1]} \times \frac{[FOXO1]}{K_{\mathrm{FOXO1-MAFA}} + [FOXO1]},$$

where, V_{mMAFA} is the maximum rate of MAFA mRNA production, $K_{\text{PDX1-MAFA}}$ is the dissociation constant of PDX1 from the binding site of MAFA promoter, and $K_{\text{FOXO1-MAFA}}$ is the dissociation constant of FOXO1 from the binding site of MAFA promoter. The rate of efflux of MAFA from the nucleus by H_2O_2 (ROS) is given by

$$v_{\text{MAFA-efflux-ROS}} = k_{\text{ROS-MAFA}} \times [MAFA] \times \frac{[R_{\text{h}}]}{[R_{\text{h}}]_{t=0}},$$

and the rate of proteasomal degradation of MAFA by GSK3 is defined as

$$v_{\text{MAFA-pdeg-GSK3}} = k_{\text{GSK3-MAFA-pdeg}} \times [MAFA] \times [GSK3]\,,$$

where, $k_{\text{ROS-MAFA}}$ is the efflux rate of MAFA from the nucleus by ROS and $k_{\text{GSK3-MAFA-pdeg}}$ is the rate of MAFA protein degradation by GSK3.

Insulin mRNA production is increased by its two major transcription factors, PDX1 and MAFA. The rate of production of insulin mRNA due to the binding of the activator transcription factors, PDX1 and MAFA, is given by

$$v_{\text{INS-prod}} = V_{\text{mINS}} \times \frac{[PDX1]}{K_{\text{PDX1-INS}} + [PDX1]} \times \frac{[MAFA]}{K_{\text{MAFA-INS}} + [MAFA]},$$

and the rate of degradation of insulin mRNA is defined as

$$v_{\text{INS-deg}} = k_{\text{dm-Ins}} \times [INS_{\text{mRNA}}]\,,$$

where, $[INS_{\text{mRNA}}]$ is the concentration of insulin mRNA, V_{mINS} is the maximum rate of insulin mRNA production, $K_{\text{PDX1-INS}}$ is the dissociation constant of PDX1 from the binding site of insulin promoter, $K_{\text{MAFA-INS}}$ is the dissociation constant of MAFA from the binding site of insulin promoter, and $k_{\text{dm-Ins}}$ is the rate of insulin mRNA degradation.

5.2.1.6 Unfolded protein response (UPR) and ER stress

In order to restore the protein folding capacity, the UPR is initiated. The UPR acts by decreasing translation, restoring protein folding, and causing ER-associated degradation (ERAD) of misfolded proteins [267]. This model considers (i) the

attenuation of protein translation by UPR, (ii) the activation of ER chaperons by UPR, and (iii) protein folding and degradation mediated by the ER chaperons.

The rate of translation of insulin mRNA to proinsulin is defined as

$$v_{\text{proinsulin-prod}} = k_{\text{tr-INS}} \times [INS_{\text{mRNA}}] \times \frac{1}{1 + v_{\text{UPR}}},$$

where, $k_{\text{tr-INS}}$ is the rate of translation of insulin mRNA and v_{UPR} represents the UPR. This equation takes into account the attenuation of the translation process by the UPR. The rate of protein folding and degradation processes mediated by the ER chaperons are described by the rate equation taken from Graham [248]:

$$v_{\text{folding-deg-chap}} = d_{\text{uu}} \times [CP] \times \frac{[INS_{\text{UF}}]}{[INS_{\text{UF}}] + K_{\text{uu}}},$$

where, $[INS_{\text{UF}}]$ denotes the concentration of proinsulin (unfolded insulin), $[CP]$ is the concentration of ER chaperons, d_{uu} is the rate of proinsulin folding/degradation and K_{uu} is the proinsulin-chaperon Michaelis-Menten constant (folding/degradation).

The rates of activation of ER chaperons by the UPR, $v_{\text{chap-act}}$, and the degradation of ER chaperons, $v_{\text{chap-deg}}$, are described as [248]:

$$\begin{aligned} v_{\text{chap-act}} &= \frac{v_{\text{UPR}}}{1 + v_{\text{UPR}}}, \\ v_{\text{chap-deg}} &= d_{\text{CP}} \times [CP], \end{aligned}$$

where, d_{CP} is the rate of chaperon decay.

The rates of folding of proinsulin molecules by ER chaperons, $v_{\text{insulin-folding}}$, insulin secretion, $v_{\text{insulin-secretion}}$, and clearance of extra-cellular insulin, $v_{\text{insulin-clearance}}$, are defined as

$$\begin{aligned} v_{\text{insulin-folding}} &= q_{\text{f}} \times v_{\text{folding-deg-chap}}, \\ v_{\text{insulin-secretion}} &= k_{\text{IS}} \times [Ins]_{\text{i.c.}} \times \frac{max\left(0, \left([Ca^{2+}]_{\text{C}} - [Ca^{2+}]_{\text{C,min}}\right)\right)}{[Ca^{2+}]_{\text{C,min}}}, \\ v_{\text{insulin-clearance}} &= k_{\text{IC}} \times [Ins]_{\text{e.c.}}, \end{aligned}$$

where, $[Ins]_{\text{i.c.}}$ is the concentration of folded insulin, q_{f} is the proinsulin folding fraction, k_{IS} is the rate of insulin secretion, $[Ca^{2+}]_{\text{C,min}}$ is the minimal Ca^{2+} concentration necessary for insulin secretion, and k_{IC} is the rate of insulin clearance. After uptake of glucose via GLUT1, the glucose is metabolized to produce ATP. The rise in ATP leads to closing of plasma membrane located ATP-sensitive K^+ (K-ATP) channels causing depolarization [249]. This facilitates the entry of Ca^{2+} into the cytosol [249] which ultimately leads to exocytosis of insulin-containing granules. Thus, Ca^{2+} concentration has to be above a certain level to stimulate insulin secretion from beta-cells.

The UPR is activated by the accumulation of unfolded proteins and is inhibited by the ER chaperons and it is represented as [248]:

$$v_{\text{UPR}} = \frac{\frac{[INS_{\text{UF}}]}{K_1}}{1 + \frac{[INS_{\text{UF}}]}{K_1} + \frac{[CP]}{K_2\left(1+\frac{[INS_{\text{UF}}]}{K_3}\right)}},$$

where, K_1 is the PERK-proinsulin dissociation constant, K_2 is the PERK-chaperon dissociation constant, and K_3 is the proinsulin-chaperon dissociation constant (chaperon sequestration).

5.2.1.7 Reactive oxygen species (ROS)

The mitochondrial ETC [268, 269], and the ER protein-folding machinery [270] are two major sources of ROS. Under physiological conditions, 0.2-2% of the electrons in the ETC do not follow the normal transfer order but instead directly leak out of the ETC and interact with oxygen to produce superoxide [271, 272]. The superoxide undergoes dismutation by the superoxide dismutase, MnSOD, to form hydrogen peroxide (H_2O_2) [271, 272].

Superoxide (R_{s}) is generated by mitochondrial ETC and is converted to H_2O_2 (R_{h}) by MnSOD (A_{s}). The rate of production of superoxide is described by

$$v_{\text{superoxide-prod}} = q_{\text{r}} \times J_{\text{O}},$$

and the rate of conversion of superoxide to H_2O_2 by MnSOD is described by [248]:

$$v_{\text{superoxide-to-H2O2}} = k_{rs} \times R_s \times A_s,$$

where, q_{r} is the fractional superoxide production and k_{rs} is the superoxide dismutation rate. The rate of clearance of H_2O_2 by catalase (A_{h}) is defined as [248]:

$$v_{\text{H2O2-clearance}} = \delta_{\text{rh}} \times R_{\text{h}} \times A_{\text{h}},$$

where, δ_{rh} is the rate H_2O_2 removal by catalase.

The protein folding process also contributes to the production of H_2O_2. The proinsulin molecule contains three disulphide bonds and the formation of each disulphide bond involves the disposal via oxidative pathways of two electrons giving rise to a molecule of H_2O_2 [270]. The rate of H_2O_2 generation by ER is defined as

$$v_{\text{H2O2-prod-ER}} = 3 \times v_{\text{folding-deg-chap}}.$$

5.2.2 Parameter estimation

The unknown parameter values and initial values of state variables were estimated using the particle swarm optimization (PSO) algorithm [273]. The PSO algorithm was implemented using the PySwarms toolkit [274]. PSO is a metaheuristic algorithm that can search very large spaces of candidate solutions, called particles. The algorithm first generates an arbitrary population of particles, and then moves these particles around in the search-space according to the particles' position and velocity. Each particle's movement is influenced by its local best-known position, as well as a global best-known position in the search-space, which is updated as better positions are found by other particles. This is expected to move the swarm towards the best solution.

The PSO algorithm was selected for parameter estimation because PSO can search very large spaces of candidate solutions. This is useful for the proposed model since it contains a large number of free parameters (around 37). The PSO has a high probability of finding the global optimum and it can converge fast since the particles (denoting different candidate solutions) can be run in parallel. This is

particularly advantageous for estimating the values of the large free parameter set of the model.

In this work, the parameter estimation was done in two stages. The first stage of parameter estimation involved the processes of glucose transport, glucose metabolism, electrical activity, and calcium dynamics. This part was selected because it does not have any feedback from the rest of the model. The number of unknown parameters in this part was 8. These estimated parameters from the first stage were then used as inputs to the second stage of the parameter estimation which included the whole model. The number of unknown parameters for the second stage of estimation was 37.

The cost functions for the optimization were defined as the root mean squared error between the experimental data and the simulated data. The details of the experimental data and the corresponding cost functions for the first and second stages of optimization are given in Table 5.3 and Table 5.4 respectively. The cost functions for the first stage of the optimization process were normalized by the mean of the experimental data and the cost functions for the second stage were normalized by the range of the experimental data.

TABLE 5.3: Details of the experimental data and the corresponding cost functions used for stage 1 of the parameter estimation.

Experiment details	**Reference**	**Cost function**
Steady state values of NADH, mitochondrial membrane potential, cytosolic, mitochondrial, ER and extra-cellular calcium at sub-stimulatory glucose level of 3mM.	[275–282]	$C_{\mathrm{SS}} = \sqrt{\frac{\sum_{t=0}^{n}\left(\frac{X_{\mathrm{t}}^{\mathrm{sim}}}{X^{\mathrm{lit}}}-1\right)^2}{n+1}}$ $X_{\mathrm{t}}^{\mathrm{sim}}$: simulated value of state variable X at time step t, X^{lit}: steady state value of X obtained from the literature.
Ratio of NADH concentration at stimulatory glucose levels (8mM, 10mM, 20mM) to NADH concentration at sub-stimulatory glucose level of 3mM. Mouse pancreatic islets were used. Islet NADH responses to step glucose elevations from a baseline concentration of 3 mM to 8 mM, 10 mM and 20 mM were recorded. 15, 28 and 17 islet recordings were used respectively for the 3 cases. The data was recorded for a duration of 10 mins and the relative auto-fluorescence was recorded.	[283]	$C_{\mathrm{NADH}} = \sqrt{\frac{\sum_{t=0}^{n}\left(\frac{[NADH]_{\mathrm{t}}^{\mathrm{sim-G8}}}{[NADH]^{\mathrm{G3}}}-ratio_{\mathrm{t}}^{\mathrm{data-G8}}\right)^2}{n+1}} + \sqrt{\frac{\sum_{t=0}^{n}\left(\frac{[NADH]_{\mathrm{t}}^{\mathrm{sim-G10}}}{[NADH]^{\mathrm{G3}}}-ratio_{\mathrm{t}}^{\mathrm{data-G10}}\right)^2}{n+1}} + \sqrt{\frac{\sum_{t=0}^{n}\left(\frac{[NADH]_{\mathrm{t}}^{\mathrm{sim-G20}}}{[NADH]^{\mathrm{G3}}}-ratio_{\mathrm{t}}^{\mathrm{data-G20}}\right)^2}{n+1}}$ $[NADH]_{\mathrm{t}}^{\mathrm{sim-G8}}$, $[NADH]_{\mathrm{t}}^{\mathrm{sim-G10}}$, $[NADH]_{\mathrm{t}}^{\mathrm{sim-G20}}$: simulated concentrations of NADH at time step t in the presence of 8mM, 10mM and 20mM glucose, $[NADH]^{\mathrm{G3}}$: steady-state concentration of NADH at 3mM glucose, $ratio_{\mathrm{t}}^{\mathrm{data-G8}}$, $ratio_{\mathrm{t}}^{\mathrm{data-G10}}$, $ratio_{\mathrm{t}}^{\mathrm{data-G20}}$: ratio of NADH

Table 5.3 (continued): Details of the experimental data and the corresponding cost functions used for stage 1 of the parameter estimation.

		concentration at stimulatory glucose levels (8mM, 10mM, 20mM) to NADH concentration at sub-stimulatory glucose level of 3mM obtained from the experimental data.
Ratio of cytosolic ATP concentrations at stimulatory glucose levels of 8.3mM, 16.7mM and 25mM to cytosolic ATP concentration at sub-stimulatory glucose level of 2.8mM. Mouse pancreatic islets were used. Relative fluorescence was recorded by increasing glucose concentration from a baseline concentration of 2.8mM to 8.3mM, 16.7mM and 25mM. The duration of the recording is 100 seconds and8 islets were used.	[284]	$C_{ATPC} = \sqrt{\frac{\sum_{t=0}^{n}\left(\frac{[ATP_C]_t^{sim-G8.3}}{[ATP_C]^{G3}} - ratio_t^{data-G8.3}\right)^2}{n+1}} + \sqrt{\frac{\sum_{t=0}^{n}\left(\frac{[ATP_C]_t^{sim-G16.7}}{[ATP_C]^{G3}} - ratio_t^{data-G16.7}\right)^2}{n+1}} + \sqrt{\frac{\sum_{t=0}^{n}\left(\frac{[ATP_C]_t^{sim-G25}}{[ATP_C]^{G3}} - ratio_t^{data-G25}\right)^2}{n+1}}$ $[ATP_C]_t^{sim-G8.3}$, $[ATP_C]_t^{sim-G16.7}$, $[ATP_C]_t^{sim-G25}$: simulated concentrations of cytosolic ATP at time step t in the presence of 8.3mM, 16.7mM and 25mM glucose, $[ATP_C]^{G3}$: steady-state concentration of cytosolic ATP at 3mM glucose, $ratio_t^{data-G8.3}$, $ratio_t^{data-G16.7}$, $ratio_t^{data-G25}$: ratio of ATP concentration at stimulatory glucose levels (8mM, 10mM, 20mM) to ATP concentration at sub-stimulatory glucose level of 3mM obtained from the experimental data.

TABLE 5.4: Details of the experimental data and the corresponding cost functions used for stage 2 of the parameter estimation.

Experiment details	**Reference**	**Cost function**
Ratio of phosphorylated and unphosphorylated stress-activated kinases, JNK and p38MAPK, at 50 μM H_2O_2. Rat pancreatic islets were used. Islets were treated with H_2O_2 for 120 min. Then the phosphorylated and unphosphorylated expression levels of JNK and p38MAPK were measured using Western blot analysis. Values were presented as mean ± SEM (n = 3).	[285]	$C_{\text{MAPK}} = \sqrt{\frac{\sum_{t=0}^{n}\left(\frac{[JNK_{\text{p}}]_{\text{t}}^{\text{sim}}}{[JNK]_{\text{t}}^{\text{sim}}} - ratio_{\text{t}}^{\text{data-JNK}}\right)^2}{n+1}} + \sqrt{\frac{\sum_{t=0}^{n}\left(\frac{[p38_{\text{p}}]_{\text{t}}^{\text{sim}}}{[p38]_{\text{t}}^{\text{sim}}} - ratio_{\text{t}}^{\text{data-p38}}\right)^2}{n+1}}$ $[JNK_{\text{p}}]_{\text{t}}^{\text{sim}}$, $[p38_{\text{p}}]_{\text{t}}^{\text{sim}}$: simulated concentrations of phosphorylated JNK and p38MAPK at time step t in the presence of 50 μM H_2O_2, $[JNK]_{\text{t}}^{\text{sim}}$, $[p38]_{\text{t}}^{\text{sim}}$: simulated concentrations of un-phosphorylated JNK and p38MAPK at time step t in the presence of 50 μM H_2O_2, $ratio_{\text{t}}^{\text{data-JNK}}$, $ratio_{\text{t}}^{\text{data-p38}}$: ratio of phosphorylated and unphosphorylated JNK and p38MAPK at 50 μM H_2O_2 obtained from the experimental data.
Ratio of insulin mRNA levels at 50 μM H_2O_2 to insulin mRNA levels at basal conditions. Rat pancreatic islets were used. Islets were treated with H_2O_2 for 48h. Then insulin mRNA levels were examined by RT-PCR. Values were presented as mean ± SEM (n = 3).	[285]	$C_{\text{insulinMRNA}} = \sqrt{\frac{\sum_{t=0}^{n}\left(\frac{[Ins_{\text{m}}]_{\text{t}}^{\text{sim}}}{[Ins_{\text{m}}]_{\text{t=0}}} - ratio_{\text{t}}^{\text{data-mrna}}\right)^2}{n+1}}$ $[Ins_{\text{m}}]_{\text{t}}^{\text{sim}}$: simulated concentration of insulin mRNA at time step t in the presence of 50 μM H_2O_2, $[Ins_{\text{m}}]_{\text{t=0}}$: basal insulin mRNA concentration,

Table 5.4 (continued): Details of the experimental data and the corresponding cost functions used for stage 2 of the parameter estimation.

		$ratio_{\mathrm{t}}^{\mathrm{data-mrna}}$: ratio of insulin mRNA at time step t in the presence of 50 μM H_2O_2 and at basal state obtained from the experimental data.
Ratio of phosphorylated AKT at insulin level of 0.12 μM to phosphorylated AKT at basal insulin levels and ratio of unphosphorylated GSK3 at insulin level of 0.12 μM to unphosphorylated GSK3 at basal insulin levels. Skeletal muscle cells from 4-7 rats were used. AKT and GSK3 activity was recorded at 5, 10 and 30 min after insulin stimulation as percentages of basal activity.	[286]	$C_{\mathrm{AKTp-GSK3}} = \sqrt{\frac{\sum_{t=0}^{n}\left(\frac{[AKT_{\mathrm{p}}]_{\mathrm{t}}^{sim}}{[AKT_{\mathrm{p}}]_{\mathrm{t=0}}} - ratio_{\mathrm{t}}^{\mathrm{data-AKTp}}\right)^2}{n+1}} + \sqrt{\frac{\sum_{t=0}^{n}\left(\frac{[GSK3]_{\mathrm{t}}^{\mathrm{sim}}}{[GSK3]_{\mathrm{t=0}}} - ratio_{\mathrm{t}}^{\mathrm{data-GSK3}}\right)^2}{n+1}}$ $[AKT_{\mathrm{p}}]_{\mathrm{t}}^{sim}$, $[GSK3]_{\mathrm{t}}^{\mathrm{sim}}$: simulated concentrations of phosphorylated AKT and un-phosphorylated GSK3 at time step t in the presence of 0.12 μM insulin, $[AKT_{\mathrm{p}}]_{\mathrm{t=0}}$, $[GSK3]_{\mathrm{t=0}}$: basal concentrations of phosphorylated AKT and un-phosphorylated GSK3, $ratio_{\mathrm{t}}^{\mathrm{data-AKTp}}$, $ratio_{\mathrm{t}}^{\mathrm{data-GSK3}}$: ratio of phosphorylated AKT and un-phosphorylated GSK3 at 0.12 μM insulin obtained from the experimental data.

Table 5.4 (continued): Details of the experimental data and the corresponding cost functions used for stage 2 of the parameter estimation.

Ratio of phosphorylated and un-phosphorylated AKT at 5.5mM glucose. Human islets isolated from 19 organ donors were used. Islets were treated with 5.5 mM glucose and the levels of AKT phosphorylation was measured for 24 h using densitometric analysis.	[287]	$C_{\mathrm{AKTp-AKT}} = \sqrt{\frac{\sum_{t=0}^{n}\left(\frac{[AKT_{\mathrm{p}}]_{\mathrm{t}}^{\mathrm{sim}}}{[AKT]_{\mathrm{t}}^{\mathrm{sim}}} - ratio_{\mathrm{t}}^{\mathrm{data-AKTp-AKT}}\right)^2}{n+1}}$ $[AKT_{\mathrm{p}}]_{\mathrm{t}}^{\mathrm{sim}}$, $[AKT]_{\mathrm{t}}^{\mathrm{sim}}$: simulated concentrations of phosphorylated AKT and un-phosphorylated AKT at time step t in the presence of 5.5mM glucose, $ratio_{\mathrm{t}}^{\mathrm{data-AKTp-AKT}}$: ratio of phosphorylated and un-phosphorylated AKT at 5.5mM glucose obtained from the experimental data.

TABLE 5.5: Model parameters and their values taken from the literature.

Parameter	**Description**	**Value**	**Reference**
V_{C}	Relative volume of cytosol w.r.t whole beta-cell volume	0.882	[288]
V_{N}	Relative volume of nucleus w.r.t whole beta-cell volume	0.117	[288]
V_{ER}	Relative volume of ER w.r.t whole beta-cell volume	0.195	[288]
V_{M}	Relative volume of mitochondria w.r.t whole beta-cell volume	0.039	[288]
K_{mG1}	Glucose concentration at which the reaction rate is half of V_{mG1}	3000 μM	[245]
K_{mATP}	Michaelis-Menten constant	500 μM	[289]
K_{GK}	Glucose concentration at which the reaction rate is half of V_{mGK}	7000 μM	[289]
n_{GK}	Hill coefficient	1.7	[289]
q_1	Michaelis-Menten-like constant for NAD^+ consumption by the Krebs cycle	1	[242]
q_2	$S_{0.5}$ value for activation the Krebs cycle by Ca^{2+}	0.1 μM	[242]
q_3	Michaelis-Menten constant for NADH consumption by the ETC	100 μM	[242]
q_4	Voltage dependence coefficient 1 of ETC activity	143 mV	[242]
q_5	Voltage dependence coefficient 2 of ETC activity	5 mV	[242]
V_{FIFO}	Rate constant of the F1FO-ATPase	35000 μM.s^{-1}	[242]
q_6	Inhibition constant of ATPase activity by ATP	10000 μM	[242]
q_7	Voltage dependence coefficient of ATPase activity	150 mV	[242]
q_8	Voltage dependence coefficient of ATPase activity	8.5 mV	[242]
V_{ANT}	Rate constant of the adenine nucleotide translocator	5000 μM.s^{-1}	[242]
α_{C}	Factor taking cytosolic ADP and ATP buffering into account	0.111	[242]

Table 5.5 (continued): Model parameters and their values taken from the literature.

α_{M}	Factor taking mitochondrial ADP and ATP buffering into account	0.139	[242]
F'	F/RT; F: Faraday constant (96480 C.mol^{-1}), R: Perfect gas constant (8315 mJ.mol^{-1}.K^{-1}), T: Temperature (310.16 K)	0.037 mV^{-1}	[242]
V_{IP3R}	Maximum Ca^{2+} flux through IP3R	0.1986 s^{-1}	[242]
K_{IP3}	Dissociation constant of IP3 binding from its receptor	1 μM	[242]
K_{a}	Dissociation constant of Ca^{2+} from the activating site of the IP3 receptor	0.3 μM	[242]
n_{a}	Hill coefficient of Ca^{2+} binding to the activating site of the IP3 receptor	3	[242]
V_{SERCA}	Maximum Ca^{2+} flux through SERCA	120 μM.s^{-1}	[242]
K_{p}	Dissociation constant of Ca^{2+} from SERCA	0.35 μM	[242]
K_{e}	Dissociation constant of ATP from SERCA	0.05 μM	[242]
V_{MCU}	Maximum Ca^{2+} flux through MCU	0.0006 μM.s^{-1}	[242]
K_{MCU}	Half-maximal activation constant for MCU	0.9682 μM	[242]
p_1	Voltage dependence coefficient of MCU activity	0.1 mV^{-1}	[242]
V_{NCX}	Maximum Ca^{2+} flux through NCX	0.35 μM.s^{-1}	[242]
p_2	Voltage dependence coefficient of NCX activity	0.016 mV^{-1}	[242]
C_{p}	Mitochondrial inner membrane capacitance divided by F	1.8 μM.mV^{-1}	[242]
f_{C}	calcium buffering factor in cytosol	0.01	[242]
f_{M}	calcium buffering factor in mitochondria	0.0003	[242]
f_{ER}	calcium buffering factor in ER	0.01	[242]
k_{pos}	Rate constant of Ca^{2+} binding to the inhibiting site of the IP3 receptor	20 μM^{-4}.s^{-1}	[242]

Table 5.5 (continued): Model parameters and their values taken from the literature.

k_{neg}	Rate constant of Ca^{2+} dissociation from the inactivating site of the IP3 receptor	0.02 s^{-1}	[242]
n_{i}	Hill coefficient of Ca^{2+} binding to the inhibiting site of the IP3 receptor	4	[242]
C_{pm}	Cell membrane capacitance	5310 ($\mu F/cm^2$)	[225]
k_{dmINS}	Rate of insulin mRNA degradation	0.000006637 s^{-1}	[290]
$k_{\text{tr-INS}}$	Rate of translation of insulin mRNA	0.03558 s^{-1}	[248]
d_{uu}	Rate of proinsulin folding/degradation	0.067 s^{-1}	[248]
K_{uu}	Proinsulin-chaperone Michaelis-Menten constant (folding/degradation)	5.93 x 10^{-2} μM	[248]
d_{CP}	Rate of chaperone decay	1/120 min^{-1}	[248]
q_{f}	Proinsulin folding fraction	0.8	[248]
k_{IS}	Rate of insulin secretion	0.0002041 s^{-1}	[248]
k_{IC}	Rate of insulin clearance	351.115 s^{-1}	[248]
K_1	PERK-proinsulin dissociation constant	5.93 μM	[248]
K_2	PERK-chaperone dissociation constant	3.56 x 10^{-2} μM	[248]
K_3	Proinsulin-chaperone dissociation constant	1.19 μM	[248]
q_{r}	Fractional superoxide production	9.766	[248]
k_{rs}	Superoxide dismutation rate	2400 $\mu M^{-1}s^{-1}$	[248]
A_{s}	MnSOD concentration	5 μM	[248]
δ_{rh}	Rate of H_2O_2 removal by catalase	17 $\mu M^{-1}s^{-1}$	[248]
A_{h}	Catalase concentration	3 μM	[248]

TABLE 5.6: Initial values of model state variables taken from the literature.

Variable	**Description**	**Initial value**	**Reference**
$[Pyr]$	Pyruvate	9 μM	[241]
$[NADH]$	NADH	60 μM	[275]
$[ATP]_{\mathrm{C}}$	Cytosolic ATP	1400 μM	[242]
$[ATP]_{\mathrm{M}}$	Mitochondrial ATP	11250 μM	[242]
Ψ_{M}	Mitochondrial membrane potential	130 mV	[276]
$[Ca^{2+}]_{\mathrm{C}}$	Cytosolic calcium	0.1 μM	[277, 278]
$[Ca^{2+}]_{\mathrm{M}}$	Mitochondrial calcium	0.1 μM	[278, 279]
$[Ca^{2+}]_{\mathrm{ER}}$	ER calcium	200 μM	[280, 281]
$[Ca^{2+}]_{\mathrm{e.c.}}$	ER calcium	2000 μM	[282]
$\mathrm{R_i}$	Fraction of inactive IP3 receptors	0.088	[242]
V_{p}	Plasma membrane potential	-64 mV	[229]
P_{C}	Fraction of closed fast channels	1	[229]
P_{O}	Fraction of open fast channels	0	[229]
J	Fraction of activated slow channels	0.86	[229]
n	Fraction of activated K^+ channel	0	[229]
$[INS_{\mathrm{mRNA}}]$	Insulin mRNA concentration	1.3424 μM	[248]
$[INS_{\mathrm{UF}}]$	Unfolded insulin protein concentration	5.93 μM	[248]
$[Chap]$	ER chaperons	1.85 x 10^{-5} μM	[248]
$[Ins]_{\mathrm{i.c.}}$	Folded insulin protein concentration	0.03 μM	[248]
$[R_{\mathrm{s}}]$	Superoxide	0.01 μM	[248]
$[R_{\mathrm{h}}]$	Hydrogen peroxide (H_2O_2)	0.1 μM	[248]
$[Ins]_{\mathrm{e.c.}}$	Extra-cellular insulin	0.00009 μM	[248]

5.3 Results

5.3.1 Parameter estimation

The values of the parameters used in the rate equations were extracted both from the literature as well as estimated from experimental data. The parameters and the initial values of the state variables extracted from the literature are given in Table 5.5 and Table 5.6 respectively.

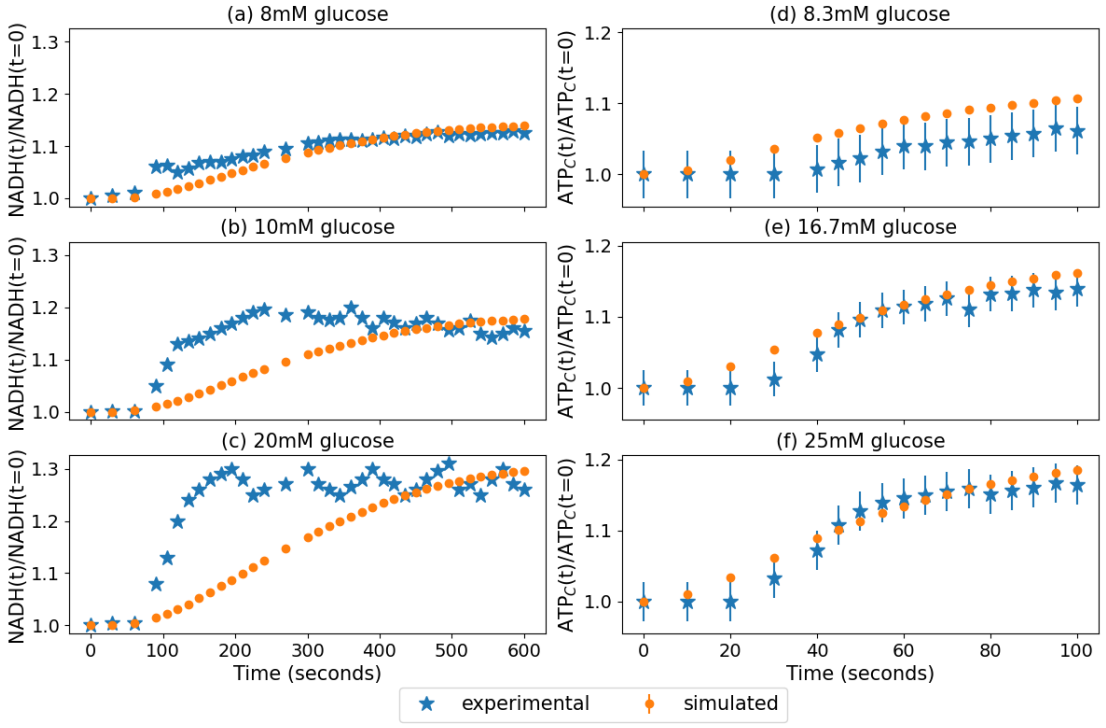

FIGURE 5.2: Stage 1 parameter estimation results: comparison of simulated data with experimental data. The simulated data are presented as mean ± SD (n = 50).

The estimation of the unknown parameter values was done in two stages. The parameter estimation for the first stage was repeated for 50 times and the estimated parameters are presented in Table 5.7 as mean ± standard deviation (SD) (n = 50). Figure 5.2 shows the comparison of the simulated data with the experimental data. The simulated data was generated for each of the 50 estimated parameter sets and is presented in Figure 5.2 as mean ± SD (n = 50). The experimental data in Figures 5.2(a)-(c) have oscillations, whereas the simulated data do not. This is because the equations of the model do not include any oscillatory mechanisms themselves. Oscillations in glucose metabolism, membrane potential, and Ca^{2+} in the beta-cell due to increased glucose concentrations have been observed in many studies [283, 291, 292]. The source of these oscillations is not clearly understood and may reflect multiple processes. These oscillations are responsible for triggering insulin secretion [240, 293–295]. The aim of this model is to study the processes of insulin transcription and folding which are not regulated by these oscillations. Hence, oscillatory mechanisms were not included in the model equations. The simulations performed with this model result in steady-states that are dependent on the glucose concentration. These simulation results could be considered as

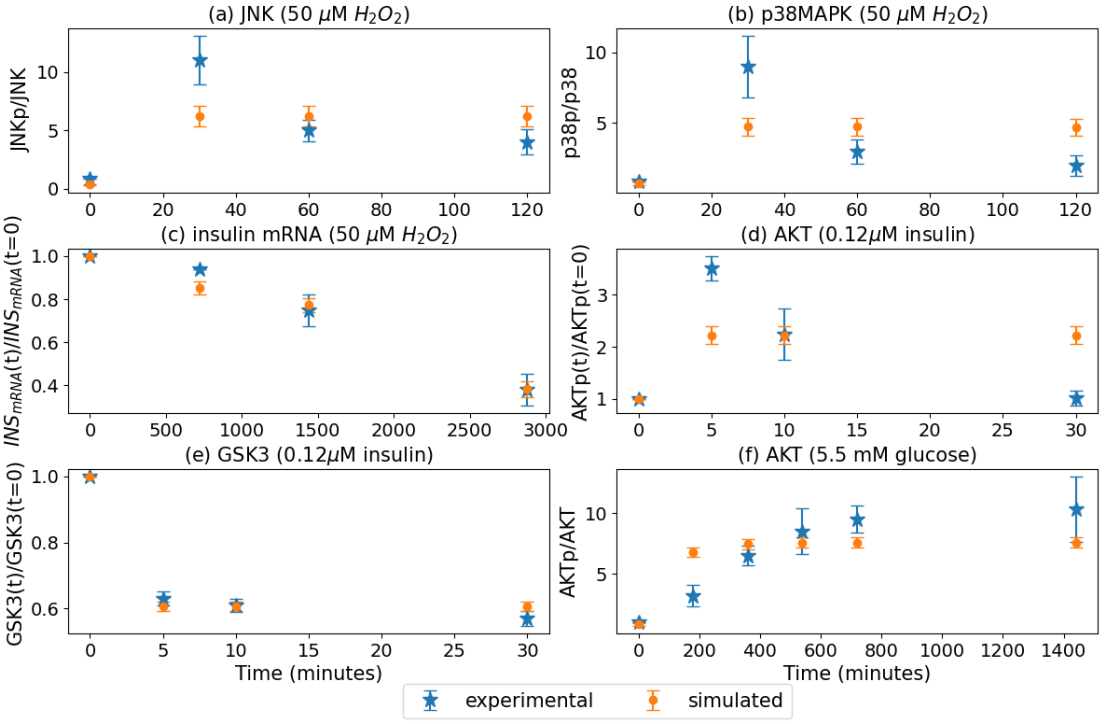

FIGURE 5.3: Stage 2 parameter estimation results: comparison of simulated data with experimental data. The simulated data are presented as mean ± SD (n = 50).

time averaged in comparison with experimental data if the data have oscillatory behaviour. Another observed difference between the experimental data and simulated data from Figures 5.2(a)-(c) is that the experimental data have an initial fast increase, whereas the simulated data have a slower initial increase. However, this difference in the initial rate of increase is not significant for this model since it is only concerned with the steady state values. In this regard, it is observed that the levels reached by the simulated data are consistent with the experimental data. For Figures 5.2(d)-(e), it is observed that the experimental data have slower initial increases, whereas the simulated data have faster initial increases. However, this discrepancy is not significant with respect to this model since it is only concerned with the steady state levels. Thus, the trends of the model simulation data are in general consistent with the experimental data.

The second stage of the parameter estimation was repeated for 50 times and the estimated parameters are presented in Table 5.8 as mean ± SD (n = 50). Figure 5.3 shows the comparison of the simulated data with the experimental data. The simulated data was generated for each of the 50 estimated parameter sets and is

presented in Figure 5.3 as mean ± SD. It is observed from Figures 5.3(a), (b) and (e) that the simulated data reach equilibrium, whereas the experimental data keep on decreasing. The possible reasons behind this have been explained in the following paragraph.

In this model, JNK is phosphorylated by H_2O_2 and UPR and is dephosphorylated at a constant rate. Now, JNK and p38MAPK regulate insulin mRNA through FOXO1, PDX1 and MAFA. The simulated response for insulin mRNA (Figure 5.3(c)) is observed to be consistent with the experimental data. However, the parameters that reproduced the correct behaviour for insulin mRNA could not reproduce the behaviour for JNK and p38MAPK as seen in the experimental data. In reality, JNK and p38MAPK have other positive and negative regulators and these other regulators could be responsible for the behaviour of JNK and p38MAPK observed from the experimental data. This is a limitation of this model. For similar reasons, the model simulations could not reproduce the exact behaviour of AKTp from the experimental data (Figure 5.3(d)). Another possible reason could be that the experimental data are based on different cell lines and conditions. Also, the cells are cultured in different mediums before start of the experiment which are not possible to replicate in the simulations. Using these different experimental data together for the parameter estimation results in the observed differences between the simulated behaviour and experimental behaviour. However, this model could reproduce the trends, that is in the presence of high H_2O_2, the phosphorylation of JNK and p38MAPK increased, and in the presence of insulin stimulation the phosphorylation of AKT increased.

TABLE 5.7: Details of the estimated parameters from stage 1 of the parameter estimation. The values are presented as mean ± SD (n = 50).

	Parameter	**Description**	**Mean ± SD**
1	V_{mG1}	Maximum reaction rate for GLUT1 that is observed at saturating glucose concentrations	50.86 ± 0.93 μMs^{-1}
2	V_{mGK}	Maximum rate of glucose consumption	375.55 ± 15.51 μMs^{-1}
3	V_{mPDH}	Maximum rate of PDH reaction	30.36 ± 0.15 μMs^{-1}
4	V_{O}	Maximum rate of NADH oxidation by ETC	32.88 ± 0.38 μMs^{-1}
5	K_{mPyr}	Michaelis-Menten constant	0.055 ± 0.008 μM
6	k_{Hyd}	Rate of ATP hydrolysis	0.056 ± 0.0005 s^{-1}
7	k_{PMCA}	Rate constant for the removal of $[Ca^{2+}]_{\mathrm{C}}$ through PMCA	37.99 ± 0.14 s^{-1}
8	a_1	Scaling factor between NADH consumption and change in membrane voltage	249.96 ± 0.1

TABLE 5.8: Details of the estimated parameters from stage 2 of the parameter estimation. The values are presented as mean ± SD (n = 50).

	Parameter	**Description**	**Mean ± SD**
1	$[AKT]_{\mathrm{t=0}}$	initial concentration of unphosphorylated AKT	3.58 ± 0.24 μM
2	$[AKT_{\mathrm{p}}]_{\mathrm{t=0}}$	initial concentration of phosphorylated AKT	2.96 ± 0.43 μM
3	$[GSK3]_{\mathrm{t=0}}$	initial concentration of unphosphorylated GSK3	3.26 ± 0.51 μM
4	$[GSK3_{\mathrm{p}}]_{\mathrm{t=0}}$	initial concentration of phosphorylated GSK3	3.37 ± 0.54 μM
5	$[JNK]_{\mathrm{t=0}}$	initial concentration of unphosphorylated JNK	4.59 ± 0.27 μM
6	$[JNK_{\mathrm{p}}]_{\mathrm{t=0}}$	initial concentration of phosphorylated JNK	1.63 ± 0.22 μM
7	$[p38MAPK]_{\mathrm{t=0}}$	initial concentration of unphosphorylated p38MAPK	4.64 ± 0.25 μM
8	$[p38MAPK_{\mathrm{p}}]_{\mathrm{t=0}}$	initial concentration of phosphorylated p38MAPK	3.24 ± 0.56 μM
9	$[FOXO1]_{\mathrm{t=0}}$	initial concentration of unphosphorylated FOXO1	3.67 ± 0.22 μM
10	$[FOXO1_{\mathrm{p}}]_{\mathrm{t=0}}$	initial concentration of phosphorylated FOXO1	3.65 ± 0.25 μM
11	$[PDX1]_{\mathrm{t=0}}$	initial concentration of PDX1	3.33 ± 0.55 μM
12	$[MAFA]_{\mathrm{t=0}}$	initial concentration of MAFA	3.53 ± 0.25 μM
13	k_{AKT}	phosphorylation rate of AKT by insulin	4.68 ± 0.19 s^{-1}
14	k_{AKTp}	AKT dephosphorylation rate	0.43 ± 0.035 s^{-1}
15	$k_{\mathrm{AKT-JNK}}$	rate of inactivation of AKT by JNK	0.21 ± 0.032 $\mu\mathrm{M}^{-1}\mathrm{s}^{-1}$
16	k_{GSK3}	phosphorylation rate of GSK3 by AKT	0.32 ± 0.05 $\mu\mathrm{M}^{-1}\mathrm{s}^{-1}$
17	k_{GSK3p}	GSK3 dephosphorylation rate	0.87 ± 0.07 s^{-1}
18	$k_{\mathrm{JNK-ROS}}$	phosphorylation rate of JNK by H_2O_2	4.66 ± 0.25 s^{-1}

Table 5.8 (continued): Details of the estimated parameters from stage 2 of the parameter estimation. The values are presented as mean ± SD (n = 50).

19	$k_{\mathrm{JNK-UPR}}$	phosphorylation rate of JNK by UPR	4.25 ± 0.57 s^{-1}
20	$k_{\mathrm{p38-ROS}}$	phosphorylation rate of p38MAPK by H_2O_2	3.56 ± 0.52 s^{-1}
21	$k_{\mathrm{p38-UPR}}$	phosphorylation rate of p38MAPK by UPR	4.48 ± 0.26 s^{-1}
22	$\mathrm{k_{MAPKp}}$	dephosphorylation rate of JNK and p38MPK	1.59 ± 0.14 s^{-1}
23	$k_{\mathrm{FOXO1-AKTp}}$	phosphorylation rate of FOXO1 by AKT	1.56 ± 0.28 $\mu\mathrm{M}^{-1}\mathrm{s}^{-1}$
24	$k_{\mathrm{FOXO1p-MAPKp}}$	phosphorylation rate of FOXO1 by JNK and p38MAPK	0.73 ± 0.14 $\mu\mathrm{M}^{-1}\mathrm{s}^{-1}$
25	V_{mPDX1}	maximum rate of PDX1 mRNA production	1.32 ± 0.26 $\mu\mathrm{Ms}^{-1}$
26	$K_{\mathrm{MAFA-PDX1}}$	dissociation constant of MAFA from the binding site of PDX1 promoter	1.9 ± 0.09 μM
27	$K_{\mathrm{FOXO1-PDX1}}$	dissociation constant of FOXO1 from the binding site of PDX1 promoter	2.67 ± 0.61 μM
28	$k_{\mathrm{PDX1-FOXO1-efflux}}$	rate of expulsion of PDX1 from nucleus by FOXO1	0.14 ± 0.025 $\mu\mathrm{M}^{-1}\mathrm{s}^{-1}$
29	$k_{\mathrm{GSK3-PDX1-pdeg}}$	rate of PDX1 protein degradation by GSK3	0.093 ± 0.007 $\mu\mathrm{M}^{-1}\mathrm{s}^{-1}$
30	V_{mMAFA}	maximum rate of MAFA mRNA production	2.27 ± 0.27 $\mu\mathrm{Ms}^{-1}$
31	$K_{\mathrm{PDX1-MAFA}}$	dissociation constant of PDX1 from the binding site of MAFA promoter	2.48 ± 0.18 μM
32	$K_{\mathrm{FOXO1-MAFA}}$	dissociation constant of FOXO1 from the binding site of MAFA promoter	0.31 ± 0.11 μM
33	$k_{\mathrm{ROS-MAFA}}$	rate of expulsion of MAFA from the nucleus by ROS	0.086 ± 0.009 s^{-1}
34	$k_{\mathrm{GSK3-MAFA-pdeg}}$	rate of MAFA protein degradation by GSK3	0.0075 ± 0.0013 $\mu\mathrm{M}^{-1}\mathrm{s}^{-1}$
35	V_{mINS}	maximum rate of insulin mRNA production	1.17 ± 0.24 $\mu\mathrm{Ms}^{-1}$
36	$K_{\mathrm{PDX1-INS}}$	dissociation constant of PDX1 from the binding site of insulin promoter	1.82 ± 0.59 μM
37	$K_{\mathrm{MAFA-INS}}$	dissociation constant of MAFA from the binding site of insulin promoter	2.15 ± 0.5 μM

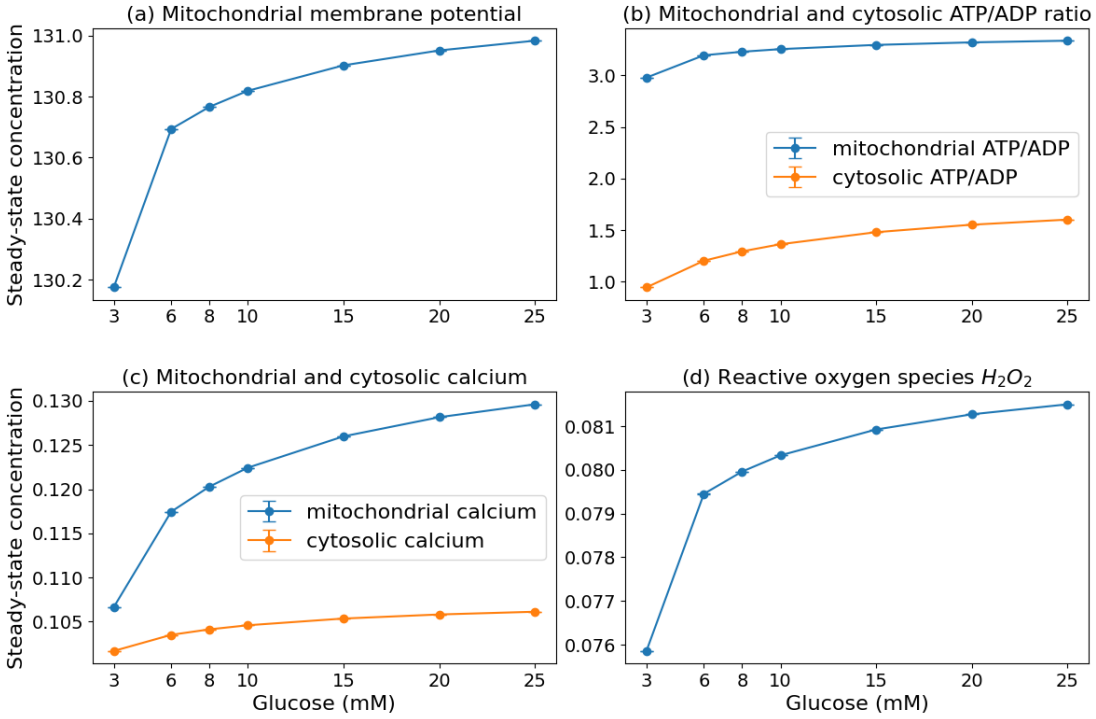

FIGURE 5.4: Qualitative validation: steady-state concentrations of (a) mitochondrial membrane potential, (b) mitochondrial and cytosolic ATP/ADP ratio, (c) mitochondrial and cytosolic calcium, and (d) H_2O_2 at glucose concentrations of 3, 6, 8, 10, 15, 20, and 25 mM. All simulated values are steady-state concentrations. All values are presented as mean ± SD (n = 50).

5.3.2 Validation

The proposed model was validated both qualitatively and quantitatively against experimental observations. Figure 5.4 shows the steady-state responses of model simulation to glucose concentrations of 3, 6, 8, 10, 15, 20, and 25 mM. The model simulations are generally consistent with the experimental observations. Several studies have shown a rise in mitochondrial membrane potential [291, 296, 297], ATP/ADP ratio [298, 299], cytosolic and mitochondrial Ca^{2+}, and ROS generation [300, 301] with increasing glucose concentration. The simulation results shown in Figure 5.4 are consistent with these experimental observations. It was observed from the results that the steady state values of mitochondrial membrane potential, ATP/ADP ratio, and cytosolic and mitochondrial Ca^{2+} increased with increasing glucose concentrations.

The model was also validated quantitatively against experimental data that are different from the data that were used for parameter estimation. The details of

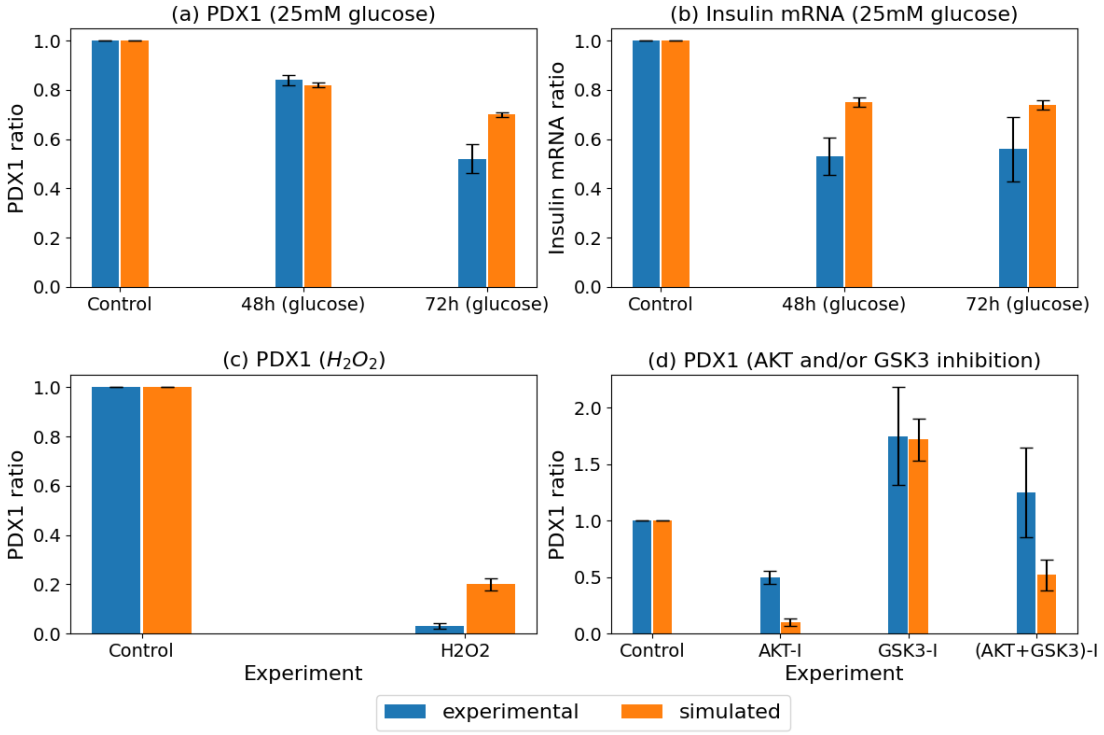

FIGURE 5.5: Quantitative validation: comparison between experimental data and simulated values of (a) relative PDX1 expressions after 48h and 72h of exposure to high glucose concentration of 25mM, (b) relative insulin mRNA expressions after 48h and 72h of exposure to high glucose concentration of 25mM, (c) relative PDX1 expression after 48h exposure to 50 μM H_2O_2, and (d) relative PDX1 expression in the presence of AKT inhibitor, GSK3 inhibitor, and both. All simulated values are steady-state concentrations. The simulated values are presented as mean $\pm$ SD (n = 50).

the experimental data used for validation are given in Table 5.9. The validations results are given in Figure 5.5. All simulated values shown in Figure 5.5 are steady-state concentrations. The validation was repeated for all 50 estimated parameter sets and the simulated values are presented as mean $\pm$ SD (n = 50). Figure 5.5(a) and Figure 5.5(b) show the comparison between experimental data and simulated values of the relative PDX1 and insulin mRNA expressions after 48h and 72h of exposure to high glucose concentration of 25mM. Figure 5.5(c) shows the relative PDX1 expression after 48h exposure to 50 μM H_2O_2. Figure 5.5(d) shows the relative PDX1 expression in the presence of AKT inhibitor, GSK3 inhibitor, and both. It is observed from the results that the model simulations closely reproduce the experimental data. The observed differences between the experimental and simulated values could be because the experimental data used for parameter estimation and validation are based on different cell lines. But overall, the model simulations

TABLE 5.9: Experimental data used for validation.

Details of experimental data	Reference
Relative PDX1 protein expression in 1.1B4 cells after 48h and 72h exposure to high glucose (25 mM). Values are mean ± SEM (n = 3).	[302]
Relative insulin mRNA expression in 1.1B4 cells after 48h and 72h exposure to high glucose (25 mM). Values are mean ± SEM (n = 3).	[302]
Oxidative stress–induced nucleo-cytoplasmic translocation of PDX-1. HIT-T15 cells were used. Cells were exposed for 48h to vehicle alone (control) and 50 μM H_2O_2. Values are mean ± SD (n = 3).	[255]
Densitometric analysis of PDX1 expression in human islets in the presence of vehicle (control), AKT inhibitor, GSK3 inhibitor, and both. Values are mean ± SD (n = 3).	[261]

are successful in reproducing the trends that are observed from the experimental data.

5.3.3 Scenarios

The proposed mathematical model was used to explore the changes in steady-state levels of insulin mRNA, PDX1, MAFA, FOXO1, GSK3, JNKp, p38MAPKp and ROS (H_2O_2) at glucose concentrations of 3mM, 10mM, 20mM and 30mM (Figure 5.6). All simulations were conducted for a duration of 48h and all values are steady-state values. From Figure 5.6 it is observed that with increasing glucose concentrations the steady-state levels of the transcription factors PDX1 and MAFA, as well as insulin mRNA decrease. At the very high glucose concentration of 30mM, their levels become almost negligible [300, 303–306]. On the other hand, the steady-state levels of FOXO1, GSK3, JNKp, p38MAPKp and ROS (H_2O_2) increase with increasing glucose concentrations. The high levels of FOXO1 and GSK3 in the nucleus in the presence of high glucose concentration leads to the decrease in the levels of PDX1 and MAFA and consequently insulin mRNA.

In addition, this mathematical model was used to explore the effect of seven scenarios on the steady state concentration of PDX1, MAFA, and insulin mRNA (Figure 5.7): (1) glucose concentration was increased to 25mM, (2) glucose concentration was decreased to 3mM, (3) glucose concentration was decreased to 3mM

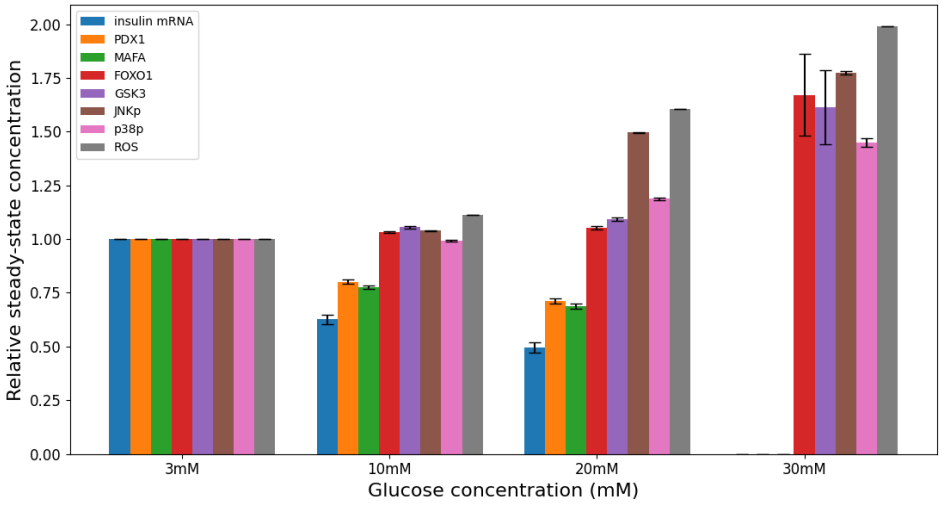

FIGURE 5.6: Simulated steady-state concentrations at glucose concentrations of 3mM, 10mM, 20mM and 30mM normalized by the steady state concentrations at 3mM glucose of insulin mRNA, PDX1, MAFA, FOXO1, GSK3, JNKp, p38MAPKp and ROS (H_2O_2). All simulations were conducted for a duration of 48 h and the values are presented as mean ± SD (n = 50).

and PDX1 level was doubled, (4) glucose concentration was decreased to 3mM and MAFA level was doubled, (5) glucose concentration was decreased to 3mM and FOXO1 concentration was decreased by two times (6) glucose concentration was decreased to 3mM and H_2O_2 concentration was decreased by two times, and (7) glucose concentration was decreased to 3mM and JNKp concentration was decreased by two times. These scenario tests were performed to analyze the influence of different variables on the steady-state levels of PDX1, MAFA and insulin mRNA. All reported steady state concentrations in Figure 5.7 are normalized by the steady state concentration of the respective variables at 25mM glucose. All scenario test simulations were conducted for a duration of 48 h.

From Figure 5.7 it is observed that when glucose concentration is decreased from 25mM to 3mM, the steady-state levels of PDX1, MAFA and insulin mRNA increase by approximately 50%, 50% and 100% respectively. Next, the effect of decreasing the glucose concentration together with increasing the PDX1 and MAFA levels was tested. It is observed that increasing the PDX1 and MAFA levels do not result in any significant increase when compared with scenario case (2). A reason behind this could be that the steady-state concentration of FOXO1 and GSK3 in the nucleus do not change when PDX1 and MAFA levels are increased. So, the

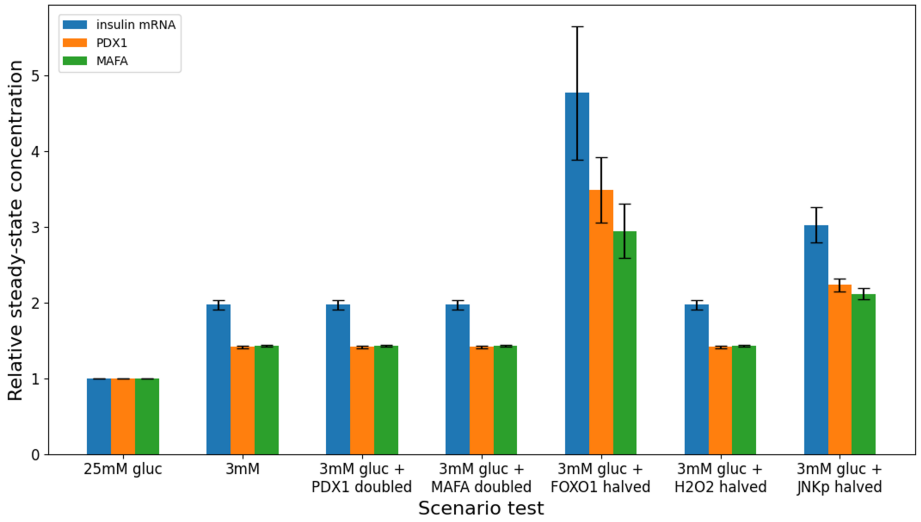

FIGURE 5.7: Effect of seven scenarios on the steady state concentration of PDX1, MAFA, and insulin mRNA: (1) glucose concentration was increased to 25mM, (2) glucose concentration was decreased to 3mM, (3) glucose concentration was decreased to 3mM and PDX1 level was doubled, (4) glucose concentration was decreased to 3mM and MAFA level was doubled, (5) glucose concentration was decreased to 3mM and FOXO1 concentration was decreased by two times (6) glucose concentration was decreased to 3mM and H_2O_2 concentration was decreased by two times, and (7) glucose concentration was decreased to 3mM and JNKp concentration was decreased by two times. All simulations were conducted for a duration of 48 h and the values are presented as mean ± SD (n = 50).

steady-state levels of PDX1, MAFA and insulin mRNA remain the same as when only glucose concentration is decreased.

In the following scenarios, the effect of decreasing the concentrations of the inhibitors of PDX1 and MAFA was tested. When FOXO1 concentration is decreased by two times together with decreasing the glucose concentration, it is observed that the steady-state levels of PDX1, MAFA and insulin mRNA increase by 250%, 200% and 380% respectively. Decreasing the H_2O_2 concentration by two times also results in an increase in steady-state levels of PDX1, MAFA and insulin mRNA by 50%, 50% and 100% respectively. Similarly, decreasing the concentration of JNKp results in an increase in steady-state levels of PDX1, MAFA and insulin mRNA by 130%, 110% and 220% respectively. This is because decreasing JNKp causes decreased translocation of FOXO1 to the nucleus and increased phosphorylation of AKT which in turn inhibits the nuclear translocation of FOXO1 as well as activation of GSK3.

Thus, from the scenario test results it is observed that regulating the concentration of FOXO1 has the highest effect on the steady-state levels of PDX1, MAFA and insulin mRNA. It has been shown in many studies that FOXO1 is an important transcription factor in the regulation of beta-cell identity transcription factors. Also, controlling the concentration of the stress-activated kinase JNKp also helps to increase the levels of PDX1 and MAFA, since JNKp is a critical regulator of FOXO1 translocation to the nucleus. FOXO1 and JNKp could be potential intervention targets for ameliorating beta-cell function in the presence of chronic hyperglycemia.

5.4 Discussion

Loss of fully differentiated beta-cell phenotype has been recently recognized as a potential mechanism underlying beta-cell dysfunction in T2D. Oxidative stress and ER stress induced by chronic hyperglycemia can lead to reduced expression of key beta-cell transcription factors including PDX1 and MAFA. This results in the loss of insulin gene expression which gradually leads to defective insulin secretion. In this work, an integrated mathematical model of the pathways and processes involved in the regulation of the transcription factors associated with mature beta-cell identity as well as insulin gene expression was developed. The aim of this model was to investigate the loss of beta-cell function through loss of beta-cell identity in the presence of chronic hyperglycemia induced oxidative stress and ER stress. The model consists of 31 coupled ODEs, which reflect the complex and coupled interactions among different proteins, metabolites, and pathways within a single beta-cell. In this model, the important processes of glucose metabolism, calcium dynamics, insulin signalling, and insulin transcription and folding were considered in order to understand the mechanisms that lead to the downregulation of beta-cell identity transcription factors, PDX1 and MAFA, and insulin gene expression in the presence of chronic hyperglycemia.

In this model, new rate equations were developed to describe the regulation of the beta-cell identity transcription factors, PDX1 and MAFA, by the insulin signalling pathway, stress-activated kinases (JNK and p38MAPK) and ROS (H_2O_2). New rate equations were also developed to describe the transcription of insulin gene by PDX1 and MAFA. This model is useful as it integrates different models describing different aspects of beta-cell function and links them with the pathways that control

the beta-cell identity transcription factors. The literature contains many models of glucose transport, glucose metabolism, calcium dynamics, and protein folding among others. However, these models focus on a particular beta-cell function, which cannot give a complete picture of how these different processes interact to maintain beta-cell function. In this model, an attempt was made to bridge this gap by integrating these models from the literature as well as proposing a new model for the regulation of beta-cell identity factors. This model is thus useful for understanding how the different processes involved in beta-cell function interact to regulate beta-cell identity transcription factors and insulin gene expression.

This model is an initial step towards integrating different beta-cell functions to obtain a more holistic model in order to understand the mechanisms regulating beta-cell identity transcription factors. It is very important to understand the pathways involved in this regulation since compromised beta-cell identity is a characteristic of T2D. This model considered two of these beta-cell identity transcription factors, PDX1 and MAFA, since these are also promoters of insulin gene expression. Decrease in the levels of PDX1 and MAFA leads to decreased insulin gene expression, which ultimately depletes the insulin stores of the beta-cell and leads to decreased insulin secretion. Thus, this model could be useful to understand beta-cell dysfunction through compromised beta-cell identity in the presence of chronic hyperglycemia. This seed model can be further enhanced by including the other transcription factors associated with mature beta-cell identity such as NKX6.1 and NEUROD1.

Another important reason for modelling these beta-cell identity transcription factors is to understand if the compromised beta-cell identity observed in T2D is reversible. Experiments in animal models have shown that this loss of beta-cell identity is reversible upon normalization of glucose levels [307, 308]. However, this reversibility still remains to be established for humans. Such computational models are useful tools to extend this understanding and identify the potential intervention targets that can lead to this reversibility, which could be a therapeutic revolution in the treatment of T2D. This model could also be used to identify intervention targets that can ameliorate insulin gene expression in the presence of chronic hyperglycemia. As shown in the scenario tests, targeting and downregulating FOXO1 increases insulin gene expression. The proposed mathematical model was used to explore the changes in steady-state levels of PDX1, MAFA and insulin mRNA at

different glucose concentrations. It was observed that PDX1, MAFA and insulin mRNA levels decreased with increasing glucose concentration, becoming almost zero at the very high glucose concentration of 30mM. In addition, the model was used to explore the effect of seven scenario tests to analyze the influence of different variables on the steady-state levels of PDX1, MAFA and insulin mRNA. It was found that transcription factor FOXO1 has the highest effect on PDX1, MAFA and insulin mRNA, followed by the stress-activated kinase JNK. Thus, FOXO1 and phosphorylated JNK could be potential intervention targets for ameliorating insulin gene expression in the presence of chronic hyperglycemia.

The values of the parameters used in the rate equations were extracted both from the literature as well as estimated from experimental data. The data used for parameter estimation are from in vitro experiments conducted on different cell lines and conditions. Also, the cells were cultured in different mediums before start of the experiment which was not possible to replicate in the simulations. These could be the possible reasons for the differences observed between experimental and simulated behaviour. In addition, this model is not exhaustive and may miss some relevant processes involved in the regulation of the proteins and metabolites included in this model. This could also lead to the observed deviation from the experimental data and inclusion of these other processes may be able to reproduce the exact behaviour as observed in the experiments. Despite these limitations, the model simulations could reproduce the trends that are observed from the experimental data. In addition, on validating against a different set of experimental data, the model simulations were successful in reproducing the trends observed from the experimental data.

The aim of the proposed model was to investigate the loss of beta-cell function through loss of beta-cell identity in the presence of chronic hyperglycemia. In this regard, the steady state change in state variables at different glucose concentrations were examined and the behaviour of the important metabolites and proteins carrying out different aspects of beta-cell function were qualitatively studied. In reality, beta-cell dysfunction and compromised beta-cell identity result after years of chronic hyperglycemia. This long-term simulation is not possible with the proposed model. However, the model can be useful in simulating the trends that are observed in reality when glucose concentration is increased above physiological levels. In other words, the model simulations facilitate the study of the short-term

mechanisms whose build-up leads to long-term beta-cell dysfunction and compromised beta-cell identity. Also, this model was developed to understand the pathways in a single beta-cell. This model can be scaled up to see the effect in insulin content and secretion in the islet level by considering the total number of beta-cells present in human islets.

This model only focuses on how oxidative stress and ER stress induced by chronic hyperglycemia can cause compromised beta-cell identity. It has been shown in different studies that chronic hyperglycemia also causes inflammation. In fact, cytokines and inflammation are also important mediators of beta-cell dysfunction. These factors could be incorporated to this seed model to study the combined effect of the different mediators of beta-cell dysfunction and compromised beta-cell identity.

This integrated mathematical model can help in considering multiple aspects related to beta-cell identity and function enabling a more holistic model which can further extend our understanding of the underlying non-linear biological mechanisms leading to compromised beta-cell identity and beta-cell dysfunction in the presence of chronic hyperglycemia. The model illustrates how multiple pathways interact to regulate the beta-cell identity transcription factors and insulin gene expression. Such integrated computational models could help to identify the most important pathways and feedback loops given specific inputs and drivers, further understand the interaction between different pathways and processes, generate hypotheses and test possible intervention strategies. This model is a seed model which can be gradually enhanced by integrating other important pathways and processes involved in regulating beta-cell identity transcription factors and beta-cell function.

Chapter 6

Conclusions and future work

6.1 Conclusions

Four research works have been presented in this thesis. Three of these research works have explored biological and social factors responsible for the pathogenesis of T2D. Three computational models have been developed in this thesis: system dynamics models (SDMs) of the system of social norms regarding body weight perception and obesity prevalence, a Boolean network model of the insulin resistance pathway and pancreatic beta-cell apoptosis pathway, and an ordinary differential equation (ODE) model of the system of signalling components involved in insulin gene expression and glucose-stimulated insulin secretion. In addition, two of the four works presented in this thesis have proposed methods for inferring computational models from cross-sectional data.

Chapter 2 details the development of six SDMs of the system of social norms regarding body weight perception and obesity prevalence based on an expert-informed causal loop diagram and data from six socio-cultural groups (Dutch, Moroccan and South-Asian Surinamese men and women). The SDMs served to explore the effect of three scenarios on group-level BMI: 'what if' weight-related behaviour were driven by (1) health awareness, (2) norms or (3) a combination of the two. The model simulations showed that norms regarding body weight perception withhold individuals from losing as much weight as they could if driven by health awareness alone. When overweight is the norm, that is, in all male groups, the norm holds group-level BMI close to overweight despite of health awareness. These results

thus suggest that norms limit the effectiveness of interventions targeting individual weight-related behaviour, especially in men. Since norms are counteracting health awareness less strongly in the female groups, there must be additional drivers of obesity in women. By studying 'what if' scenarios using computational modelling approaches, it is possible to test policy strategies under the exact same conditions. Although the SDMs do not include potential solutions for influencing norms, they show that justice should be done to influences on both the individual as well as the group level. The results suggest that norms limit the effectiveness of interventions targeting individual weight-related behaviour, especially in men.

Chapter 3 presents a method for inferring computational models from cross-sectional data using Langevin dynamics. This method can be applied to any system that can be described as effectively following a free energy landscape which is stable and not influenced by any external force. The usefulness of the proposed method lies in the fact that it provides an approximate estimate of the underlying dynamics from the cross-sectional data. This will be useful when there is no knowledge of how other factors or variables are related to the variable of interest. This method can be a useful tool to get an approximate idea of the underlying dynamics of the system when data is available only for a single time-point. Later, this 'baseline' model can be developed into causal model and the timescale of the model predictions can be estimated with the help of expert knowledge. The proposed method is sufficiently simple to use as well as interpretable to initiate the iterative development of computational models for any system that can be described as effectively following a free energy landscape and thus help in studying the progression of important processes.

Chapter 4 details the development of a Boolean network model of the insulin resistance pathway and pancreatic beta-cell apoptosis pathway which are responsible for the pathogenesis of T2D. The proposed model made predictions that closely resembled the expression levels of genes in T2D as reported in the literature. The results show that when the input signals ER stress, oxidative stress, and cytokines are activated, then the output apoptosis is also activated, and some of the important genes that are known mediators of apoptosis from the literature are also activated in these states. Thus, this Boolean network model can be used to analyse the behaviour of different proteins in a qualitative manner in the presence of ER stress, oxidative stress, and pro-inflammatory cytokines.

Chapter 5 details the development of an integrated mathematical model of the pathways and processes involved in the regulation of the transcription factors associated with mature beta-cell identity as well as insulin gene expression. The aim of this model was to investigate the loss of beta-cell function through loss of beta-cell identity in the presence of chronic hyperglycemia induced oxidative stress and ER stress. This model is an initial step towards integrating different beta-cell functions to obtain a more holistic model in order to understand the mechanisms regulating beta-cell identity transcription factors. The model illustrates how multiple pathways interact to regulate the beta-cell identity transcription factors and insulin gene expression. This model could also be used to identify intervention targets that can ameliorate insulin gene expression in the presence of chronic hyperglycemia. As shown through the model simulations, targeting and downregulating FOXO1 increased insulin gene expression. The proposed model is a seed model which can be gradually enhanced by integrating other important pathways and processes involved in regulating beta-cell identity transcription factors and beta-cell function.

6.2 Future work

It has been shown in many studies that social determinants, such as, income, employment insecurity, education, housing, living conditions, and access to nutritious food are central to the development and progression of obesity and T2D. Moreover, the incidence and prevalence of T2D appear to be socially graded, as individuals with lower income and less education are more likely to develop T2D than more advantaged individuals. It would be interesting to couple these social determinants with the system dynamics model of social norms to understand the combined effect of these factors in the development of obesity and T2D.

Chronic inflammation has been found to be an important factor of beta-cell dysfunction in T2D. It has been observed in various studies that pro-inflammatory cytokines, such as IL-1β, TNF-α, IFN-γ, induce beta-cell dysfunction. In future, it would be interesting to integrate the signalling pathways involving these pro-inflammatory cytokines to the beta-cell dysfunction model to study the combined effect of hyperglycemia and inflammation on beta-cell dysfunction in T2D.

List of Author's Awards, Patents, and Publications[1]

Journal Articles

- **Pritha Dutta**, Lichun Ma, Yusuf Ali, Peter M.A. Sloot, and Jie Zheng. Boolean network modeling of β-cell apoptosis and insulin resistance in type 2 diabetes mellitus. *BMC systems biology*, 13(2):36, 2019.

- Loes Crielaard*, **Pritha Dutta***, Rick Quax, Mary Nicolaou, Nadege Merabet, Karien Stronks, and Peter M.A. Sloot. Social norms and obesity prevalence: From cohort to system dynamics models. *Obesity Reviews*, 21(9):e13044, 2020.

- **Pritha Dutta**, Rick Quax, Loes Crielaard, Luca Badiali, and Peter M.A. Sloot. Inferring temporal dynamics from cross-sectional data using Langevin dynamics. *Royal Society Open Science*, 8(11):211374, 2021.

[1]The superscript * indicates joint first authors

Bibliography

[1] Pouya Saeedi, Inga Petersohn, Paraskevi Salpea, Belma Malanda, Suvi Karuranga, Nigel Unwin, Stephen Colagiuri, Leonor Guariguata, Ayesha A Motala, Katherine Ogurtsova, et al. Global and regional diabetes prevalence estimates for 2019 and projections for 2030 and 2045: Results from the international diabetes federation diabetes atlas. *Diabetes research and clinical practice*, 157:107843, 2019. 1

[2] Mary A Burke and Frank W Heiland. Evolving societal norms of obesity: what is the appropriate response? *Jama*, 319(3):221–222, 2018. 2, 11

[3] H Madrigal, A Sanchez-Villegas, MA Martinez-Gonzalez, J Kearney, MJ Gibney, J De Irala, and JA Martínez. Underestimation of body mass index through perceived body image as compared to self-reported body mass index in the european union. *Public health*, 114(6):468–473, 2000. 2, 11

[4] E Halliwell. Social comparison theory and body image. In *Encyclopedia of body image and human appearance*, pages 751–757. Elsevier, 2012. 2, 3, 11, 12, 13, 16, 70

[5] Johanna Ralston, Hannah Brinsden, Kent Buse, Vanessa Candeias, Ian Caterson, Trevor Hassell, Shiriki Kumanyika, Patricia Nece, Sania Nishtar, Ian Patton, et al. Time for a new obesity narrative. *The Lancet*, 392(10156): 1384–1386, 2018. 2, 75

[6] David B Bahr, Raymond C Browning, Holly R Wyatt, and James O Hill. Exploiting social networks to mitigate the obesity epidemic. *Obesity*, 17(4): 723–728, 2009. 2, 11

[7] Pedro J Teixeira, Eliana V Carraça, Marta M Marques, Harry Rutter, Jean-Michel Oppert, Ilse De Bourdeaudhuij, Jeroen Lakerveld, and Johannes Brug. Successful behavior change in obesity interventions in adults: a systematic review of self-regulation mediators. *BMC medicine*, 13(1):84, 2015. 2, 12

[8] Xueying Zhang, David W Cowling, and Hao Tang. The impact of social norm change strategies on smokers' quitting behaviours. *Tobacco Control*, 19 (Suppl 1):i51–i55, 2010. 3, 12

[9] John Sterman. System dynamics: systems thinking and modeling for a complex world. 2002. 3, 12

[10] Marieke B Snijder, Henrike Galenkamp, Maria Prins, Eske M Derks, Ron JG Peters, Aeilko H Zwinderman, and Karien Stronks. Cohort profile: the healthy life in an urban setting (helius) study in amsterdam, the netherlands. *BMJ open*, 7(12):e017873, 2017. 3, 12, 14, 15, 77

[11] Roland L Weinsier, Louis J Wilson, and Jeannette Lee. Medically safe rate of weight loss for the treatment of obesity: a guideline based on risk of gallstone formation, 1995. 4, 29, 35

[12] National Institutes of Health et al. Clinical guidelines for the identification, evaluation, and treatment of overweight and obesity in adults-the evidence report. *Obes Res*, 6(2):51S–209S, 1998. 4, 29, 35

[13] Pia V Röder, Bingbing Wu, Yixian Liu, and Weiping Han. Pancreatic regulation of glucose homeostasis. *Experimental & molecular medicine*, 48(3): e219–e219, 2016. xv, 5, 6

[14] Martin Schröder and Randal J Kaufman. The mammalian unfolded protein response. *Annu. Rev. Biochem.*, 74:739–789, 2005. 6, 101, 104, 112

[15] Heather P Harding and David Ron. Endoplasmic reticulum stress and the development of diabetes: a review. *Diabetes*, 51(suppl 3):S455–S461, 2002. 6

[16] Seiichi Oyadomari, Eiichi Araki, and M Mori. Endoplasmic reticulum stress-mediated apoptosis in pancreatic β-cells. *Apoptosis*, 7(4):335–345, 2002. 6, 101, 112

[17] Yu Ihara, Shinya Toyokuni, Koji Uchida, Hiroyuki Odaka, Tomoyuki Tanaka, Hitoshi Ikeda, and Hiroshi Hiai. Pancreatic (b-cells of gk rats, a model of type 2 diabetes. *Diabetes*, 48, 1999. 6

[18] R Paul Robertson, Jamie Harmon, Phuong Oanh T Tran, and Vincent Poitout. β-cell glucose toxicity, lipotoxicity, and chronic oxidative stress in type 2 diabetes. *Diabetes*, 53(suppl 1):S119–S124, 2004. 6

[19] Slgurd Lenzen, Jens Drinkgern, and Markus Tiedge. Low antioxidant enzyme gene expression in pancreatic islets compared with various other mouse tissues. *Free Radical Biology and Medicine*, 20(3):463–466, 1996. 6, 124

[20] Markus Tiedge, Stephan Lortz, Jens Drinkgern, and Sigurd Lenzen. Relation between antioxidant enzyme gene expression and antioxidative defense status of insulin-producing cells. *Diabetes*, 46(11):1733–1742, 1997. 6, 124

[21] Joseph L Evans, Ira D Goldfine, Betty A Maddux, and Gerold M Grodsky. Oxidative stress and stress-activated signaling pathways: a unifying hypothesis of type 2 diabetes. *Endocrine reviews*, 23(5):599–622, 2002. 6, 104, 112

[22] Joseph L Evans, Ira D Goldfine, Betty A Maddux, and Gerold M Grodsky. Are oxidative stress- activated signaling pathways mediators of insulin resistance and β-cell dysfunction? *Diabetes*, 52(1):1–8, 2003. 6

[23] Katherine Esposito, Francesco Nappo, Raffaele Marfella, Giovanni Giugliano, Francesco Giugliano, Myriam Ciotola, Lisa Quagliaro, Antonio Ceriello, and Dario Giugliano. Inflammatory cytokine concentrations are acutely increased by hyperglycemia in humans: role of oxidative stress. *Circulation*, 106(16): 2067–2072, 2002. 6

[24] Marc Y Donath and Steven E Shoelson. Type 2 diabetes as an inflammatory disease. *Nature Reviews Immunology*, 11(2):98, 2011. 7, 102

[25] Kathrin Maedler, Giatgen A Spinas, Roger Lehmann, Pavel Sergeev, Markus Weber, Adriano Fontana, Nurit Kaiser, and Marc Y Donath. Glucose induces β-cell apoptosis via upregulation of the fas receptor in human islets. *Diabetes*, 50(8):1683–1690, 2001.

[26] Joachim Spranger, Anja Kroke, Matthias Möhlig, Kurt Hoffmann, Manuela M Bergmann, Michael Ristow, Heiner Boeing, and Andreas FH Pfeiffer. Inflammatory cytokines and the risk to develop type 2 diabetes: results of the prospective population-based european prospective investigation into cancer and nutrition (epic)-potsdam study. *Diabetes*, 52(3):812–817, 2003.

[27] Decio L Eizirik and T Mandrup-Poulsen. A choice of death–the signal-transduction of immune-mediated beta-cell apoptosis. *Diabetologia*, 44(12): 2115–2133, 2001.

[28] Marc Y Donath. Targeting inflammation in the treatment of type 2 diabetes: time to start. *Nature Reviews Drug Discovery*, 13(6):465–476, 2014. 7, 102

[29] Steven E Shoelson, Jongsoon Lee, and Allison B Goldfine. Inflammation and insulin resistance. *The Journal of Clinical Investigation*, 116(7):1793–1801, 2006. 7, 102

[30] Iqra Hameed, Shariq R Masoodi, Shahnaz A Mir, Mudasar Nabi, Khalid Ghazanfar, and Bashir A Ganai. Type 2 diabetes mellitus: from a metabolic disorder to an inflammatory condition. *World Journal of Diabetes*, 6(4):598, 2015. 7, 102

[31] Diana-Elena Gratie, Bogdan Iancu, and Ion Petre. Ode analysis of biological systems. In *International School on Formal Methods for the Design of Computer, Communication and Software Systems*, pages 29–62. Springer, 2013. 7

[32] Julian D Schwab, Silke D Kühlwein, Nensi Ikonomi, Michael Kühl, and Hans A Kestler. Concepts in boolean network modeling: What do they all mean? *Computational and structural biotechnology journal*, 18:571–582, 2020. 7

[33] Rafael V Carvalho, Fons J Verbeek, and Clarimar J Coelho. Bio-modeling using petri nets: a computational approach. In *Theoretical and Applied Aspects of Systems Biology*, pages 3–26. Springer, 2018. 7

[34] Gary An, Qi Mi, Joyeeta Dutta-Moscato, and Yoram Vodovotz. Agent-based models in translational systems biology. *Wiley Interdisciplinary Reviews: Systems Biology and Medicine*, 1(2):159–171, 2009. 7

[35] Lorella Marselli, Mara Suleiman, Matilde Masini, Daniela Campani, Marco Bugliani, Farooq Syed, Luisa Martino, Daniele Focosi, Fabrizio Scatena, Francesco Olimpico, et al. Are we overestimating the loss of beta cells in type 2 diabetes? *Diabetologia*, 57(2):362–365, 2014. 8

[36] Chutima Talchai, Shouhong Xuan, Hua V Lin, Lori Sussel, and Domenico Accili. Pancreatic β cell dedifferentiation as a mechanism of diabetic β cell failure. *Cell*, 150(6):1223–1234, 2012. 8, 123

[37] Shuangli Guo, Chunhua Dai, Min Guo, Brandon Taylor, Jamie S Harmon, Maike Sander, R Paul Robertson, Alvin C Powers, Roland Stein, et al. Inactivation of specific β cell transcription factors in type 2 diabetes. *The Journal of clinical investigation*, 123(8):3305–3316, 2013. 8, 123, 124

[38] Jean-Christophe Jonas, Arun Sharma, Wendy Hasenkamp, Hasan Ilkova, Giovanni Patanè, Ross Laybutt, Susan Bonner-Weir, and Gordon C Weir. Chronic hyperglycemia triggers loss of pancreatic β cell differentiation in an animal model of diabetes. *Journal of Biological Chemistry*, 274(20):14112–14121, 1999. 8, 123

[39] Melissa F Brereton, Maria Rohm, and Frances M Ashcroft. β-cell dysfunction in diabetes: a crisis of identity? *Diabetes, obesity and metabolism*, 18:102–109, 2016.

[40] Francesca Cinti, Ryotaro Bouchi, Ja Young Kim-Muller, Yoshiaki Ohmura, P Rodrigo Sandoval, Matilde Masini, Lorella Marselli, Mara Suleiman, Lloyd E Ratner, Piero Marchetti, et al. Evidence of β-cell dedifferentiation in human type 2 diabetes. *The Journal of Clinical Endocrinology & Metabolism*, 101(3):1044–1054, 2016. 123, 124

[41] Michael G White, Helen L Marshall, Rebecca Rigby, Guo Cai Huang, Aimen Amer, Trevor Booth, Steve White, and James AM Shaw. Expression of mesenchymal and α-cell phenotypic markers in islet β-cells in recently diagnosed diabetes. *Diabetes care*, 36(11):3818–3820, 2013. 123

[42] Avital Swisa, Benjamin Glaser, and Yuval Dor. Metabolic stress and compromised identity of pancreatic beta cells. *Frontiers in genetics*, 8:21, 2017. xv, 9

[43] Maria S Remedi and Christopher Emfinger. Pancreatic β-cell identity in diabetes. *Diabetes, obesity and metabolism*, 18:110–116, 2016. 124

[44] Abu Saleh Md Moin and Alexandra E Butler. Alterations in beta cell identity in type 1 and type 2 diabetes. *Current diabetes reports*, 19(9):1–12, 2019. 8

[45] Harry Rutter, Natalie Savona, Ketevan Glonti, Jo Bibby, Steven Cummins, Diane T Finegood, Felix Greaves, Laura Harper, Penelope Hawe, Laurence Moore, et al. The need for a complex systems model of evidence for public health. *The Lancet*, 390(10112):2602–2604, 2017. 11

[46] Dean Rickles, Penelope Hawe, and Alan Shiell. A simple guide to chaos and complexity. *Journal of Epidemiology & Community Health*, 61(11):933–937, 2007. 11

[47] Sarah Durkin. Anti-smoking social norms are associated with increased cessation behaviours among lower and higher socioeconomic status smokers: a population-based cohort study. 2018. 12

[48] Mary A Burke, Frank W Heiland, and Carl M Nadler. From "overweight" to "about right": evidence of a generational shift in body weight norms. *Obesity*, 18(6):1226–1234, 2010. 13

[49] Maria del Mar Bibiloni, Jordi Pich, Antoni Pons, and Josep A Tur. Body image and eating patterns among adolescents. *BMC public health*, 13(1): 1104, 2013. 13

[50] Slining Yaemsiri, Meghan M Slining, and Sunil K Agarwal. Perceived weight status, overweight diagnosis, and weight control among us adults: the nhanes 2003–2008 study. *International journal of obesity*, 35(8):1063–1070, 2011. 14

[51] Doeschka J Anschutz and Rutger CME Engels. The effects of playing with thin dolls on body image and food intake in young girls. *Sex roles*, 63(9-10): 621–630, 2010.

[52] Hayley K Dohnt and Marika Tiggemann. Development of perceived body size and dieting awareness in young girls. *Perceptual and Motor Skills*, 99(3): 790–792, 2004. 13

[53] James O Hill, Holly R Wyatt, and John C Peters. Energy balance and obesity. *Circulation*, 126(1):126–132, 2012. 14

[54] Dustin T Duncan, Kathleen Y Wolin, Melissa Scharoun-Lee, Eric L Ding, Erica T Warner, and Gary G Bennett. Does perception equal reality? weight misperception in relation to weight-related attitudes and behaviors among overweight and obese us adults. *International Journal of Behavioral Nutrition and Physical Activity*, 8(1):20, 2011. 14

[55] Solveig Uglem, Tonje H Stea, Wenche Frølich, and Margareta Wandel. Body weight, weight perceptions and food intake patterns. a cross-sectional study among male recruits in the norwegian national guard. *BMC Public Health*, 11(1):1–7, 2011. 14

[56] NM Byrne and AP Hills. How much exercise should be promoted to raise total daily energy expenditure and improve health? *Obesity Reviews*, 19: 14–23, 2018. 14

[57] Kraisid Tontisirin and Hartwig de Haen. Human energy requirements. *Report of a Joint FAO/WHO/UNU Expert Consultation, Rome*, pages 17–24, 2001. 14, 15, 23, 26

[58] Karien Stronks, Marieke B Snijder, Ron JG Peters, Maria Prins, Aart H Schene, and Aeilko H Zwinderman. Unravelling the impact of ethnicity on health in europe: the helius study. *BMC public health*, 13(1):402, 2013. 15

[59] Geert Hofstede. Dimensionalizing cultures. *Online Readings in Psychology and Culture*, 2(1):1–26, 2011. 15

[60] Rajiv Jhangiani, Hammond Tarry, and Charles Stangor. Principles of social psychology-1st international edition. 2014. 15, 45, 46, 47

[61] Geert Hofstede. *Country comparison India/Morocco/Netherlands/Suriname. Hofstede Insights*, 2019 (Accessed July 22, 2019). URL `https://www.hofstede-insights.com/country-comparison/india`. 15, 41

[62] Qaisar Raza, Marieke B Snijder, Jacob C Seidell, Ron JG Peters, and Mary Nicolaou. Comparison of cardiovascular risk factors and dietary intakes among javanese surinamese and south-asian surinamese in the netherlands. the helius study. *BMC Research Notes*, 10(1):23, 2017. 15

[63] Kim M Pulvers, Rebecca E Lee, Harsohena Kaur, Matthew S Mayo, Marian L Fitzgibbon, Shawn K Jeffries, James Butler, Qingjiang Hou, and Jasjit S Ahluwalia. Development of a culturally relevant body image instrument among urban african americans. *Obesity research*, 12(10):1641–1651, 2004. 17

[64] MS Gary and JW Forrester. Mistakes and misunderstandings examining dimensional inconsistency. *MIT Syst Dyn Educ Proj*, 1992:1–6, 1992. 19, 21

[65] Danny Lai and Rebekah Wahba. System dynamics model correctness checklist. *MIT D-Memo D-4851*, 1:15, 2001.

[66] Mirjana Pejić-Bach and Vlatko Čerić. Developing system dynamics models with" step-by-step" approach. *Journal of information and organizational sciences*, 31(1):171–185, 2007.

[67] Thomas Binder, Andreas Vox, Salim Belyazid, Hordur Haraldsson, and Mats Svensson. Developing system dynamics models from causal loop diagrams. In *Proceedings of the 22nd International Conference of the System Dynamic Society*, pages 1–21, 2004.

[68] Anthony J Masys. *Security by Design: Innovative Perspectives on Complex Problems*. Springer, 2018. 19, 20, 21

[69] *Ventana Systems. Variable types.*, 2012 (Accessed June 5, 2019). URL `https://www.vensim.com/documentation/index.html?ref_variable_types.htm`. 20

[70] Gertraud Maskarinec, Eva Erber, Andrew Grandinetti, Martijn Verheus, Robert Oum, Beth N Hopping, Mark M Schmidt, Aileen Uchida, Deborah Taira Juarez, Krista Hodges, et al. Diabetes incidence based on linkages with health plans: the multiethnic cohort. *Diabetes*, 58(8):1732–1738, 2009. 23

[71] Walter C Willett, William H Dietz, and Graham A Colditz. Guidelines for healthy weight. *New England Journal of Medicine*, 341(6):427–434, 1999. 23

[72] M Nicolaou, MGJ Gademan, MB Snijder, RHH Engelbert, H Dijkshoorn, CB Terwee, and K Stronks. Validation of the squash physical activity questionnaire in a multi-ethnic population: The helius study. *PLoS One*, 11(8): e0161066, 2016. 26

[73] Kentaro Murakami and M Barbara E Livingstone. Prevalence and characteristics of misreporting of energy intake in us adults: Nhanes 2003–2012. *British Journal of Nutrition*, 114(8):1294–1303, 2015. 29

[74] Maurice Edward Shils and Moshe Shike. *Modern nutrition in health and disease*. Lippincott Williams & Wilkins, 2006. 29

[75] Martijn B Katan and David S Ludwig. Extra calories cause weight gain—but how much? *Jama*, 303(1):65–66, 2010. 29

[76] Emma Peeling and Allan Tucker. Making time: pseudo time-series for the temporal analysis of cross section data. In *International Symposium on Intelligent Data Analysis*, pages 184–194. Springer, 2007. 29, 78

[77] Allan Tucker and David Garway-Heath. The pseudotemporal bootstrap for predicting glaucoma from cross-sectional visual field data. *IEEE Transactions on Information Technology in Biomedicine*, 14(1):79–85, 2009.

[78] Yuanxi Li, Stephen Swift, and Allan Tucker. Modelling and analysing the dynamics of disease progression from cross-sectional studies. *Journal of biomedical informatics*, 46(2):266–274, 2013.

[79] Paul M Magwene, Paul Lizardi, and Junhyong Kim. Reconstructing the temporal ordering of biological samples using microarray data. *Bioinformatics*, 19(7):842–850, 2003.

[80] Kieran R Campbell and Christopher Yau. Uncovering pseudotemporal trajectories with covariates from single cell and bulk expression data. *Nature communications*, 9(1):2442, 2018.

[81] Anupam Gupta and Ziv Bar-Joseph. Extracting dynamics from static cancer expression data. *IEEE/ACM Transactions on Computational Biology and Bioinformatics*, 5(2):172–182, 2008.

[82] Arianna Dagliati, Nophar Geifman, Niels Peek, John H Holmes, Lucia Sacchi, Seyed Erfan Sajjadi, and Allan Tucker. Inferring temporal phenotypes with topological data analysis and pseudo time-series. In *Conference on Artificial Intelligence in Medicine in Europe*, pages 399–409. Springer, 2019.

[83] Pavithra Kumar, Yuqi Tan, and Patrick Cahan. Understanding development and stem cells using single cell-based analyses of gene expression. *Development*, 144(1):17–32, 2017. 29, 78

[84] David J Wales and Jonathan PK Doye. Global optimization by basin-hopping and the lowest energy structures of lennard-jones clusters containing up to 110 atoms. *The Journal of Physical Chemistry A*, 101(28):5111–5116, 1997. 30

[85] H Goldstein, CP Poole, and JL Safko. Variational principles and lagrange's equations. *Classical Dynamics, 3rd ed. Addison-Wesley*, pages 45–51, 2001. 31

[86] Atefeh Taherian Fard and Mark A Ragan. Modeling the attractor landscape of disease progression: a network-based approach. *Frontiers in genetics*, 8: 48, 2017. 32

[87] Boelkins M. Active calculus - single variable. `https://activecalculus.org/single/sec-1-8-tan-line-approx.html`, 2018. Accessed June 6, 2019. xvi, 33

[88] Yaman Barlas. Formal aspects of model validity and validation in system dynamics. *System Dynamics Review: The Journal of the System Dynamics Society*, 12(3):183–210, 1996. 40, 72

[89] US Department of Health, Human Services, et al. Us department of agriculture. 2015–2020 dietary guidelines for americans. december 2015, 2019. 42

[90] NHS UK. *What should my daily intake of calories be?*, Published 2016. Accessed June 5, 2019. URL `https://www.nhs.uk/common-health-questions/food-and-diet/what-should-my-daily-intake-of-calories-be/`.

[91] Voedingscentrum. Energie (calorieën). Published 2019. Accessed June 5, 2019. URL `https://www.voedingscentrum.nl/encyclopedie/energie.aspx`. 42

[92] Central Bureau for Statistics. Population; age, migration background, gender and region, 1 january. *Obtained on*, 14, 2019. 42

[93] Paul A McAuley, Haiying Chen, Duck-chul Lee, Enrique Garcia Artero, David A Bluemke, and Gregory L Burke. Physical activity, measures of obesity, and cardiometabolic risk: the multi-ethnic study of atherosclerosis (mesa). *Journal of Physical activity and health*, 11(4):831–837, 2014. 44, 45

[94] Gregory L Burke, Alain G Bertoni, Steven Shea, Russell Tracy, Karol E Watson, Roger S Blumenthal, Hyoju Chung, and Mercedes R Carnethon. The impact of obesity on cardiovascular disease risk factors and subclinical vascular disease: the multi-ethnic study of atherosclerosis. *Archives of internal medicine*, 168(9):928–935, 2008. 44, 45

[95] Lena Arnolda Brouwer, Bea Lalmahomed, and Henna Josias. *Different times, different girls: an investigation into the running away of Moroccan, Turkish, Hindustani and Creole girls*. Van Arkel, 1992. 45, 46

[96] Maja Deković, Trees Pels, and Suzanne Model. *Child rearing in six ethnic families: The multi-cultural Dutch experience*. Edwin Mellen Press, 2006. 45, 46

[97] Gjaanchand Mungra. *Hindustani families in the Netherlands*, volume 35. Center for Research on Social Opposites, 1990.

[98] Diana D van Bergen, Anton JLM van Balkom, Johannes H Smit, and Sawitri Saharso. "i felt so hurt and lonely": Suicidal behavior in south asian-surinamese, turkish, and moroccan women in the netherlands. *Transcultural psychiatry*, 49(1):69–86, 2012. 45, 46

[99] Deborah Gibson-Smith, Mariska Bot, Marieke Snijder, Mary Nicolaou, Eske M Derks, Karien Stronks, Ingeborg A Brouwer, Marjolein Visser, and Brenda WJH Penninx. The relation between obesity and depressed mood in a multi-ethnic population. the helius study. *Social psychiatry and psychiatric epidemiology*, 53(6):629–638, 2018.

[100] Umar Z Ikram, Marieke B Snijder, Matty AS de Wit, Aart H Schene, Karien Stronks, and Anton E Kunst. Perceived ethnic discrimination and depressive symptoms: the buffering effects of ethnic identity, religion and ethnic social network. *Social psychiatry and psychiatric epidemiology*, 51(5):679–688, 2016. 46

[101] Hibbah Araba Osei-Kwasi, Mary Nicolaou, Katie Powell, Laura Terragni, Lea Maes, Karien Stronks, Nanna Lien, Michelle Holdsworth, et al. Systematic mapping review of the factors influencing dietary behaviour in ethnic minority groups living in europe: a dedipac study. *International Journal of Behavioral Nutrition and Physical Activity*, 13(1):85, 2016. 47, 48

[102] Karen Hosper, Marije Deutekom, and Karien Stronks. The effectiveness of" exercise on prescription" in stimulating physical activity among women in ethnic minority groups in the netherlands: protocol for a randomized controlled trial. *BMC Public Health*, 8(1):406, 2008. 48

[103] David Kahan. Adult physical inactivity prevalence in the muslim world: Analysis of 38 countries. *Preventive medicine reports*, 2:71–75, 2015.

[104] Eman Sharara, Chaza Akik, Hala Ghattas, and Carla Makhlouf Obermeyer. Physical inactivity, gender and culture in arab countries: a systematic assessment of the literature. *BMC public health*, 18(1):639, 2018. 47

[105] Ryan E Rhodes, Heather M Macdonald, and Heather A McKay. Predicting physical activity intention and behaviour among children in a longitudinal sample. *Social science & medicine*, 62(12):3146–3156, 2006. 48

[106] A-M Hendriks, JS Gubbels, MWJ Jansen, and SPJ Kremers. Health beliefs regarding dietary behavior and physical activity of surinamese immigrants of indian descent in the netherlands: a qualitative study. *International Scholarly Research Notices*, 2012, 2012.

[107] Mary Nicolaou, Evalina Vlaar, Irene Van Valkengoed, Barend Middelkoop, Karien Stronks, and Vera Nierkens. Development of a diabetes prevention program for surinamese south asians in the netherlands. *Health Promotion International*, 29(4):680–691, 2014. 47, 48, 49

[108] M Nicolaou, S Benjelloun, K Stronks, RM Van Dam, JC Seidell, and CM Doak. Influences on body weight of female moroccan migrants in the netherlands: a qualitative study. *Health & Place*, 18(4):883–891, 2012. 47, 49

[109] World Health Organization. *WHO Global Health Observatory Data Repository [online database.*, Published 2013. Accessed May 21, 2013. URL `http://apps.who.int/gho/data/view.main`. 48

[110] World Health Organization. *Country Profiles on Nutrition, Physical Activity and Obesity in the 53 WHO European Region Member States: Netherlands.; 2013.*, Accessed June 5, 2019. URL `http://www.euro.who.int/__data/assets/pdf_file/0018/243315/Netherlands-WHO-Country-Profile.pdf`. 48

[111] M 'e rove Gijsberts and Jaco Dagevos. *Annual Report Integration 2009*. Social and Cultural Planning Office, 2009. 48

[112] Julia Lawton, N Ahmad, L Hanna, M Douglas, and N Hallowell. 'i can't do any serious exercise': barriers to physical activity amongst people of pakistani and indian origin with type 2 diabetes. *Health education research*, 21(1):43–54, 2006.

[113] Shelina Visram, Ann Crosland, John Unsworth, and Sue Long. Engaging women from south asian communities in cardiac rehabilitation. *International Journal of Therapy and Rehabilitation*, 15(7):298–305, 2008.

[114] Janani Sriskantharajah and Joe Kai. Promoting physical activity among south asian women with coronary heart disease and diabetes: what might help? *Family practice*, 24(1):71–76, 2007.

[115] Salma Khanam and Vassiliki Costarelli. Attitudes towards health and exercise of overweight women. *The journal of the Royal Society for the Promotion of Health*, 128(1):26–30, 2008.

[116] Stephen Abbott and Michael Riga. Delivering services to the bangladeshi community: the views of healthcare professionals in east london. *Public Health*, 121(12):935–941, 2007.

[117] Mihir Patel, Erica Phillips-Caesar, and Carla Boutin-Foster. Barriers to lifestyle behavioral change in migrant south asian populations. *Journal of immigrant and minority health*, 14(5):774–785, 2012. 48

[118] Issad Baddou, Asmaa El Hamdouchi, Imane El Harchaoui, Kaoutar Benjeddou, Naima Saeid, Mohammed Elmzibri, Khalid El Kari, and Hassan Aguenaou. Objectively measured physical activity and sedentary time among children and adolescents in morocco: A cross-sectional study. *BioMed research international*, 2018, 2018. 48

[119] Adina Batnitzky. Obesity and household roles: gender and social class in morocco. *Sociology of health & illness*, 30(3):445–462, 2008. 48

[120] Robert Crawford. Risk ritual and the management of control and anxiety in medical culture. *Health:*, 8(4):505–528, 2004. 48, 49

[121] Kathryn Dean. Self-care components of lifestyles: the importance of gender, attitudes and the social situation. *Social science & medicine*, 29(2):137–152, 1989.

[122] Dorit Teuscher, Andrea J Bukman, Marleen A van Baak, Edith JM Feskens, Reint Jan Renes, and Agnes Meershoek. Challenges of a healthy lifestyle for socially disadvantaged people of dutch, moroccan and turkish origin in the netherlands: a focus group study. *Critical Public Health*, 25(5):615–626, 2015.

[123] Mary Nicolaou, Colleen M Doak, Rob M van Dam, Johannes Brug, Karien Stronks, and Jaap C Seidell. Cultural and social influences on food consumption in dutch residents of turkish and moroccan origin: a qualitative study. *Journal of nutrition education and behavior*, 41(4):232–241, 2009. 48, 49

[124] A Blokstra, CM Burns, and JC Seidell. Perception of weight status and dieting behaviour in dutch men and women. *International Journal of Obesity*, 23(1):7–17, 1999. 49, 74

[125] M Nicolaou, AH Palsma, and K Stronks. The diet of young adults of turkish and moroccan descent. *A problem analysis and recommendations for nutritional interventions. Amsterdam: AMC, Department of Social Medicine*, 2007. 49

[126] Gemeente Amsterdam. *2.1.11 Bevolking Naar Leeftijdsgroepen En Migratieachtergrond, 1 Januari 2019.*, 2019. URL `https://www.voedingscentrum.nl/encyclopedie/energie.aspx`. 50

[127] Mary A Burke and Frank Heiland. Social dynamics of obesity. *Economic Inquiry*, 45(3):571–591, 2007. 70

[128] Trisha A Pruis and Jeri S Janowsky. Assessment of body image in younger and older women. *The Journal of General Psychology: Experimental, Psychological, and Comparative Psychology*, 137(3):225–238, 2010. 70

[129] Jennie Popay, Margaret Whitehead, and David J Hunter. Injustice is killing people on a large scale—but what is to be done about it?, 2010. 72

[130] Oli Williams and Simone Fullagar. Lifestyle drift and the phenomenon of 'citizen shift'in contemporary uk health policy. *Sociology of health & illness*, 41(1):20–35, 2019. 72

[131] Peter Craig, Srinivasa Vittal Katikireddi, Alastair Leyland, and Frank Popham. Natural experiments: an overview of methods, approaches, and contributions to public health intervention research. *Annual review of public health*, 38:39–56, 2017. 73

[132] Nicholas A Christakis and James H Fowler. The spread of obesity in a large social network over 32 years. *New England journal of medicine*, 357(4):370–379, 2007. 73

[133] Jane Wardle, Anne M Haase, Andrew Steptoe, Maream Nillapun, Kiriboon Jonwutiwes, and France Bellisie. Gender differences in food choice: the contribution of health beliefs and dieting. *Annals of behavioral medicine*, 27(2):107–116, 2004. 74

[134] Wenchi Liang, Mona C Shediac-Rizkallah, David D Celentano, and Charles Rohde. A population-based study of age and gender differences in patterns of health-related behaviors. *American journal of preventive medicine*, 17(1):8–17, 1999. 74

[135] Vanessa M Buote, Anne E Wilson, Erin J Strahan, Stephanie B Gazzola, and Fiona Papps. Setting the bar: Divergent sociocultural norms for women's and men's ideal appearance in real-world contexts. *Body image*, 8(4):322–334, 2011. 74

[136] Lenny R Vartanian and Jacqueline G Shaprow. Effects of weight stigma on exercise motivation and behavior: a preliminary investigation among college-aged females. *Journal of health psychology*, 13(1):131–138, 2008. 74

[137] Erin J Strahan, Anne E Wilson, Kate E Cressman, and Vanessa M Buote. Comparing to perfection: How cultural norms for appearance affect social comparisons and self-image. *Body image*, 3(3):211–227, 2006. 74

[138] Mary Nicolaou, Colleen Doak, Rob van Dam, Karen Hosper, Jaap Seidell, and Karien Stronks. Body size preference and body weight perception among two migrant groups of non-western origin. *Public health nutrition*, 11(12): 1332–1341, 2008. 74

[139] William Coffey and Yu P Kalmykov. *The Langevin equation: with applications to stochastic problems in physics, chemistry and electrical engineering*, volume 27. World Scientific, 2012. 78, 84

[140] Adrienne Chung and Rajiv N Rimal. Social norms: A review. *Review of Communication Research*, 4:1–28, 2016. 80, 84

[141] Paul E Smaldino and Joshua M Epstein. Social conformity despite individual preferences for distinctiveness. *Royal Society open science*, 2(3):140437, 2015. 80, 84

[142] Kylie Ball, Robert W Jeffery, Gavin Abbott, Sarah A McNaughton, and David Crawford. Is healthy behavior contagious: associations of social norms with physical activity and healthy eating. *International Journal of Behavioral Nutrition and Physical Activity*, 7(1):86, 2010. 80

[143] Jennifer E Pelletier, Dan J Graham, and Melissa N Laska. Social norms and dietary behaviors among young adults. *American journal of health behavior*, 38(1):144–152, 2014.

[144] Marla E Eisenberg and Jean L Forster. Adolescent smoking behavior: measures of social norms. *American journal of preventive medicine*, 25(2):122–128, 2003.

[145] Dana M Litt and Michelle L Stock. Adolescent alcohol-related risk cognitions: the roles of social norms and social networking sites. *Psychology of addictive behaviors*, 25(4):708, 2011. 80

[146] Loes Crielaard, Pritha Dutta, Rick Quax, Mary Nicolaou, Nadège Merabet, Karien Stronks, and Peter MA Sloot. Social norms and obesity prevalence: From cohort to system dynamics models. *Obesity Reviews*, 21(9):e13044, 2020. 80, 81, 99

[147] Stephen L Morgan and Christopher Winship. *Counterfactuals and causal inference*. Cambridge University Press, 2015. 81

[148] Robert Swendsen. *An introduction to statistical mechanics and thermodynamics*. Oxford University Press, USA, 2020. 84

[149] Richard Durrett. *Stochastic calculus: a practical introduction*, volume 6. CRC press, 1996. 84

[150] James E Gentle. *Random number generation and Monte Carlo methods*. Springer Science & Business Media, 2006. 85

[151] Bernard W Silverman. *Density estimation for statistics and data analysis*, volume 26. CRC press, 1986. 85

[152] Michael R Lowe, Emily H Feig, Samantha R Winter, and Eric Stice. Short-term variability in body weight predicts long-term weight gain. *The American journal of clinical nutrition*, 102(5):995–999, 2015. 92, 93

[153] Esther Van't Riet, Marjan Alssema, Josina M Rijkelijkhuizen, Piet J Kostense, Giel Nijpels, and Jacqueline M Dekker. Relationship between a1c and glucose levels in the general dutch population: the new hoorn study. *Diabetes care*, 33(1):61–66, 2010. 92, 93

[154] Anitra DM Koopman, Simone P Rauh, Esther van 't Riet, Lenka Groeneveld, Amber A Van Der Heijden, Petra J Elders, Jacqueline M Dekker, Giel Nijpels, Joline W Beulens, and Femke Rutters. The association between social jetlag, the metabolic syndrome, and type 2 diabetes mellitus in the general population: the new hoorn study. *Journal of biological rhythms*, 32 (4):359–368, 2017. 92

[155] Femke Rutters, Giel Nijpels, Petra Elders, Coen DA Stehouwer, Amber A van der Heijden, Lenka Groeneveld, Leen M 'T Hart, Jacqueline M Dekker, and Joline WJ Beulens. Cohort profile: the hoorn studies. *International journal of epidemiology*, 47(2):396–396j, 2018. 92, 93

[156] Marijka Batterham, Linda C Tapsell, and Karen E Charlton. Baseline characteristics associated with different bmi trajectories in weight loss trials: a case for better targeting of interventions. *European journal of clinical nutrition*, 70(2):207–211, 2016. 94

[157] Truls Østbye, Rahul Malhotra, and Lawrence R Landerman. Body mass trajectories through adulthood: results from the national longitudinal survey of youth 1979 cohort (1981–2006). *International journal of epidemiology*, 40 (1):240–250, 2011. 94

[158] World Health Organization. *Obesity: preventing and managing the global epidemic*. Number 894. World Health Organization, 2000. 94

[159] Tatsuo Tomita. Apoptosis in pancreatic β-islet cells in type 2 diabetes. *Bosnian Journal of Basic Medical Sciences*, 16(3):162, 2016. 101

[160] Alexandra E Butler, Juliette Janson, Susan Bonner-Weir, Robert Ritzel, Robert A Rizza, and Peter C Butler. β-cell deficit and increased β-cell apoptosis in humans with type 2 diabetes. *Diabetes*, 52(1):102–110, 2003. 123

[161] Miriam Cnop, Nils Welsh, Jean-Christophe Jonas, Anne Jörns, Sigurd Lenzen, and Decio L Eizirik. Mechanisms of pancreatic β-cell death in type 1 and type 2 diabetes: many differences, few similarities. *Diabetes*, 54(suppl 2):S97–S107, 2005. 101

[162] Anne Bertolotti, Yuhong Zhang, Linda M Hendershot, Heather P Harding, and David Ron. Dynamic interaction of bip and er stress transducers in the unfolded-protein response. *Nature Cell Biology*, 2(6):326, 2000. 102

[163] David Ron and Peter Walter. Signal integration in the endoplasmic reticulum unfolded protein response. *Nature Reviews Molecular Cell Biology*, 8(7):519, 2007. 102, 112

[164] Kamil Erguler, Myrtani Pieri, and Constantinos Deltas. A mathematical model of the unfolded protein stress response reveals the decision mechanism for recovery, adaptation and apoptosis. *BMC systems biology*, 7(1):16, 2013. 102

[165] Yu Ihara, Shinya Toyokuni, Koji Ichida, Hiroyuki Odaka, et al. Hyperglycemia causes oxidative stress in pancreatic beta-cells of gk rats, a model of type 2 diabetes. *Diabetes*, 48(4):927, 1999. 102

[166] Hongxiang Hui, Francesco Dotta, Umberto Di Mario, and Riccardo Perfetti. Role of caspases in the regulation of apoptotic pancreatic islet beta-cells death. *Journal of Cellular Physiology*, 200(2):177–200, 2004. 102, 112

[167] Cecilia Brannmark, Elin Nyman, Siri Fagerholm, Linnéa Bergenholm, Eva-Maria Ekstrand, Gunnar Cedersund, and Peter Stralfors. Insulin signaling in type 2 diabetes-experimental and modeling analyses reveal mechanisms of insulin resistance in human adipocytes. *Journal of Biological Chemistry*, pages jbc–M112, 2013. 102

[168] Meenu R Rajan, Elin Nyman, Cecilia Brännmark, Charlotta S Olofsson, and Peter Strålfors. Inhibition of foxo1 transcription factor in primary human adipocytes mimics the insulin resistant state of type 2 diabetes. *Biochemical Journal*, page BCJ20180144, 2018. 102

[169] Joydeep Sarkar, Gaurav Dwivedi, Qian Chen, Iris E Sheu, Mark Paich, Colleen M Chelini, Paul M D'Alessandro, and Samuel P Burns. A long-term mechanistic computational model of physiological factors driving the onset of type 2 diabetes in an individual. *PloS One*, 13(2):e0192472, 2018. 102

[170] István Albert, Juilee Thakar, Song Li, Ranran Zhang, and Réka Albert. Boolean network simulations for life scientists. *Source Code for Biology and Medicine*, 3(1):16, 2008. 103

[171] Ayako Yachie-Kinoshita, Kento Onishi, Joel Ostblom, Matthew A Langley, Eszter Posfai, Janet Rossant, and Peter W Zandstra. Modeling signaling-dependent pluripotency with boolean logic to predict cell fate transitions. *Molecular Systems Biology*, 14(1):e7952, 2018. 103, 106, 109

[172] Reka Albert and Juilee Thakar. Boolean modeling: a logic-based dynamic approach for understanding signaling and regulatory networks and for making

useful predictions. *Wiley Interdisciplinary Reviews: Systems Biology and Medicine*, 6(5):353–369, 2014. 103, 106

[173] Florent Allagnat, Foteini Christulia, Fernanda Ortis, Pierre Pirot, Stephan Lortz, Sigurd Lenzen, Decio L Eizirik, and Alessandra K Cardozo. Sustained production of spliced x-box binding protein 1 (xbp1) induces pancreatic beta cell dysfunction and apoptosis. *Diabetologia*, 53(6):1120–1130, 2010. 104, 112

[174] Fumihiko Urano, XiaoZhong Wang, Anne Bertolotti, Yuhong Zhang, Peter Chung, Heather P Harding, and David Ron. Coupling of stress in the er to activation of jnk protein kinases by transmembrane protein kinase ire1. *Science*, 287(5453):664–666, 2000. 104, 112

[175] Kathryn L Lipson, Sonya G Fonseca, Shinsuke Ishigaki, Linh X Nguyen, Elizabeth Foss, Rita Bortell, Aldo A Rossini, and Fumihiko Urano. Regulation of insulin biosynthesis in pancreatic beta cells by an endoplasmic reticulum-resident protein kinase ire1. *Cell Metabolism*, 4(3):245–254, 2006. 112

[176] Chunyan Xu, Beatrice Bailly-Maitre, and John C Reed. Endoplasmic reticulum stress: cell life and death decisions. *The Journal of Clinical Investigation*, 115(10):2656–2664, 2005. 104, 112

[177] Michael C Wei, Wei-Xing Zong, Emily H-Y Cheng, Tullia Lindsten, Vily Panoutsakopoulou, Andrea J Ross, Kevin A Roth, Grant R MacGregor, Craig B Thompson, and Stanley J Korsmeyer. Proapoptotic bax and bak: a requisite gateway to mitochondrial dysfunction and death. *Science*, 292 (5517):727–730, 2001. 104

[178] Karen D McCullough, Jennifer L Martindale, Lars-Oliver Klotz, Tak-Yee Aw, and Nikki J Holbrook. Gadd153 sensitizes cells to endoplasmic reticulum stress by down-regulating bcl2 and perturbing the cellular redox state. *Molecular and Cellular Biology*, 21(4):1249–1259, 2001. 104

[179] S1 Oyadomari and M Mori. Roles of chop/gadd153 in endoplasmic reticulum stress. *Cell Death and Differentiation*, 11(4):381, 2004. 104, 112

[180] Stefan J Marciniak, Chi Y Yun, Seiichi Oyadomari, Isabel Novoa, Yuhong Zhang, Rivka Jungreis, Kazuhiro Nagata, Heather P Harding, and David Ron. Chop induces death by promoting protein synthesis and oxidation in the stressed endoplasmic reticulum. *Genes & Development*, 18(24):3066–3077, 2004. 104

[181] Paul D Ray, Bo-Wen Huang, and Yoshiaki Tsuji. Reactive oxygen species (ros) homeostasis and redox regulation in cellular signaling. *Cellular Signalling*, 24(5):981–990, 2012. 104, 112

[182] Kei Tobiume, Atsushi Matsuzawa, Takumi Takahashi, Hideki Nishitoh, Keiichi Morita, Kohsuke Takeda, Osamu Minowa, Kohei Miyazono, Tetsuo Noda, and Hidenori Ichijo. Ask1 is required for sustained activations of

jnk/p38 map kinases and apoptosis. *EMBO Reports*, 2(3):222–228, 2001. 104, 112

[183] XiaoZhong Wang and David Ron. Stress-induced phosphorylation and activation of the transcription factor chop (gadd153) by p38 map kinase. *Science*, 272(5266):1347–1349, 1996. 104, 112

[184] Juliet A Emamaullee and AM James Shapiro. Interventional strategies to prevent β-cell apoptosis in islet transplantation. *Diabetes*, 55(7):1907–1914, 2006. 104

[185] Véronique Baud and Michael Karin. Signal transduction by tumor necrosis factor and its relatives. *Trends in Cell Biology*, 11(9):372–377, 2001. 104

[186] Hamid Akash, Muhammad Sajid, Kanwal Rehman, and Aamira Liaqat. Tumor necrosis factor-alpha: Role in development of insulin resistance and pathogenesis of type 2 diabetes mellitus. *Journal of Cellular Biochemistry*, 2018. 104

[187] Christoph Reinhard, Blanche Shamoon, Venkatakrishna Shyamala, and Lewis T Williams. Tumor necrosis factor α-induced activation of c-jun n-terminal kinase is mediated by traf2. *The EMBO Journal*, 16(5):1080–1092, 1997.

[188] Mike Rothe, Vidya Sarma, Vishva M Dixit, and David V Goeddel. Traf2-mediated activation of nf-kappa b by tnf receptor 2 and cd40. *Science*, 269 (5229):1424–1427, 1995. 104

[189] Peng Li, Deepak Nijhawan, Imawati Budihardjo, Srinivasa M Srinivasula, Manzoor Ahmad, Emad S Alnemri, and Xiaodong Wang. Cytochrome c and datp-dependent formation of apaf-1/caspase-9 complex initiates an apoptotic protease cascade. *Cell*, 91(4):479–489, 1997. 104

[190] Tencho Tenev, Anna Zachariou, Rebecca Wilson, Mark Ditzel, and Pascal Meier. Iaps are functionally non-equivalent and regulate effector caspases through distinct mechanisms. *Nature Cell Biology*, 7(1):70, 2005. 104, 113

[191] Martin Holcik, Hilary Gibson, and Robert G Korneluk. Xiap: apoptotic brake and promising therapeutic target. *Apoptosis*, 6(4):253–261, 2001. 104, 113

[192] Xavier Saelens, Nele Festjens, Lieselotte Vande Walle, Maria Van Gurp, Geert van Loo, and Peter Vandenabeele. Toxic proteins released from mitochondria in cell death. *Oncogene*, 23(16):2861, 2004. 104, 113

[193] Rachel J Perry, Varman T Samuel, Kitt F Petersen, and Gerald I Shulman. The role of hepatic lipids in hepatic insulin resistance and type 2 diabetes. *Nature*, 510(7503):84, 2014. 104

[194] Svetlana E Nikoulina, Theodore P Ciaraldi, Sunder Mudaliar, Pharis Mohideen, Leslie Carter, and Robert R Henry. Potential role of glycogen synthase kinase-3 in skeletal muscle insulin resistance of type 2 diabetes. *Diabetes*, 49(2):263–271, 2000.

[195] Francesca Favaretto, Gabriella Milan, Gayle B Collin, Jan D Marshall, Fabio Stasi, Pietro Maffei, Roberto Vettor, and Jürgen K Naggert. Glut4 defects in adipose tissue are early signs of metabolic alterations in alms1gt/gt, a mouse model for obesity and insulin resistance. *PloS One*, 9(10):e109540, 2014. 104

[196] Jongsoon Lee and Myung-Sunny Kim. The role of gsk3 in glucose homeostasis and the development of insulin resistance. *Diabetes Research and Clinical Practice*, 77(3):S49–S57, 2007. 104, 113

[197] Philip Cohen and Sheelagh Frame. The renaissance of gsk3. *Nature Reviews Molecular Cell Biology*, 2(10):769, 2001. 104, 113

[198] Zhiyong Cheng and Morris F White. Targeting forkhead box o1 from the concept to metabolic diseases: lessons from mouse models. *Antioxidants & Redox Signaling*, 14(4):649–661, 2011. 104, 113

[199] Stavroula Kousteni. Foxo1, the transcriptional chief of staff of energy metabolism. *Bone*, 50(2):437–443, 2012.

[200] Andreas Barthel and Dieter Schmoll. Novel concepts in insulin regulation of hepatic gluconeogenesis. *American Journal of Physiology-Endocrinology And Metabolism*, 285(4):E685–E692, 2003. 104, 113

[201] Leila Khamzina, Alain Veilleux, Sébastien Bergeron, and André Marette. Increased activation of the mammalian target of rapamycin pathway in liver and skeletal muscle of obese rats: possible involvement in obesity-linked insulin resistance. *Endocrinology*, 146(3):1473–1481, 2005. 104, 113

[202] Laura S Harrington, Greg M Findlay, Alex Gray, Tatiana Tolkacheva, Simon Wigfield, Heike Rebholz, Jill Barnett, Nick R Leslie, Susan Cheng, Peter R Shepherd, et al. The tsc1-2 tumor suppressor controls insulin–pi3k signaling via regulation of irs proteins. *The Journal of Cell Biology*, 166(2):213–223, 2004. 113

[203] O Jameel Shah, Zhiyong Wang, and Tony Hunter. Inappropriate activation of the tsc/rheb/mtor/s6k cassette induces irs1/2 depletion, insulin resistance, and cell survival deficiencies. *Current Biology*, 14(18):1650–1656, 2004. 104, 113

[204] Dung-Fang Lee, Hsu-Ping Kuo, Chun-Te Chen, Jung-Mao Hsu, Chao-Kai Chou, Yongkun Wei, Hui-Lung Sun, Long-Yuan Li, Bo Ping, Wei-Chien Huang, et al. Ikkβ suppression of tsc1 links inflammation and tumor angiogenesis via the mtor pathway. *Cell*, 130(3):440–455, 2007. 104

[205] Umut Özcan, Qiong Cao, Erkan Yilmaz, Ann-Hwee Lee, Neal N Iwakoshi, Esra Özdelen, Gürol Tuncman, Cem Görgün, Laurie H Glimcher, and Gökhan S Hotamisligil. Endoplasmic reticulum stress links obesity, insulin action, and type 2 diabetes. *Science*, 306(5695):457–461, 2004. 104

[206] Vincent Aguirre, Tohru Uchida, Lynne Yenush, Roger Davis, and Morris F White. The c-jun nh2-terminal kinase promotes insulin resistance during association with insulin receptor substrate-1 and phosphorylation of ser307. *Journal of Biological Chemistry*, 275(12):9047–9054, 2000. 113

[207] Jiro Hirosumi, Gürol Tuncman, Lufen Chang, Cem Z Görgün, K Teoman Uysal, Kazuhisa Maeda, Michael Karin, and Gökhan S Hotamisligil. A central role for jnk in obesity and insulin resistance. *Nature*, 420(6913):333, 2002. 104, 113

[208] Yingjiang Zhou, Justin Lee, Candace M Reno, Cheng Sun, Sang Won Park, Jason Chung, Jaemin Lee, Simon J Fisher, Morris F White, Sudha B Biddinger, et al. Regulation of glucose homeostasis through a xbp-1–foxo1 interaction. *Nature Medicine*, 17(3):356, 2011. 104

[209] Wei Zhang, Ville Hietakangas, Sheena Wee, Siew Choo Lim, Jayantha Gunaratne, and Stephen M Cohen. Er stress potentiates insulin resistance through perk-mediated foxo phosphorylation. *Genes & Development*, 27(4): 441–449, 2013. 104

[210] Nobumichi Ohoka, Satoshi Yoshii, Takayuki Hattori, Kikuo Onozaki, and Hidetoshi Hayashi. Trb3, a novel er stress-inducible gene, is induced via atf4–chop pathway and is involved in cell death. *The EMBO Journal*, 24(6): 1243–1255, 2005. 104, 113

[211] Ho-Jin Koh, Taro Toyoda, Michelle M Didesch, Min-Young Lee, Mark W Sleeman, Rohit N Kulkarni, Nicolas Musi, Michael F Hirshman, and Laurie J Goodyear. Tribbles 3 mediates endoplasmic reticulum stress-induced insulin resistance in skeletal muscle. *Nature Communications*, 4:1871, 2013. 104, 113

[212] Peter J Klover, Alicia H Clementi, and Robert A Mooney. Interleukin-6 depletion selectively improves hepatic insulin action in obesity. *Endocrinology*, 146(8):3417–3427, 2005. 104

[213] Peter J Klover, Teresa A Zimmers, Leonidas G Koniaris, and Robert A Mooney. Chronic exposure to interleukin-6 causes hepatic insulin resistance in mice. *Diabetes*, 52(11):2784–2789, 2003.

[214] Jane K Howard and Jeffrey S Flier. Attenuation of leptin and insulin signaling by socs proteins. *Trends in Endocrinology & Metabolism*, 17(9):365–371, 2006. 104

[215] Minoru Kanehisa and Susumu Goto. Kegg: kyoto encyclopedia of genes and genomes. *Nucleic Acids Research*, 28(1):27–30, 2000. 105

[216] Åsmund Flobak, Anaïs Baudot, Elisabeth Remy, Liv Thommesen, Denis Thieffry, Martin Kuiper, and Astrid Lægreid. Discovery of drug synergies in gastric cancer cells predicted by logical modeling. *PLoS computational biology*, 11(8):e1004426, 2015. 122

[217] Assieh Saadatpour, Rui-Sheng Wang, Aijun Liao, Xin Liu, Thomas P Loughran, István Albert, and Réka Albert. Dynamical and structural analysis of a t cell survival network identifies novel candidate therapeutic targets for large granular lymphocyte leukemia. *PLoS computational biology*, 7(11): e1002267, 2011.

[218] Herman F Fumia and Marcelo L Martins. Boolean network model for cancer pathways: predicting carcinogenesis and targeted therapy outcomes. *PloS one*, 8(7):e69008, 2013.

[219] Silvia Von der Heyde, Christian Bender, Frauke Henjes, Johanna Sonntag, Ulrike Korf, and Tim Beissbarth. Boolean erbb network reconstructions and perturbation simulations reveal individual drug response in different breast cancer cell lines. *BMC systems biology*, 8(1):1–22, 2014. 122

[220] Jacques Rahier, Yves Guiot, RM Goebbels, Christine Sempoux, and Jean-Claude Henquin. Pancreatic β-cell mass in european subjects with type 2 diabetes. *Diabetes, Obesity and Metabolism*, 10:32–42, 2008. 123

[221] H Siebe Spijker, Heein Song, Johanne H Ellenbroek, Maaike M Roefs, Marten A Engelse, Erik Bos, Abraham J Koster, Ton J Rabelink, Barbara C Hansen, Anne Clark, et al. Loss of β-cell identity occurs in type 2 diabetes and is associated with islet amyloid deposits. *Diabetes*, 64(8):2928–2938, 2015. 123, 124

[222] Marlon E Cerf. Transcription factors regulating β-cell function. *European Journal of Endocrinology*, 155(5):671–679, 2006. 124

[223] Jochen Seufert, Gordon C Weir, Joel F Habener, et al. Differential expression of the insulin gene transcriptional repressor ccaat/enhancer-binding protein beta and transactivator islet duodenum homeobox-1 in rat pancreatic beta cells during the development of diabetes mellitus. *The Journal of clinical investigation*, 101(11):2528–2539, 1998.

[224] Chuan Zhang, Takashi Moriguchi, Miwako Kajihara, Ritsuko Esaki, Ayako Harada, Homare Shimohata, Hisashi Oishi, Michito Hamada, Naoki Morito, Kazuteru Hasegawa, et al. Mafa is a key regulator of glucose-stimulated insulin secretion. *Molecular and cellular biology*, 25(12):4969–4976, 2005. 124

[225] Teresa Ree Chay and Joel Keizer. Minimal model for membrane oscillations in the pancreatic beta-cell. *Biophysical journal*, 42(2):181–189, 1983. 125, 126, 128, 137, 154

[226] Joel Keizer and Gerhard Magnus. Atp-sensitive potassium channel and bursting in the pancreatic beta cell. a theoretical study. *Biophysical Journal*, 56 (2):229–242, 1989. 125

[227] Gerhard Magnus and Joel Keizer. Model of β-cell mitochondrial calcium handling and electrical activity. ii. mitochondrial variables. *American Journal of Physiology-Cell Physiology*, 274(4):C1174–C1184, 1998. 125

[228] Gerhard Magnus and Joel Keizer. Model of β-cell mitochondrial calcium handling and electrical activity. i. cytoplasmic variables. *American Journal of Physiology-Cell Physiology*, 274(4):C1158–C1173, 1998. 125

[229] Paul Smolen and Joel Keizer. Slow voltage inactivation of ca 2+ currents and bursting mechanisms for the mouse pancreatic beta-cell. *The Journal of membrane biology*, 127(1):9–19, 1992. 125, 126, 128, 129, 134, 135, 137, 155

[230] Joel Keizer and Paul Smolen. Bursting electrical activity in pancreatic beta cells caused by ca (2+)-and voltage-inactivated ca2+ channels. *Proceedings of the National Academy of Sciences*, 88(9):3897–3901, 1991. 125, 129, 134, 135

[231] Gerhard Magnus and J Keizer. Minimal model of beta-cell mitochondrial ca2+ handling. *American Journal of Physiology-Cell Physiology*, 273(2): C717–C733, 1997. 125

[232] Richard Bertram, Paul Smolen, Arthur Sherman, David Mears, Illani Atwater, Franz Martin, and Bernat Soria. A role for calcium release-activated current (crac) in cholinergic modulation of electrical activity in pancreatic beta-cells. *Biophysical Journal*, 68(6):2323–2332, 1995. 125

[233] Teresa Ree Chay. Electrical bursting and luminal calcium oscillation in excitable cell models. *Biological cybernetics*, 75(5):419–431, 1996. 125

[234] Richard Bertram, Leslie S Satin, Morten Gram Pedersen, Dan S Luciani, and Arthur Sherman. Interaction of glycolysis and mitochondrial respiration in metabolic oscillations of pancreatic islets. *Biophysical Journal*, 92(5):1544–1555, 2007. 126

[235] Frank Diederichs. Mathematical simulation of membrane processes and metabolic fluxes of the pancreatic β-cell. *Bulletin of mathematical biology*, 68(7):1779–1818, 2006.

[236] Frank Diederichs. Ion homeostasis and the functional roles of serca reactions in stimulus–secretion coupling of the pancreatic β-cell: A mathematical simulation. *Biophysical chemistry*, 134(3):119–143, 2008.

[237] Leonid E Fridlyand, Natalia Tamarina, and Louis H Philipson. Modeling of ca2+ flux in pancreatic β-cells: role of the plasma membrane and intracellular stores. *American Journal of Physiology-Endocrinology and Metabolism*, 285 (1):E138–E154, 2003.

[238] Richard Bertram, Joseph Previte, Arthur Sherman, Tracie A Kinard, and Leslie S Satin. The phantom burster model for pancreatic β-cells. *Biophysical journal*, 79(6):2880–2892, 2000.

[239] Richard Bertram and Arthur Sherman. A calcium-based phantom bursting model for pancreatic islets. *Bulletin of mathematical biology*, 66(5):1313–1344, 2004. 126

[240] Richard Bertram, Arthur Sherman, and Leslie S Satin. Metabolic and electrical oscillations: partners in controlling pulsatile insulin secretion. *American Journal of Physiology-Endocrinology And Metabolism*, 293(4):E890–E900, 2007. 156

[241] Leonid E Fridlyand and Louis H Philipson. Glucose sensing in the pancreatic beta cell: a computational systems analysis. *Theoretical Biology and Medical Modelling*, 7(1):1–44, 2010. 126, 128, 129, 132, 155

[242] Benjamin Wacquier, Laurent Combettes, Guy Tran Van Nhieu, and Geneviève Dupont. Interplay between intracellular ca 2+ oscillations and ca 2+-stimulated mitochondrial metabolism. *Scientific reports*, 6(1):1–16, 2016. 126, 128, 129, 130, 131, 132, 133, 134, 136, 137, 152, 153, 154, 155

[243] Arash Moshkforoush, Baarbod Ashenagar, Nikolaos M Tsoukias, and B Rita Alevriadou. Modeling the role of endoplasmic reticulum-mitochondria microdomains in calcium dynamics. *Scientific reports*, 9(1):1–16, 2019.

[244] Hong Qi, Linxi Li, and Jianwei Shuai. Optimal microdomain crosstalk between endoplasmic reticulum and mitochondria for ca 2+ oscillations. *Scientific reports*, 5(1):1–11, 2015.

[245] Camilla Luni, Jamey D Marth, and Francis J Doyle III. Computational modeling of glucose transport in pancreatic β-cells identifies metabolic thresholds and therapeutic targets in diabetes. *PloS one*, 7(12):e53130, 2012. 126, 128, 129, 131, 152

[246] Alessandro Bertuzzi, Serenella Salinari, and Geltrude Mingrone. Insulin granule trafficking in β-cells: mathematical model of glucose-induced insulin secretion. *American Journal of Physiology-Endocrinology and Metabolism*, 293 (1):E396–E409, 2007.

[247] Morten Gram Pedersen, Alberto Corradin, Gianna M Toffolo, and Claudio Cobelli. A subcellular model of glucose-stimulated pancreatic insulin secretion. *Philosophical Transactions of the Royal Society A: Mathematical, Physical and Engineering Sciences*, 366(1880):3525–3543, 2008. 126

[248] Erica J Graham. *Mathematical models of mechanisms underlying long-term type 2 diabetes progression*. The University of Utah, 2012. 126, 128, 130, 143, 144, 145, 154, 155

[249] Patrick E MacDonald, Jamie W Joseph, and Patrik Rorsman. Glucose-sensing mechanisms in pancreatic β-cells. *Philosophical Transactions of the Royal Society B: Biological Sciences*, 360(1464):2211–2225, 2005. 132, 135, 144

[250] Richard Bertram, Morten Gram Pedersen, Dan S Luciani, and Arthur Sherman. A simplified model for mitochondrial atp production. *Journal of theoretical biology*, 243(4):575–586, 2006. 133

[251] Sreenath S Andrali, Megan L Sampley, Nathan L Vanderford, and Sabire Özcan. Glucose regulation of insulin gene expression in pancreatic β-cells. *Biochemical Journal*, 415(1):1–10, 2008. 138

[252] Vincent Poitout, Derek Hagman, Roland Stein, Isabella Artner, R Paul Robertson, and Jamie S Harmon. Regulation of the insulin gene by glucose and fatty acids. *The Journal of nutrition*, 136(4):873–876, 2006. 138

[253] Dominique A Glauser and Werner Schlegel. The emerging role of foxo transcription factors in pancreatic β cells. *Journal of Endocrinology*, 193(2): 195–207, 2007. 138

[254] Jian Ma, Smita Matkar, Xin He, and Xianxin Hua. Foxo family in regulating cancer and metabolism. In *Seminars in cancer biology*, volume 50, pages 32–41. Elsevier, 2018. 138

[255] Dan Kawamori, Yoshitaka Kajimoto, Hideaki Kaneto, Yutaka Umayahara, Yoshio Fujitani, Takeshi Miyatsuka, Hirotaka Watada, Ingo B Leibiger, Yoshimitsu Yamasaki, and Masatsugu Hori. Oxidative stress induces nucleo-cytoplasmic translocation of pancreatic transcription factor pdx-1 through activation of c-jun nh2-terminal kinase. *Diabetes*, 52(12):2896–2904, 2003. 138, 164

[256] Tadahiro Kitamura, Jun Nakae, Yukari Kitamura, Yoshiaki Kido, William H Biggs, Christopher VE Wright, Morris F White, Karen C Arden, Domenico Accili, et al. The forkhead transcription factor foxo1 links insulin signaling to pdx1 regulation of pancreatic β cell growth. *The Journal of clinical investigation*, 110(12):1839–1847, 2002.

[257] Dan Kawamori, Hideaki Kaneto, Yoshihisa Nakatani, Taka-aki Matsuoka, Munehide Matsuhisa, Masatsugu Hori, and Yoshimitsu Yamasaki. The forkhead transcription factor foxo1 bridges the jnk pathway and the transcription factor pdx-1 through its intracellular translocation. *Journal of Biological Chemistry*, 281(2):1091–1098, 2006. 138

[258] Darren AE Cross, Dario R Alessi, Philip Cohen, Mirjana Andjelkovich, and Brian A Hemmings. Inhibition of glycogen synthase kinase-3 by insulin mediated by protein kinase b. *Nature*, 378(6559):785–789, 1995. 138

[259] Marie-Josée Boucher, Lars Selander, Lennart Carlsson, and Helena Edlund. Phosphorylation marks ipf1/pdx1 protein for degradation by glycogen synthase kinase 3-dependent mechanisms. *Journal of Biological Chemistry*, 281 (10):6395–6403, 2006. 138

[260] Song-iee Han, Shinsaku Aramata, Kunio Yasuda, and Kohsuke Kataoka. Mafa stability in pancreatic β cells is regulated by glucose and is dependent on its constitutive phosphorylation at multiple sites by glycogen synthase kinase 3. *Molecular and Cellular Biology*, 27(19):6593, 2007.

[261] Rohan K Humphrey, Shu-Mei Yu, Luis E Flores, and Ulupi S Jhala. Glucose regulates steady-state levels of pdx1 via the reciprocal actions of gsk3 and akt kinases. *Journal of Biological Chemistry*, 285(5):3406–3416, 2010. 138, 164

[262] Yukari Ido Kitamura, Tadahiro Kitamura, Jan-Philipp Kruse, Jeffrey C Raum, Roland Stein, Wei Gu, and Domenico Accili. Foxo1 protects against pancreatic β cell failure through neurod and mafa induction. *Cell metabolism*, 2(3):153–163, 2005. 138

[263] Nicola J Darling and Simon J Cook. The role of mapk signalling pathways in the response to endoplasmic reticulum stress. *Biochimica et Biophysica Acta (BBA)-Molecular Cell Research*, 1843(10):2150–2163, 2014. 138

[264] Yong Son, Yong-Kwan Cheong, Nam-Ho Kim, Hun-Taeg Chung, Dae Gill Kang, and Hyun-Ock Pae. Mitogen-activated protein kinases and reactive oxygen species: how can ros activate mapk pathways? *Journal of signal transduction*, 2011, 2011. 138

[265] Jordi Lanuza-Masdeu, M Isabel Arévalo, Cristina Vila, Albert Barberà, Ramon Gomis, and Carme Caelles. In vivo jnk activation in pancreatic β-cells leads to glucose intolerance caused by insulin resistance in pancreas. *Diabetes*, 62(7):2308–2317, 2013. 138

[266] Jun Shirakawa and Yasuo Terauchi. Selective and sequential loss of transcriptional factors: A hallmark of β-cell failure in type 2 diabetes? *Journal of diabetes investigation*, 5(4):359, 2014. 138

[267] Sumaira Z Hasnain, Johannes B Prins, and Michael A McGuckin. Oxidative and endoplasmic reticulum stress in b-cell dysfunction in diabetes. *J Mol Endocrinol*, 56(2):33–54, 2016. 142

[268] Pierre Maechler, Ning Li, Marina Casimir, Laurène Vetterli, Francesca Frigerio, and Thierry Brun. Role of mitochondria in β-cell function and dysfunction. *The Islets of Langerhans*, pages 193–216, 2010. 144

[269] Hideaki Kaneto, Naoto Katakami, Munehide Matsuhisa, and Taka-aki Matsuoka. Role of reactive oxygen species in the progression of type 2 diabetes and atherosclerosis. *Mediators of inflammation*, 2010, 2010. 144

[270] DF Steiner, S-Y Park, J Støy, LH Philipson, and GI Bell. A brief perspective on insulin production. *Diabetes, Obesity and Metabolism*, 11:189–196, 2009. 144, 145

[271] Michael P Murphy. How mitochondria produce reactive oxygen species. *Biochemical journal*, 417(1):1–13, 2009. 144

[272] Ru-Zhou Zhao, Shuai Jiang, Lin Zhang, and Zhi-Bin Yu. Mitochondrial electron transport chain, ros generation and uncoupling. *International journal of molecular medicine*, 44(1):3–15, 2019. 144

[273] James Kennedy and Russell Eberhart. Particle swarm optimization. In *Proceedings of ICNN'95-international conference on neural networks*, volume 4, pages 1942–1948. IEEE, 1995. 145

[274] Lester James Miranda. Pyswarms: a research toolkit for particle swarm optimization in python. *Journal of Open Source Software*, 3(21):433, 2018. 145

[275] George H Patterson, Susan M Knobel, Per Arkhammar, Ole Thastrup, and David W Piston. Separation of the glucose-stimulated cytoplasmic and mitochondrial nad (p) h responses in pancreatic islet β cells. *Proceedings of the National Academy of Sciences*, 97(10):5203–5207, 2000. 147, 155

[276] Akos A Gerencser, Shona A Mookerjee, Martin Jastroch, and Martin D Brand. Measurement of the absolute magnitude and time courses of mitochondrial membrane potential in primary and clonal pancreatic beta-cells. *PLoS One*, 11(7):e0159199, 2016. 155

[277] Jean-Claude Henquin, Myriam Nenquin, Patrick Stiernet, and Bo Ahren. In vivo and in vitro glucose-induced biphasic insulin secretion in the mouse: pattern and role of cytoplasmic ca2+ and amplification signals in β-cells. *Diabetes*, 55(2):441–451, 2006. 155

[278] Donner F Babcock, James Herrington, Paul C Goodwin, Young Bae Park, and Bertil Hille. Mitochondrial participation in the intracellular ca2+ network. *The Journal of cell biology*, 136(4):833–844, 1997. 155

[279] Anna Weiser, Jerome N Feige, and Umberto De Marchi. Mitochondrial calcium signaling in pancreatic β-cell. *International Journal of Molecular Sciences*, 22(5):2515, 2021. 155

[280] Anders Tengholm, Bo Hellman, and Erik Gylfe. Glucose regulation of free ca2+ in the endoplasmic reticulum of mouse pancreatic beta cells. *Journal of Biological Chemistry*, 274(52):36883–36890, 1999. 155

[281] Anders Tengholm, Bo Hellman, and Erik Gylfe. The endoplasmic reticulum is a glucose-modulated high-affinity sink for ca2+ in mouse pancreatic β-cells. *The Journal of physiology*, 530(3):533–540, 2001. 155

[282] David A Bushinsky and Rebeca D Monk. Calcium. *The Lancet*, 352(9124): 306–311, 1998. 147, 155

[283] Dan S Luciani, Stanley Misler, and Kenneth S Polonsky. Ca2+ controls slow nad (p) h oscillations in glucose-stimulated mouse pancreatic islets. *The Journal of physiology*, 572(2):379–392, 2006. 147, 156

[284] Takashi Tanaka, Kazuaki Nagashima, Nobuya Inagaki, Hidetaka Kioka, Seiji Takashima, Hajime Fukuoka, Hiroyuki Noji, Akira Kakizuka, and Hiromi Imamura. Glucose-stimulated single pancreatic islets sustain increased cytosolic atp levels during initial ca2+ influx and subsequent ca2+ oscillations. *Journal of Biological Chemistry*, 289(4):2205–2216, 2014. 148

[285] Hideaki Kaneto, Gang Xu, Nobuharu Fujii, Shokei Kim, Susan Bonner-Weir, and Gordon C Weir. Involvement of c-jun n-terminal kinase in oxidative stress-mediated suppression of insulin gene expression. *Journal of Biological Chemistry*, 277(33):30010–30018, 2002. 149

[286] Jeffrey F Markuns, Jørgen FP Wojtaszewski, and Laurie J Goodyear. Insulin and exercise decrease glycogen synthase kinase-3 activity by different mechanisms in rat skeletal muscle. *Journal of Biological Chemistry*, 274(35): 24896–24900, 1999. 150

[287] R Aikin, S Hanley, D Maysinger, M Lipsett, M Castellarin, S Paraskevas, and L Rosenberg. Autocrine insulin action activates akt and increases survival of isolated human islets. *Diabetologia*, 49(12):2900–2909, 2006. 151

[288] PM Dean. Ultrastructural morphometry of the pancreatic β-cell. *Diabetologia*, 9(2):115–119, 1973. 152

[289] Leonid E Fridlyand, Li Ma, and Louis H Philipson. Adenine nucleotide regulation in pancreatic β-cells: modeling of atp/adp-ca2+ interactions. *American Journal of Physiology-Endocrinology and Metabolism*, 289(5):E839–E848, 2005. 152

[290] Michael Welsh, David A Nielsen, Albert J MacKrell, and Donald F Steiner. Control of insulin gene expression in pancreatic beta-cells and in an insulin-producing cell line, rin-5f cells. ii. regulation of insulin mrna stability. *Journal of Biological Chemistry*, 260(25):13590–13594, 1985. 154

[291] Henrik Kindmark, Martin KoHERE!HERE!hler, Graham Brown, Robert Branstrom, Olof Larsson, and Per-Olof Berggren. Glucose-induced oscillations in cytoplasmic free ca2+ concentration precede oscillations in mitochondrial membrane potential in the pancreatic β-cell. *Journal of Biological Chemistry*, 276(37):34530–34536, 2001. 156, 162

[292] Peter Krippeit-Drews, Martina Düfer, and Gisela Drews. Parallel oscillations of intracellular calcium activity and mitochondrial membrane potential in mouse pancreatic b-cells. *Biochemical and biophysical research communications*, 267(1):179–183, 2000. 156

[293] Olof Idevall-Hagren and Anders Tengholm. Metabolic regulation of calcium signaling in beta cells. In *Seminars in cell & developmental biology*, volume 103, pages 20–30. Elsevier, 2020. 156

[294] Anders Tengholm and Erik Gylfe. Oscillatory control of insulin secretion. *Molecular and cellular endocrinology*, 297(1-2):58–72, 2009.

[295] Patrick E MacDonald and Patrik Rorsman. Oscillations, intercellular coupling, and insulin secretion in pancreatic β cells. *PLoS biology*, 4(2):e49, 2006. 156

[296] Emma Heart, Richard F Corkey, Jacob D Wikstrom, Orian S Shirihai, and Barbara E Corkey. Glucose-dependent increase in mitochondrial membrane potential, but not cytoplasmic calcium, correlates with insulin secretion in single islet cells. *American Journal of Physiology-Endocrinology and Metabolism*, 290(1):E143–E148, 2006. 162

[297] Jakob D Wikstrom, Shana M Katzman, Hibo Mohamed, Gilad Twig, Solomon A Graf, Emma Heart, Anthony JA Molina, Barbara E Corkey, Lina Moitoso de Vargas, Nika N Danial, et al. β-cell mitochondria exhibit membrane potential heterogeneity that can be altered by stimulatory or toxic fuel levels. *Diabetes*, 56(10):2569–2578, 2007. 162

[298] Philippe Detimary, Patrick Gilon, and Jean-Claude Henquin. Interplay between cytoplasmic ca2+ and the atp/adp ratio: a feedback control mechanism in mouse pancreatic islets. *Biochemical Journal*, 333(2):269–274, 1998. 162

[299] Philippe Detimary, Georges Van den Berghe, and Jean-Claude Henquin. Concentration dependence and time course of the effects of glucose on adenine and guanine nucleotides in mouse pancreatic islets. *Journal of Biological Chemistry*, 271(34):20559–20565, 1996. 162

[300] R Paul Robertson. Chronic oxidative stress as a central mechanism for glucose toxicity in pancreatic islet beta cells in diabetes. *Journal of Biological Chemistry*, 279(41):42351–42354, 2004. 162, 164

[301] Koji Sakai, Kazuya Matsumoto, Takeshi Nishikawa, Mihoshi Suefuji, Kazuhiko Nakamaru, Yoshiaki Hirashima, Junji Kawashima, Tetsuya Shirotani, Kenshi Ichinose, Michael Brownlee, et al. Mitochondrial reactive oxygen species reduce insulin secretion by pancreatic β-cells. *Biochemical and biophysical research communications*, 300(1):216–222, 2003. 162

[302] Srividya Vasu, Neville H McClenaghan, Jane T McCluskey, and Peter R Flatt. Cellular responses of novel human pancreatic β-cell line, 1.1 b4 to hyperglycemia. *Islets*, 5(4):170–177, 2013. 164

[303] Naoki Shimo, Taka-aki Matsuoka, Takeshi Miyatsuka, Satomi Takebe, Yoshihiro Tochino, Mitsuyoshi Takahara, Hideaki Kaneto, and Iichiro Shimomura. Short-term selective alleviation of glucotoxicity and lipotoxicity ameliorates

the suppressed expression of key β-cell factors under diabetic conditions. *Biochemical and biophysical research communications*, 467(4):948–954, 2015. 164

[304] Jamie S Harmon, Catherine E Gleason, Yoshito Tanaka, Elizabeth A Oseid, Kimberly K Hunter-Berger, and R Paul Robertson. In vivo prevention of hyperglycemia also prevents glucotoxic effects on pdx-1 and insulin gene expression. *Diabetes*, 48(10):1995–2000, 1999.

[305] Yoshito Tanaka, Catherine E Gleason, Phuong Oanh T Tran, Jamie S Harmon, and R Paul Robertson. Prevention of glucose toxicity in hit-t15 cells and zucker diabetic fatty rats by antioxidants. *Proceedings of the National Academy of Sciences*, 96(19):10857–10862, 1999.

[306] Jamie S Harmon, Roland Stein, and R Paul Robertson. Oxidative stress-mediated, post-translational loss of mafa protein as a contributing mechanism to loss of insulin gene expression in glucotoxic beta cells. *Journal of biological chemistry*, 280(12):11107–11113, 2005. 164

[307] Melissa F Brereton, Michaela Iberl, Kenju Shimomura, Quan Zhang, Alice E Adriaenssens, Peter Proks, Ioannis I Spiliotis, William Dace, Katia K Mattis, Reshma Ramracheya, et al. Reversible changes in pancreatic islet structure and function produced by elevated blood glucose. *Nature communications*, 5 (1):1–11, 2014. 168

[308] Zhiyu Wang, Nathaniel W York, Colin G Nichols, and Maria S Remedi. Pancreatic β cell dedifferentiation in diabetes and redifferentiation following insulin therapy. *Cell metabolism*, 19(5):872–882, 2014. 168